

Extensions and Applications of the Common-Reflection-Surface Stack Method

Erweiterungen und Anwendungen der Common-Reflection-Surface-Stack-Methode

Zur Erlangung des akademischen Grades eines
DOKTORS DER NATURWISSENSCHAFTEN

von der Fakultät für Physik der
Universität Karlsruhe (TH)
genehmigte

DISSERTATION

von

Dipl.-Geophys. Jürgen Mann

aus

Leonberg

Tag der mündlichen Prüfung:

12. Juli 2002

Referent:

Prof. Dr. Peter Hubral

Korreferent:

Prof. Dr. Serge Shapiro

Abstract

A common task in seismic reflection imaging is to generate a structural image of the subsurface. This means that discontinuities in the recorded pre-stack data, the reflection events, have to be transformed into discontinuities of the medium properties, the reflectors, in the depth domain. The kinematic aspects of wave propagation provide the location of the subsurface reflectors. If the dynamic properties of wave propagation are also considered, the image additionally provides amplitudes that are related to the local reflection coefficients along these reflectors. A crucial problem of the imaging task is that the transformation from the pre-stack time domain to the depth domain requires the knowledge of the propagation velocities in the subsurface, at least at large scale: a smooth macro-velocity model is usually sufficient. However, such a model is, in general, not available a priori and has to be iteratively and interactively elaborated with significant effort.

In contrast to such *model-based* imaging methods, the imaging method presented in this thesis, the *Common-Reflection-Surface (CRS) stack*, is an entirely *data-oriented* approach that avoids the explicit parameterization of the depth model. Instead, the CRS stack directly makes use of the inherent redundancy in the pre-stack data and parameterizes the reflection events in the time domain. In this way, reflection energy stemming from one and the same reflector segment (or CRS) can be identified and summed: by means of coherence analysis in the pre-stack data, a second-order approximation of the kinematic reflection response of the CRS, the so-called CRS stacking operator, can be determined that fits best the actual reflection event. This approach is suited to simulate a zero-offset (ZO) section of high quality and high signal-to-noise ratio from the pre-stack data. Additionally, the parameters of the CRS stacking operators are available at any simulated ZO location. These kinematic CRS wavefield attributes are useful for a variety of applications, e. g., the estimation of the projected first Fresnel zone for ZO, the geometrical spreading factor, attribute-based time migration, and inversion, just to name a few.

In this thesis, I derive the CRS stacking operator for 2-D data acquisition based on the concepts of geometrical optics using object and image points. I introduce a new, extended strategy to determine the CRS wavefield attributes in an efficient way. This extended CRS stack strategy is able to handle more general situations compared to previously existing strategies: conflicting dip situations where two events intersect each other in the ZO section can now be handled such that each contributing event is detected and parameterized separately. A new attractive application of the wavefield attributes is introduced by merging concepts of Kirchhoff time migration and the CRS stack: by means of the approximate *diffraction* response of a hypothetical subsurface diffractor, the CRS stack results can be re-mapped to provide an attribute-based time migration

result and, in principle, a conventional time migration velocity model. As an additional feature, I transfer the concept of operator tapering from Kirchhoff migration to the CRS stack approach.

I present an object-oriented implementation of the extended CRS stack strategy that includes several applications of the wavefield attributes. The implementation is designed to handle irregular acquisition geometries and uses a data format compatible to a common industry standard. I discuss the practical aspects of aperture sizes, tapering, and the implementation of the search strategies for the wavefield attributes.

This implementation is applied to three different marine data sets, one of them synthetic, the other two acquired offshore Chile and Costa Rica, respectively. The results for the real data examples are compared with the results obtained by means of conventional imaging methods, namely the normal moveout/dip moveout(NMO/DMO)/stack processing chain. On the one hand, this comparison reveals the superior ability of the CRS stack approach to image steep events and to detect and characterize reflection events in the pre-stack data, even in the case of poor data quality. On the other hand, the data examples also demonstrate the limitations of the CRS stack method: the method breaks down whenever the reflections can no longer be described with sufficient accuracy by means of an approximate operator of second-order or, even worse, the subsurface is so complex that no coherent reflection events can be found in the pre-stack data at all. The latter situation causes all usual imaging methods to fail, the former is problematic for most data-oriented methods.

For the different data examples, I present several useful applications of the CRS wavefield attributes: the identification of diffraction and reflection events, the estimation of the projected first Fresnel zone, attribute-based time migration, and the identification of multiples. Except the last one, such applications cannot be performed with the parameters obtained by conventional data-oriented imaging. For the deep-offshore data, I additionally discuss the results of post-stack depth migrations of the conventional result and the CRS result, respectively, as the time domain images do not fully reveal the actual improvement.

Zusammenfassung

Vorbemerkung

Mit Ausnahme dieses Kapitels ist die vorliegende Arbeit in Englisch verfasst. Die grundlegenden Aspekte der Arbeit sind im Folgenden zusammengefasst. Da für die meisten der vorkommenden englischen Fachtermini keine adäquaten deutschen Ausdrücke zur Verfügung stehen, habe ich diese Ausdrücke in ihrer Originalform wiedergegeben. Zur leichteren Erkennbarkeit sind solche Begriffe *kursiv* gesetzt. Die Mischung beider Sprachen führt zwangsläufig zu gewissen Inkonsistenzen hinsichtlich Geschlecht und fallspezifischer Suffizes. In Fällen, in denen vergleichbare Termini im Deutschen existieren oder als Fremdworte etabliert sind, orientiere ich mich dabei an den gebräuchlichen Schemata, ansonsten verwende ich faktisch willkürliche Zuordnungen, die meinem persönlichen Sprachempfinden am wenigsten widersprechen.

Zu Gunsten der Lesbarkeit habe ich in dieser Zusammenfassung weitgehend auf die Angaben von Referenzen und zur Herkunft der Datenbeispiele verzichtet. Diese Informationen sind im Hauptteil der Arbeit zu finden.

Einführung

Die Reflexionsseismik ist neben anderen Methoden wie Gravimetrie, Geoelektrik, Tellurik, Georadar und der Messung des Erdmagnetfelds und natürlich auch anderen seismischen Methoden wie Refraktionsseismik und Teleseismik ein etabliertes Messverfahren in der Geophysik. Während zahlreiche der genannten Methoden schon seit langer Zeit bekannt und gebräuchlich sind, hat sich die Reflexionsseismik erst im Laufe des zwanzigsten Jahrhunderts zur Anwendungsreife entwickelt. Mittlerweile stellt diese Methodik das wichtigste und erfolgreichste Werkzeug zur Exploration von Rohstoffen dar, wobei der Schwerpunkt eindeutig im Bereich der fossilen Kohlenwasserstoffvorkommen liegt.

In der Reflexionsseismik wird die Ausbreitung durch künstliche Quellen angeregter Raumwellen in elastischen Medien untersucht, die üblicherweise mit Hilfe der elastodynamischen Wellengleichung beschrieben wird. Dabei werden Situationen betrachtet, in denen die Raumwellen an Diskontinuitäten im Untergrund reflektiert werden. Primäres Ziel der Reflexionsseismik ist es, aus den gemessenen Daten (der Partikelverschiebung oder dem Druck an der Messoberfläche als Funktion

der Zeit) ein strukturelles Abbild des Untergrunds zu erzeugen. Die Lage der Diskontinuitäten im Untergrund ergibt sich dabei aus den kinematischen Aspekten der Wellenausbreitung, während weitergehende Aussagen auch die korrekte Behandlung der dynamischen Effekte verlangen. Der nächste Schritt ist dann die Erzeugung eines mit den Messdaten konsistenten Modells der elastischen Parameter im Untergrund, der so genannte Inversionsprozess.

Der Übergang vom so genannten Zeitbereich (gegeben durch die Positionen von Quelle und Empfänger sowie der Zeit) in den Tiefenbereich bedarf eines zumindest groben Modells der Ausbreitungsgeschwindigkeiten. Nur mit einem hinreichend genauen Initialmodell kann durch iterative Anwendung des Abbildungsverfahrens und einer Aktualisierung des Modells das Abbildungsproblem gelöst werden. Diese Vorgehensweise wird als Modell-basiert bezeichnet. Diese Problematik kann umgangen werden, in dem das Abbildungsverfahren im Zeitbereich durchgeführt wird: Bei so genannten Daten-orientierten Abbildungsverfahren wird keine explizite Parametrisierung der lokalen elastischen Parameter benötigt. Stattdessen werden integrale Größen verwendet, die sich unmittelbar aus den gemessenen Daten bestimmen lassen. Im Rahmen dieser Arbeit betrachte ich Verfahren, die Datensätze mit koinzidenten Quellen und Empfängern aus den Messdaten simulieren. Solche Datensätze weisen ein hohes Signal/Rauschverhältnis auf und lassen sich mit verhältnismäßig einfachen Verfahren in den Tiefenbereich abbilden.

Solche Daten-orientierte Abbildungsverfahren machen unmittelbaren Gebrauch von der inhärenten Redundanz reflexionsseismischer Messdaten, die in aller Regel aus den Messungen einer Vielzahl von Einzelexperimenten mit zahlreichen Empfängern bestehen. Dazu werden Näherungen der für bestimmte Situationen erwarteten Laufzeitkurven oder -flächen an die Reflexionsereignisse in den Daten angepasst. Ein klassisches Verfahren dieser Art ist der *common-midpoint (CMP) stack*, bei dem die seismischen Spuren gemeinsam verwendet werden, die sich einen gemeinsamen Mittelpunkt von Quelle und Empfänger teilen. Für Untergrundmodelle mit horizontalen, ebenen Schichtgrenzen lässt sich eine Laufzeitapproximation zweiter Ordnung herleiten, die durch einen einzigen Parameter beschrieben werden kann. Für allgemeinere Fälle mit geneigten Reflektoren oder sich schneidenden Reflexionsereignissen stößt der *CMP stack* jedoch an seine Grenzen.

Ein allgemeineres Verfahren, der so genannte *normal moveout (NMO)/dip moveout (DMO)/stack*, berücksichtigt zuerst den Einfluss der Messgeometrie und des Überbaus, anschließend den Einfluss der Reflektorneigung. Letztere wird dabei jedoch nicht parametrisiert, so dass keine weiteren Informationen über den Untergrund erhalten werden können. Betrachtet man den *NMO/DMO/stack* zu einem einzigen Bearbeitungsschritt zusammengefasst, so werden die Daten im Wesentlichen entlang der kinematischen Reflexionsantwort der jeweiligen Isochrone für *zero-offset (ZO)*, d. h. für koinzidente Quellen und Empfänger, aufsummiert. Offensichtlich lässt daher auch dieses Verfahren keine optimale Anpassung der Laufzeitapproximation an die Reflexionsereignisse zu: Formuliert in den lokalen Eigenschaften des Reflektors (Lage, Orientierung und Krümmung) berücksichtigt der *NMO/DMO/stack* nur die Kombinationen dieser Größen, die implizit durch die *ZO*-Isochrone gegeben sind. Der *CMP stack* ist in dieser Hinsicht sogar noch restriktiver, da er streng genommen Orientierung (horizontal) und Krümmung (Null) festlegt.

Offensichtlich besteht ein Bedarf, eine Laufzeitapproximation zu verwenden, die den genannten Reflektoreigenschaften explizit Rechnung trägt. Da dabei zusätzlich auch noch die integralen Eigenschaften des Überbaus mit eingehen, bedarf eine solche Laufzeitapproximation zusätzlicher

integraler Parameter. Diese können mit Hilfe von hypothetischen Experimenten in Beziehung zu den Eigenschaften eines Reflektorsegments (*common reflection surface (CRS)*) gesetzt werden. Eine Herleitung einer solchen Laufzeitapproximation mit Hilfe von Konzepten der geometrischen Optik wird im nächsten Abschnitt kurz umrissen. Die approximative kinematische Reflexionsantwort eines beliebig orientierten und gekrümmten Reflektorsegments dient schließlich dazu, alle Informationen in den Messdaten zu sammeln, die zu ein und demselben Reflektorsegment im Tiefenbereich gehören – ohne dabei die tatsächlichen Eigenschaften des Reflektorsegments im Tiefenbereich kennen zu müssen.

Theorie

Um zu einer Laufzeitapproximation für ein beliebiges Reflektorsegment mit einem inhomogenen Überbau zu gelangen, wird zunächst ein einzelner Reflektor mit homogenem Überbau betrachtet. In diesem Fall lassen sich die Isochronen zu jeder gemessenen Laufzeit analytisch berechnen. Die Einhüllende aller Isochronen bildet dabei den Reflektor. Für einen beliebigen, aber festen Reflexionspunkt zeigt sich, dass die Laufzeiten aller Experimente, die in diesem so genannten *common reflection point (CRP)* reflektiert werden, von einer charakteristischen Größe abhängen. Bemerkenswerter Weise kann diese Größe vollständig durch Eigenschaften des Reflexionsereignisses ausgedrückt werden, ohne dass der Reflexionspunkt explizit bekannt ist: Ein Punkt auf der zugehörigen *CRP*-Trajektorie und die dortige Steigung der Reflexionsantwort längs der Akquisitionslinie reichen aus, um alle anderen Punkte der *CRP*-Trajektorie zu beschreiben. Damit ist eine Daten-orientierte Beschreibung der Reflexionsantwort eines einzelnen Reflexionspunkts (definiert durch Lage und Orientierung) bekannt.

Da im Rahmen dieser Arbeit die Simulation von *ZO*-Datensätzen das Ziel ist, führe ich nun den so genannten Normalstrahl ein. Dieser Strahl beschreibt die Laufwege der Energie von einer Quelle zum Reflexionspunkt und zurück zum Empfänger, der mit der Quelle koinzidiert. Dieser Strahl steht – unter Voraussetzung einmaliger Reflexion im Untergrund – stets senkrecht zum Reflektor. Um die *CRP*-Trajektorie für homogenen Überbau für den inhomogenen Fall zu verallgemeinern, mache ich nun von Methoden der geometrischen Optik Gebrauch. In einem ersten hypothetischen Experiment wird eine Punktquelle im Reflexionspunkt S_{NIP} , dem *normal incidence point (NIP)*, betrachtet. In Abbildung 1 sind die dadurch initiierten Wellenfronten dieser *NIP*-Welle für ein einfaches Modell mit drei homogenen Schichten rot dargestellt. Die Wellenfront taucht an der Lokation x_0 unter dem Winkel α und mit dem Krümmungsradius R_{NIP} auf. Für einen Betrachter an dieser Stelle scheint die Wellenfront vom Punkt S_{NIP}^* zu kommen. Eine hypothetische Punktquelle in S_{NIP}^* in einem homogenen Ersatzmedium mit der Geschwindigkeit v_0 würde ebenfalls eine Wellenfront mit denselben Werten α und R_{NIP} generieren. Allerdings weicht die Laufzeit im Ersatzmedium i. A. von der gemessenen *ZO*-Laufzeit entlang des tatsächlichen Normalstrahls ab. Da die Laufzeit im Ersatzmedium direkt durch R_{NIP} und v_0 gegeben ist, lässt sich diese Laufzeitdifferenz berechnen und als Korrektur auf die *CRP*-Trajektorie anwenden. Damit steht eine Approximation für einen beliebigen inhomogenen Überbau zur Verfügung.

Im nächsten Schritt wird die kinematische *ZO*-Reflexionsantwort für ein gekrümmtes Reflektorsegment bestimmt. Dazu wird ein weiteres hypothetisches Experiment, das Normalwellenexperi-

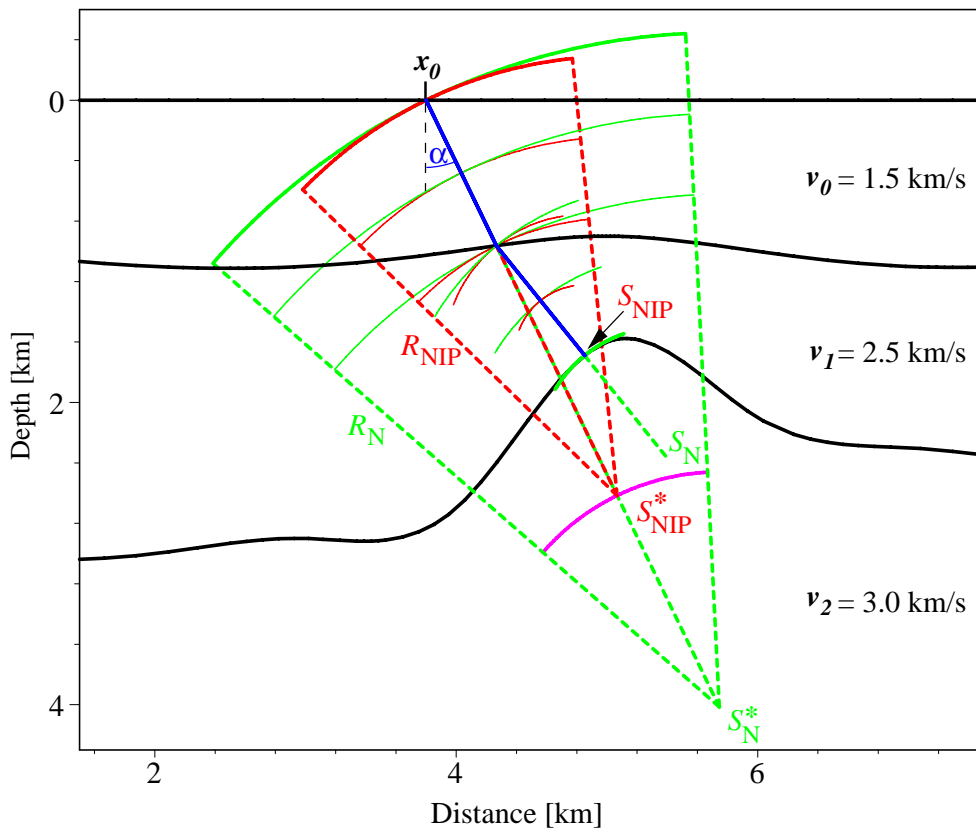


Abbildung 1: Einfaches Modell mit drei homogenen Schichten. Für den Reflexionspunkt S_{NIP} sind die Krümmungsradien der Wellenfronten der NIP -Welle (rot) und der Normalwelle (grün) längs des Normalstrahls (blau) durch Bogensegmente dargestellt. Die NIP -Welle scheint vom Bildpunkt S_{NIP}^* auszugehen, während der Krümmungsmittelpunkt S_N des Reflektorsegments in den Bildpunkt S_N^* übergeht. Ein hypothetisches Reflektorsegment durch S_{NIP}^* im Ersatzmedium mit v_0 führt zu denselben Werten für α , R_{NIP} und R_N .

ment betrachtet: Das Reflektorsegment wird simultan in allen Punkten angeregt, ein so genanntes *exploding reflector experiment*. Die zugehörigen Wellenfronten und die scheinbare Quelle der auftauchenden Wellenfront sind in Abbildung 1 grün dargestellt. Die ZO -Antwort kann mit den gleichen Überlegungen wie für die NIP -Welle für inhomogenen Überbau approximiert werden.

Der letzte Schritt ist schließlich, an jeden Punkt der ZO -Antwort des Reflektorsegments eine CRP -Trajektorie anzuhängen. Damit wird ein flächenhafter Operator aufgespannt, der die kinematische Reflexionsantwort eines beliebig gekrümmten und orientierten Reflektorsegments approximiert. Da es sich dabei um eine schwer handhabbare parametrische Darstellung handelt, werden für die praktische Anwendung Taylor-Entwicklungen zweiter Ordnung der Laufzeit t (parabolische Form) bzw. t^2 (hyperbolische Form) als CRS -Operatoren verwendet.

Offensichtlich fallen für einen Diffraktor die beiden hypothetischen Experimente zusammen, R_N

geht in R_{NIP} über. Dies bedeutet jedoch, dass bei Kenntnis der Reflexionsantwort auch eine Approximation der kinematischen Antwort eines hypothetischen Diffraktors im selben unbekanntem Tiefenpunkt verfügbar ist. Dies erlaubt die Umsetzung zahlreicher Konzepte, die aus anderen Abbildungsverfahren bekannt sind: So kann als neu eingeführte Anwendung z. B. die Bildlokation für eine Kirchhoff-Zeitmigration abgeschätzt werden, um eine Zeitmigration ohne Geschwindigkeitsmodell durchzuführen. Als weitere Anwendungen der kinematischen Wellenfeldattribute α , R_{NIP} und R_{N} gehe ich auf die Abschätzung der projizierten Fresnelzone und die Klassifizierung von Reflexionsereignissen ein. Beiden Anwendungen basieren auf der Kenntnis der approximativen Diffraktionsantwort.

Die *CRS*-Operatoren wurden für ein 2-D Modell mit Hilfe von Konzepten aus der geometrischen Optik hergeleitet. Der Vergleich mit der Theorie für den *CRS stack* für 3-D Akquisition zeigt jedoch, dass auch die Theorie für 2-D kinematisch korrekte Ergebnisse bei Anwendung auf 3-D Daten liefert. Die Wellenfeldattribute sind dabei in der Ebene definiert, die durch die Akquisitionslinie und die Auftauchrichtung des Normalstrahls aufgespannt wird. Da ich nur kinematische Aspekte der Wellenausbreitung betrachte, lassen sich die Ergebnisse auch auf elastische Medien übertragen, sofern diese eine getrennte Behandlung von Kompressions- und Scherwellen zulassen. Die Konversion zwischen den verschiedenen Wellenmoden kann jedoch nicht beschrieben werden. Für kleine Quelle/Empfängerabstände sind die Amplituden konvertierter Wellen jedoch in aller Regel so klein, dass sie für die Simulation von *ZO*-Sektionen vernachlässigt werden können.

Implementierung

Mit den *CRS*-Operatoren stehen Laufzeitapproximationen zweiter Ordnung für die kinematische Reflexionsantwort eines beliebigen gekrümmten Reflektorsegments mit inhomogenem Überbau zur Verfügung. Im Folgenden betrachte ich exemplarisch die hyperbolische Näherung

$$t_{\text{hyp}}^2(x_m, h) = \left[t_0 + \frac{2 \sin \alpha (x_m - x_0)}{v_0} \right]^2 + \frac{2 t_0 \cos^2 \alpha}{v_0} \left[\frac{(x_m - x_0)^2}{R_{\text{N}}} + \frac{h^2}{R_{\text{NIP}}} \right]. \quad (1)$$

Die Laufzeit t_0 und der Auftauchort x_0 des Normalstrahls sind dabei durch die zu simulierende *ZO*-Lokation vorgegeben. x_m beschreibt den Mittelpunkt zwischen Quelle und Empfänger, h den halben Abstand zwischen ihnen. Die oberflächennahe Geschwindigkeit setze ich im Moment als bekannt und konstant voraus. Damit hängt die Laufzeit t nur noch von den drei kinematischen Wellenfeldattributen α , R_{NIP} und R_{N} ab. Die wesentliche Problemstellung des *CRS stack* ist nun, die Laufzeitapproximation (1) durch Variation der Wellenfeldattribute optimal an die Reflexionsereignisse in den Messdaten anzupassen. Dies ist durch Kohärenzanalysen entlang der verschiedenen getesteten *CRS*-Operatoren in den mehrfach-überdeckten Messdaten möglich.

Ein repräsentatives Beispiel für die Kohärenz als Funktion der Wellenfeldattribute ist in Abbildung 2 dargestellt. Offensichtlich muss zur Bestimmung der optimalen Wellenfeldattribute ein globales Optimierungsproblem mit drei Parametern gelöst werden, wobei die Kohärenz eine multimodale Funktion darstellt. Wegen der direkten Abhängigkeit der Kohärenz von den Messdaten ist

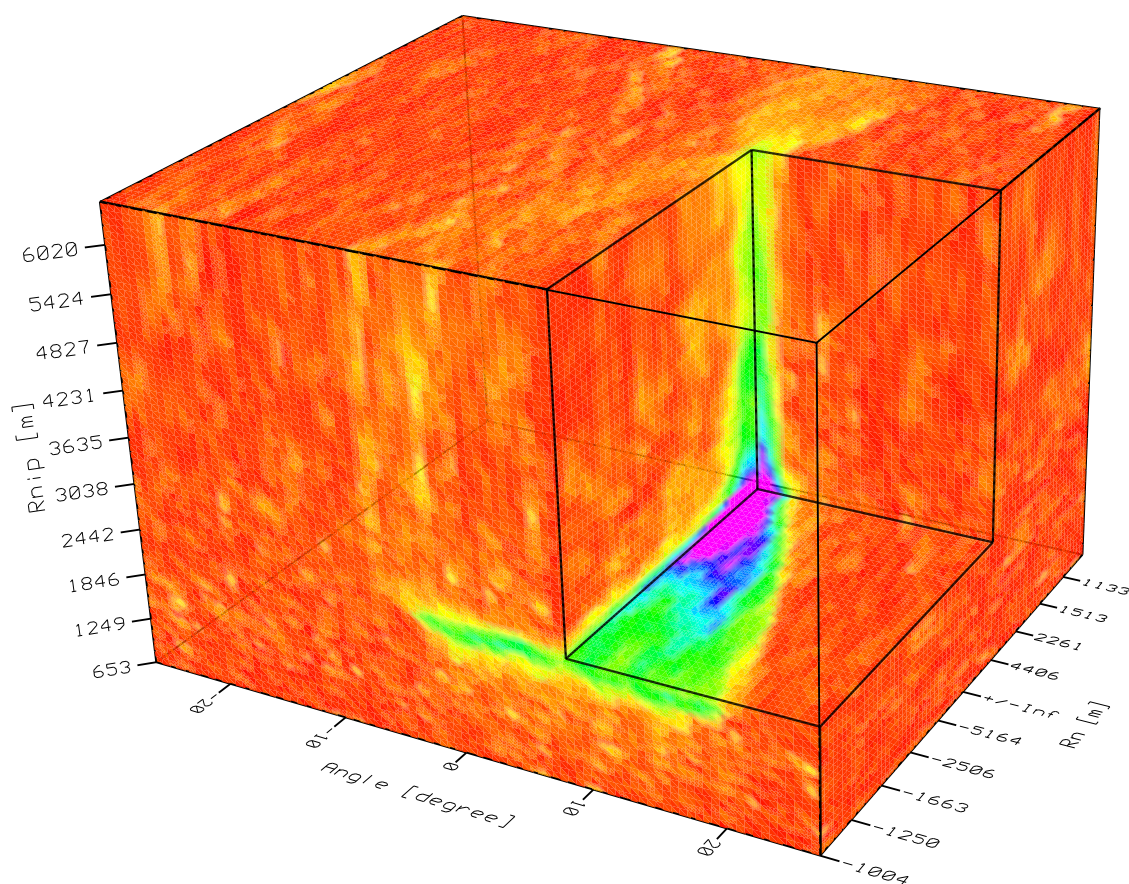


Abbildung 2: Kohärenzwerte als Funktion der Wellenfeldattribute für eine ZO-Lokation auf einem Reflexionsereignis. Die innere Ecke des ausgesparten Volumens liegt im globalen Maximum. Die größten dargestellten Werte (magenta) entsprechen 30 % des globalen Maximums, so dass auch kleinere Nebenmaxima sichtbar werden. Die R_N -Achse ist nicht linear.

eine analytische Beschreibung nicht möglich. Die Berechnung eines solchen Kohärenzvolumens ist sehr rechenaufwändig und kann daher nicht für jede zu simulierende ZO-Lokation durchgeführt werden.

Müller (1999) hat eine effiziente pragmatische Lösung des Problems vorgeschlagen und angewendet: Die Zerlegung des dreiparametrischen Problems in drei einparametrische Optimierungen, die in verschiedenen Messkonfigurationen angewendet werden. Zuerst wird dabei ein automatisierter konventioneller *CMP stack* (s. o.) angewendet. Im Resultat dieser Anwendung wird dann zunächst der Auftauchwinkel α und anschließend der Krümmungsradius der Normalwelle R_N bestimmt. Aus der Stapelgeschwindigkeit v_{stack} und dem Winkel α kann dann der Krümmungsradius der NIP-Welle R_{NIP} berechnet werden. Mit dieser Vorgehensweise können Initialwerte für die Wellenfeldattribute bestimmt werden, die bei Bedarf noch mit einer lokalen Optimierung mit drei

Parametern verfeinert werden können.

Diese pragmatische Suchstrategie ist sehr effizient, wird jedoch problematisch, falls mehrere Reflexionsereignisse zu ein und derselben *ZO*-Lokation beitragen. Sich schneidende Ereignisse werden dabei als *conflicting dip*-Situationen bezeichnet. Mein Ziel ist, die pragmatische Strategie so zu erweitern, dass in solchen Situationen jedes beitragende Ereignis separat identifiziert und parametrisiert wird. Dabei soll die Effizienz der pragmatischen Strategie so weit wie möglich erhalten bleiben. Der erste Suchschritt, der *CMP stack*, ist allerdings kaum dazu geeignet, sich schneidende Ereignisse zu separieren: Die Stapelgeschwindigkeit stellt kein geeignetes Kriterium für diese Separation dar. Liegen jedoch sich schneidende Ereignisse in einem Punkt vor, so trennen sich diese wieder an benachbarten *ZO*-Lokationen. Es ist daher in aller Regel möglich, solche Situationen auch noch im Resultat des *CMP stack* zu identifizieren.

Ich schlage daher eine erweiterte *CRS*-Suchstrategie vor, die ebenfalls mit dem *CMP stack* beginnt, in dessen Resultat jedoch nicht nur ein Ereignis für jede *ZO*-Lokation bestimmt wird, sondern auch lokale Kohärenzmaxima berücksichtigt werden. Hierbei wird zuerst die Kohärenz als Funktion des Auftauchwinkels berechnet und daraus das globale Maximum und – unter Anwendung gewisser Schwellwertkriterien – zusätzlich noch $n - 1$ lokale Maxima sowie die zugehörigen Auftauchwinkel $\alpha^{(i)}$ ($i = 1, \dots, n$) bestimmt. Im nächsten Schritt wird dann für jeden gefundenen Winkel noch der Krümmungsradius $R_N^{(i)}$ ermittelt. Nun zeigt sich jedoch, dass die Berechnung von R_{NIP} im Fall von mehreren detektierten Maxima nicht mehr aus der Stapelgeschwindigkeit v_{stack} erfolgen kann, da diese nur für das dominante Ereignis vorliegt. Um die noch fehlenden Attribute $R_{NIP}^{(i)}$ zu bestimmen, muss daher ein weiterer Suchschritt durchgeführt werden. Angesichts der Laufzeitapproximation ist dazu jedoch weder das *CMP gather* ($x_m - x_0 = \text{const}$) noch das Ergebnis des *CMP stack* ($h=0$) geeignet. Im ersten Fall ist R_{NIP} nicht vom Auftauchwinkel α zu separieren, im letzteren tritt R_{NIP} gar nicht auf. Als geeignete Untermenge der Messdaten schlage ich das *common-shot* (*CS*) *gather* gemeinsam mit dem *common-receiver* (*CR*) *gather* vor. Diese Untermenge lässt sich durch die Beziehung $|x_m - x_0| = |h|$ beschreiben und enthält alle Spuren, die entweder durch eine gemeinsame Quelle oder einen gemeinsamen Empfänger gekennzeichnet sind. Dort kann dann ein Krümmungsradius $R_{CS}^{(i)}$ bestimmt werden, der unmittelbar von den bekannten Werten $R_N^{(i)}$ und den gesuchten Werten $R_{NIP}^{(i)}$ abhängt. Damit sind alle Wellenfeldattribute für jedes beitragende Ereignis separat bestimmt und können wiederum als Initialwerte für die lokale Optimierung dienen.

Auf die Details der einzelnen Suchschritte kann ich im Rahmen dieser Zusammenfassung nicht eingehen. Ich möchte hier nur erwähnen, dass sich die Diskretisierung der getesteten Parameter an der durch die Messdaten vorgegebenen Auflösung orientiert. Die Festlegung des Parameterbereichs ist für die Stapelgeschwindigkeit und den Auftauchwinkel in den meisten Fällen verhältnismäßig einfach, während der Bereich des Krümmungsradius' R_N nur durch die maximale Steigung von Reflexionsereignissen im Zeitbereich grob begrenzt werden kann.

Weitere Betrachtungen befassen sich mit der Wahl geeigneter Aperturen für die Attributbestimmung und die Summation längs der optimalen Operatoren. Dabei wird für die *ZO*-Apertur die projizierte Fresnelzone für ein einfaches 1-D Modell mit vertikalem Gradienten der Durchschnittsgeschwindigkeit angesetzt, während die Wahl der *CMP*-Apertur mangels besserer Alternativen dem Anwender überlassen bleibt. Die Apertur für den flächenhaften Operator wird als Ellipse mit den Halbachsen *CMP*-Apertur und *ZO*-Apertur aufgespannt. Diese Form ist sehr effizient handhabbar

und trägt intuitiv dem approximativen Charakter der Laufzeitbeschreibung Rechnung.

Datenbeispiele

Im Rahmen der vorliegenden Arbeit wird die Implementierung der erweiterten *CRS*-Strategie auf drei verschiedene marine Datensätze angewendet. Zusätzlich werden verschiedene Anwendungen der Wellenfeldattribute präsentiert. Da die Darstellung der wesentlichen Ergebnisse zahlreicher Abbildungen bedarf, beschränke ich mich an dieser Stelle auf die Besonderheiten der einzelnen Beispiele, sowie einige besonders aufschlussreiche Abbildungen.

Synthetisches Datenbeispiel Sigsbee 2A

Dieser Datensatz wurde zu Forschungszwecken für ein Modell simuliert, das eine Situation nachempfunden, wie sie z. B. im Golf von Mexiko beobachtet wurde: Ein Salzkörper mit komplexer Geometrie ist in ein geschichtetes sedimentäres Umfeld eingebettet, das seinerseits von moderater Komplexität ist. Die Daten wurden durch eine Finite-Differenzen-Approximation der akustischen Wellengleichung simuliert, die Wasseroberfläche wurde nicht als freie Oberfläche berücksichtigt. Der Datensatz enthält demzufolge weder an der Wasseroberfläche reflektierte Multiplen, noch konvertierte Wellen.

Die Komplexität des simulierten Wellenfelds variiert außerordentlich stark in den Daten: Reflexionsereignisse, die nicht durch den Salzkörper hindurch propagiert sind, lassen sich mit Hilfe des *CRS stack* sehr gut und zuverlässig abbilden, während alle anderen Ereignisse sehr komplex sind und durch eine Laufzeitapproximation zweiter Ordnung nicht mehr hinreichend genau approximiert werden können. Als zusätzliche Komplikation treten an Synklinalen des Salzkörpers noch Multiplen auf, die vom *CRS stack* mit abgebildet werden. Mit Hilfe der Wellenfeldattribute können diese Multiplen jedoch als solche identifiziert werden.

Das Sigsbee 2A-Modell enthält zusätzlich zu den Reflektoren noch zwei Reihen von "künstlichen" Diffraktoren, die bestens geeignet sind, die Vorteile der erweiterten Suchstrategie sowie die Konsistenz der Wellenfeldattribute und ihrer Anwendungen zu demonstrieren. Abbildung 3 zeigt einen Vergleich der beiden Suchstrategien für einen Ausschnitt der Ergebnisse. Die erweiterte Suchstrategie ist in der Lage, die sich schneidenden Ereignisse zu parametrisieren und ihre Interferenz zu simulieren. Die zugehörigen Attribute zeigen für die stark gekrümmten Ereignisse genau das erwartete Verhalten für Diffraktoren: $R_{NIP} \approx R_N$. Die Attribut-basierte Zeitmigration fokussiert diese Diffraktionsereignisse recht gut. Dieses Beispiel zeigt eindrucksvoll, dass die erweiterte Strategie vollständigere und physikalischere Ergebnisse als die pragmatische Strategie liefert.

Reales Datenbeispiel CINCA SO104-13

Der zweite vorgestellte Datensatz wurde im Bereich des Peru-Chile Tiefseegrabens vor der Küste Perus akquiriert. Dieser Datensatz zeichnet sich durch eine Vielzahl dominierender Diffraktionsereignisse aus, die durch die stark zerklüftete Struktur der Meeresbodens verursacht werden.

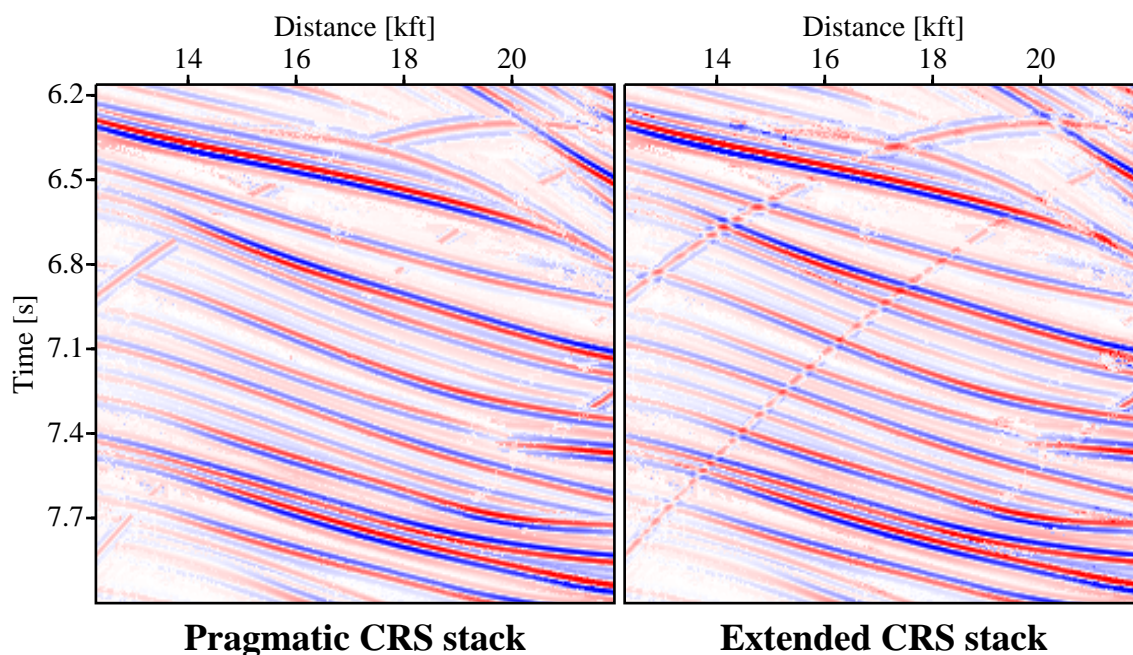


Abbildung 3: Datensatz Sigsbee 2A: Ausschnitte aus den optimierten *CRS stack*-Ergebnissen mit der pragmatischen (links) und der erweiterten (rechts) Suchstrategie. Während im ersten Fall die steilen Ereignisse weitgehend unterdrückt werden, hat die erweiterte Strategie sich schneidende Ereignisse nahezu überall detektiert und deren Interferenz simuliert.

Dementsprechend ist eine Interpretation dieser Daten im unmigrierten Zeitbereich nahezu unmöglich. Auch hier zeigt sich die Leistungsfähigkeit der Attribut-basierten Zeitmigration: Das migrierte Ergebnis ist zwar Implementierungs-bedingt etwas verrauscht, zeigt aber eine deutlich besser interpretierbare Struktur des Untergrunds, insbesondere Fragmente der abtauchenden ozeanischen Platte. Steile Abschnitte können allerdings kaum abgebildet werden, da diese mit der gegebenen Akquisitionsgeometrie praktisch nicht beleuchtet werden. Abbildung 4 zeigt einen Ausschnitt aus den Ergebnissen der Zeitmigration mit der pragmatischen und der erweiterten Suchstrategie. Auch hier sind die Verbesserungen augenfällig.

Für diesen Datensatz liegen sowohl konventionelle Stapelsektionen als auch ein Migrationsgeschwindigkeitsmodell vor. Damit besteht in diesem Fall die Möglichkeit, eine *post-stack*-Tiefenmigration durchzuführen um ein Tiefenabbild zu erhalten. Dabei zeigt sich die erheblich bessere Qualität der *CRS*-Ergebnisse hinsichtlich Signal/Rauschverhältnis und Kontinuität der Reflektoren sehr deutlich. Wegen der Größe der zugehörigen Abbildung verweise ich an dieser Stelle auf den Hauptteil dieser Arbeit.

Als weitere Anwendung der Wellenfeldattribute möchte ich noch die Klassifikation der Reflexionsereignisse nennen. Durch Vergleich der Krümmungsradien R_{NIP} und R_{N} lassen sich Diffraktions- und Reflexionsereignisse unterscheiden. Allein mit den simulierten *ZO*-Sektionen ist dies praktisch nicht möglich.

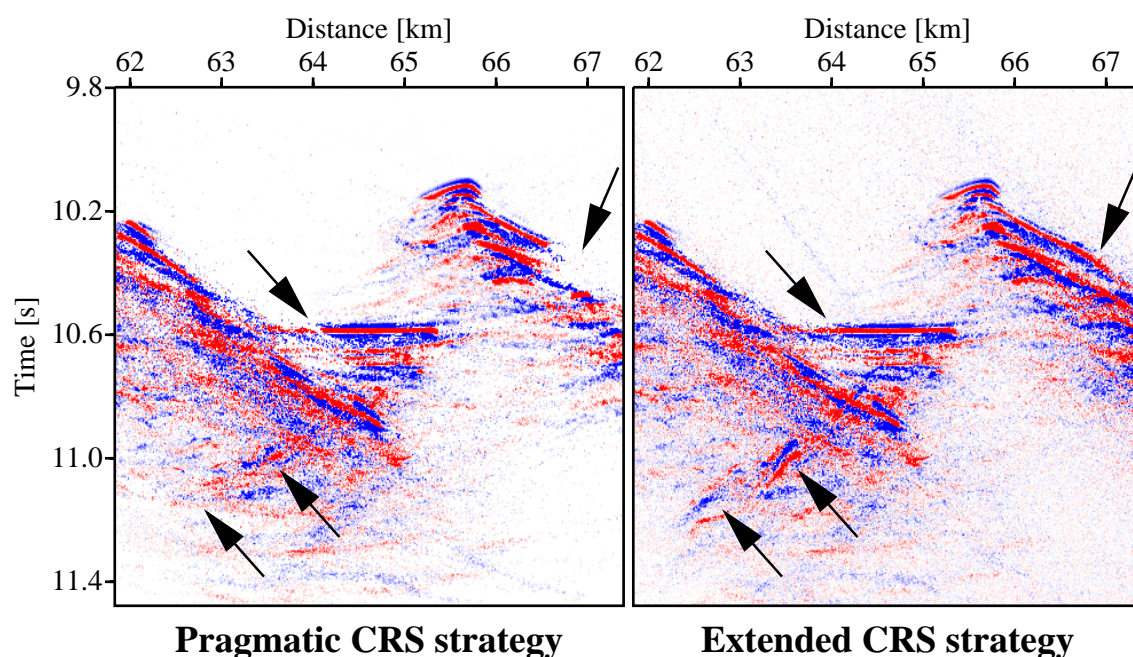


Abbildung 4: Datensatz CINCA SO104-13: Ausschnitte aus den Attribut-basierten Zeitmigrationen erzeugt mit der pragmatischen (links) und der erweiterten (rechts) Suchstrategie. Die wesentlichen Unterschiede sind durch Pfeile markiert.

Reales Datenbeispiel BGR99-07

Der dritte vorgestellte Datensatz ist ebenfalls ein mariner Datensatz. Er wurde westlich von Costa Rica über dem Mittelamerikanischen Graben akquiriert. Besonderheiten dieses Datensatzes sind starke Multiplen des Meeresbodenereignisses sowie des darunter liegenden *bottom simulating reflector* (*BSR*). Der *BSR* entsteht dabei durch einen negativen Impedanzsprung an der Untergrenze von Gashydraten. Des Weiteren variiert der Frequenzgehalt der Daten recht erheblich und erschwert damit die Wahl geeigneter Parameter für die Anwendung des *CRS stack*.

Mein besonderes Augenmerk gilt bei diesem Datensatz der Abschwächung und Identifizierung der Multiplen. Die genannten Multiplen zeichnen sich durch eine deutliche Anomalie in den Wellenfeldattributen aus. Es liegt daher nahe, die Bereiche der getesteten Wellenfeldattribute so einzuschränken, dass die Attributkombinationen der Multiplen nicht mehr zugelassen werden. Dies kann durch Vorgabe eines Modells für die kleinste erlaubte Stapelgeschwindigkeit erfolgen, die sich ihrerseits aus den Ergebnissen des *CMP stack* ableiten lässt. Dieser Versuch mit einem sehr einfachen Modell schwächt die Multiplen allerdings nicht überall im erwarteten Ausmaß ab. Um dieses Verhalten zu verstehen, wird eine *post-stack*-Tiefenmigration mit konstanter Geschwindigkeit durchgeführt, um ein kinematisch korrektes Abbild des Meeresbodens zu erhalten. Für die daraus bestimmte Geometrie des Meeresbodens werden die Wellenfeldattribute der primären und multiplen Ereignisse berechnet. Diese Simulation steht in guter Übereinstimmung mit den aus den Daten abgeleiteten Attributen und zeigt deutlich, warum die Abschwächung der Multiplen

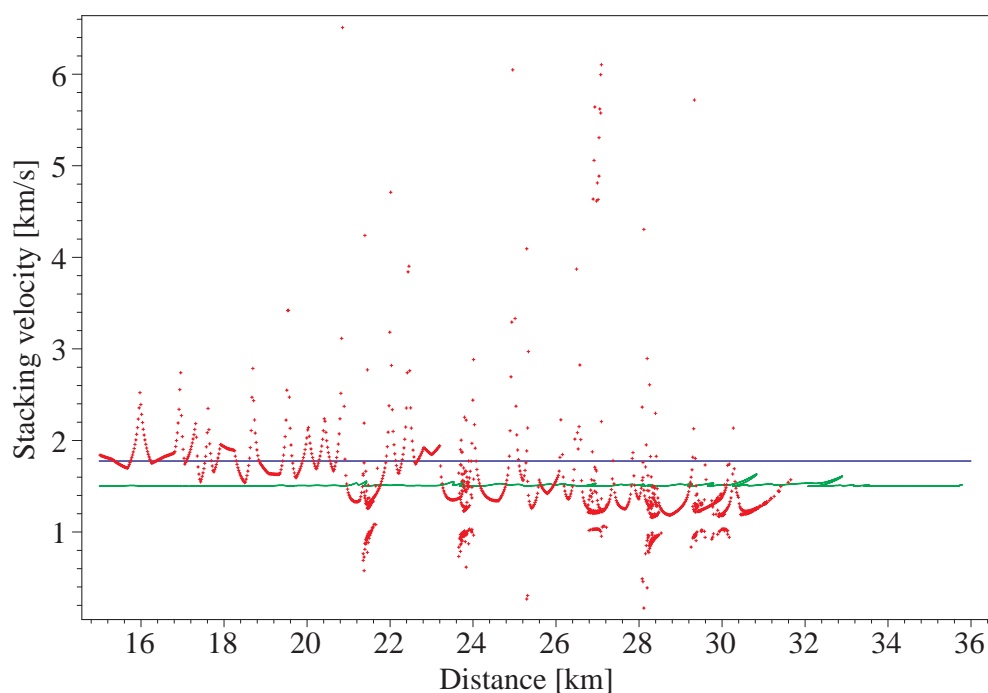


Abbildung 5: Datensatz BGR99-07: vorwärts-berechnete Stapelgeschwindigkeiten des vom Meeresboden stammenden P-P Primärerereignisses (grün) sowie der entsprechenden P-P-P-P Multiplen (rot). Die blau Linie deutet die gewählte Untergrenze für die Stapelgeschwindigkeit an.

nur partiell erfolgreich ist: In Abbildung 5 sind die simulierten Stapelgeschwindigkeiten und die vorgegebene Untergrenze dazu dargestellt. Die Multiple des Meeresbodens zeigt trotz dessen einfacher Geometrie ein unerwartet kompliziertes Verhalten, das durch ein einfaches Modell nicht ohne weiteres beschrieben werden kann.

Die – wenn auch nicht überall erfolgreiche – Abschwächung der Multiplen erhöht die Wahrscheinlichkeit, dass konkurrierende Primärerereignisse mit teilweise deutlich kleineren Amplituden detektiert und parametrisiert werden. Damit besteht bei einer erneuten Stapelung entlang der *CRS*-Operatoren (ohne dass dazu erneut die Attribute bestimmt werden müssen) die Möglichkeit, gezielt Operatoren zu unterdrücken, die gemäß ihrer Wellenfeldattribute Multiplen beschreiben könnten.

Schlussfolgerungen und Ausblick

Im Rahmen dieser Arbeit wurde ein Daten-orientiertes seismisches Abbildungsverfahren für 2-D Datenakquisition vorgestellt. An die Stelle einer expliziten Parametrisierung der elastischen Eigenschaften des Untergrunds tritt die Parametrisierung der Reflexionsereignisse im Zeitbereich. Drei kinematische Wellenfeldattribute beschreiben dabei näherungsweise die Reflexionsantwort

eines beliebigen, gekrümmten Reflektorsegments im Untergrund.

Mit diesem Verfahren wird nicht unmittelbar das letztendlich erwünschte strukturelle Abbild im Tiefenbereich generiert, sondern zuerst die Redundanz der Messdaten ausgenutzt, um alle Informationen zu sammeln, die zu ein und demselben Reflektorsegment gehören. Nachfolgend angewendete Verfahren zum Übergang in den Tiefenbereich profitieren von dem hohen Signal/Rauschverhältnis der simulierten *ZO*-Sektion und den zusätzlichen Informationen in den Wellenfeldattributen.

Mit Hilfe von Konzepten aus der geometrischen Optik wurde mittels Wellenfronten hypothetischer Experimente eine Beziehung zwischen den Eigenschaften des Reflektorsegments im Untergrund und seiner kinematischen Reflexionsantwort hergeleitet. Dies führte zu zwei Taylor-Entwicklungen zweiter Ordnung, die die Laufzeit des Reflexionsereignisses in der Umgebung des Normalstrahls approximieren. Neben der Abschätzung der projizierten Fresnelzone wurden neue Anwendungen der Wellenfeldattribute eingeführt: Die Klassifizierung der Ereignisse und eine Attribut-basierte Zeitmigration.

Ausgehend von der pragmatischen Suchstrategie von Müller (1999) habe ich eine erweiterte Strategie vorgeschlagen, die eine vollständigere und physikalischere Simulation von *ZO*-Sektionen erlaubt: Eine Erweiterung der Suchalgorithmen für den Auftauchwinkel und den Krümmungsradius der Normalwelle, sowie eine zusätzliche Suche im *CS/CR gather* ermöglichen eine separate Identifizierung und Parametrisierung von Reflexionsereignissen in Situationen, in denen mehrere Ereignisse gleichzeitig beitragen.

Ich habe eine Objekt-orientierte Implementierung der erweiterten *CRS*-Strategie vorgestellt, die mittlerweile in der Kohlenwasserstoff-Exploration eingesetzt wird. Neben einer flexibleren Integration von a priori verfügbarer Information wurden zusätzlich die Berücksichtigung der projizierten Fresnelzone und das Konzept des *operator tapering* zur Vermeidung von systematischen Artefakten integriert. Als neue Anwendung der Wellenfeldattribute wurde die Attribut-basierte Zeitmigration als Nebenprodukt des *CRS stack* realisiert.

Die Anwendung auf synthetische und reale Datensätze zeigte, dass der *CRS stack* konventionellen Verfahren zur Simulation von *ZO*-Sektionen hinsichtlich Signal/Rauschverhältnis und Kontinuität der abgebildeten Reflexionsereignisse in der Regel überlegen ist. Bei hoher Komplexität des gemessenen Wellenfelds hingegen bricht die Methode aufgrund der Laufzeitapproximation zweiter Ordnung jedoch zusammen. Dies gilt allerdings gleichermaßen für die konventionellen Verfahren, da sie ebenfalls auf derartigen Approximationen beruhen.

Die in dieser Arbeit vorgestellte Methodik wurde für 2-D Datenakquisition längs einer geraden Linie und die Simulation von *ZO*-Sektionen entwickelt. Die Beschränkung auf eine gerade Akquisitionslinie ist ein reines Implementierungsproblem und kann durch eine flexiblere Beschreibung des Profils ersetzt werden. Einzige Bedingung ist, dass die Profillinie innerhalb der Apertur nicht zu stark gekrümmt ist. Das *CRS*-Konzept wurde inzwischen auch auf den 3-D *ZO*-Fall verallgemeinert, eine Integration der neu entwickelten Verbesserungen aus der 2-D Implementierung steht hingegen noch aus. Eine andere Entwicklungsrichtung ist die Verwendung von Strahlen mit finitem Quell/Empfängerabstand als Ausgangspunkt für die Laufzeitapproximation. Damit ist sowohl die Behandlung von großen Messauslagen als auch von konvertierten Wellen möglich. Die Implementierung dieses *finite-offset CRS stack* wird derzeit abgeschlossen.

Schließlich möchte ich auf die Berücksichtigung der Topographie der Messoberfläche eingehen. Die vorliegende Implementierung geht von einer ebenen Messfläche aus, was für die betrachteten marinen Datenbeispiele in sehr guter Näherung zutrifft. Bei Landdaten hingegen kann die Topographie im Allgemeinen jedoch nicht vernachlässigt werden. Die Elevation von Quellen und Empfängern kann direkt in die *CRS*-Laufzeitapproximation integriert werden. Diese Vorgehensweise ist wesentlich genauer als die üblichen Verfahren zur Berücksichtigung der Topographie, die meist von senkrecht verlaufenden Strahlen ausgehen, da der Auftauchwinkel des Normalstrahls einer der Suchparameter des *CRS stack* ist. Die Implementierung dieser Erweiterung ist Gegenstand der derzeitigen Arbeiten.

Contents

Abstract	i
Zusammenfassung	iii
1 Introduction	1
1.1 Investigation of the earth's interior	1
1.2 Model-based vs. data-oriented imaging methods	2
1.3 Data-oriented seismic imaging methods	2
1.3.1 Common-midpoint stack	2
1.3.2 Normal moveout/dip moveout/stack	3
1.3.3 Multi-parameter stacking operators	4
1.4 Structure of the thesis	5
2 Theory	7
2.1 Common-Reflection-Point trajectory	7
2.1.1 CRP trajectory for homogeneous overburden	7
2.1.2 CRP trajectory for inhomogeneous overburden	10
2.2 Kinematic ZO response of a reflector segment	13
2.3 Multi-coverage reflection response of a reflector segment	13
2.4 Conventional imaging methods in terms of CRP trajectories	15
2.4.1 Migration to zero-offset	15
2.4.2 Kirchhoff migration	17
2.5 Taylor expansions of the CRS response	17

2.6	Attribute-based time migration	18
2.7	Projected first Fresnel zone	23
2.8	2-D CRS stack for 3-D multi-coverage data	26
2.9	Validity for elastic media	28
3	Implementation	31
3.1	Global optimization problem	31
3.2	CRS stack in subsets of the pre-stack data	33
3.3	Pragmatic search strategy	35
3.3.1	Automatic CMP stack	35
3.3.2	Linear and hyperbolic ZO stack	36
3.3.3	Limitations	37
3.4	Extended CRS stack strategy	38
3.4.1	Detection of conflicting dip situations	38
3.4.2	Determination of R_{NIP}	40
3.5	Search algorithms	41
3.5.1	Automatic CMP stack	41
3.5.2	Linear ZO stack	43
3.5.3	Hyperbolic ZO stack	44
3.5.4	Hyperbolic CS/CR stack	46
3.5.5	Refinement of the one-parameter searches	46
3.6	Apertures and tapering	47
3.6.1	ZO aperture	47
3.6.2	CMP aperture	49
3.6.3	Aperture for the CRS super gather	49
3.6.4	Operator tapering	49
3.7	Influence of the near-surface velocity	52
4	Synthetic data example: Sigsbee 2A	53
4.1	Model and simulated pre-stack data	53

4.2	Application of the CRS stack	58
4.2.1	Automatic CMP stack	58
4.2.2	Linear and hyperbolic ZO stack	66
4.2.3	Final results	67
4.2.4	Conflicting dip handling	69
4.3	Applications of the wavefield attributes	74
4.3.1	Projected first Fresnel zone	76
4.3.2	Attribute-based time migration	76
4.4	Conclusions	78
5	Real data example: CINCA SO104-13	81
5.1	Data acquisition and pre-processing	81
5.2	Application of the CRS stack	87
5.3	Applications of the wavefield attributes	92
5.3.1	Projected first Fresnel zone	97
5.3.2	Classification of events	97
5.3.3	Attribute-based time migration	99
5.4	Post-stack depth migration	102
5.5	Conclusions	104
6	Real data example: BGR99-07	105
6.1	Data acquisition and pre-processing	105
6.2	Application of the CRS stack	107
6.2.1	Automatic CMP stack and multiple attenuation	110
6.2.2	Final results	116
6.3	Applications of the wavefield attributes	120
6.3.1	Projected first Fresnel zone	120
6.3.2	Identification of multiples	125
6.4	Conclusions	126
7	Conclusions and outlook	129

A	Sign conventions and data visualization	133
A.1	Emergence and incidence angles	133
A.2	Wavefront and interface curvatures	134
A.3	Seismic amplitudes	135
A.4	Wavefield attribute sections	135
B	Coherence measure semblance	137
C	Flexible polyhedron search	139
C.1	The search algorithm	139
C.2	Adaptation to the CRS stack method	141
D	Pulse stretch and CRS stack	145
E	Acquisition geometry of pre-stack data	147
F	Used hardware and software	149
	List of Figures	151
	List of Tables	155
	References	157
	Danksagung	163
	Lebenslauf	165

Chapter 1

Introduction

1.1 Investigation of the earth's interior

Mankind has access to almost any location on earth's surface, its seas and lakes, and its atmosphere. Thus, a direct investigation of the structures, material properties, and dynamic processes in these environments is—in principle—possible. In contrast, the largest part of our planet, usually referred to as the solid earth, is almost inaccessible for direct investigations. Even with the deepest (and extremely expensive) wells, only tiny local details of the solid earth can be examined. Consequently, the solid earth can virtually only be investigated by means of indirect measurements.

A variety of geophysical methods has been introduced for such indirect observations, for example passive measurements of the earth's gravity and magnetic fields, the thermal heat flow, tectonic movements etc., or active measurements with artificial electric and electro-magnetic fields. Another way to explore the solid earth is to investigate the propagation of elastic energy, either with artificial energy sources as in exploration seismics or as passive measurement in seismology. Obviously, all these measurements depend on quite different features of the solid earth, like mass distribution, elastic properties, thermal and electrical conductivity, material flows—just to name a few.

All indirect measurements represent *integral* properties of the solid earth (neglecting external influences for the sake of simplicity). However, it is more desirable to derive *local* properties from these measurements. For example, the aim is to derive the density distribution from gravity measurements, a task that suffers from the inherent ambiguity of potential theory. Similarly, the elastic wavefield measured as particle displacement at the earth's surface is influenced by the elastic properties of the entire medium through which the elastic energy propagates. To obtain the desired local distribution of the elastic properties, two additional processes commonly called *imaging* and *inversion* have to be performed. In the following, I will focus on the imaging problem for seismic reflection measurements, i. e., the elastic wave propagation phenomena of body waves initiated by artificial sources. As the name already indicates, the main interest is in seismic energy *reflected* at discontinuities of the medium rather than refracted or scattered energy.

1.2 Model-based vs. data-oriented imaging methods

In reflection seismics, the aim of imaging methods is to derive an image from the measured seismic reflection data that associates the observed discontinuities in the data with discontinuities of the elastic properties of the subsurface. In other words, reflection events in the acquired data have to be transformed into reflecting interfaces in the subsurface. The usually subsequently applied inversion aims at setting up a complete, volumetric model of elastic properties that are consistent with the measured data. Although the “natural” and finally desired domain of the image (and the inversion result) is the depth domain, seismic reflection imaging can also be performed in the time domain, i. e., the domain in which the acquired data is given or subsets of this domain. At a first glance, time domain imaging might appear to make no sense. However, the application of imaging methods in the time domain has some crucial advantages: to go from the time to the depth domain, an explicit model of the local elastic properties of the subsurface is required, accurate at least on a comparatively large scale. In other words, for the imaging process the output of the inversion is required and vice versa. Methods that directly provide a depth domain image thus require an a priori known model of the elastic properties. If this start model is sufficiently close to the true situation, iterative and interactive application of the imaging method and an update of the underlying model can be applied to solve the imaging problem. In the following, I refer to this kind of approach as *model-based*.

In contrast, time domain imaging processing like time migration can already be performed with a model of integral properties. Time migration in its conventional form is, of course, also model-based. However, it is far easier to elaborate a model of integral properties like root-mean-square (RMS) velocities rather than local ones like interval velocities. Furthermore, this method is less sensitive to errors in the model.

A further simplification can be achieved if the imaging process can be performed without any explicit parameterization of a velocity model, but by means of integral properties that can be directly determined from the acquired data. A typical imaging task of this kind is to use the redundancy in the multi-coverage reflection data to simulate a single section that corresponds to a measurement with coincident source and receiver pairs, a zero-offset (ZO) section. In the following, I will briefly discuss three different approaches that are able to handle situations of different complexity: the classical common-midpoint (CMP) stack, the normal moveout(NMO)/dip moveout(DMO)/stack, and multi-parameter stacking methods like the Common-Reflection-Surface (CRS) stack.

1.3 Data-oriented seismic imaging methods

1.3.1 Common-midpoint stack

Data-oriented seismic time domain imaging has its roots in the work of Dürbaum (1954). The first widely used data-oriented approach is the classical *common-midpoint (CMP) stack* method introduced by Mayne (1962)¹. As the name indicates, this approach is performed in particular

¹Mayne originally used the term “common reflection point stacking”. However, it is more appropriate to consider it as an CMP stack, as the original term is strictly only correct for horizontally layered media.

subsets of the pre-stack data, namely the CMP gathers in which all seismic traces are gathered that have source/receiver midpoints in the same CMP bin. A second-order Taylor expansion of the traveltimes around shot/receiver offset zero is used to approximate the kinematic reflection response of the subsurface in the CMP gather. A single integral property, the so-called stacking velocity v_{stack} , is the parameter of this CMP trajectory. For simple subsurface models, v_{stack} has an evident physical meaning: for a horizontal reflector with homogeneous overburden, it coincides with the interval velocity of the overburden. For a horizontally stratified medium with iso-velocity layers, v_{stack} represents an average velocity of the overburden, the RMS velocity. For similar models with dipping interface(s), these relations still hold but include an additional dip-dependent term. However, for arbitrary inhomogeneous models with curved interfaces, it is, in general, not possible to directly associate v_{stack} with a physical velocity: it might become infinity or imaginary in certain situations. Apparently, this parameterization is misleading in the general case. Later on, I will express v_{stack} in terms of parameters that always have a well-defined physical meaning.

The CMP stack turned out to be a very robust strategy to simulate a ZO section from pre-stack data. This reduces the amount of data and increases the signal-to-noise ratio. For horizontally layered media, the CMP stack collects the energy pertaining to one and the same reflection point at each location in the time domain, thus making use of the redundancy of multi-coverage seismic reflection data. However, the CMP stack method suffers from some inherent limitations: in case of conflicting dip situations where two or more reflection events intersect each other at the same ZO location, the CMP stack is, in general, not suited to handle such ambiguities. Furthermore, the CMP stack combines the responses of different reflection points in case of dipping and/or curved reflections.

1.3.2 Normal moveout/dip moveout/stack

To overcome the limitations of the CMP stack, a new approach was developed that firstly handles the influence of the acquisition geometry due to the overburden of a reflector, followed by an additional correction that considers the dip of the reflector. The former process is known as *normal moveout (NMO) correction*, the latter one as *dip moveout (DMO) correction* (see, e. g., Judson et al., 1980; Yilmaz and Claerbout, 1980; Deregowski and Rocca, 1981; Hale, 1984). Whereas the NMO correction is easy to understand, the DMO correction appears somewhat esoteric. This is due to the—from an academic point of view—artificial separation of these two processes. Putting both together again, one observes that the NMO/DMO stacking operator (ignoring some approximations) is nothing else but the kinematic reflection response of the zero-offset (ZO) isochron given by a traveltimes on a seismic trace and the velocity model. As the actual reflection point has to be located on this isochron, its kinematic reflection response is located within the NMO/DMO stacking operator. Stacking along the response of the ZO isochron is usually referred to as migration to zero-offset (MZO) (Perroud et al., 1997).

As summarized by Deregowski (1986), the NMO/DMO/stack approach is able to correctly consider conflicting dip situations: by summing the contributions of all possible dips for a particular ZO traveltimes into the CMP gather, the contributions stemming from the same reflection point are moved into the same CMP gather. Whereas the direct application of an MZO obviously requires the knowledge of the interval velocity model to obtain the isochron, the separation of MZO

into NMO and DMO corrections has a significant advantage for practical application: the NMO correction can be performed by means of an integral property, namely the NMO velocity, that can be determined from the pre-stack data in a data-oriented way. For constant velocities, the DMO operator does not depend on the velocity. Thus, it is common practice to apply a constant velocity DMO such that no interval velocity model is required at all. As a consequence, the DMO process does not provide any additional parameters as its operator (an approximation of the NMO-corrected MZO operator) only depends on the ZO traveltime.

1.3.3 Multi-parameter stacking operators

Whereas the CMP stack in a strict sense considers plane, horizontal interfaces in the subsurface, the NMO/DMO/stack approach also handles arbitrary interfaces with different dips, although these dips are not explicitly parameterized. To derive stacking operators that fit closer to the actual reflection events and characterize the reflectors in more detail, stacking operators with additional parameters are required. These parameters are related to local properties of the reflectors, namely their locations, orientations, and curvatures. In this terminology, the CMP stack only considers the location of a reflector, but assumes its orientation to be horizontal and its curvature to be zero. Consequently, the CMP stack yields best results if these assumptions are actually met in the subsurface. In contrast, the MZO considers all combinations of locations, orientations, and curvatures implicitly given by the ZO isochron. Thus, the MZO operators fits best the actual reflection event if the reflector (locally) coincides with the ZO isochron.

These observations directly lead to the idea of stacking operators that are based on the actual local properties the reflector. Such multi-parameter stacking operators have been introduced with different approaches. Gelchinsky and co-workers introduced their *homeomorphic imaging methods* that are either performed in specific subsets of the pre-stack data or—as the CRS stack—within entire super gathers that are no longer confined to a particular source/receiver geometry. In the latter case, the homeomorphic imaging method is called *Multifocusing* (Gelchinsky et al., 1997). An overview of the related other homeomorphic imaging methods can be found in Müller (1999), a detailed description of the theory and its application is given in Gelchinsky and Keydar (1999), Gelchinsky et al. (1999a), and Gelchinsky et al. (1999b), followed by synthetic and real data examples in Landa et al. (1999). The Multifocusing operator has the form a double square root expression.

Another approach is based on operators given by delayed hyperbolae derived by means of concepts of geometrical optics. The so-called *Polystack* method was introduced by de Bazelaire (1988), Thore et al. (1994), and de Bazelaire and Viallix (1994). This kind of stacking procedure is performed in the CMP gathers (just as CMP stack) but provides, in general, a better fit to the actual reflection event than the conventional CMP stack operator. This approach can be implemented in a quite efficient way.

Finally, the CRS stack operator discussed in this thesis was firstly presented by Tygel et al. (1997). By means of paraxial ray theory, a parabolic stacking operator can be derived. A Taylor expansion of the squared traveltime leads to a hyperbolic operator that coincides with the results of Höcht

et al. (1999) who used to concepts of geometrical optics. The basic idea is to approximate the kinematic reflection response of an arbitrarily curved reflector segment by means of two hypothetical experiments: the common propagation direction and the curvatures of the resulting hypothetical wavefronts serve as parameters for the stacking operator and establish a relationship between the time domain and the properties of a subsurface reflector segment. For the 2-D ZO simulation considered in this thesis, three parameters or *kinematic wavefield attributes*, namely one emergence angle and two wavefront curvatures, parameterize the spatial stacking operator. The operator can be directly determined in the pre-stack data, i. e., data-oriented, by means of coherence analysis. Thus, the CRS stack represents a generalized velocity analysis method that is no longer confined to specific subsets of the pre-stack data.

Müller (1999) implemented and applied the CRS stack method by means of an efficient pragmatic search strategy. His very impressive results clearly demonstrated that the CRS stack approach is superior to conventional stacking procedures. Therefore, my aim in this thesis is to overcome some limitations of the pragmatic search strategy and to provide a flexible and powerful implementation of an extended CRS stack strategy. Furthermore, I develop new applications of the wavefield attributes and include additional features like operator tapering and projected first Fresnel zones.

1.4 Structure of the thesis

In this chapter, I briefly introduce the basic aim of seismic reflection imaging and two different concepts to address this problem: model-based and data-oriented approaches. A short discussion of three different data-oriented ZO simulation methods is given for the CMP stack, the NMO/DMO/stack approach, and multi-parameter stacking methods like CRS.

In Chapter 2, I derive the exact Common-Reflection-Point (CRP) trajectory for unconverted waves and a reflector with homogeneous, isotropic overburden. Based on concepts of geometrical optics, I approximate the CRP trajectory for inhomogeneous overburden and the kinematic ZO response of a curved reflector segment (or CRS). By attaching CRP trajectories to each point on the ZO response, the spatial kinematic reflection response of the CRS is derived. Stacking operators of conventional imaging methods like Kirchhoff migration and MZO are briefly described as special cases of the CRS approach. Taylor expansions of the CRS response provide the CRS stacking operators suited for an actual implementation. Based on the CRS wavefield attributes, I introduce a time migration scheme and express the projected Fresnel zone. Finally, the relation to the more general 3-D problem is discussed.

In Chapter 3, I consider the implementational aspects of the CRS stack. The global optimization problem to be solved is decomposed into separate optimizations in different subsets of the pre-stack data. To overcome limitations of previously implemented search strategies, I investigate conflicting dips situations and propose an extended strategy that allows to detect and characterize an arbitrary number of contributing events for one and the same ZO location. I give a detailed description of the implementation of the particular processing steps and the stacking aperture. Finally, I transfer the concept of operator tapering to the CRS stack and discuss the influence of the near-surface velocity.

The synthetic marine Sigsbee 2A data set is presented in Chapter 4. Due to the strong variations of the wavefield complexity, these data are well suited to test the CRS stack implementation. In addition to the stacked section and the wavefield attribute sections, I present the advantages of the extended search strategy in conflicting dip situations. As applications of the wavefield attributes, I show the estimation of the projected first Fresnel zone for ZO and the attribute-based time migration result.

In Chapter 5, I present a marine data set acquired deep-offshore Chile and the corresponding CRS stack results. The CRS stacked section is compared to the conventional result obtained by means of NMO/DMO/stack. As these data are strongly dominated by diffraction patterns, this comparison is also performed with Stolt migration results of the stacked sections. Applications of the wavefield attributes are again the projected first Fresnel zone and the attribute-based time migration. Due to the multitude of diffraction patterns, the latter is very helpful for these data. An additional application of the attributes is the classification of events, as diffraction and reflection events can hardly be distinguished in the stacked sections. By means of a macro-velocity model for these data, I also present the post-stack depth migrated results of the conventional result and the CRS stack result, respectively.

The third data set was acquired offshore Costa Rica. In Chapter 6 I present these data and the CRS processing results. These data contain strong multiple events, therefore I show a simple approach to attenuate these multiples during the CRS stack. The properties of the seafloor multiple are investigated by means of forward modeling. Again, the CRS stack result is compared with the conventional processing result. I apply the wavefield attributes to estimate the projected first Fresnel zone for ZO and to identify multiples in the stack result.

In Chapter 7, I conclude the experiences and results and give an outlook on various future extensions and generalizations of the CRS stack approach like finite-offset (FO) CRS stack, 3-D ZO and FO CRS stack, consideration of topography etc.

Details concerning sign conventions and the way the data examples are visualized can be found in Appendix A, followed by a brief discussion of the coherence measure semblance in Appendix B. In Appendix C, I describe the local optimization algorithm used in the current implementation. The relation between the pulse stretch phenomenon and the CRS stack is discussed in Appendix D, followed by the implemented strategy to (approximately) extract 2-D pre-stack data from quasi 2-D acquisition in Appendix E. Finally, a list of the used hardware and software is given in Appendix F.

Chapter 2

Theory

Seismic reflection acquisition is usually performed in a way such that each point on a reflecting interface in the subsurface is illuminated several times by different pairs of sources (also called shots) and receivers. This redundancy in the data allows to separate the effects caused by the overburden of a reflector from the reflector's properties. Furthermore, the signal-to-noise ratio can be significantly increased by combining the redundant information pertaining to one and the same reflection point in depth. This information is located along the so-called *Common-Reflection-Point* (CRP) trajectory in the pre-stack data.

For the 2-D case considered in this thesis, the CRP trajectory is derived by means of geometrical optics, firstly for a reflector with homogeneous overburden, followed by an approximation for inhomogeneous overburden. With the CRP trajectory, the kinematic reflection response of an entire curved reflector segment or Common-Reflection-Surface (CRS) will be derived. Two second-order approximations of this kinematic reflection response finally provide two alternative stacking operators for the CRS stack implementation.

To illustrate the relation of the CRS approach to other commonly used seismic reflection imaging methods, the Kirchhoff migration (also called diffraction stack) and the migration to zero-offset (MZO) are briefly explained in terms of CRP trajectories.

In the remaining sections, I comment on the more general 3-D problem and its relation to the 2-D application presented in this thesis. Based on the second-order approximations of the traveltimes surface, the estimation of the projected first Fresnel zone and an attribute-based time migration is introduced. Finally, I briefly discuss the validity of the formulae for elastic media.

2.1 Common-Reflection-Point trajectory

2.1.1 CRP trajectory for homogeneous overburden

In seismic reflection acquisition it is common practice to acquire data with a multitude of receivers that record the local seismic wavefield (or components of it) initiated by shots triggered

in sequence at different locations. Consequently, the resulting data contain redundant information as one and the same point on a reflecting interface is illuminated several times by independent seismic experiments.

At this stage, I only consider the 2-D case where all shots and receivers are located along a straight line and can, thus, be described by scalar coordinates x_s and x_g , respectively. The subsurface model is assumed to be either 2-D or 2.5-D (i. e., 3-D without variations in y -direction). Both situations are equivalent with respect to the kinematic aspects of the wave propagation considered in this thesis. In the following, I will use the midpoint coordinate x_m and the half-offset h rather than x_s and x_g to identify a seismic trace. For 2-D acquisition, these coordinates are defined as

$$h = \frac{x_g - x_s}{2} \quad \text{and} \quad x_m = \frac{x_g + x_s}{2}. \quad (2.1)$$

The entire data acquired along a 2-D line sets up a three-dimensional data volume in (x_m, h, t) coordinates, where t denotes the time measured since the respective shot was triggered. To collect the redundant information pertaining to one and the same point on a reflecting interface in the subsurface, a relation between this point and its corresponding reflection event in the pre-stack time domain has to be established. In the context of this thesis, the term event refers to the entire kinematic reflection response of a structure in the subsurface. Depending on the considered subsurface structure, the event might be either a traveltimes surface or a traveltimes curve in the data volume.

Following the approach of Höcht et al. (1999), the CRP trajectory is in the following derived based on the principles of geometrical optics. I firstly assume an arbitrary reflector with a homogeneous overburden with the known constant velocity v . The kinematic reflection response of the reflector is given by the traveltimes surface $t = t(x_m, h)$. The reflector can be reconstructed from the traveltimes surface by computing the envelope of all isochrons defined by $t(x_m, h)$ and v . For this homogeneous case, all isochrons can be analytically described by

$$F(x, z; x_m, h) = \frac{(x - x_m)^2}{\left(\frac{vt}{2}\right)^2} + \frac{z^2}{\left(\frac{vt}{2}\right)^2 - h^2} - 1 = 0. \quad (2.2)$$

This family of ellipses with the parameters x_m and h immediately follows from Fermat's principle of stationary traveltimes. Due to the redundancy of the data, it is sufficient to consider only a subset of this family of isochrons: for any arbitrary configuration of shots and receivers, the envelope of the associated isochrons defines the illuminated part of the reflector. Here, I consider the common-offset (CO) configuration, i. e., $h = \text{const}$. Solving Equation (2.2) together with the condition for the envelope, $dF/dx_m = 0$, yields the envelope

$$x = x_m + \frac{t}{2h^2 t'} \left[\left(\frac{vt}{2}\right)^2 - h^2 \right] \left\{ 1 - \sqrt{1 + 4h^2 \left[\frac{t t'}{t^2 - \left(\frac{2h}{v}\right)^2} \right]^2} \right\}, \quad (2.3a)$$

$$z = \sqrt{\left[\left(\frac{vt}{2}\right)^2 - h^2 \right] \left[1 - \frac{(x - x_m)^2}{\left(\frac{vt}{2}\right)^2} \right]}, \quad (2.3b)$$

with $t' = \partial t / \partial x_m$. For Equations (2.3), z is assumed to be positive and imaginary solutions were omitted. The simple case $h = 0$ is not considered for this solution, but will be discussed separately later on.

Now, I consider an arbitrary point $(\hat{x}_m, \hat{h}, \hat{t})$ on the reflection event. The associated traveltime \hat{t} and the slope $\hat{t}' = \partial t / \partial x_m|_{x_m=\hat{x}_m, h=\hat{h}}$ are assumed to be known. Substituting \hat{x}_m , \hat{h} , \hat{t} , and \hat{t}' for x_m , h , t , and t' in Equations (2.3) readily provides the corresponding point $R = (\hat{x}, \hat{z})$ on the reflector. By computing the first derivative of the CO isochron at R , I also obtain the tangent and—perpendicular to it—the normal to the reflector at this location.

I calculate the points where the tangent and the normal intersect the x -axis. The former is denoted by x_T , the latter by x_0 . From the results (not displayed) I can calculate the distance between these points which reads

$$2r_T = x_0 - x_T = \frac{\hat{t}^2 - \left(\frac{2\hat{h}}{v}\right)^2}{\hat{t}\hat{t}'}. \quad (2.4a)$$

Due to its derivation, this distance only depends on the location R and the orientation of the reflector at R . Consequently, r_T is independent of the chosen point $(\hat{x}_m, \hat{h}, \hat{t})$ on the reflection event and represents a characteristic quantity of the reflection point R . It is fully determined by a single point on the reflection event $(\hat{x}_m, \hat{h}, \hat{t})$ and the corresponding slope \hat{t}' at this point.

The normal to the reflector at R defines the ZO ray that illuminates the point R . Its length is given by $v t_0 / 2$ where t_0 denotes the ZO traveltime. The ZO ray emerges at the surface location $(x_0, 0)$. Any point on the reflection event that pertains to the reflection point R has to satisfy Equations (2.3) for $x = \hat{x}$ and $z = \hat{z}$. Using all the all these equations, a relation between the chosen arbitrary point $(\hat{x}_m, \hat{h}, \hat{t})$ and any other point (x, h, t) on the reflection event stemming from the reflection point R can be derived:

$$x_m - r_T \sqrt{\left(\frac{h}{r_T}\right)^2 + 1} = \hat{x}_m - r_T \sqrt{\left(\frac{\hat{h}}{r_T}\right)^2 + 1}, \quad (2.4b)$$

$$\frac{t^2 - \left(\frac{2h}{v}\right)^2}{1 + \sqrt{\left(\frac{h}{r_T}\right)^2 + 1}} = \frac{\hat{t}^2 - \left(\frac{2\hat{h}}{v}\right)^2}{1 + \sqrt{\left(\frac{\hat{h}}{r_T}\right)^2 + 1}}, \quad (2.4c)$$

where r_T is given by Equation (2.4a). In other words, if a point $(\hat{x}_m, \hat{h}, \hat{t})$ on the reflection event and the slope \hat{t}' are given, all other points on the reflection event that pertain to the same reflection point $R = (\hat{x}, \hat{z})$ are given by Equations (2.4). These points set up the searched-for CRP trajectory. Obviously, the coordinates of the reflection point R are not explicitly required to describe the CRP trajectory.

For a chosen point in the ZO section, i. e., $\hat{x}_m = x_0$, $\hat{h} = 0$, and $\hat{t} = t_0$, Equations (2.4) simplify to

$$x_m(h) = x_0 + r_T \left(\sqrt{\frac{h^2}{r_T^2} + 1} - 1 \right), \quad (2.5a)$$

$$t^2(h) = \frac{4h^2}{v^2} + \frac{t_0^2}{2} \left(\sqrt{\frac{h^2}{r_T^2} + 1} + 1 \right), \quad (2.5b)$$

with

$$2r_T = \frac{t_0}{t'_0}. \quad (2.5c)$$

For the considered homogeneous overburden, the horizontal slowness p , also called the ray parameter, can be used for an alternative representation of Equation (2.5c). Introducing the emergence angle α of the ZO ray measured with respect to the surface normal (which coincides with the local reflector dip measured with respect to the surface $z = 0$), the well known relation $p = t'_0/2 = \sin \alpha/v$ yields

$$2r_T = \frac{vt_0}{2 \sin \alpha}. \quad (2.5d)$$

2.1.2 CRP trajectory for inhomogeneous overburden

With Equations (2.5), an exact analytic description of the CRP trajectory for homogeneous overburden is available. Now, my aim is to derive an approximation of the CRP trajectory for reflectors with an inhomogeneous overburden. The relationship between both cases can be established by means of the concept of object and image points that is well known from geometrical optics (see, e. g., Born and Wolf, 1959).

To illustrate this approach, a simple model consisting of three homogeneous layers is shown in Figure 2.1. I computed the ZO ray emerging at the location $(x_0, 0)$ for an arbitrarily chosen point S_{NIP} on the second interface. As the ZO ray is normal to the reflector at S_{NIP} , the suffix indicates that this is the *normal incidence point* (NIP). The refraction of the ZO ray is, of course, described by Snell's law.

Now, two hypothetical experiments are introduced to relate the properties of the reflector at S_{NIP} , namely its location, orientation, and curvature, to quantities that can be observed at the acquisition surface: for the first experiment, a point source is placed at S_{NIP} and initiates the so-called *NIP wavefront*. The radius of curvature of this NIP wavefront along the ZO ray can be described by two equations: within the homogeneous layers it changes according to the so-called *transmission law* for wavefront curvatures (Hubral and Krey, 1980):

$$R_{P_2} = R_{P_1} + v_i \Delta t, \quad (2.6a)$$

where P_1 and P_2 denote two points on the ZO ray in the considered layer, v_i is the interval velocity in this layer, and Δt is the time in which the wavefront propagates from P_1 to P_2 . This law simply states that the radius of curvature increases by the length of the normal ray segment located inside the considered homogeneous layer. This phenomenon is usually called spherical divergence

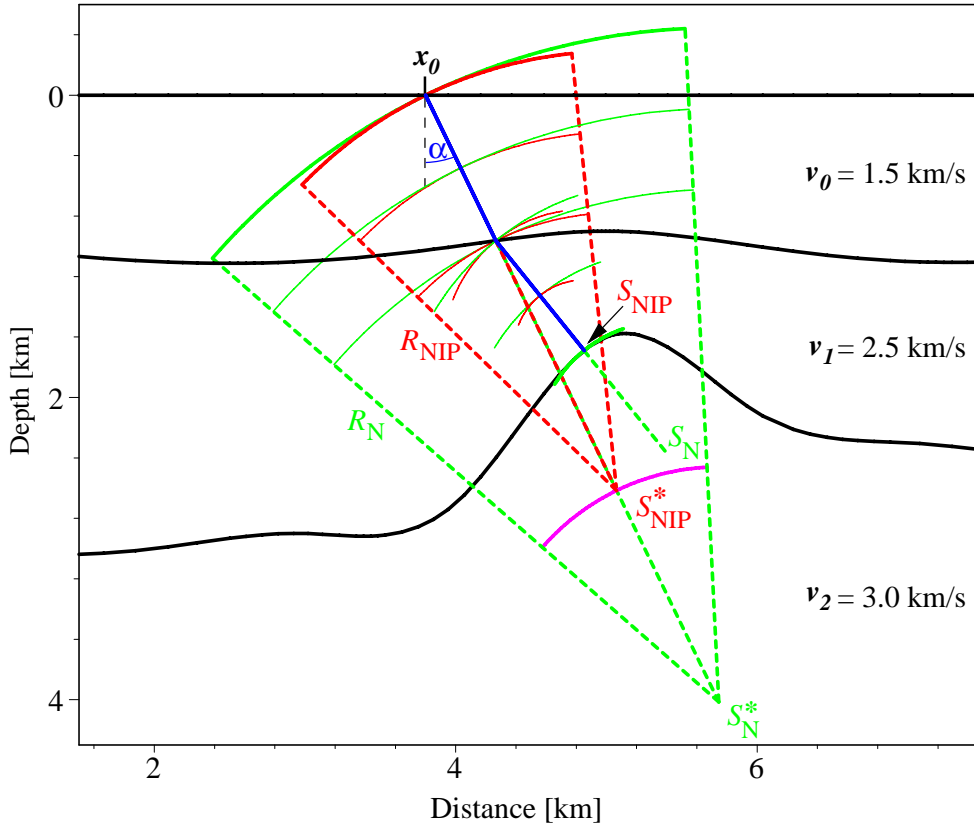


Figure 2.1: Simple model consisting of three homogeneous layers. For a chosen reflection point S_{NIP} , circular approximations of the wavefronts of the NIP wave (red) and the normal wave (green) are depicted. The ZO ray is shown as blue line. The apparent source of the NIP wavefront stemming from the object point S_{NIP} is the center of curvature S_{NIP}^* . S_{N} denotes the center of curvature of the reflector segment at S_{NIP} . The corresponding image point is given by S_{N}^* . The hypothetical reflector segment at S_{NIP}^* (magenta) would yield the same emergence angle α and radii of curvature R_{N} and R_{NIP} at x_0 for a homogeneous model with velocity v_0 .

or, more general, geometrical spreading. The latter also accounts for curvature changes due to interfaces discussed in the following.

The change of the radius of curvature due to the refraction at an interface is given by the so-called *refraction law* for wavefront curvatures which reads

$$\frac{1}{R_{\text{R}}} = \frac{v_{\text{R}} \cos^2 \gamma_{\text{I}}}{v_{\text{I}} R_{\text{I}} \cos^2 \gamma_{\text{R}}} + \frac{\frac{v_{\text{R}} \cos \gamma_{\text{I}}}{v_{\text{I}}} - \cos \gamma_{\text{R}}}{R_{\text{F}} \cos^2 \gamma_{\text{R}}}, \quad (2.6b)$$

with $R_{\text{I/R}}$ denoting the radii of wavefront curvature, $v_{\text{I/R}}$ the interval velocities, and $\gamma_{\text{I/R}}$ the angles between the directions of propagation and the normal to the interface. The indices I(ncident) and R(efracted) refer to the properties before and after refraction, respectively. The curvature of

the interface at its intersection with the ZO ray is given by R_F . For details concerning the sign conventions see Appendix A.2. For the third related law, the *reflection law* (which is not required for the hypothetical experiments), refer to Hubral and Krey (1980). It describes the change of the wavefront curvature due to reflection at an interface.

At the emergence point of the ZO ray $(x_0, 0)$, the NIP wavefront finally arrives after half the ZO reflection traveltime $t_0/2$ with the propagation direction described by α and the radius of curvature R_{NIP} . If I only consider the NIP wavefront in a vicinity around x_0 where it can be approximated by a circular wavefront, the center of curvature defines the image point $\mathfrak{S}_{\text{NIP}}$.

The second experiment is performed in the same way, but now starting with a wavefront that has the local curvature of the reflector at $\mathfrak{S}_{\text{NIP}}$, i. e., an exploding reflector experiment. The center of curvature of the considered reflector segment is denoted by \mathfrak{S}_N . As all rays are perpendicular to the reflector segment in this case, the resulting wavefront is called *normal wavefront*. It also arrives at $(x_0, 0)$ after the time $t_0/2$ and with the same propagation direction as the NIP wavefront. The radius of curvature at $(x_0, 0)$ is denoted by R_N , the image point for a circular approximation of the normal wavefront defined by its center of curvature is \mathfrak{S}_N . With these two experiments, the properties of the reflector segment, location, orientation, and curvature, are now expressed in terms of the ZO traveltime t_0 , the emergence angle α and the two radii of curvature R_{NIP} and R_N .

To find an approximation for the CRP trajectory for inhomogeneous overburden, I will now consider an auxiliary medium with the constant velocity v_0 . For models with iso-velocity layers like in Figure 2.1, v_0 coincides with the interval velocity of the first layer. For arbitrary inhomogeneous models, v_0 denotes the near-surface velocity that is assumed to be constant in the vicinity of $(x_0, 0)$ and—at this stage—also to be explicitly known.

By means of the image points $\mathfrak{S}_{\text{NIP}}^*$ and \mathfrak{S}_N^* , an hypothetical reflector segment in the auxiliary medium can be defined that would yield exactly the same wavefront curvatures and emergence angle for the two hypothetical experiments. This reflector segment is located at $\mathfrak{S}_{\text{NIP}}^*$ with the dip α and the radius of curvature $R_N - R_{\text{NIP}}$ (see magenta arc segment in Figure 2.1). In general, the associated ZO traveltime $t_0^* = 2R_{\text{NIP}}/v_0$ differs from the ZO traveltime t_0 obtained from the actual, inhomogeneous model. For the circular approximations of the NIP and normal wavefronts, this traveltime difference applies to any shot/receiver pair, thus $t^* - t$ coincides with $t_0^* - t_0$ or

$$t = t^* - t_0^* + t_0 = t^* - \frac{2R_{\text{NIP}}}{v_0} + t_0. \quad (2.7)$$

This equation relates the event obtained for the actual medium to the event stemming from the hypothetical reflection point $\mathfrak{S}_{\text{NIP}}^*$ in the auxiliary medium. This relation allows to approximate the CRP trajectory for inhomogeneous overburden: the CRP trajectory for the hypothetical reflection point $\mathfrak{S}_{\text{NIP}}^*$ is given by Equations (2.5) with $t_0 = 2R_{\text{NIP}}/v_0$ and $v = v_0$. Together with Equation (2.7), this finally yields the approximate CRP trajectory for inhomogeneous overburden:

$$x_m(h) = x_0 + r_T \left(\sqrt{\frac{h^2}{r_T^2} + 1} - 1 \right), \quad (2.8a)$$

$$\left[t(h) - \left(t_0 - \frac{2R_{\text{NIP}}}{v_0} \right) \right]^2 = \frac{4h^2}{v_0^2} + \frac{2R_{\text{NIP}}^2}{v_0^2} \left(\sqrt{\frac{h^2}{r_T^2} + 1} + 1 \right), \quad (2.8b)$$

with

$$r_T = \frac{R_{\text{NIP}}}{2 \sin \alpha}. \quad (2.8c)$$

Note that for Equation (2.8a), Snell's law is satisfied in the auxiliary medium at $\mathfrak{S}_{\text{NIP}}^*$ rather than in the actual model at $\mathfrak{S}_{\text{NIP}}$. This introduces an additional approximation.

2.2 Kinematic ZO response of a reflector segment

So far, I only considered a reflection point defined by its location and orientation. Now the kinematic reflection response of the entire reflector segment around the object point $\mathfrak{S}_{\text{NIP}}$ will be approximated for the ZO case: assuming a circular normal wavefront, I simply have to consider its radius at x_0 and at an arbitrary location \tilde{x}_0 . This situation is depicted in Figure 2.2: the travel-time difference $\Delta t = \tilde{t}_0 - t_0$ for the rays emerging at \tilde{x}_0 and x_0 is given by $2(\tilde{R}_N - R_N)/v_0$. The triangle defined by $\mathfrak{S}_{\text{N}}^*$, $(\tilde{x}_0, 0)$, and $(x_0, 0)$ (the surface location vertically above $\mathfrak{S}_{\text{N}}^*$) yields

$$\tilde{R}_N^2 = (R_N \cos \alpha)^2 + [R_N \sin \alpha + (\tilde{x}_0 - x_0)]^2. \quad (2.9)$$

Note that α is negative for the shown example. Using the relation between \tilde{R}_N and $\tilde{t}_0 - t_0$, this equation can be solved for \tilde{t}_0 . The appropriate solution reads:

$$\tilde{t}_0 = t_0 + \frac{2R_N}{v_0} \left(\sqrt{1 + \frac{(\tilde{x}_0 - x_0)^2}{R_N^2} + \frac{2 \sin \alpha (\tilde{x}_0 - x_0)}{R_N}} - 1 \right). \quad (2.10)$$

Using again the ray parameter $p = \sin \alpha/v$ with $\alpha = \tilde{\alpha}$ and $v = v_0$, the slope of the ZO hyperbola (2.10) defines the emergence angle $\tilde{\alpha}$:

$$\sin \tilde{\alpha}(\tilde{x}_0) = \frac{v d\tilde{t}_0}{2 d\tilde{x}_0} = \frac{\tilde{x}_0 - x_0 + R_N \sin \alpha}{R_N \sqrt{1 + \frac{(\tilde{x}_0 - x_0)^2}{R_N^2} + \frac{2 \sin \alpha (\tilde{x}_0 - x_0)}{R_N}} + 1}. \quad (2.11)$$

2.3 Multi-coverage reflection response of a reflector segment

In the two preceding sections, the CRP trajectory for a reflection point with inhomogeneous overburden and the ZO reflection response of the reflector segment at this point was derived. Both approaches can now be combined to set up a moveout surface in the multi-coverage data domain. The basic idea is to attach a CRP trajectory to each point given by the ZO reflection response. For a ZO location \tilde{x}_0 , the CRP trajectory (Equations 2.5) is defined by $t_0 = \tilde{t}_0$, $x_0 = \tilde{x}_0$, $\alpha = \tilde{\alpha}$, and $R_{\text{NIP}} = \tilde{R}_{\text{NIP}}$, where \tilde{t}_0 and $\tilde{\alpha}$ are given by Equations (2.10) and (2.11) whereas \tilde{R}_{NIP} is not yet determined. The radius R_{NIP} is assumed to be constant along the normal wavefront and, thus, is

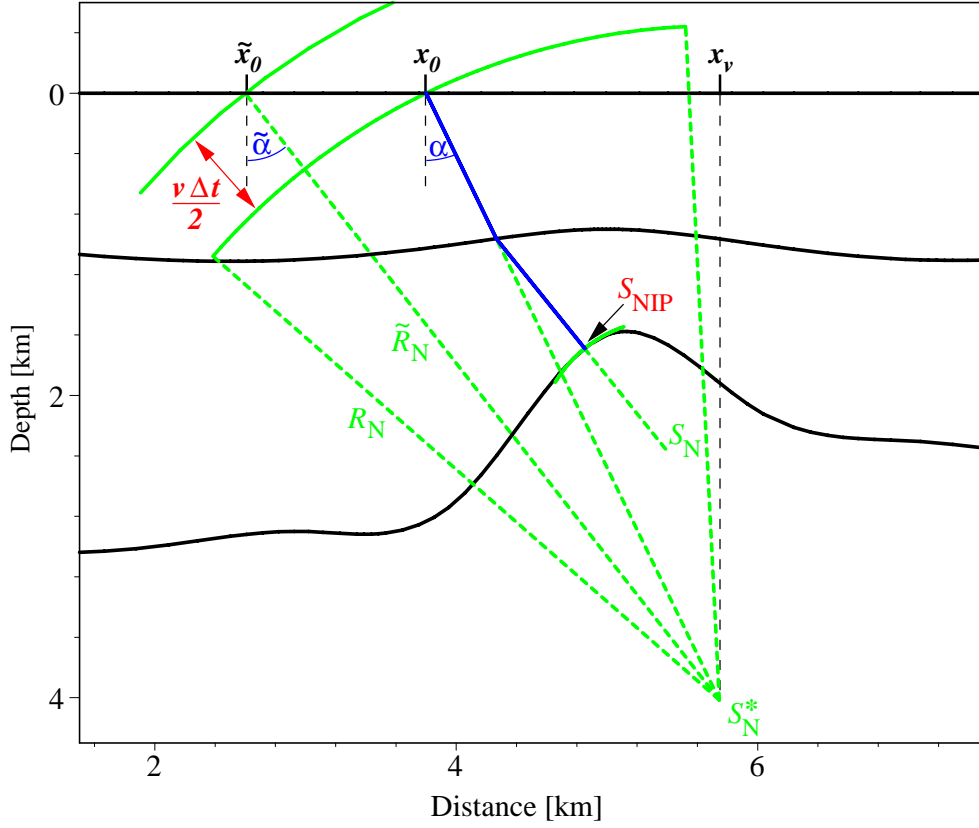


Figure 2.2: Circular normal wavefronts (green) stemming from the image point S_N^* for two different ZO locations x_0 and \tilde{x}_0 , respectively. The interfaces, the actual ZO ray to x_0 (blue), and the object points S_N and S_{NIP} are displayed to allow an easier comparison with Figure 2.1.

subject to the same change as the radius of the normal wavefront:

$$\begin{aligned} \tilde{R}_{NIP}(\tilde{x}_0) &= \tilde{R}_N(\tilde{x}_0) - R_N + R_{NIP} = \frac{v_0(\tilde{t}_0 - t_0)}{2} + R_{NIP} \\ &= R_N \left[\sqrt{\frac{(\tilde{x}_0 - x_0)^2}{R_N^2} + \frac{2 \sin \alpha (\tilde{x}_0 - x_0)}{R_N} + 1} - 1 \right] + R_{NIP}. \end{aligned} \quad (2.12)$$

The time shift (2.7) is constant for all CRP trajectories: according to Equations (2.10) and (2.12), $\tilde{t}_0 - 2\tilde{R}_{NIP}/v_0 = t_0 - 2R_{NIP}/v_0$. This is a consequence of the assumption $R_{NIP} = \text{const}$ along the normal wavefront. With the initial values given by Equations (2.10)-(2.12) and the CRP trajectory (2.8) for inhomogeneous overburden, I finally obtain a family of CRP trajectories parameter-

ized by \tilde{x}_0 :

$$x_m(\tilde{x}_0, h) = \tilde{x}_0 + \tilde{r}_T(\tilde{x}_0) \left(\sqrt{\frac{h^2}{\tilde{r}_T^2(\tilde{x}_0)} + 1} - 1 \right), \quad (2.13a)$$

$$\left[t(\tilde{x}_0, h) - \left(t_0 - \frac{2R_{\text{NIP}}}{v_0} \right) \right]^2 = \frac{4h^2}{v_0^2} + \frac{2\tilde{R}_{\text{NIP}}^2(\tilde{x}_0)}{v_0^2} \left(\sqrt{\frac{h^2}{\tilde{r}_T^2(\tilde{x}_0)} + 1} + 1 \right), \quad (2.13b)$$

with

$$\tilde{r}_T = \frac{\tilde{R}_{\text{NIP}}(\tilde{x}_0)}{2 \sin \alpha(\tilde{x}_0)}. \quad (2.13c)$$

This is the searched-for approximation of the kinematic reflection response of an arbitrarily curved reflector segment in depth. However, the given representation parameterized with \tilde{x}_0 is not able to handle a caustic in the normal wavefront at $(x_0, 0)$. To handle this singularity, an alternative representation parameterized with $\tilde{\alpha}$ was discussed by Höcht et al. (1999). As Taylor expansions of Equations (2.13) are used for the actual implementation of the CRS stack, it does not matter which representation is used. Thus, there is no need to discuss the alternative representation in the scope of this thesis.

2.4 Conventional imaging methods in terms of CRP trajectories

In the preceding section, the kinematic reflection response of a CRS in depth was derived by attaching CRP trajectories to each point on the kinematic ZO reflection response of the CRS. Three kinematic wavefield attributes, α , R_{NIP} , and R_{N} , are required to define this reflection response. To reveal the relationship between the CRS stack approach and conventional imaging methods, the same approach can be used to approximate their stacking operators. In the following, I will discuss this for the *migration to ZO* (MZO) and the Kirchhoff migration. As only the stacking operators are considered, but not the image locations, these considerations apply to Kirchhoff depth migration as well as to Kirchhoff time migration. It will turn out that both imaging methods, MZO and Kirchhoff migration, are special cases in terms of the CRS approach.

2.4.1 Migration to zero-offset

The MZO is based on the kinematic reflection response of the ZO isochron associated with a point (x_0, t_0) in the time domain. If the macro-velocity model is a priori known, the isochron is fully determined and its kinematic reflection response can be computed to provide a stacking operator for the point (x_0, t_0) .

As the macro-velocity is, in general, not available, the MZO is usually split into two separate, approximate processes that can be repeated iteratively: firstly, the moveout due to the overburden of a reflector is considered by means of a *normal moveout* (NMO) *correction*. This step is commonly applied with NMO velocities¹ derived by means of velocity analysis in the CMP gathers

¹see Equation (3.7) for the definition of NMO velocities used in this thesis.

and, thus, represents a data-oriented method, just as the CRS stack approach. A second processing step, the so-called *dip moveout* (DMO) *correction* is performed by a stacking operation in the NMO-corrected common-offset (CO) gathers. It accounts for the moveout due to the reflector's dip.² For constant velocity models, the DMO operator does not explicitly depend on the velocity at all. Thus, the DMO correction is often applied with a constant velocity approximation.

If I consider a Kirchhoff-type approach to constant velocity DMO, the sample at a point (x_m, τ) in the NMO-corrected pre-stack data is “smeared” along the the DMO ellipse, which is the kinematic ZO reflection response of the corresponding CO isochron

$$\frac{t_0^2(x_0)}{\tau^2} + \frac{(x_0 - x_m)^2}{h^2} = 1 \quad \text{or} \quad t_0(x_0) = \tau \sqrt{1 - \frac{(x_0 - x_m)^2}{h^2}}. \quad (2.14)$$

An alternative way is to consider a point (x_0, t_0) in the ZO section and to stack along the kinematic NMO-corrected reflection response of the corresponding ZO isochron

$$\tau(x_m) = \frac{t_0}{\sqrt{1 - \frac{(x_m - x_0)^2}{h^2}}}. \quad (2.15)$$

Of course, both equations are identical, but derived from different points of view.

To correctly apply a DMO correction, additional velocity analyses in the NMO/DMO-corrected image gathers are required: for the correct model, all events in the corrected pre-stack data volume should be perfectly flat in offset direction. For details on the NMO correction refer, e. g., to Yilmaz (1987). An introduction to the DMO correction and related references can be found in Deregowski (1986). A comprehensive description of the MZO in terms of cascaded migration/demigration and its relation to NMO/DMO can be found in Mann (1997).

To compare the MZO and the CRS approach, I assume that the model is already known, i. e., the isochron is fully determined for a chosen point (x_0, t_0) . In the following, it serves as CRS in the depth. The kinematic ZO response of the isochron is, per definition, the point (x_0, t_0) . This implies that the normal wavefront stemming from the isochron focuses at $(x_0, 0)$, thus $R_N = 0$. R_{NIP} is implicitly given by the isochron, for the homogeneous case it simply reads $R_{NIP} = vt_0/2$. Consequently, the MZO is the special case of the CRS response where $R_N = 0$. All CRP trajectories are attached to the point (x_0, t_0) and set up a fan-shaped reflection response.

The MZO does neither consider the actual curvature of the reflector at the actual reflection point, nor the actual location and orientation of the reflector segment, but all combinations of location and orientation given by the ZO isochron. Thus, it is no surprise that the MZO reflection response, in general, fits quite badly the actual reflection response, except if the subsurface structure is, by chance, shaped like the ZO isochron. An example of an MZO response constructed by means of CRP trajectories can be found in Müller (1999), Figure 3.1: even for the simple case of homogeneous overburden, the area of tangency³ between the MZO response and the actual reflection response is very small.

²From an alternative point of view not discussed here, the DMO correction accounts for the reflection point dispersal occurring in an NMO/stack chain.

³In this context, the area of tangency is defined by the maximum time shift between the two surfaces: it has to be sufficiently small to allow constructive interference of the contributing traces.

Note that the derived representation of the CRS response (2.13) is not able to handle the case $R_N = 0$, but the alternative representation by Höcht et al. (1999) has to be considered.

2.4.2 Kirchhoff migration

For pre-stack and post-stack Kirchhoff migration, the kinematic reflection response of a diffraction point in depth is considered. In terms of the CRS stack approach, this reflection response is associated with a reflector segment with infinite curvature and undefined orientation. According to the hypothetical experiments shown in Figure 2.1, this implies $R_N = R_{\text{NIP}}$, again a special case of the CRS stack approach. The actual curvature and orientation of the reflector segment in depth is not used. Thus, only events stemming from strongly curved reflector segments are accurately described by the Kirchhoff operator. A Kirchhoff operator constructed by means of CRP trajectories can be found in Müller (1999), Figure 3.1: the area of tangency between the Kirchhoff operator and the actual reflection event is larger than for the MZO, but the operator extends into areas far off the reflection event where no coherent energy stemming from the reflector can be found.

I conclude that any imaging method that does not use all three wavefield attributes characterizing the subsurface reflector segment, but only a subset or a combination of them, yields operators that fit the actual reflection response worse than the CRS response. However, note that the CRS response is an approximation of the true reflection response: it is only valid for rays in a vicinity of the considered ZO ray emerging at x_0 . This limitation does not necessarily apply to other imaging methods.

2.5 Taylor expansions of the CRS response

The parametric representation of the CRS response (2.13) and its alternative counterpart introduced by Höcht et al. (1999) are very difficult to handle in an implementation of the CRS stack approach. An explicit function of $x_m - x_0$ and h is much easier to evaluate for each contributing trace. Taylor expansions of the CRS response provide such explicit representations. Although they complicate the geometrical interpretation, the second order approximation of the traveltimes is preserved. To achieve an acceptable computational efficiency, they can hardly be avoided.

For the implementation of the CRS stack, I make use of two Taylor expansions of second order: an expansion for t and one for t^2 . The former is used to obtain a simple analytic approximation of the projected first Fresnel zone (see Section 2.7), the latter serves as CRS stacking operator for the coherence analyses and the stack itself.

The Taylor expansion of t , also referred to as parabolic CRS approximation, reads

$$t_{\text{par}}(x_m, h) = t_0 + \frac{2 \sin \alpha (x_m - x_0)}{v_0} + \frac{\cos^2 \alpha}{v_0} \left[\frac{(x_m - x_0)^2}{R_N} + \frac{h^2}{R_{\text{NIP}}} \right]. \quad (2.16)$$

It represents a paraboloid with vertical symmetry axis and its apex located in the ZO section, shifted in time and midpoint with respect to x_0 and t_0 . For a diffractor, we obtain the special case

of a paraboloid of revolution ($R_N = R_{\text{NIP}}$). In the general case, it is either an elliptic paraboloid ($R_N R_{\text{NIP}} > 0$) or a hyperbolic paraboloid ($R_N R_{\text{NIP}} < 0$).

The Taylor expansion of t^2 , the so-called hyperbolic approximation, yields a surface with its apex again in the ZO section. The same considerations with respect to the apex location apply for this approximation that reads

$$t_{\text{hyp}}^2(x_m, h) = \left[t_0 + \frac{2 \sin \alpha (x_m - x_0)}{v_0} \right]^2 + \frac{2 t_0 \cos^2 \alpha}{v_0} \left[\frac{(x_m - x_0)^2}{R_N} + \frac{h^2}{R_{\text{NIP}}} \right]. \quad (2.17)$$

Depending on the attributes, this quadric represents a hyperboloid of two sheets, an ellipsoid, or a more general surface that is elliptic in the ZO plane and hyperbolic in the CMP gather, or vice versa. In the following, I will refer to events that can be approximated by such a surface as “hyperbolic”.

Both approximations can also be derived by means of paraxial ray theory, where a linear relationship between the properties of the central ray and a paraxial ray in its vicinity is assumed. Bortfeld (1989) introduced the so-called *ray propagator* formalism to express the integral properties along a paraxial ray in terms of their counterparts along the central ray. As the CRS wavefield attributes α , R_{NIP} , and R_N represent the integral properties along the central ray in the ZO case, they provide an alternative formulation of the ray propagator matrix for ZO. A derivation of Equations (2.16) and (2.17) based on this approach can be found in Schleicher et al. (1993) and Tygel et al. (1997).

Ursin (1982) showed that hyperbolic approximations of the traveltimes are more accurate than their parabolic counterparts for inhomogeneous media. Müller (1999) and Jäger (1999) made similar observation for the two Taylor expansions of the CRS operator (2.17) and (2.16). Thus, the hyperbolic operator (2.17) is used for the coherence analysis and as stacking surface. For the simple case of a planar reflector with homogeneous overburden, the hyperbolic approximation provides an exact kinematic representation of the actual reflection event.

2.6 Attribute-based time migration

The final goal of seismic reflection imaging is, of course, to obtain a structural image of the subsurface. Kirchhoff pre-stack depth migration performs this task directly in only one step and, thus, appears to be the most “natural” approach to this problem. However, depth migration requires a velocity model and the migration result is very sensitive to errors in this model. If the migration result is not assigned to the diffractor in the depth domain, but to the apex of the kinematic diffraction response in the time domain, the result is far less sensitive to velocity errors. For not too complex models, this so-called *time migration* also yields a structural image, but now still in the time domain.

As I already discussed, the Kirchhoff migration operator is a special case of the CRS operator with $R_{\text{NIP}} = R_N$, i. e., the CRS operator approximates the Kirchhoff operator in this situation up to second order. A reflector segment at R is characterized by its wavefield attributes α , R_{NIP} , and R_N at its associated ZO location P_0 . As a hypothetical diffractor at the same depth location R has an

undefined orientation, the normal ray down to the reflector segment is also a possible raypath for the diffracted wavefront. Of course, the traveltime t_0 and the emergence angle α along the normal ray are the same for the actual reflector segment as well as the hypothetical diffractor. This also applies to R_{NIP} , as this attribute does not depend on the reflector's curvature. Consequently, the only difference is given by R_{N} , which coincides with R_{NIP} for a diffractor.

In other words, if the CRS stacking operator for an arbitrary reflector segment is known, an approximation of the associated Kirchhoff migration operator is readily available by simply substituting R_{NIP} for R_{N} in Equation (2.17):

$$t_{\text{D}}^2(x_{\text{m}}, h) = \left[t_0 + \frac{2 \sin \alpha (x_{\text{m}} - x_0)}{v_0} \right]^2 + \frac{2 t_0 \cos^2 \alpha}{v_0 R_{\text{NIP}}} \left[(x_{\text{m}} - x_0)^2 + h^2 \right]. \quad (2.18)$$

This represents either a hyperboloid of revolution or an ellipsoid of revolution, depending on the sign of R_{NIP} . Its apex is located in the ZO plane $h = 0$.

The approximated diffraction response might be used as alternative stacking operator to simulate a ZO section with Kirchhoff-type operators, although the CRS operator better approximates the actual reflection events. A more attractive application was proposed by Mann et al. (2000): the apex of the approximate diffraction response also provides an approximation of the image location of a Kirchhoff time migration. Due to the symmetry of the response, the apex can be calculated in any vertical plane containing the symmetry axis. This applies to the ZO plane $h = 0$, where $\partial t_{\text{D}}(x_{\text{m}}, h = 0) / \partial x_{\text{m}} = 0$ yields the apex location

$$x_{\text{apex}} = x_0 - \frac{R_{\text{NIP}} t_0 v_0 \sin \alpha}{2 R_{\text{NIP}} \sin^2 \alpha + t_0 v_0 \cos^2 \alpha}, \quad (2.19a)$$

$$t_{\text{apex}}^2 = \frac{t_0^3 v_0 \cos^2 \alpha}{2 R_{\text{NIP}} \sin^2 \alpha + t_0 v_0 \cos^2 \alpha}. \quad (2.19b)$$

Parameterized in terms of the apex location $(x_{\text{apex}}, t_{\text{apex}})$ instead of the ZO location (x_0, t_0) and with $h = 0$, the approximate ZO diffraction response (2.18) reads

$$t_{\text{D}}^2(x) = t_{\text{apex}}^2 + \frac{4(x - x_{\text{apex}})^2}{v_{\text{c}}^2} \quad \text{with} \quad (2.20a)$$

$$v_{\text{c}}^2 = \frac{2 v_0^2 R_{\text{NIP}}}{2 R_{\text{NIP}} \sin^2 \alpha + v_0 t_0 \cos^2 \alpha}. \quad (2.20b)$$

For homogenous media, i. e., $R_{\text{NIP}} = t_0 v_0 / 2$, v_{c} coincides with the medium velocity v_0 . For horizontally layered media, i. e., $\alpha = 0$, v_{c} reduces to the NMO velocity v_{NMO} (see Equation (3.7)) that also coincides with the root mean square (RMS) velocity v_{RMS} .

Thus, a summation along the approximate diffraction response (2.18) with its result assigned to its apex approximates a Kirchhoff time migration with a constant velocity v_{c} . Such time migrations with locally constant migration velocities are common practice in the industry. With the CRS attributes, the velocity v_{c} can be directly determined—an explicit model of migration velocities is no longer required.

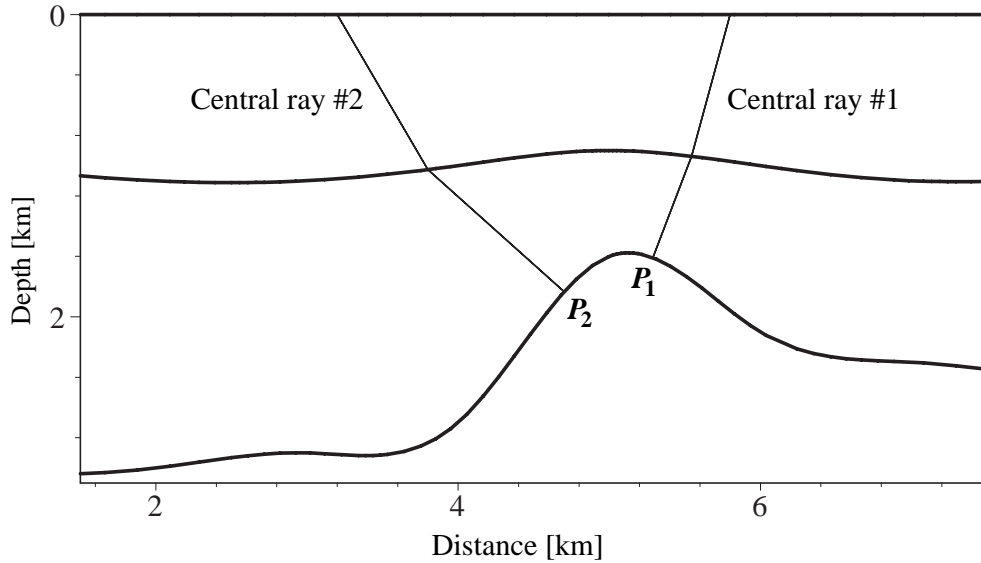


Figure 2.3: Model with three iso-velocity layers (see Figure 2.1) and two chosen central ZO rays reflected at the second interface at P_1 and P_2 , respectively.

In usual Kirchhoff migration, the location of the area of tangency between operator and event is unknown. Thus, the summation has to be performed inside a large aperture to ensure that the region of tangency is actually included. This is time consuming and does not yield the best possible result, see Schleicher et al. (1997). In the CRS approach, I already know the ZO location P_0 that lies inside the area of tangency. Restricting the stacking aperture to the vicinity of P_0 , I can readily perform a limited aperture migration without any additional effort.

The approximate reflection response given by the CRS stacking operator (2.17) fits better the actual reflection event than the diffraction response (2.18). Therefore, I finally propose to stack along the former operator instead of the latter and to assign the result to the apex $(x_{\text{apex}}, t_{\text{apex}})$. In this way, all three CRS wavefield attribute contribute to the time migration and the same stacking operator can be used for the ZO simulation as well as the time migration.

To illustrate this attribute-based time migration approach, I selected two different ZO rays reflected at the second interface of the iso-velocity layer model introduced in Figure 2.1. The model and the two chosen ZO rays reflected at P_1 and P_2 , respectively, are depicted in Figure 2.3. I forward-calculated the kinematic ZO reflection response of the second interface, the kinematic ZO responses of the two hypothetical diffractors located at P_1 and P_2 , as well as the CRS wavefield attributes along the corresponding ZO rays.

The kinematic ZO diffraction and reflection responses and their attribute-based approximations are displayed in Figure 2.4 and 2.5 separately for each of the two selected ZO rays. As expected, the CRS operators (magenta lines) fit very closely the actual ZO reflection responses (green crosses) in the vicinity of the ZO locations P_0 (black dots), where the ZO rays from P_1 or P_2 , respectively, emerge at the surface.

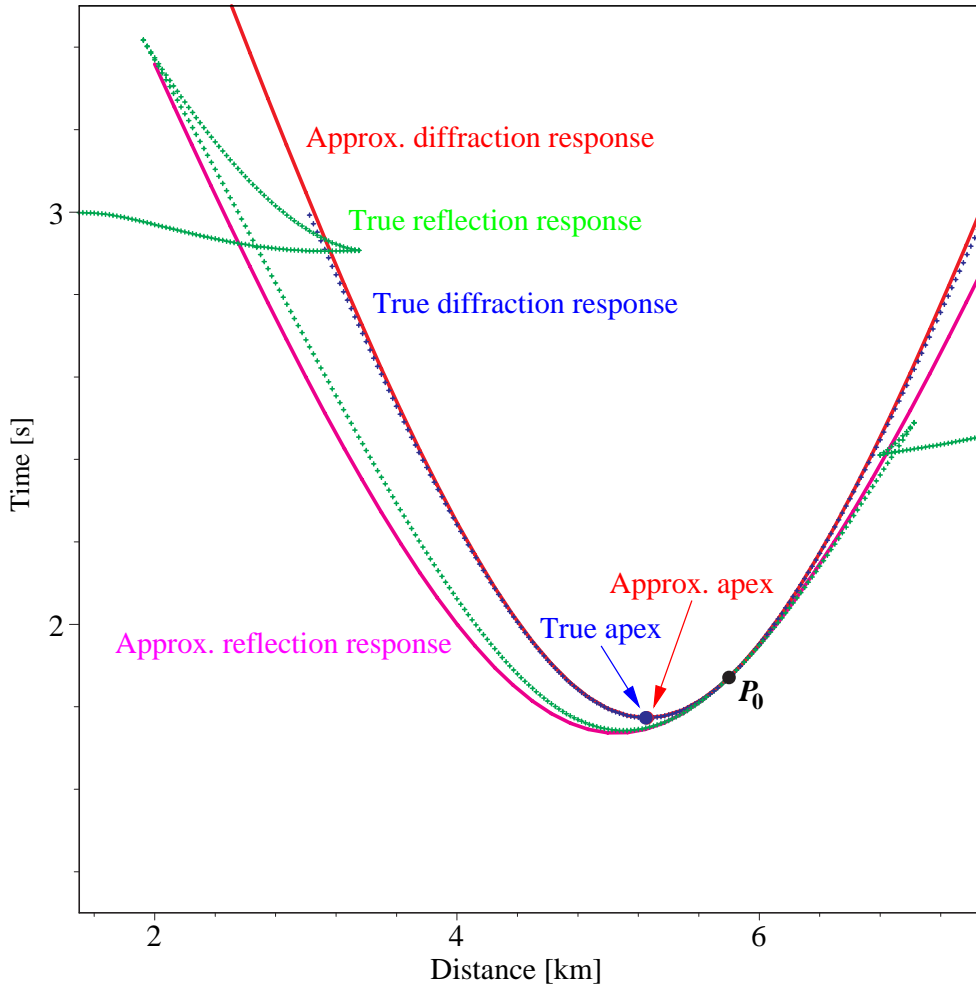


Figure 2.4: True ZO reflection response of second interface, true diffraction response of point P_1 and their attribute-based approximations. The approximated apex location almost perfectly coincides with the true apex location. P_0 is the ZO location corresponding to point P_1 in depth.

Of course, the true ZO diffraction responses (blue crosses) and their attributed-based approximations (red lines) are also tangent to the reflection event at P_0 , but the areas of tangency are smaller than for the CRS operators—a direct consequence of the fact that the CRS operator also accounts for the reflector’s curvatures at P_1 and P_2 . Thus, it is advantageous to stack along the CRS operators instead of the approximate diffraction responses: the achieved signal-to-noise ratio will be higher in this case.

The true image locations of the model-based, i. e., optimum, time migration are depicted by blue dots, the approximate image locations of a constant velocity time migration with v_c are displayed as red dots. All image locations are given by the apices of the respective (approximate) diffraction responses. I observe that if the image location is not too far from the ZO location P_0 (Example 1,

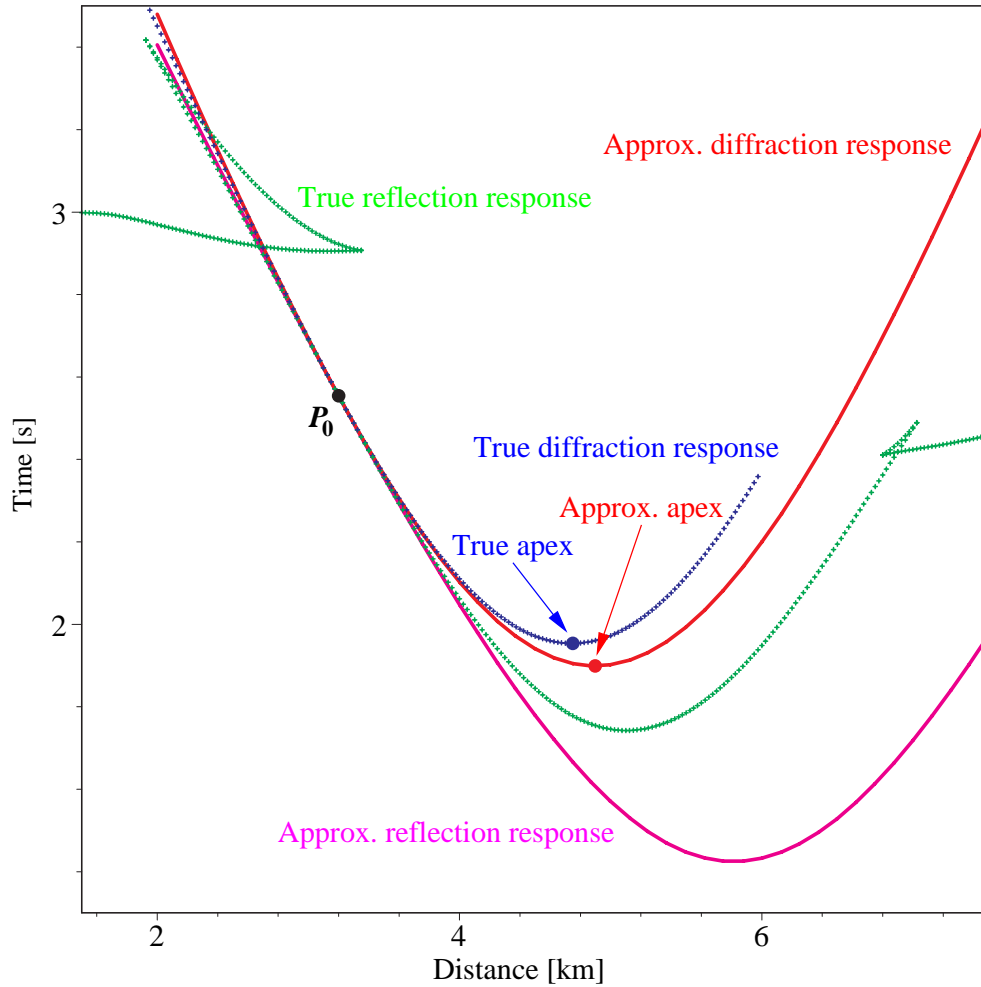


Figure 2.5: True ZO reflection response of second interface, true diffraction response of point P_2 and their attribute-based approximations. The approximated apex location slightly deviates from the true apex location. P_0 is the ZO location corresponding to point P_2 in depth.

Figure 2.4), the approximate apex location given by $(x_{\text{apex}}, t_{\text{apex}})$ almost perfectly coincides with the true image location: in this case, I can expect a migration result superior to the conventional time migration result placed at the correct image location. For larger distances between P_0 and $(x_{\text{apex}}, t_{\text{apex}})$ (Example 2, Figure 2.5), the accuracy of the image location decreases. However, we have to keep in mind that time migration is in practice often applied with the assumption of a (locally) constant migration velocity and the used migration velocity model might itself be inaccurate.

Note that the migration velocity v_c in Equations (2.20) is defined by the wavefield attributes at the ZO location (x_0, t_0) . In a conventional constant velocity time migration, the migration velocity is defined at the apex (2.19) of the migration operator.

2.7 Projected first Fresnel zone

The zero-order ray theory used in geometrical optics is a high frequency approximation of the actual wave propagation phenomena. However, the actual frequency content in seismic reflection data is usually quite low if I compare the dominant wavelength of the seismic wavelet with the scale of the subsurface structures to be imaged. Consequently, it is not adequate to assume that the seismic energy propagates along mathematical rays within a virtually infinitesimal volume. Instead, wave propagation is affected by a finite volume in the subsurface around the considered ray. The major contributions depend on the subsurface within the so-called *first Fresnel volume*. This implies that the maximum achievable resolution in the measured data is a function of the frequency content of the data.

The intersection of the first Fresnel volume with a reflector yields the so-called *first interface Fresnel zone* that defines the maximum achievable resolution in terms of reflector properties. The first interface Fresnel zone in the depth domain corresponds to the *projected first Fresnel zone* in the time domain: the major contribution stemming from a particular reflector segment in the depth domain can be found inside the associated projected first Fresnel zone in the time domain. Thus, the projected first Fresnel zone represents an optimum stacking aperture for any stacking procedure: a larger aperture will decrease the resolution of the results in terms of reflector properties, a smaller aperture, however, will not increase the resolution any more. In the latter case, the number of contributing traces decreases. Due to the unavoidable noise in the data, this reduces the stability of data-oriented imaging methods.

To define the first interface Fresnel zone around an arbitrarily chosen central ray, I consider the diffraction traveltimes from the source down to each point on the reflector and up to the receiver. The first interface Fresnel zone around a reflection point \mathbf{x}_P is set up by all points \mathbf{x}_R on the reflector for which the diffraction traveltime t_d and the reflection traveltime t_R along the central ray satisfy

$$|t_d(\mathbf{x}_R) - t_R(\mathbf{x}_P)| \leq \frac{T}{2}, \quad (2.21)$$

where T denotes the period of a mono-frequent source signal (Kravtsov and Orlov, 1990). For the ZO case and a frequency of 30 Hz, this situation is depicted in Figure 2.6: \mathbf{x}_R is computed along the central ZO rays (solid black lines). The dashed magenta lines represent the diffraction rays that satisfy $T/2 = |t_d - t_R|$, i. e., they define the border of the interface Fresnel zones (magenta reflector segments). Note that the Fresnel volume and, consequently, the interface and projected Fresnel zones depend on the considered acquisition geometry. For transient wavelets, $T/2$ has to be replaced by some measure of the effective wavelet length τ_e , a topic that is discussed in Section 3.6.1.

Hubral et al. (1993) introduced the concept of the projected first Fresnel zone for ZO as a time domain counterpart to the first interface Fresnel zone in the depth domain: its is defined by the emergence locations of all normal rays reflected within the first interface Fresnel zone. The normal rays yielding the borders of the projected first Fresnel zones (magenta segments of the acquisition line) are shown as solid magenta lines in Figure 2.6.

So far, the determination of the projected as well as the interface Fresnel zone requires the knowledge of the subsurface model. However, Hubral et al. (1993) demonstrated how the projected first

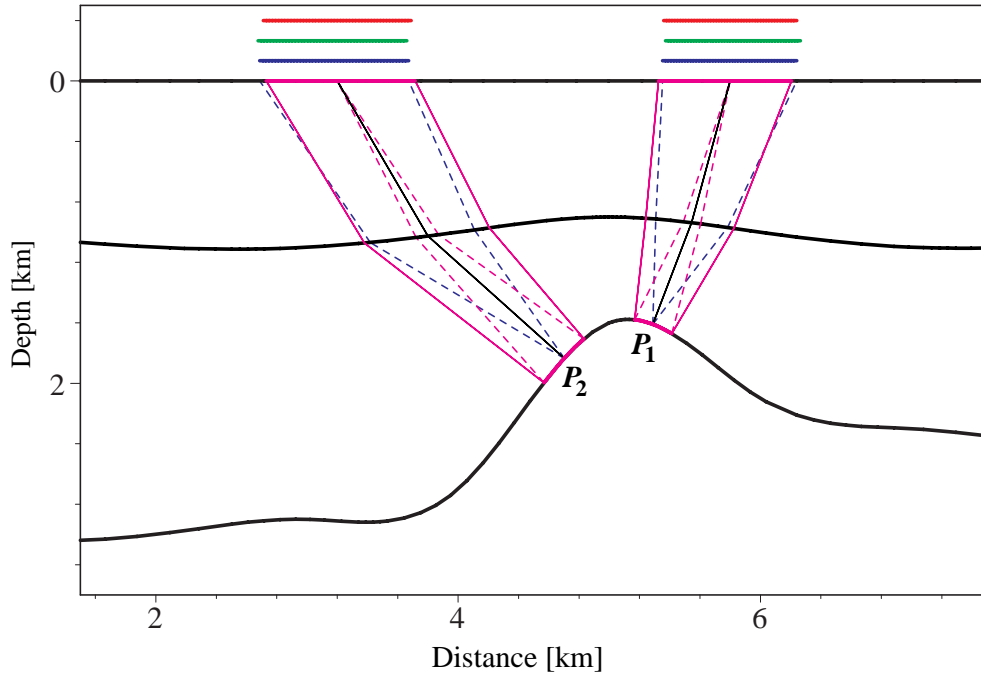


Figure 2.6: The first Fresnel zones at the reflector for the two ZO rays shown in Figure 2.3 and their projections onto the acquisition line along the normal rays at the borders of the Fresnel zones are shown in magenta. The “reversed” definition (2.22) evaluated with the true traveltimes yields the projected first Fresnel zones shown in blue. The hyperbolic and parabolic approximations are depicted in green and red, respectively. A dominant frequency of 30 Hz was assumed. Solid lines represent normal ZO rays, dashed lines are diffracted rays.

Fresnel zone can be estimated from traveltimes, only. Their first step was to express the diffraction traveltimes t_d by means of paraxial ray theory in terms of the ray propagator matrix associated with the reflected central ray. This leads to a paraxial approximation of the interface Fresnel zone that can be expressed in 3-D by a symmetric 2×2 Fresnel zone matrix \mathbf{H} . It describes an ellipse in the plane tangent to the reflector at the considered reflection point. Again using paraxial ray theory, \mathbf{H} can be projected to the acquisition surface yielding the projected Fresnel zone matrix \mathbf{H}_p that defines an ellipse around the receiver at the acquisition surface. This matrix can be directly calculated from traveltimes: it is given by the difference of the second spatial derivatives (or Hessian matrices) of the ZO and CMP reflection traveltimes along the acquisition surface, evaluated at the emergence location of the normal ray.

Schleicher et al. (1997) generalized this approach to arbitrary acquisition geometries. They compared the minimum aperture for a Kirchhoff migration with the generalized expression for the projected Fresnel zone matrix \mathbf{H}_p and observed that \mathbf{H}_p coincides with the difference of the Hessian matrices of the actual reflection response and the (hypothetical) diffraction response stemming from the considered point on the reflector. As the diffraction and reflection events are always

tangent to each other along the CRP trajectory, the projected first Fresnel zone around the CRP trajectory can be directly determined from the difference of the reflection traveltime t_{R} and the diffraction traveltime t_{D} . In analogy to the condition for the interface Fresnel zone (2.21), the projected first Fresnel zone around a receiver is then defined by

$$|t_{\text{D}}(\mathbf{x}) - t_{\text{R}}(\mathbf{x})| \leq \frac{T}{2}, \quad (2.22)$$

where the vector \mathbf{x} denotes the shot and receiver positions for an arbitrary acquisition geometry. For the 2-D ZO case, \mathbf{x} simply reduces to the midpoint displacement $x_{\text{m}} - x_0$. In Figure 2.6, the diffraction rays associated with t_{D} are depicted as dashed blue lines. Note that t_{D} is not equivalent to the diffraction traveltime t_{d} that refers to the dashed magenta rays.

The true diffraction and reflection traveltimes t_{D} and t_{R} depend on the subsurface model. However, the CRS approach provides approximations of the reflection traveltimes as well as the diffraction traveltimes. For the latter, I simply have to set $R_{\text{N}} := R_{\text{NIP}}$, see preceding section. In principle, one might conclude that these approximations allow to estimate the projected first Fresnel zone for any arbitrary acquisition configuration. However, comparing the special case of ZO discussed by Hubral et al. (1993) with the generalization to arbitrary acquisition geometry of Schleicher et al. (1997), I observe that the Hessian matrix of the reflection event in the CMP gather coincides with the Hessian matrix of the diffraction event in the ZO section.⁴ As a consequence, no offset-dependent information can be obtained from Equation (2.22) if t_{D} and t_{R} are expressed as paraxial approximations based on a normal central ray: only the projected first Fresnel zone for ZO can be estimated.

For the analytic approximations of the traveltimes, the borders of the projected first Fresnel zone are simply given by $|t_{\text{D}}(x_{\text{m}} - x_0, h) - t_{\text{R}}(x_{\text{m}} - x_0, h)| = T/2$. Using the parabolic approximation (2.16) for t_{R} and the same with $R_{\text{N}} := R_{\text{NIP}}$ for t_{D} , I obtain

$$\frac{T}{2} = \left| \frac{\cos^2 \alpha (x - x_{\text{m}})^2}{v_0} \left(\frac{1}{R_{\text{N}}} - \frac{1}{R_{\text{NIP}}} \right) \right|. \quad (2.23)$$

As expected, this equation contains no offset-dependent terms. Solved for $x_{\text{m}} - x_0$ it yields an approximation of the projected first Fresnel zone for the ZO configuration. Its width W_{F} is given by

$$\frac{W_{\text{F}}}{2} = |x_{\text{m}} - x_0| = \frac{1}{\cos \alpha} \sqrt{\frac{v_0 T}{2 \left| \frac{1}{R_{\text{N}}} - \frac{1}{R_{\text{NIP}}} \right|}}. \quad (2.24)$$

Using the hyperbolic approximation (2.17) instead of its parabolic counterpart, the same approach

⁴This fact is related to the so-called NIP wave theorem (Hubral, 1983) that states that for a CMP configuration the reflection traveltimes coincide with the diffraction traveltimes of a diffractor at the NIP up to second order in t based on a normal central ray. For arbitrary central rays, this relation does, in general, not hold. This generalization, the so-called CDP wave theorem, was introduced by Schleicher (1993).

yields the implicit function

$$G(x_m - x_0, h) = \left| \sqrt{\left[t_0 + \frac{2 \sin \alpha (x_m - x_0)}{v_0} \right]^2 + \frac{2 t_0 \cos^2 \alpha}{v_0} \left[\frac{(x_m - x_0)^2}{R_N} + \frac{h^2}{R_{\text{NIP}}} \right]} - \sqrt{\left[t_0 + \frac{2 \sin \alpha (x_m - x_0)}{v_0} \right]^2 + \frac{2 t_0 \cos^2 \alpha}{v_0 R_{\text{NIP}}} \left[(x_m - x_0)^2 + h^2 \right]} \right| = \frac{T}{2}. \quad (2.25)$$

This function cannot be solved analytically for $h(x_m - x_0)$ or vice versa, therefore its dependency on h is not obvious. However, numerical solutions for various sets of attributes demonstrate that Equation (2.25) reveals the expected behavior: the offset dependency is indeed negligible and does not represent any physical property. Consequently, only the projected first Fresnel zone for ZO can be estimated, just as with the parabolic approximations.⁵ For $h = 0$, Equation (2.25) reduces to

$$\frac{T}{2} = \left| \sqrt{\left[t_0 + \frac{2 \sin \alpha (x_m - x_0)}{v_0} \right]^2 + \frac{2 t_0 \cos^2 \alpha}{v_0 R_N} (x_m - x_0)^2} - \sqrt{\left[t_0 + \frac{2 \sin \alpha (x_m - x_0)}{v_0} \right]^2 + \frac{2 t_0 \cos^2 \alpha}{v_0 R_{\text{NIP}}} (x_m - x_0)^2} \right|, \quad (2.26)$$

an equation that can still be only solved numerically for $x_m - x_0$. Furthermore, the two solutions for $x_m - x_0$ are, in general, not symmetric with respect to x_0 . The symmetric analytic solution (2.24) based on the parabolic approximations is more attractive for the implementation.

Both approximations of the projected first Fresnel zone are depicted in Figure 2.6 as green and red lines, respectively. They are very similar to the true projected Fresnel zone (magenta) and the approximation according to Equation (2.22) (blue).

2.8 2-D CRS stack for 3-D multi-coverage data

In the preceding sections, I considered 2-D or kinematically equivalent 2.5-D situations to derive the approximate kinematic response of a reflector segment in depth. However, real data sets are always acquired above an 3-D subsurface. What happens if the 2-D CRS stack approach is applied to such 2-D data acquired over a 3-D model? To get some insight into this problem, I will briefly discuss the generalization of the CRS stack approach to 3-D.

⁵The hyperbolic approximation (2.17) can be derived from the parabolic approximation (2.16) by squaring and omitting the higher order terms. A Taylor expansion of the hyperbolic approximation again yields its parabolic counterpart. Thus, the negligible offset-dependency of Equation (2.25) is entirely artificial.

The hypothetical experiments with a point source in the NIP and an exploding reflector segment, now actually a common reflection *surface*, around the NIP can be directly transferred to the 3-D problem. The ZO ray normal to the reflector at the NIP is, in general, no longer restricted to a (vertical) plane in the subsurface, but might be arbitrarily bended. Obviously, one scalar angle is no longer sufficient to describe the propagation direction of the NIP and normal wavefronts along the normal ray at the acquisition surface, but two angles are required: the angle between the ray and the surface normal as well as the azimuth angle. The emerging NIP and normal wavefronts are now no longer curves but surfaces in the 3-D space. The curvature of such a spatial wavefront along the normal ray can be expressed in terms of a symmetric curvature matrix with three independent elements. Thus, eight wavefield attributes characterize the two hypothetical wavefronts in 3-D: two angles and two curvature matrices, each with three elements. For a detailed description of these wavefronts and the CRS stacking operator in 3-D, refer to Höcht (2002).

If data is acquired along a straight line above such a 3-D model, a certain observation azimuth is selected: together with the emerging normal ray, the acquisition line defines a so-called *observation plane* which is depicted in Figure 2.7. The curvatures of the wavefronts can only be investigated in the direction given by the seismic line, thus R_{NIP} and R_{N} represent the radii of curvature of the spatial NIP and normal wavefronts in the observation plane. The emergence angle α is the angle between the central ray and the normal to the acquisition line within the observation plane. Note that the observation plane is not fixed along a simulated ZO trace but will, in general, be different for each detected event.

The 2-D CRS stack correctly handles out-of-plane reflections and, thus, provides a correct 2-D ZO section also for 3-D situations. Thus, adjacent 2-D ZO sections represent actually a 3-D ZO volume. However, from only one azimuth direction it is not possible to determine either the observation plane or the full set of eight wavefield attributes. The 2-D wavefield attributes of at least three different azimuth directions are required to obtain all eight 3-D wavefield attributes.

I conclude that the 2-D CRS stack and most applications of the wavefield attributes remain valid in the 3-D situation. Although the presented derivation of the CRS stack operator is based on a 2-D model, the method *does not* imply a 2-D model. However, all wavefield attributes refer to the (unknown) observation plane. The only application of the wavefield attributes discussed in this thesis that explicitly assumes a 2-D model is the attribute-based time migration (see Section 2.6): applied to the 3-D situation, this migration will migrate the simulated ZO samples only along the acquisition line. In general, the apex of the time migration operator in 3-D will no be located above this line. For a correct time migration in 3-D, the 2-D wavefield attributes are not sufficient: they provide no information for the migration perpendicular to the observation plane.

Similar considerations apply to the inversion of the wavefield attributes to set up a depth model (Majer, 2000). For the inversion of the 2-D wavefield attributes the explicit assumption of a 2-D model is required (in addition to further assumptions like homogeneous layers etc.).

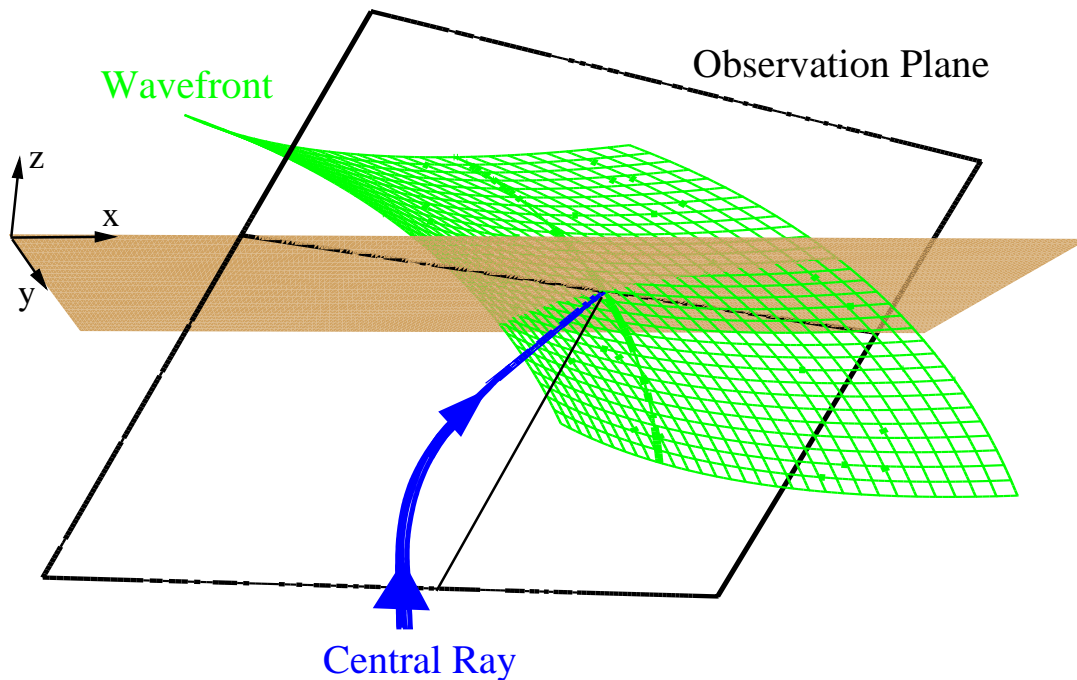


Figure 2.7: Definition of the observation plane (black rectangle) in the 3-D case according to Höcht (2002). The plane is given by the acquisition line (black line on brown acquisition surface) and the emerging central ray (blue). The second black line is normal to the acquisition line in the observation plane.

2.9 Validity for elastic media

For the derivations above, I characterized the medium by means of a single parameter, namely the propagation velocity. Such a description implies an acoustic medium with constant or slowly varying density. However, as I am only interested in the kinematic aspects of the wave propagation, the formulae derived above can readily be applied to isotropic elastic media, provided the spatial variation of the elastic parameters is small compared to the scale of the considered wavelength: in this case, compression (P) waves and shear (S) waves can be separated. Only at interfaces in the subsurface, a conversion between the wave modes can occur. If such conversions can be neglected, the isotropic elastic medium kinematically behaves like an acoustic medium—of course, with the appropriate propagation velocity for the considered wave mode.

For the simulation of ZO sections, a paraxial vicinity of the central normal ray is considered. In this vicinity, the amplitude of a converted wave is far smaller than the amplitude of the incident wave: the incident wave has only a very small displacement component in the polarization direction of the converted wave. Thus, for the ZO simulation, converted waves can usually be neglected. In other words, the derived CRS formulae can be applied to isotropic elastic media, either for P-P reflections *or* for S-S reflections.

In a more general sense, the CRS approach as presented in the scope of this thesis only relies on a) the existence of coherent reflection events in the pre-stack data (this implies that a description by means of wavefronts and rays is possible) and b) a more or less homogeneous top layer within the considered aperture. Under these conditions, the NIP and normal wavefronts can be described. Their relation to the subsurface reflector might, in principle, be arbitrarily complex.

Chapter 3

Implementation

In the preceding chapter, an approximation of the kinematic reflection response of an arbitrarily curved reflector segment in depth was derived. Three kinematic wavefield attributes, namely the emergence angle α of the normal ray and the radii of curvature R_{NIP} and R_{N} of the NIP and the normal wave, respectively, serve as parameters for the CRS operator.

To apply the CRS stack in an entirely data-oriented way, these attributes have to be determined automatically from the pre-stack data. In this chapter, I will firstly describe the associated optimization problem, followed by two efficient approaches to solve this problem step by step. A detailed discussion of the implemented algorithms is given including the choice of the tested attribute ranges and of appropriate apertures.

3.1 Global optimization problem

The hyperbolic (Equation (2.16)) and parabolic (Equation (2.17)) Taylor expansions of the CRS reflection response provide simple analytic second-order approximations of the true reflection traveltimes in the pre-stack data. Now, the task is to determine the CRS wavefield attributes that parameterize the CRS operators fitting best the actual reflection events. At this stage, I assume that the near-surface velocity v_0 is known and constant within the paraxial vicinity of the considered normal ray.

Obviously, a criterion is required to quantify the fit of the operator to the event in the pre-stack data. As the CRS stack should detect the optimum stacking operators automatically, a statistical approach appears to be most appropriate: along the best fitting operator, the coherence of the pre-stack data has to be as high as possible. Different coherence measures might be used to evaluate this fit. In this thesis, I use the well-known coherence measure *semblance* (Neidell and Taner, 1971) that provides a normalized ratio of the correlated and uncorrelated seismic energy in a data volume around the CRS operator in the pre-stack data, see Appendix B. A direct comparison and fit of kinematic reflection traveltimes is not attractive as it would require the (manual) picking of reflection events in the usually noisy pre-stack data. Such an event-based approach is not

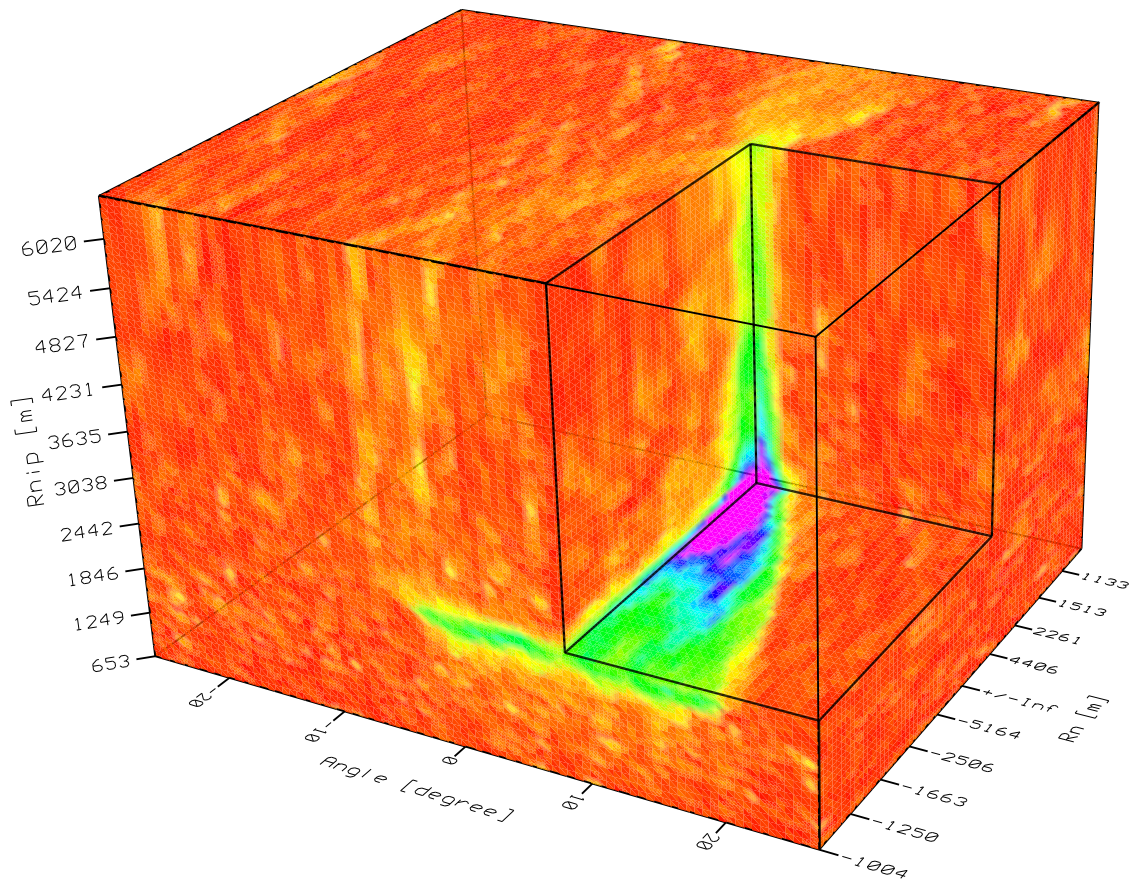


Figure 3.1: Coherence values as a function of the wavefield attributes for a ZO sample located on a reflection event. The inner corner of the excavated subvolume is located at the global maximum. The coherence criterion is semblance, the largest displayed value (magenta) is set to 30 % of the maximum coherence to reveal the local maxima. Note the non-linear R_N axis.

applicable for automatic applications that try to provide a ZO simulation at any ZO location, irrespective if there is an identifiable primary event or not.

The determination of the best fitting operator for a chosen point (x_0, t_0) in the ZO section to be simulated consists of a global optimization problem with the three parameters α , R_{NIP} , and R_N . The coherence criterion evaluated along the associated CRS operators serves as objective function. To illustrate this optimization problem, the used coherence criterion (namely semblance) is plotted as a function of the three wavefield attributes in Figure 3.1 for a ZO sample located on a reflection event. Obviously, this “coherence volume” contains a multitude of local maxima. Even worse, the objective function directly depends on the pre-stack data, thus no analytic derivatives of the objective function are available that might be used to find the global and local maxima.

The optimization problem has to be solved separately for each ZO sample to be simulated. As thousands of traces might be located inside the considered aperture, it is, from a practical point of view, virtually unacceptable to compute such coherence volumes for each ZO sample: a far more efficient way to obtain the global and, possibly, also local maxima of the objective function is required. Not only the global maximum might correspond to an actual reflection event, but several events might contribute to one and the same ZO location. Such events differ in their curvatures and/or their dips in the ZO section to be simulated.¹ The latter phenomenon, irrespective of the events' curvatures, is well-known as *conflicting dip* situation. Analogously, cases in which the events only differ in their local curvature might be called *conflicting curvature* situations.

I conclude that a non-linear global optimization problem with three parameters has to be solved. Local maxima have, in general, also to be considered as parameters of actual reflection events. Derivatives of the objective function are not available, thus many established optimization algorithms are not applicable. A direct solution of the global optimization problem is too time consuming. Furthermore, it is never granted that the largest maxima (including the global maximum) are actually detected rather than any other local maxima.

A *local* optimization problem with three-parameters is far easier to solve than its global counterpart. However, the searched-for global and, in general, also additional local maxima can only be found if initial parameters in their vicinity can be provided as starting values to the local optimization algorithm. The determination of such initial wavefield attributes is the main task in the CRS processing sequence: this step has to be sufficiently efficient and, at the same time, sufficiently reliable and accurate. The fact that many well-established processing methods are applied to subsets of the pre-stack data volume suggests to transfer this approach to the CRS stack method. This directly leads to the next section where I consider the CRS stack problem for certain acquisition configurations.

3.2 CRS stack in subsets of the pre-stack data

The spatial CRS stacking operators (2.16) and (2.17) depend on the three wavefield attributes α , R_{NIP} , and R_{N} . In the general case of an arbitrary source/receiver configuration, these attributes are independent of each other. However, for certain configurations associated with subsets of the entire pre-stack data volume, the number of independent parameters in these equations reduces: if there is a linear relationship between $x_{\text{m}} - x_0$ and h , here expressed in the parametric form

$$(x_{\text{m}} - x_0)(\xi) = \lambda_x \xi, \quad (3.1a)$$

$$h(\xi) = \lambda_h \xi, \quad (3.1b)$$

it is obvious that the last term in Equations (2.16) and (2.17),

$$\frac{(x_{\text{m}} - x_0)^2(\xi)}{R_{\text{N}}} + \frac{h^2(\xi)}{R_{\text{NIP}}} = \frac{\xi^2}{R_{\text{C}}} \quad \text{with} \quad \frac{1}{R_{\text{C}}} = \frac{\lambda_x^2}{R_{\text{N}}} + \frac{\lambda_h^2}{R_{\text{NIP}}}, \quad (3.2)$$

¹Events that do not differ in dips and/or curvatures might, of course, be due to different ray paths and reflection points. This kind of ambiguity in the simulated ZO section cannot be resolved and, thus, does not have to be considered at all for the CRS stack method.

only depends on the combined curvature R_C . The spatial stacking operators reduce to curves in the configuration defined by λ_x and λ_h . This configuration represents a 2-D subset of the pre-stack data volume, namely a vertical plane through the point $(x_0, 0)$. In this way, the number of attributes is reduced as is the number of pre-stack data traces used to determine the attributes α and R_C .

In the following, I will only consider the hyperbolic CRS operator (2.17). Of course, analogous considerations also apply to its parabolic counterpart (2.16). For a chosen configuration according to Equation (3.1), the hyperbolic CRS operator reads

$$t_{\text{hyp}}^2(\xi; \lambda_x, \lambda_h) = \left[t_0 + \frac{2 \sin \alpha \lambda_x \xi}{v_0} \right]^2 + \frac{2 t_0 \cos^2 \alpha \xi^2}{v_0 R_C(\lambda_x, \lambda_h)}. \quad (3.3)$$

This equation represents either a hyperbola or an ellipse with two parameters and its apex shifted with respect to x_0 . Only in the special case $\lambda_x = 0$, $\lambda_h \neq 0$, namely the CMP configuration, the apex is located at x_0 and Equation (3.3) further reduces to

$$t_{\text{hyp}}^2(\xi; \lambda_x = 0, \lambda_h \neq 0) = t_0^2 + \frac{2 t_0 q \xi^2}{v_0} \quad \text{with} \quad q = \frac{\cos^2 \alpha}{R_{\text{NIP}}}, \quad (3.4)$$

an expression that only depends on the combined parameter q .

If a reflection event in the pre-stack data actually had a hyperbolic shape according to Equation (2.17), two arbitrary different configurations $\lambda_x^{(i)}$, $\lambda_h^{(i)}$, $i = 1, 2$, are sufficient to solve the combined curvatures $R_C^{(i)}$ for the searched-for attributes R_N and R_{NIP} . The emergence angle α is directly available from at least one of the two configurations.

In practice, this condition is hardly met: the actual event is, in general, not of hyperbolic shape and the data contain noise that deteriorates the wavefield attributes. Therefore, three aspects have to be considered:

- a sufficient number of data traces has to be available in the vicinity of the chosen configurations to allow a reliable determination of the attributes α and R_C .
- the azimuths of the configurations in the midpoint/offset plane must be well separated such that all three wavefield attributes significantly contribute.
- an appropriate aperture has to be defined in which the hyperbolic approximation is sufficiently accurate.

If these criteria are satisfied, the obtained attributes are usually close to the searched-for maximum associated with the spatial stacking operator. Thus, the global optimization problem with three parameters can be decomposed into two separate optimization problems with two parameters. If I determine the emergence angle only in one of the two chosen configurations, one of the optimization problems even reduces to one parameter.

3.3 Pragmatic search strategy

3.3.1 Automatic CMP stack

The most efficient solution of the posed optimization problem with three parameters can be achieved if it can be decomposed into three separate optimization problems with one parameter each. Müller (1998) and Müller et al. (1998) proposed the most obvious and—apparently—the only applicable approach to realize this optimum decomposition. From the considerations in Section 3.2 it is obvious that there is exactly one configuration where the CRS operator depends on only one (combined) parameter: the CMP configuration ($\lambda_x = 0, \lambda_h \neq 0$) with q as the only parameter according to Equation (3.4). A comparison of this equation with the well-known CMP stack formula

$$t^2(h) = t_0^2 + \frac{4h^2}{v_{\text{stack}}^2} \quad (3.5)$$

reveals that the CRS stack reduces to this classic processing method for this configuration. The stacking velocity v_{stack} can now be alternatively expressed in terms of the CRS wavefield attributes:

$$v_{\text{stack}}^2 = \frac{2R_{\text{NIP}} v_0}{t_0 \cos^2 \alpha} = \frac{2v_0}{t_0 q}. \quad (3.6)$$

The $\cos^2 \alpha$ factor in this equation can be readily derived for a plane dipping reflector with homogeneous overburden, where the angle α represents not only the emergence angle of the normal ray, but also the dip of the reflector. This fact again emphasizes that the CMP traveltimes up to second order do not depend on the reflector's curvature (see the so-called NIP wave theorem in Hubral, 1983). In terms of the CRS wavefield attributes, this is even more obvious, as R_{N} does not appear in Equation (3.6). At this stage, I want to emphasize that v_{stack} does—in contrast to the near-surface velocity v_0 —not represent a physical wave propagation velocity. Only for simple models, v_{stack} can be seen as a kind of average velocity of the reflector's overburden. Additionally and quite obvious from Equation (3.6), the stacking velocity also depends on the dip $2 \sin \alpha / v_0$ of the events in the ZO section. Split into a dip-dependent and a dip-independent term, Equation (3.5) can be rewritten as

$$t^2 = t_0^2 + \frac{4h^2}{v_{\text{NMO}}^2} + \frac{4h^2 \sin^2 \alpha}{v_{\text{NMO}}^2} \quad \text{with} \quad v_{\text{NMO}} = \frac{2R_{\text{NIP}} v_0}{t_0}. \quad (3.7)$$

The so-called *normal moveout* velocity v_{NMO} is here and throughout the entire thesis defined as the apparent velocity that accounts for the offset-dependent moveout $t(h) - t_0$ due to the overburden of a reflector, irrespective of its dip. This dip-independent velocity, sometimes also called zero-dip NMO velocity (e. g., in Yilmaz, 1987), is the required velocity for a correct application of a NMO/DMO/stack processing chain (see Section 2.4.1).²

²The NMO velocity is often defined as the velocity that “flattens” an event during an NMO correction. However, the application of a subsequent DMO correction to such a flattened event leads to an inconsistency. Therefore, I stick to the definition given above. Furthermore, the term “normal moveout” according to my definition also implies that the NMO correction is a 1-D task that shifts the event only along a considered trace, i. e., actually normal to the midpoint/offset plane. In contrast, a DMO correction also includes a lateral shift of the events, i. e., a 2-D operation.

The NMO velocity reduces to the well known root-mean-square velocity v_{RMS} for a model with plane horizontal interfaces separating iso-velocity layers. v_{RMS} represents a weighted average of the actual interval velocities in this case. In the general case, however, the NMO velocity might take any arbitrary value. For negative values of R_{NIP} that occur if the NIP wavefront passes an odd number of caustics on its way to the acquisition surface, v_{NMO} is imaginary. If the NIP wavefront happens to emerge as a plane wave, its value tends to infinity. If such situations occur, the squared inverse of v_{NMO} is a more convenient representation of this parameter, as it is always real and finite.³ This clearly demonstrates that the NMO velocity is, in general, not a physical propagation velocity but a pure imaging parameter that can be directly related to the hypothetical NIP wave experiment.

This first step to determine the CRS wavefield attributes is called *automatic CMP stack* due to its similarity to the familiar CMP stack method and the fact that it can be applied without any user interaction. This step is convenient and familiar, but it also has some disadvantages that will be discussed later on.

3.3.2 Linear and hyperbolic ZO stack

According to Section 3.2, any other subset of the pre-stack data with a significant azimuth difference compared to the CMP gather is suited to determine the two other required parameters to obtain the three CRS wavefield attributes. But how can the resulting optimization problem be further decomposed into two separate steps? The first order terms in Equations (2.16) and (2.17) only depend on the emergence angle α and the midpoint displacement $x_m - x_0$. For small midpoint displacements and large values of the combined parameter R_C , this first order term provides a sufficiently accurate approximation of the traveltimes in the chosen gather.⁴ Thus, a search for α only is, in principle, possible within a small aperture around x_0 .

A suitable configuration for such an approach should satisfy all the mentioned criteria as well as possible. The first criterion, the azimuth difference, is obviously satisfied best by the ZO section ($\lambda_x \neq 0, \lambda_y = 0$) which is orthogonal to the CMP gather. Furthermore, R_C coincides with R_N in this gather. As the latter is in most cases larger than R_{NIP} , the first order approximation is applicable in a comparatively larger aperture. Unfortunately, the ZO section cannot be acquired due to technical reasons and is, thus, never contained in the pre-stack data volume. However, the result of the automatic CMP stack is a simulated ZO section that additionally provides a higher signal-to-noise ratio than the pre-stack data itself.

Due to this observation, the determination of the emergence angle α can be performed in the CMP stacked section with the assumption $R_N = \infty$. Due to the simple relation between the dip of the ZO events and the emergence angles of the corresponding ZO rays, this operation is similar to the

³The case of near-surface caustics in the NIP or normal wavefront, respectively, cannot be handled by the presented Taylor expansions of the CRS response. Consequently, such situations with vanishing values of R_{NIP} ($v_{\text{NMO}} = 0$) and/or R_N are not considered for the implementation. The former case is quite unlikely, the latter is, unfortunately, more likely and might lead to gaps in the simulated ZO section.

⁴The hyperbolic approximation (2.17) also contains a corresponding second-order term that can be readily included in a one-parameter search for α .

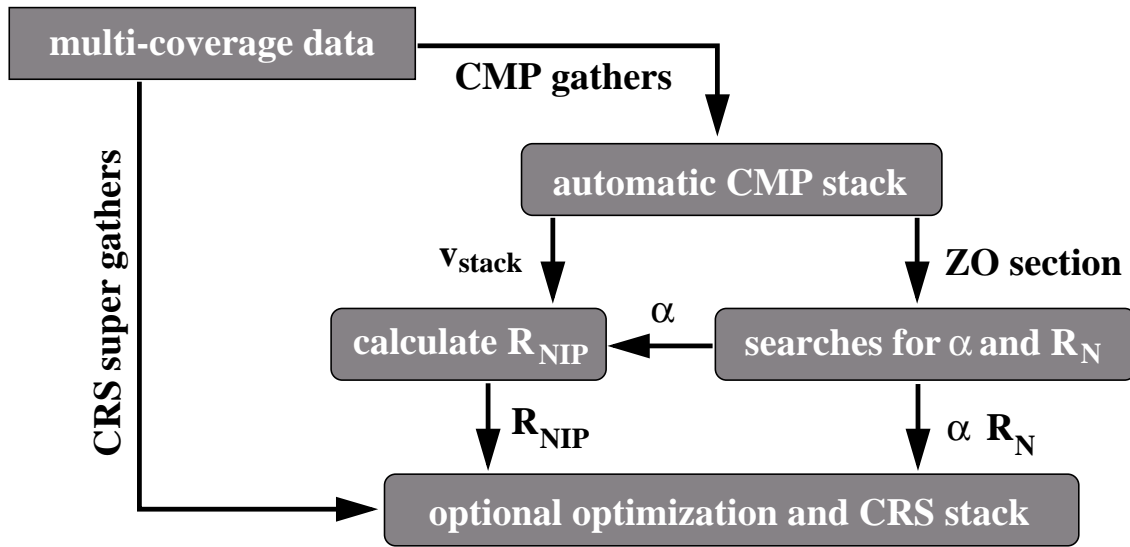


Figure 3.2: Simplified flowchart of the pragmatic search strategy. The indicated processing steps have to be performed for each ZO sample to be simulated. All traces within the spatial CRS aperture are denoted as CRS super gather.

so-called *slant stack*, basically a linear Radon transform of the ZO section. As a linear stacking operator is used to determine α in the ZO section, I call this process the *linear ZO stack*.

So far, the stacking velocity v_{stack} and the emergence angle α are available. With Equation (3.6), the radius of curvature R_{NIP} can be readily calculated. Thus, R_{N} is the only remaining parameter to be determined. According to the consideration above, the CMP stacked section again provides the optimum input: it does not depend on R_{NIP} and provides a higher signal-to-noise ratio. With the already known emergence angle, the optimum hyperbolic operator (3.3) can be determined in a one parameter search. I denote this search step as *hyperbolic ZO stack*.

3.3.3 Limitations

The pragmatic search strategy is, due to its close relationship to familiar imaging methods like CMP stack and slant stack, very attractive and allows to transfer the experiences with these classical methods to the CRS approach. A flowchart of this strategy is shown in Figure 3.2. However, this strategy has two limitations:

The first one is due to the fact that only a subset of the entire pre-stack data volume is used. This requires that a sufficient number of traces with a more or less normal distribution with respect to offset is available. This restriction only partly applies to the ZO stacks, where a normal distribution is usually available.

The second limitation is more crucial. According to Equation (3.6), the automatic CMP stack depends only on a combination of α and R_{NIP} . Furthermore, the sign of α does not contribute.

As a consequence, conflicting dip situations cannot be addressed with this approach from the very beginning. Even worse, in conflicting dip situations the detected stacking velocity does, in general, not parameterize one of the contributing events, but might be influenced by all contributing events.

3.4 Extended CRS stack strategy

Now, my aim is to establish a CRS stack strategy that overcomes the limitations of the pragmatic approach while pertaining its efficiency as far as possible. I make no attempt to overcome the first limitation of the pragmatic approach that relies on a sufficient number of traces in the CMP gather, or CMP fold, as this condition is usually met for 2-D acquisition. If the CMP fold were actually too low, the direct solution of the global optimization problem with three parameters should be feasible with an acceptable computational effort.

The more challenging problem is to consider conflicting dip situations in the CRS processing sequence. From the considerations above, it is obvious that conflicting dip situations cannot be handled in the CMP gather, whereas the unavailable ZO section is suited best for this task. At a first glance, there is no way to extend the pragmatic search strategy to serve these needs.

Any other configuration than CMP is, in principle, suited to determine the emergence angle α together with R_C for the chosen configuration. One might argue that this problem is equivalent to the ZO stacks that can be decomposed into a search for the dip and a search for the curvature of the event in the chosen configuration. Various tests with synthetic and real data sets clearly demonstrated that this decomposition frequently fails if it is applied to pre-stack data. This approach works for the ZO stacks only because they are applied to an already stacked section with a higher signal-to-noise ratio. Consequently, an optimization problem had to be solved for two parameters simultaneously if an arbitrary configuration would be chosen, implying a significant drawback in efficiency.

A straightforward consideration allows to adapt the pragmatic search strategy such that conflicting dip and curvature situations can also be handled. If two or more events contribute to the same ZO location, this can hardly be resolved by means of the automatic CMP stack: the curvatures of the ZO events do not contribute and their dips might be similar, but with opposite sign. However, if they actually differ in dip and/or curvature, they will definitely separate again on neighboring traces in the CMP stacked section. Thus, the CMP stacked section, although not generated under consideration of such conflicting dip and/or curvature situations, is anyway suited for such an analysis performed *subsequently*. This approach was firstly introduced by Mann (2001a,b).

3.4.1 Detection of conflicting dip situations

The result of the automatic CMP stack is suited as input for the ZO stacks, even in case of conflicting dips and/or curvatures. Conflicting dip situations are equivalent to situations with different emergence angles $\alpha^{(i)}$, where the index i denotes the different contributing events. To handle such situations, I simply have to determine additional coherence maxima in the linear ZO stack. In

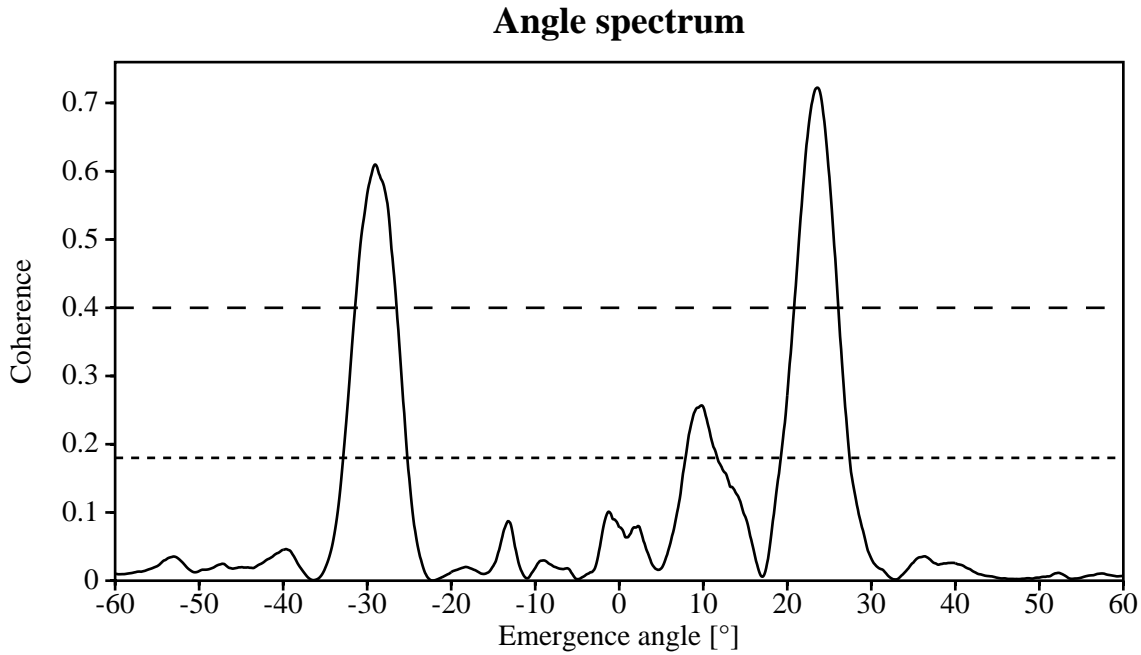


Figure 3.3: Coherence as a function of emergence angle α calculated along a linear operator in the CMP stacked section for a chosen point (x_0, t_0) . The three distinct maxima correspond to two diffraction events at $\approx -29^\circ$ and $\approx 24^\circ$ and one weak reflection event at $\approx 10^\circ$. The long-dashed line represents the absolute threshold for the global maximum, the short-dashed line the relative threshold for global maxima.

contrast to the DMO correction that collects the information of all *possible* contributing events with different dips, the CRS stack method has to parameterize each of the *actually detected* events separately. This implies that I have to explicitly define a discrete number of contributing events at each ZO location to be simulated, based on the coherence analysis performed in the CMP stacked section.

An “angle spectrum”, i. e., the coherence as function of the emergence angle is depicted in Figure 3.3 for a ZO sample located on an actual event. Three distinct maxima can be observed that, in this example, correspond to two diffraction events and one reflection event intersecting each other in the chosen ZO location. Furthermore, there are various local maxima that do not appear to belong to any visible events. To detect the presumably relevant maxima, I propose to apply a set of criteria for the global and local maxima:

- The global coherence maximum has to exceed a given threshold, else no local maxima are accepted. This avoids computational overhead in noisy areas far off actual reflection events.
- The local coherence maxima have to exceed a given threshold relative to the global maximum. This reflects the assumption that actual reflection events should yield similar coherence values for the same aperture and traveltime.

- Maxima must be clearly separated. Before a change of the sign of the slope of the angle spectrum is considered as flank of a potential local maximum, the coherence has to decrease to a given fraction of the last detected maximum. This criterion rejects the multiple detection of noise-dependent fluctuations of one and the same coherence peak.

With this criteria, the number of contributing events and the emergence angles $\alpha^{(i)}$ can be determined with the linear ZO stack. Evidently, the hyperbolic ZO stack can be readily performed separately for each detected value $\alpha^{(i)}$, thus providing radii of curvature $R_N^{(i)}$ for all contributing dips. In principle, one might again allow a set of local coherence maxima to also resolve the conflicting curvature problem such that one or more radii of curvature of the normal wavefront is assigned to each emergence angle. To avoid a too complicated handling of the wavefield attributes and as the conflicting curvature situation is of less interest, this extension is not included in the current implementation. Nevertheless, this approach remains as an option for future extensions.

Due to the comparatively small aperture applicable for the linear ZO stack, this processing step tends to detect small, more or less linear, artifacts in the data, too. To reject such artifacts, I propose to apply the three coherence criteria listed above again with the coherence values obtained from the hyperbolic ZO stack. This also reduces the number of unnecessary computations.

3.4.2 Determination of R_{NIP}

So far, the extended strategy provides an entire set of emergence angles $\alpha^{(i)}$ and the associated radii of curvature $R_N^{(i)}$ for a discrete number of i contributing events at each ZO location. However, the remaining radii of curvature $R_{\text{NIP}}^{(i)}$ can, in general, no longer be calculated from the stacking velocity v_{stack} and the emergence angles $\alpha^{(i)}$: an entire set of angles is available, but only a single (and possibly inaccurate) stacking velocity is provided by the automatic CMP stack. To resolve this ambiguity, Mann (2001a,b) proposed to introduce an additional search for the radii of curvature $R_{\text{NIP}}^{(i)}$ in a different subset of the pre-stack data volume: the fact that neither the ZO nor the CMP configuration is suited to resolve this ambiguity lead to the configuration right in the middle of both with respect to the azimuth in the midpoint/offset plane. In terms of the configuration parameters, this configuration can be described by $|\lambda_x| = |\lambda_h|$. In terms of shot and receiver coordinates, this parameterizes the common-shot (CS) and the common-receiver (CR) gather. With the combined curvatures $R_C^{(i)}$ determined in this configuration, i complete sets of wavefield attributes are available. As the emergence angles are already known from the linear ZO stack, the required additional search depends on only one parameter, thus ensuring a high computational efficiency.

Combining all these extensions, I can set up a flowchart of the *extended CRS search strategy* that is able to cope with conflicting dip (and, as a future option, also with conflicting curvature) situations. The simplified flowchart is shown in Figure 3.4. The basic difference to its pragmatic counterpart depicted in Figure 3.2 is that the automatic CMP stack only serves to provide a preliminary simulated ZO section. The associated stacking velocities are not used due to inherent ambiguities. The additional search in the CS/CR gather resolves this ambiguities. If no conflicting dip situations are encountered during the ZO stacks, no ambiguities have to be resolved. Thus, in such cases the additional search in the CS/CR gathers is not required and the pragmatic search strategy can still be applied.

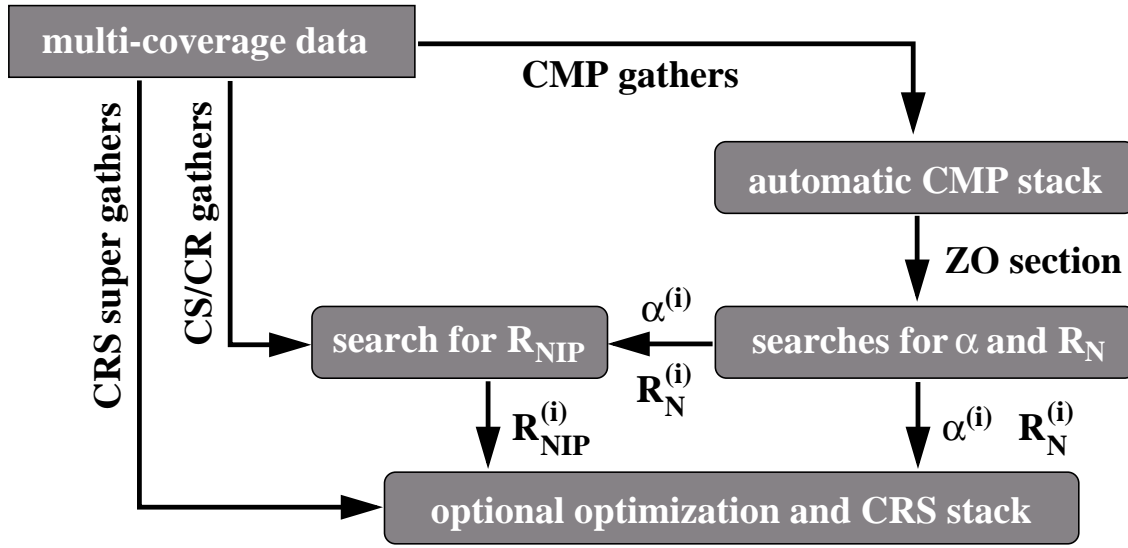


Figure 3.4: Simplified flowchart of the extended CRS search strategy. The indicated processing steps have to be performed for each ZO sample to be simulated. All traces within the spatial CRS aperture are denoted as CRS super gather.

3.5 Search algorithms

3.5.1 Automatic CMP stack

In the CMP gather ($x_m = x_0$), the stacking operator depends on only one parameter, namely the stacking velocity, that, in turn, can be expressed as a combination of the emergence angle α and the radius of curvature R_{NIP} (Equation (3.7)). According to Equation (3.4), the operator is either a hyperbola or an ellipse with its apex at $h = 0$. To determine the stacking velocity yielding the highest coherence along the corresponding operator, it appears to be most appropriate to test stacking operators for which the moveouts for the largest considered offset are located on a regular grid rather than using a regular grid of velocity values. This approach accounts for the fact that the highest achievable resolution is directly given by the data: assuming that data is not under-sampled, an actual event cannot be missed during the search if the neighboring tested operators are separated by a distance in the same order of magnitude as the sampling interval of the pre-stack data. Due to the symmetry of the operator with respect to the offset zero, the implementation of this search is straightforward. A set of tested stacking operators for a given ZO location (x_0, t_0) is depicted in Figure 3.5.

The derivation of the CRS operator in the theory chapter is based on the assumption of primary reflection events that are reflected only once in the subsurface. However, real data often also contain multiple reflection events. As an example, very strong multiples can be observed in marine data if the seafloor has a sufficiently high reflection coefficient. As the free water surface has a reflection coefficient close to -1 , much energy is trapped in the water column and reverberates be-

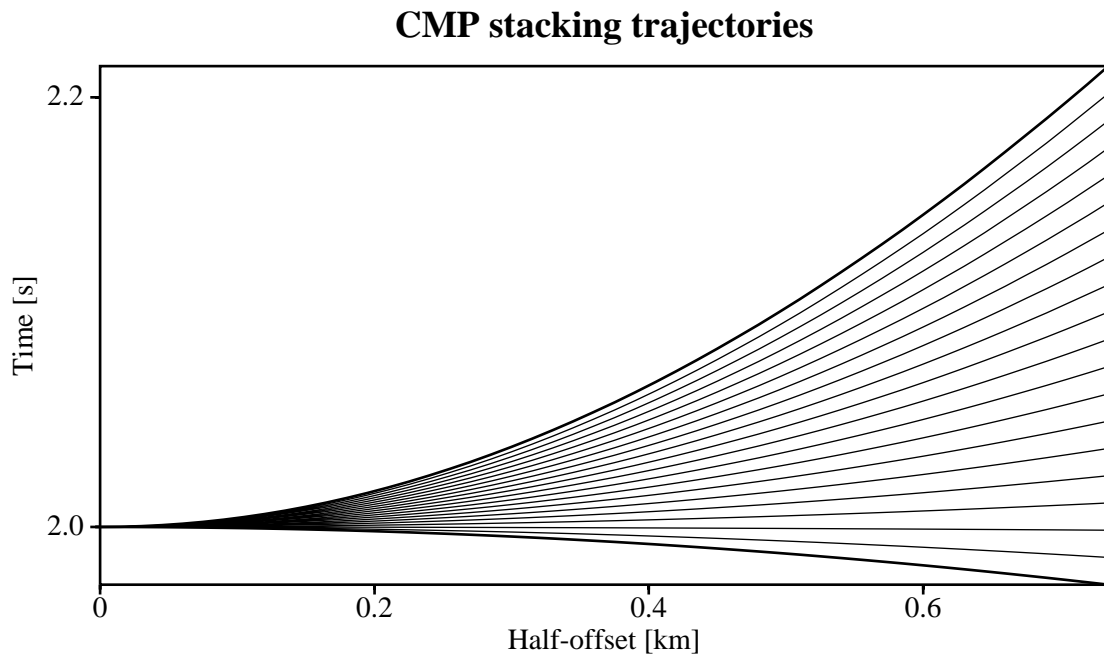


Figure 3.5: Tested stacking operators for the automatic CMP stack for the ZO traveltime $t_0 = 2$ s. The “largest” tested stacking velocity is $4.5i$ km/s, the lowest 1.5 km/s (bold curves). Of course, this comparison is only possible for their squared counterparts. For illustration purposes, the displayed distance between neighboring operators is larger than the actually used sampling interval.

tween water surface and seafloor. Such kinds of multiples might cause events of hyperbolic nature. Thus, the CRS stack method will parameterize them and produce a stack result for the multiples. The wavefield attributes associated with multiples do not represent the same geometrical properties as for primary events. Together with the wavefield attributes for neighboring primary events, this bears the potential to identify some kinds of multiples, namely those with significant CMP moveout differences compared to the primary events.

This fact is well known from the classical CMP stack where, e. g., multiples generated in the water column are associated with low stacking velocities compared to neighboring primary events. Such multiples can, in principle, be attenuated by introducing appropriate constraints on the tested stacking velocity range: if the stacking velocity associated with a (multiple) event is outside this test range, the event cannot be optimally fit by the operator, thus leading to a low stack power and coherence value. This concept can be readily transferred to the CRS stack approach as the same considerations also apply to the automatic CMP stack. The current implementation supports two alternative options to attenuate multiples in this way:

- A given stacking velocity model for the *lowest* stacking velocity to be tested is considered, the upper limit is given as a constant parameter. This method, as applied to the BGR99-07 data presented in Chapter 6, only requires a comparatively crude stacking velocity model.

- If a sufficiently accurate stacking velocity model is known a priori, the model can be used to define the stacking velocity constraints within a percentile variation of the model values. This method strongly increases the computational efficiency. However, it bears the risk to miss events if the model is (locally) wrong.

The stacking velocity model can, instead of using an a priori known model from preceding or additional processing steps, also be derived by means of an iterative application of the automatic CMP stack. A simple example of this approach is presented in Chapter 6 that clearly reveals the limitations of this multiple attenuation approach: the stacking velocity associated with multiple events might in some situations behave too complicated to allow for a simple derivation of a constrained model.

One task is to identify and attenuate multiple events, another task is to detect alternative events contributing to the same ZO location, namely the searched-for primary events. From Figure 3.6 one can observe that it is, in general, *not* appropriate to search for the stacking velocity yielding the highest coherence value, i. e., the *supremum* within the tested range, rather than to determine the local *maximum*: for the displayed example, the former does neither yield the stacking velocity associated with the multiple event nor its counterpart for the primary event. Thus, the current implementation only allows actual maxima provided they exist. Else, the supremum serves as default value. Note that this approach is not able to separate interfering primaries and multiples. Nevertheless, it attenuates multiples and increases the likelihood to detect and separate the different events in the following processing steps.

In its strict sense, a CMP gather contains all traces that exactly match the midpoint coordinate of the trace to be simulated. For field data acquisition, such a condition is definitely inapplicable. Instead, all traces are assigned to so-called bins, in this case CMP bins that include all traces within a certain range of the midpoint displacement $x_m - x_0$. The current implementation relies on an appropriate CMP binning information in the pre-stack data. This information is usually available as it is required for conventional time domain processing, too.

3.5.2 Linear ZO stack

The search for the emergence angles $\alpha^{(i)}$ is performed by generating angle spectra as shown in Figure 3.3 on a regular angle grid. These spectra are analyzed according to the criteria given in Section 3.4.1 to separate contributions from actual events and noise-related artifacts. Note that the number of detected conflicting events is always a discrete number. This feature significantly differs from the DMO correction which collects the contributions of all possible dips. On the one hand, the extended CRS stack provides far more information about each contributing event. On the other hand, the discrete handling of these events might lead to abruptly appearing and vanishing events, thus locally introducing an artificially high lateral frequency content.

The linear ZO stack, as well as the subsequent hyperbolic ZO stack discussed in the next section, are applied to the simulated ZO section obtained from the automatic CMP stack rather than to subsets of the actually acquired pre-stack data. Consequently, no assignment of the traces into bins and, thus, no approximation of the traces' coordinates is required.

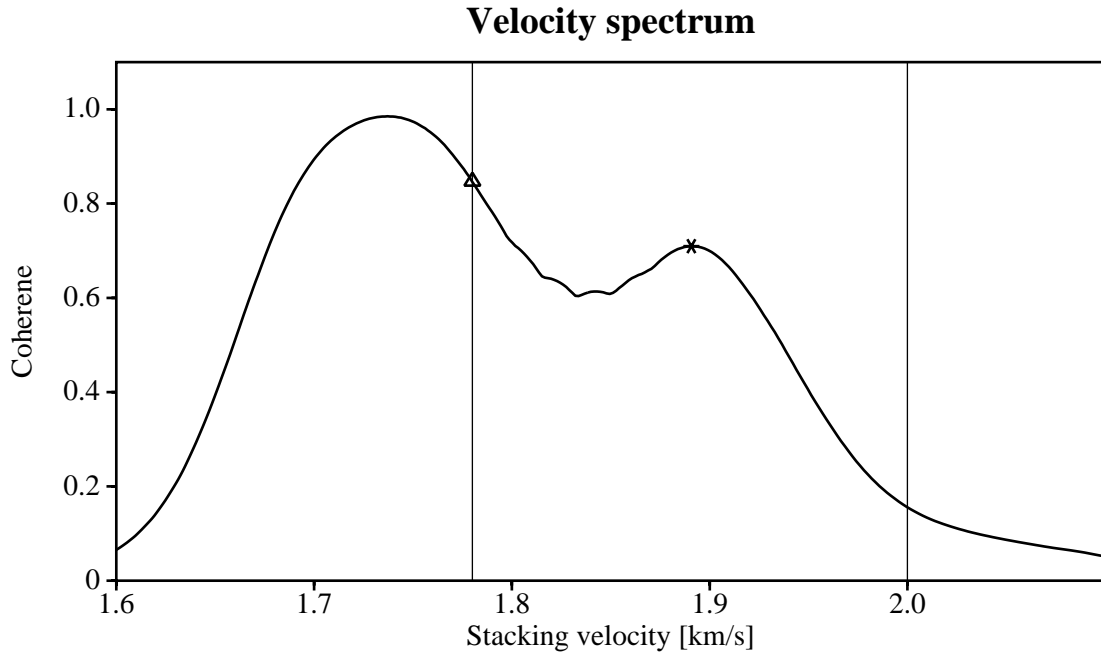


Figure 3.6: Coherence as a function of the stacking velocity for a ZO sample located on a reflection event. The global maximum pertains to a multiple event, whereas the local maximum represents the searched-for primary event. The thin lines depict the velocity constraints for the second iteration. Note that the supremum (triangle) in this range does not coincide with the searched-for local maximum (cross).

3.5.3 Hyperbolic ZO stack

The determination of the radius of curvature R_N from the CMP stacked section is more demanding than the search for the stacking velocity: the stacking hyperbola (3.2) is, in general, not symmetric with respect to the midpoint location x_0 . Thus, the data-oriented sampling interval of tested stacking operators has to be handled with care. As a further complication, a reasonable range of tested R_N values is not obvious. The upper limit of $|R_N|$ is easily recognized as infinity, corresponding to a plane emerging normal wavefront (red line in Figure 3.7). The lower limit is more difficult: for the extreme case of a diffractor, R_N coincides with R_{NIP} , but as caustics in the normal wave are quite likely, this does not really provide useful limits for R_N .

To define the range of appropriate hyperbolic operators, I consider the behavior of the actual reflection events: if the average medium velocity above a reflector is not smaller than the near-surface velocity v_0 , the slope of the corresponding reflection event does not exceed $1/v_0$, the slope of a direct wave. As a consequence, the actual reflection event (excluding alternative branches of triplications) around a ZO sample located on this event can be found within the two straight lines through the ZO location with the slopes $\pm 1/v_0$. These lines are shown in magenta in Figure 3.7. The maximum slope of the event occurs for very steep reflectors and for strongly curved reflectors,

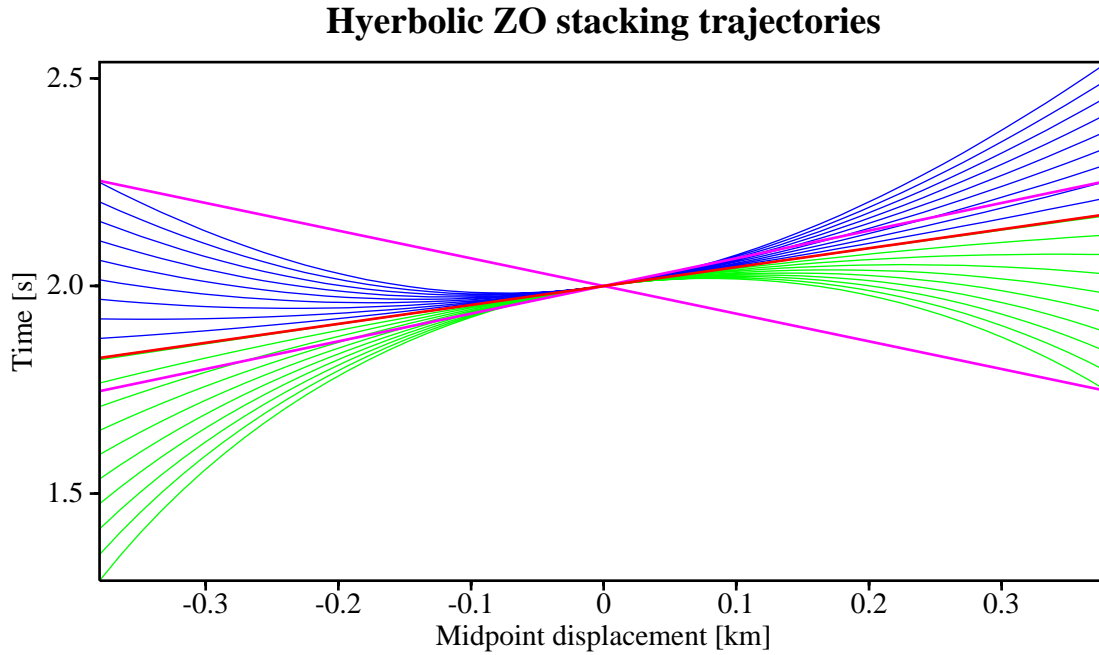


Figure 3.7: Hyperbolic stacking operators in the ZO section for a ZO sample at $t = 2$ s and an emergence angle of 20° . To ensure the given sampling interval, the blue hyperbolae are attached to the left border of the aperture, whereas the green trajectories are attached to the right-hand side. The magenta lines with the slope $\pm 1/v_0$ define the limits in which the branch of an actual reflection event is located. The red line depicts a plane wavefront emerging with the given emergence angle.

namely at the tails of their diffraction pattern.

In terms of the moveout depending on the midpoint displacement $x_m - x_0$, the hypothetical direct waves define the limits for the ZO hyperbolae to be tested. To get a better control of the sampling interval, the parameter range is split into two parts as shown in Figure 3.7: by attaching the ZO operators to the different sides of the considered aperture, I can ensure that neighboring operators are nowhere separated by more than the given sampling interval within the considered ZO aperture. In addition to the limits given by the hypothetical direct waves, the ZO operators also have to satisfy the already determined slope, indirectly given by the emergence angle α , at $x_m = x_0$.

As can be seen from Figure 3.7, this strategy also includes stacking operators that are at some locations steeper than any possible actual event. Additionally, most of them are partly located outside the area limited by the hypothetical direct waves. However, this does not imply an inherent contradiction: remember that the CRS operator is a second order approximation of the traveltimes. Thus, it might fit some parts of the actual events pretty well but might deviate for larger midpoint displacements with slopes beyond the limits of $\pm 1/v_0$. The coherence analysis will, by its own, only select reasonable operators. In the worst case, this approach leads to some computational overhead.

In the current implementation, I make no efforts to determine more than one maximum during the search for R_N , i. e., to resolve conflicting curvature situations. Nevertheless, this extension should be feasible with similar concepts as discussed for the analysis of conflicting dip situations. As the range of tested radii R_N is chosen such as to include virtually all reasonable values, the supremum in this range should always coincide with the global maximum in this range. Of course, this consideration only makes sense for ZO locations on an actual event. The determination of the supremum is in any case simpler and faster than to determine the maximum, provided the latter actually exists.

3.5.4 Hyperbolic CS/CR stack

The general problem to be solved for the CS/CR stack is almost the same as for the hyperbolic ZO stack: again a shifted hyperbola, in general not symmetric to x_0 , has to be determined, whereas its slope at x_0 is already known. Equation (3.2) relates the radius of curvature R_C to the searched-for counterpart R_{NIP} and the already known R_N for the chosen configuration, namely $1/R_C = 1/R_{NIP} + 1/R_N$. As the emergence angle α is also available, the stacking velocity constraints applied in the automatic CMP stack can be directly transferred to constraints for the radius R_{NIP} according to Equation (3.6). Thus, the constraints for the combined curvature R_C are well defined and attempts to attenuate multiples by means of velocity constraints can be consistently performed also in conflicting dip situations where the hyperbolic CS/CR search is required.

In contrast to the linear and hyperbolic ZO stacks, the CS/CR stack is again performed in the pre-stack data with its, in general, irregular geometry. Thus, the strict definition of this gather, $|x_m - x_0| = |h|$, is not applicable. Instead, a kind of binning is required that can be expressed by

$$||x_m - x_0| - |h|| < \varepsilon, \quad (3.8)$$

where ε is a user-given quantity that indirectly controls the number of traces inside the CS/CR gather. Usually, this parameter is set to the average shot distance, but a larger value might also be useful to increase the fold in this gather. Of course, such an artificially increased fold leads to a reduced lateral resolution.

3.5.5 Refinement of the one-parameter searches

Each of the one-parameter searches described in Sections 3.5.1-3.5.4 is applied on an initial grid of the respective parameter that should be chosen as coarse as possible to increase the computational performance. However, the grid has to be sufficiently dense to actually detect the searched-for maxima. This is especially important for the linear ZO stack with its sharp coherence maxima (see Figure 3.3). Once the global maximum and possibly additional local maxima are detected on the coarse grid, the search can be refined in the vicinity of the maxima. This iterative refinement requires only few calculations compared to the search on the initial, coarse grid as it can be confined to a small region around the maxima. The current implementation performs a refined search between the two grid points surrounding the detected maximum. The sampling interval is reduced to a tenth of the sampling interval used in the preceding iteration. With two or three iterations, a very high resolution of the attributes can be achieved.

3.6 Apertures and tapering

Pre-stack data cover only a finite area in the midpoint/offset plane, thus a so-called acquisition aperture is always inherent to the data. In Section 2.7, I discussed the projected first Fresnel zone as the optimum stacking aperture for an optimum resolution of the aimed-for image. This physically justified stacking aperture is usually smaller than the acquisition aperture, except for ZO locations close to the margins of the pre-stack data volume. In addition to this consideration, I have to be aware of the fact that the CRS operator is a second order approximation of the reflection traveltimes in terms of midpoint displacement $x_m - x_0$ and half-offset h . In general, this approximation only holds in a certain, paraxial vicinity around the considered central ray.

Obviously, the projected Fresnel zone as well as the approximate nature of the CRS operator demand to restrict the coherence analyses and the stack to an aperture in the midpoint/offset plane. As I showed in Section 2.7, the projected first Fresnel zone for ZO can be expressed in terms of the CRS wavefield attributes. Thus, this physical constraint can be evaluated during the CRS stack. For finite offsets, however, this approach provides no useful information. The influence of the second-order approximation is even harder to evaluate, as it implicitly depends on the complexity of the (unknown) subsurface model.

3.6.1 ZO aperture

Equation (2.24) provides an estimate of the projected first Fresnel zone for ZO in terms of the CRS wavefield attributes. Consequently, one might consider the respective ZO aperture for each tested set of wavefield attributes from the very beginning. However, this approach is not applicable for two reasons:

- The projected Fresnel zone depends on all three wavefield attributes. During the linear ZO stack, R_N is not yet available. This applies to both, the pragmatic and the extended CRS stack strategy.
- The coherence analysis is very sensitive to the number of contributing traces. As a consequence, coherence values calculated within different apertures are not comparable.

Nevertheless, the projected Fresnel zone is suited to check the appropriate size of the ZO aperture *after* the CRS processing. This is demonstrated for the data sets presented later on. For the actual processing, an estimate of the projected Fresnel zone is used for a simple model, namely a horizontal interface with a homogeneous overburden with velocity v . In this case, the Fresnel zone at the interface and its projection to the surface have the same size. Using the same notation as in Section 2.7, the Fresnel zone for an interface at depth z_0 can be readily computed from

$$\frac{T}{2} = |t_R(z_0) - t_d(x_m - x_0, z_0)| = \frac{2}{v} \left| z_0 - \sqrt{z_0^2 + (x_m - x_0)^2} \right|. \quad (3.9)$$

Recasted in terms of the ZO traveltime t_0 and solved for $x_m - x_0$, the half-width of the Fresnel zone reads

$$\frac{W_F}{2} = |x_m - x_0| = \frac{v}{2} \sqrt{\frac{T^2}{4} + Tt_0} \approx \frac{v}{2} \sqrt{Tt_0}, \quad (3.10)$$

where the second order term of T is neglected in a high frequency approximation. The same result can be obtained from Equation (2.24) with the obvious wavefield attributes $\alpha = 0$, $R_N = \pm\infty$, and $R_{NIP} = vt_0/2$. In other words, approximation (3.10) is consistent with second-order paraxial ray theory.

As already mentioned in Section 2.7, the projected first Fresnel zone is only strictly defined for a mono-frequency wave with the period T . For the transient wavelets in actual seismic reflection data, $T/2$ in the equations above has to be replaced by a measure of the effective wavelet length τ_ϵ . However, such a measure is not well defined: Schleicher and Santos (2001) collected *eleven* different definitions for τ_ϵ that roughly vary by a factor of 3 for a zero-phase Ricker wavelet. The current CRS stack implementation expects the inverse of τ_ϵ as a user-given parameter. For the data examples presented in Chapters 4, 5, and 6, I used the dominant frequency of the input data. Of course, this frequency might be scaled to obtain another definition of the effective wavelet length. For a more rigorous definition of the projected Fresnel zone, I stick to the mono-frequency description in the following.

For a more flexible definition of the ZO aperture, the velocity is now no longer considered to be constant, but is replaced by an RMS velocity as a function of the ZO traveltime t_0 . The current implementation supports a constant vertical velocity gradient with $v(t_0 = 0) = v_0$ and $v(t_0 = t_{\max}) = v_{\max}$. For small traveltimes t_0 , W_F might be too small to include a sufficient number of traces. To circumvent this, a user-given constant $W_{F,\min}/2$ can be added to W_F to ensure a minimum width. Additionally, a maximum width $W_{F,\max}/2$ can be used to avoid extremely large (although physically sound) apertures for large traveltimes. This option is especially useful for data sets with large recording times (and depths) but comparatively small offset ranges like the data presented in Chapter 5: without this confinement, the result would be strongly dominated by the ZO stacks, whereas offset-dependent information would hardly contribute.⁵

The actual size of the projected first Fresnel zone deviates from the estimated value due to the curvature of the considered reflector as well as the complexity of the overburden. According to my experiences, it is more reliable (although more time consuming) to use a possibly too large aperture instead of a too small one for the determination of the CRS wavefield attributes. Furthermore, an overestimation of the projected first Fresnel zone provides additional space to apply a taper function (see Section 3.6.4) without affecting the actual first Fresnel zone. The current implementation accounts for this by using an aperture that is $\sqrt{2}$ times larger than the value given by Equation (3.10) such that it also includes the projected second Fresnel zone as supposed by Sun (2000) for Kirchhoff migration. This finally applied ZO aperture is depicted in Figure 3.8a for a chosen ZO location. It reads

$$\frac{W_F}{2} = |x_m - x_0| = \min \left[W_{F,\max}, \frac{v_0 + (v_{\max} - v_0) \frac{t_0}{t_{\max}}}{2} \sqrt{2Tt_0} + W_{F,\min} \right]. \quad (3.11)$$

⁵This is a consequence of the inappropriate acquisition geometry of these data rather than the pragmatic or extended CRS search strategy, respectively.

3.6.2 CMP aperture

The CRS wavefield attributes provide no offset-dependent information about the appropriate aperture in the CMP gather. Thus, there is no obvious way how to define this aperture without an explicit model. With the knowledge of the projected first Fresnel zone for any finite offset, one might at least restrict the CMP aperture to the part of the CMP gather located inside the envelope of all these Fresnel zones in the midpoint/offset plane. However, the CRS wavefield attributes do not provide the required information. A crude, simple model as used for the ZO aperture discussed in the preceding section is also not sufficient as the projected Fresnel zone for such a 1-D model is always symmetric with respect to the considered CMP gather. Consequently, the CMP gather is always located inside the envelope of all estimated projected Fresnel zones for any arbitrary offset.

The fact that no evident solution for this problem can be derived led to a rather unsatisfactory implementation: the definition of the CMP aperture is left to the user. In other words, I rely on the user's experiences with the familiar CMP stack and NMO correction that might serve to empirically adjust this aperture as these methods are subject to a similar⁶ aperture problem. The current implementation supports a linear interpolation of the CMP aperture between two user-given points (t_1, h_1) and (t_2, h_2) in the time/half-offset plane, completed by a constant extrapolation outside this range. This simple definition is depicted in Figure 3.8b.

3.6.3 Aperture for the CRS super gather

So far, I considered a physical aperture based on a simple 1-D model for the ZO case and a user-given empirical CMP aperture that serve for the ZO stacks and the automatic CMP stack, respectively. For the stack along the entire, spatial CRS operator, either with the initial or the optimized attributes, a spatial definition of the aperture is required, too. As the CMP aperture is defined empirically, it is no surprise that the entire CRS aperture is also based on empiricism: the current implementation uses an elliptic aperture in the midpoint/offset plane with the half-axes given by the ZO and CMP apertures, respectively. The main reason for this choice is the simple mathematical formulation of an ellipse. Furthermore, this aperture shape intuitively accounts for the approximate nature of the CRS operator (2.17). The spatial CRS aperture formed by the CMP and ZO aperture shown in Figures 3.8a and b, respectively, is depicted in Figure 3.8c for a chosen ZO time t_0 .

3.6.4 Operator tapering

To introduce the concept of tapering into the CRS stack, I briefly discuss some aspects of Kirchhoff migration. Although the mathematical description of Kirchhoff migration cannot be directly transferred to the CRS stack, a geometrical interpretation of the related artifacts demonstrates why and how a taper should be applied to the CRS stack operator.

⁶The aperture problem is not exactly the same as for the mentioned standard imaging methods: the CRS stack approach does not suffer from the pulse stretch phenomenon (see Appendix D). Thus, for small traveltimes the CMP aperture might be chosen somewhat larger for the CRS stack.

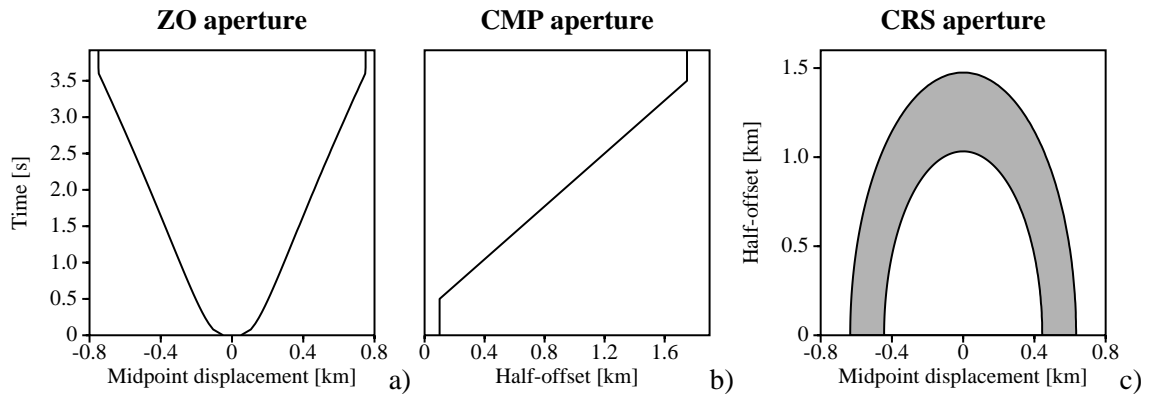


Figure 3.8: a) ZO aperture for a dominant frequency of 30 Hz and an average velocity ranging from 1.5 km/s to 3 km/s. The minimum aperture is set to 50 m, the maximum to 750 m. b) CMP aperture given by the points $(t_0, h) = (0.5 \text{ s}, 0.1 \text{ km})$ and $(3.5 \text{ s}, 1.75 \text{ km})$. c) Spatial CRS aperture set up by the ZO and CMP apertures at $t_0 = 3 \text{ s}$. A taper function is applied to the shaded area: the ratio between the half-axes of the inner and the outer ellipse is 70% such that it basically covers the projected second Fresnel zone for ZO.

For the application of Kirchhoff migration, the stacking aperture should, in principle, extend to infinite offset and midpoint displacement. Of course, the always finite acquisition aperture does not allow to meet this requirement. Furthermore, the use of large stacking apertures is not only computationally very expensive, but also involves more noise from locations where the stacking operator is far off the actual reflection event. Thus, the use of a limited aperture is unavoidable. Schleicher et al. (1997) demonstrated that the first projected Fresnel zone is the optimum stacking aperture: it is large enough to obtain true-amplitude results and provides an optimum signal-to-noise ratio. A smaller aperture leads to wrong amplitudes and a lower signal-to-noise ratio as less traces can interfere constructively.

However, the truncation of the stacking operator and/or the data leads to systematic artifacts in the migration result. Mathematically, these artifacts can be explained by means of the Method of Stationary Phase (see, e. g., Bleistein, 1984): the main contributions to the stack result stem from the stationary point where the operator is tangent to the actual reflection event, and from the borders of the truncated operator and/or data set.⁷ To avoid the unwanted contributions from the truncations, a weight function, the so-called taper function, has to be applied to the operator and/or data. In the following, I only consider the operator tapering. According to the stationary phase analysis, this weight function has to meet two conditions:

- its amplitude at the borders of the operator has to vanish
- its amplitude may only vary slowly along the operator

⁷The contributions from the borders decay with increasing distance to the lateral location of the considered diffractor. Additionally, the separation of the correct migrated image and the artifacts increases with increasing aperture size. For infinite aperture, the artifacts vanish.

Note that this taper function is applied in addition to the true-amplitude weights. As the entire projected first Fresnel zone is required to recover true amplitudes, the taper can obviously only be applied *outside* this Fresnel zone. Therefore, Sun (2000) supposed to apply the taper in the projected second Fresnel zone.

The actual application of such a *limited aperture migration* is a non-trivial task: the calculation of the projected first and second Fresnel zones requires dynamic ray tracing or an additional analysis of the kinematic ray tracing results by means of paraxial ray theory. Even worse, the stationary point enclosed by the Fresnel zone is, in general, not known. For the CRS stack approach, these problems are partly resolved: as discussed above, the projected Fresnel zone for ZO can be estimated from the CRS wavefield attributes. The stationary point for ZO is already known from the very beginning, as it is—per definition—the ZO location to be simulated.

To transfer the tapering approach from Kirchhoff migration to the CRS stack, a geometrical interpretation is better suited than the Stationary Phase method as the latter is not applicable to the CRS stack approach. Hertweck et al. (2001a,b) gave a comprehensive geometrical explanation of the artifacts caused by truncated operators and data: Kirchhoff migration relies on destructive interference of all contributions except for those stemming from the stationary point and its vicinity. At truncations of the data or operator, this destructive interference is incomplete and, thus, leads to the familiar artifacts, e. g., the artifacts known as “migration smiles”. From this geometrical interpretation in the *time domain*, it is obvious that similar effects can also occur for other stacking operations performed within a limited aperture, irrespective if the Stationary Phase Method is applicable or not: if the truncated operator happens to end within an event, this border might contribute more to the stacking result than the desired contribution from the region of tangency.

As already mentioned, Kirchhoff migration yields its optimum results if it is applied within the projected first Fresnel zone surrounded by a tapered area covering at least the projected second Fresnel zone. This does not necessarily apply to the CRS stack approach, as the latter fits approximate *reflection* responses to the data rather than stacking along *diffraction* responses. Nevertheless, the projected first Fresnel zone represents a physical limit for the achievable resolution in terms of reflector properties. Larger apertures will reduce this resolution as the reflector properties will be spatially averaged. Thus, the current implementation of the CRS stack uses just the same concept as for Kirchhoff migration: full contributions from the projected first Fresnel zone, tapering in the projected second Fresnel zone. The tapered area is depicted as shaded area in Figure 3.8c. The applied taper function is a Hanning window

$$f(\beta) = \frac{1 + \cos \beta}{2} \quad 0 \leq \beta \leq \pi, \quad (3.12)$$

where β is zero at the border of the projected first Fresnel zone (inner ellipse) and linearly increases such that it reaches π at the border of the projected second Fresnel zone (outer ellipse). The current implementation provides two stack results, one performed inside the 1-D model based aperture according to Section 3.6.1, and one calculated inside the aperture estimated from the CRS wavefield attributes according to Equation (2.24). The latter usually provides a higher resolution, whereas the former corresponds more closely to the aperture used to determine the wavefield attributes.

3.7 Influence of the near-surface velocity

For the derivation of the CRS reflection response in Chapter 2, I assumed that the near-surface velocity is constant and known. From the Taylor expansions of this reflection response (Equations (2.16) and (2.17)), it is obvious that the approximate operators only depend on *three* coefficients, whereas three wavefield attributes *plus* the near-surface velocity are used to express these coefficients. As a consequence, one and the same stacking operator (fitting best an actual reflection event) can be described by different sets of these four properties. As long as the near-surface velocity is constant within the considered aperture, apparently *any arbitrary* near-surface velocity can be used—the optimum stacking operator and, thus, the stack result will not be affected. The wavefield attributes, however, only have their expected geometrical meaning if the used near-surface velocity is correct. By simply comparing the coefficients of the CRS operators for different near-surface velocities, a system of equations can be established that allows to transform the wavefield attributes to be in accordance with any given near-surface velocity, optimally, of course, the correct one.

This observation might lead to the conclusion that the near-surface velocity does not matter at all if either the wavefield attributes are not used or if they are appropriately transformed with the correct velocity afterwards. However, there are pitfalls related to an arbitrary choice of the near-surface velocity v_0 : the emergence angle α is related to the slope of the event via v_0 . If v_0 is chosen inappropriately, the range of actually tested event slopes is either too small or too large. Of course, the former case might readily lead to a loss of detected events, whereas the latter leads to computational overhead and/or loss of resolution. Similar considerations apply to the search for the radius of curvature R_N of the normal wavefront that relies on the assumption that no event is steeper than $\pm 1/v_0$ in the ZO section.

In conclusion, the near-surface velocity is *no* independent parameter that can be searched for. Nevertheless, some applications of the wavefield attributes actually rely on a correct near-surface velocity, for example the inversion scheme described by Majer (2000)⁸. Furthermore, v_0 enters into the calculation of the tested attributes ranges. A significant deviation from the true velocity will deteriorate the results.

⁸Under the assumption of a homogeneous top layer, the inversion scheme allows to determine the correct near-surface velocity v_0 according to the relation $R_{NIP} = vt_0/2$.

Chapter 4

Synthetic data example: Sigsbee 2A

4.1 Model and simulated pre-stack data

The so-called Sigsbee 2A data set was simulated for a marine 2-D model that represents a situation as observed, e. g., in the Gulf of Mexico: a stratified background model associated with a relatively smooth macro-velocity model contains a salt body with a quite complicated geometry. All layers of the Sigsbee 2A model are assumed to be isotropic. The underlying model was designed by the *Subsalt Multiples Attenuation and Reduction Technologies* (SMAART) oil industry joint venture to provide a reference data set for the application of various seismic imaging technologies.

To prevent any “biased” processing and interpretation of these data, only the simulated pre-stack data volume was distributed by the SMAART joint venture. Neither the detailed model used for the actual simulation of the data nor the smooth macro-velocity model required for a depth migration was available to the users of the data. Meanwhile, after the processing of these data by several research groups, the model has been published by Pfaffenholz (2001).

The geometry of the data is given in imperial units. Although this does not comply to the SI standards, I preserved these units to allow for an easier comparison with other results obtained for these data.

The pre-stack data volume was simulated by means of a finite-difference (FD) approximation of the acoustic wave equation. Thus, the data volume contains all kinds of (unconverted) interbed multiples. The sea surface was not considered as a free surface, therefore water column related multiples were not simulated. Sources and receivers are located 25 ft below the sea surface, the measured quantity is pressure. All results obtained from these data refer to the datum given by the source and receiver locations. I compiled all relevant acquisition parameters in Table 4.1. Although these parameters suggest a perfectly regular acquisition geometry, not all shot gathers actually contain 348 traces, see Figure 4.1.

To get a first impression of the data and the (unknown) 2-D model, a near-offset section extracted from the pre-stack data is shown in Figure 4.2. I used the first four receivers (i. e., the four receivers with the smallest offsets) of each shot gather to obtain a geometry similar to the ZO sections simulated by means of the CRS stack. According to the acquisition parameters, the actual offsets of

Shot and receiver geometry		Midpoint and offset geometry	
Number of shots	500	Number of CMP bins	2053
Shot interval	150 ft	Maximum CMP fold	87
Number of receivers	348	CMP bin interval	37.5 ft
Receiver interval	75 ft	Offset range	0...26025 ft

Recording parameters		Frequency content	
Recording time	12 s	Dominant frequency	20 Hz
Sampling interval	8 ms	Maximum frequency	40 Hz

Table 4.1: Sigsbee 2A data: acquisition parameters of the pre-stack data set. The first receiver in each shot gather always coincides with the corresponding shot.

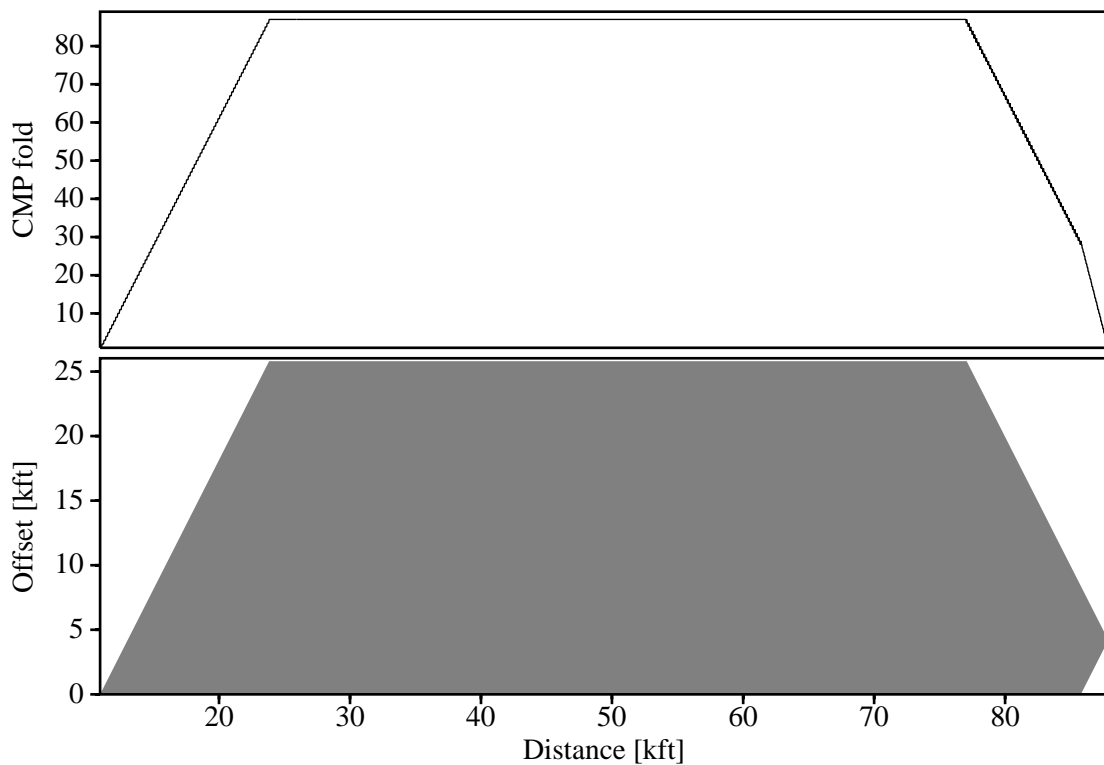


Figure 4.1: Sigsbee 2A data: CMP fold and area covered with pre-stack data. The shot gathers on the right-hand side do not contain all 348 receivers. In usual marine acquisition, the number of receivers is constant. The data was simulated with positive offsets. Consequently, the virtual streamer was towed in the direction of decreasing midpoint coordinate.

neighboring traces are 0, 75, 150 and 225 ft, respectively. These offsets were ignored in Figure 4.2, i. e., no moveout correction was applied for this representation. The near-offset section contains 2000 traces ranging from CMP bin number 25 to 2024. In the following, I will only consider a traveltimes range from 2 to 11 s: the area above the seafloor event is not of interest and a ZO simulation close to the largest traveltimes in the pre-stack data necessarily fails due to the lack of data for larger offsets. The forward-calculated near-offset section in Figure 4.2 represents the reference result for any ZO simulation method applied to these data.

The near-offset section reveals the stratified areas close to the seafloor and to the left of the salt body. In these areas, the near-offset section roughly indicates the subsurface structures. However, the complicated geometry of the salt body causes numerous diffraction patterns and bow-tie structures without any similarity to a geologically plausible subsurface structure. To resolve the diffraction patterns and bow-tie structures to some extent, I applied an NMO correction to the near-offset section followed by a constant velocity Stolt time migration (Stolt, 1978). As no velocity model is available, I used the P-wave propagation velocity of the water column (4920 ft/s) for both processes. The result of this processing sequence is shown in Figure 4.3. Several structural features of the subsurface model can be identified in this time-migrated section, e. g., the top of the salt body and—at the side edges of the salt body—also its lower boundary. In the stratified areas on the left, some faults can be observed.

It is important to note that the result shown in Figure 4.3 was obtained by applying a *post-stack* migration algorithm to *unstacked* near-offset data. Actually, less than 2 % of the multi-coverage data was used to generate this result. This might give rise to the misleading conclusion that multi-coverage acquisition is not necessary. Of course, this is only due to the fact that this synthetic data set contains a sufficient number of near-offset traces and is not contaminated with noise. Furthermore, the redundancy in the multi-coverage data is also required to elaborate a macro-velocity model for a migration to the depth domain or the kinematic wavefield attributes of the CRS stack method. For real data sets, the strategy used to obtain the time-migrated result in Figure 4.3 is usually not applicable, but a preceding stacking procedure is required to obtain a simulated ZO section from the entire pre-stack data set as input for the time migration algorithm. Under such more realistic conditions, the simple assumption of a constant velocity model strongly deteriorates the result compared to its counterpart derived from the near-offset traces only. This can be readily seen in Figure 4.4 which was generated in the same way as Figure 4.3 but using the entire pre-stack data set and an additional stacking operation before the time migration. Especially the image of the bottom of the salt body is now strongly influenced by the wrong model assumptions.

According to the time-migrated section in Figure 4.3, the salt body has a strongly curved surface. The syncline segments of the salt top generate the bow-tie structures seen in the near-offset section. However, in the vicinity of the bow-tie structures, I observe a multitude of events in the near-offset section. To get some insight into the wave propagation under such conditions, I built a simple model with two homogeneous layers forming a syncline structure similar to a feature of the top of the salt body. By means of ray tracing, various ZO and CO experiments were performed with this model. The model and the ZO rays for different ray codes are depicted in Figure 4.5: in the ZO case, the ray tracing yields a set of multiples with traveltimes close to the traveltimes along the primary normal ZO ray. For finite offsets, the situation is similar. In addition to the simulated unconverted reflected waves, various diffracted and refracted waves contribute to the

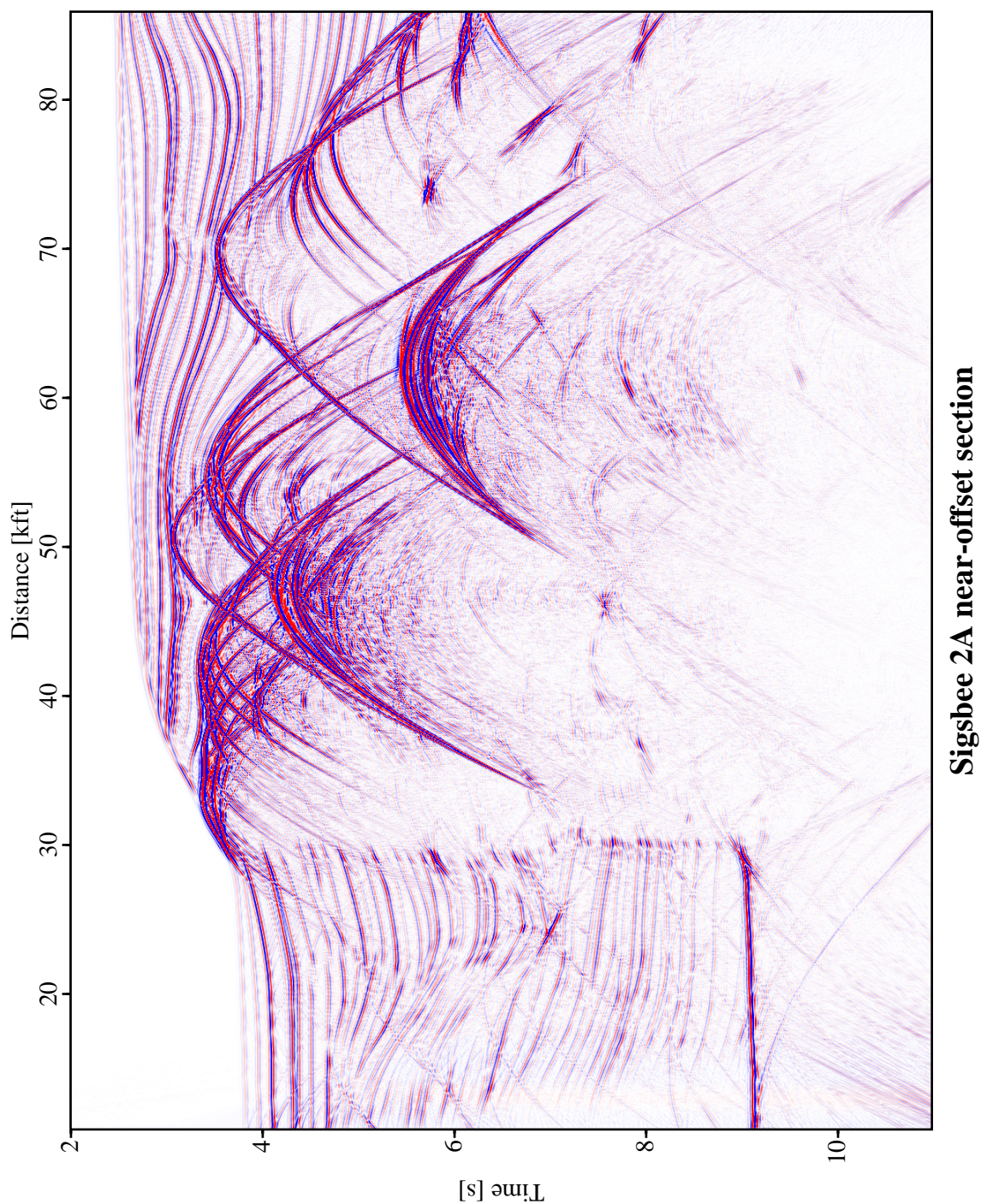


Figure 4.2: Sigsbee 2A data: near-offset section extracted from the pre-stack data. The offsets vary between 0 and 225 ft on neighboring traces. The image of the salt body is dominated by bow-tie structures and diffraction patterns.

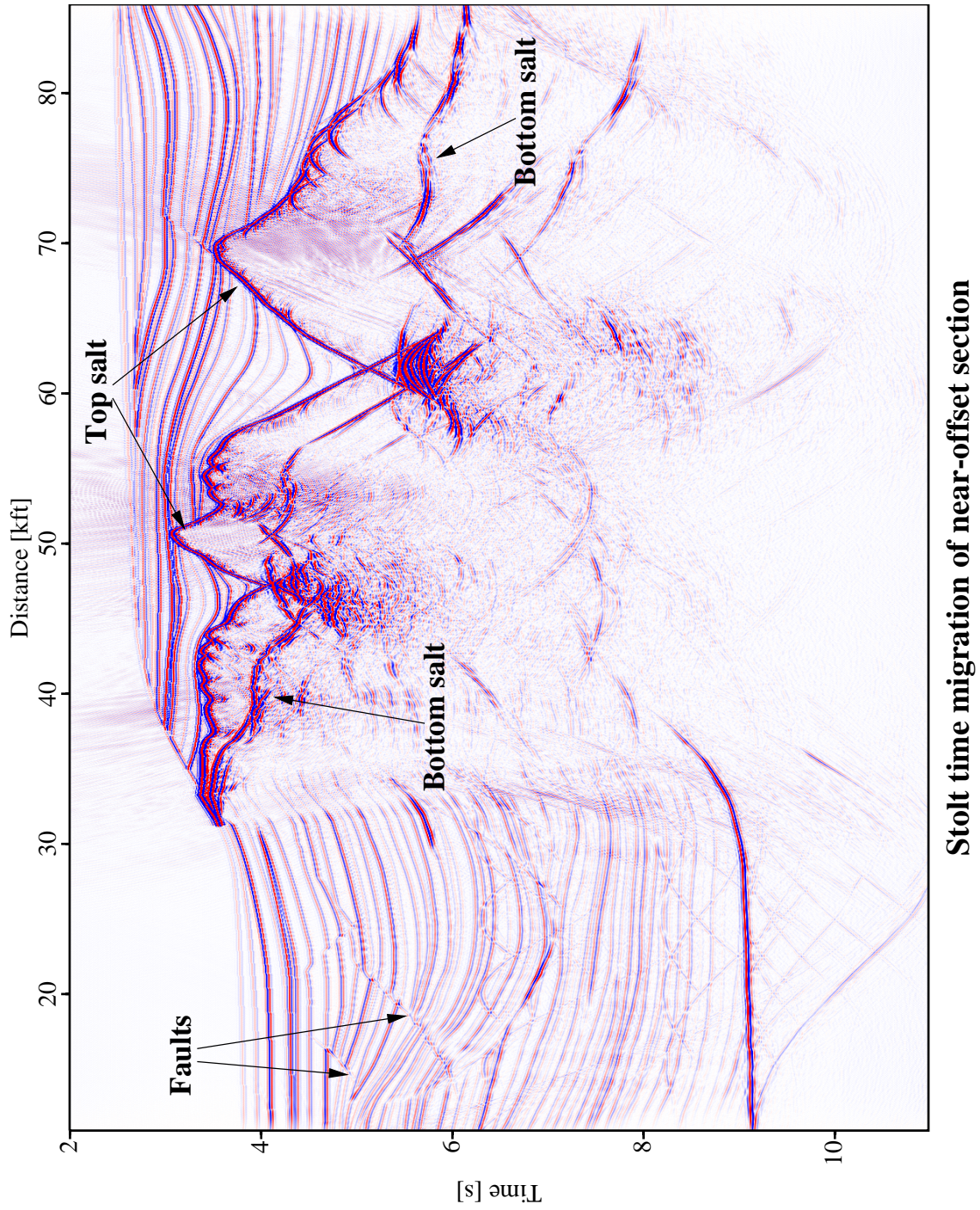


Figure 4.3: Sigsbee 2A data: constant velocity Stolt time migration of the NMO-corrected near-offset section. Water velocity (4920 ft/s) was used for the NMO correction and the migration.

complete wavefield. However, the CRS stack method assumes primary events associated with central ZO rays with normal incidence on the reflector, only. This assumption is strongly violated in this situation, thus I cannot expect to receive a reasonable image of the syncline structures and anything beneath it. Furthermore, due to the usually strong velocity contrast between salt and the surrounding sediments, most of the energy is trapped in the region above the salt body.

4.2 Application of the CRS stack

The Sigsbee 2A data set is well suited to test the CRS stack approach and its implementation under complicated but well defined conditions: it includes events I expect to be imaged and characterized correctly, but also complex events for which the assumptions made in the CRS stack approach are no longer met. The absence of water-column related multiples, which usually have to be attenuated by means of additional processing steps not discussed in this thesis, is advantageous for the CRS stack approach that considers primary events with normal incidence on the reflectors. Due to the acoustic simulation of the data, no converted waves contribute to the wavefield. The simulation of the data set is not based on zero order ray theory, thus their assumptions are not inherently included in the data. This is a very important fact, as otherwise imaging methods based on ray theory were applied to data inherently meeting the same assumptions. This applies, e. g., to the CRS stack example discussed by Jäger et al. (2001). The complexity of the synthetic data set used in this example is only partly realistic and only intended to discuss the concepts of the CRS stack.

The processing of the pre-stack data set for the Sigsbee 2A model with the CRS stack implementation lead to a total number of 62 output sections. Obviously, only a small subset of these sections can be shown and discussed in this thesis, although all of them provide useful information about the data and the appropriate choice of the processing parameters. I will focus on the final results and the most important intermediate results, complemented by a few auxiliary sections that provide insight into the effect of particular processing steps. I compiled the basic processing parameters in Table 4.2. The spatial and temporal sampling intervals of the pre-stack data set were preserved. The quite different computational effort required for the successive processing steps is given in Table 4.3. Of course, the listed CPU times strongly depend on the used hardware, operating system, compiler, and the implementation of the CRS stack itself (see Appendix F for details).

To reduce the computation time, I picked the sea floor event from the near-offset section extracted from the pre-stack data (Figure 4.2) and reduced it by the estimated duration of the source pulse wavelet. The ZO simulation is only performed for ZO traveltimes exceeding these picked traveltimes.

4.2.1 Automatic CMP stack

The extended CRS strategy relies on a sufficiently high quality of the CMP stacked section generated in the first processing step. Thus, I have to examine this section and the associated sections with the detected stacking velocities and the coherence values, respectively:

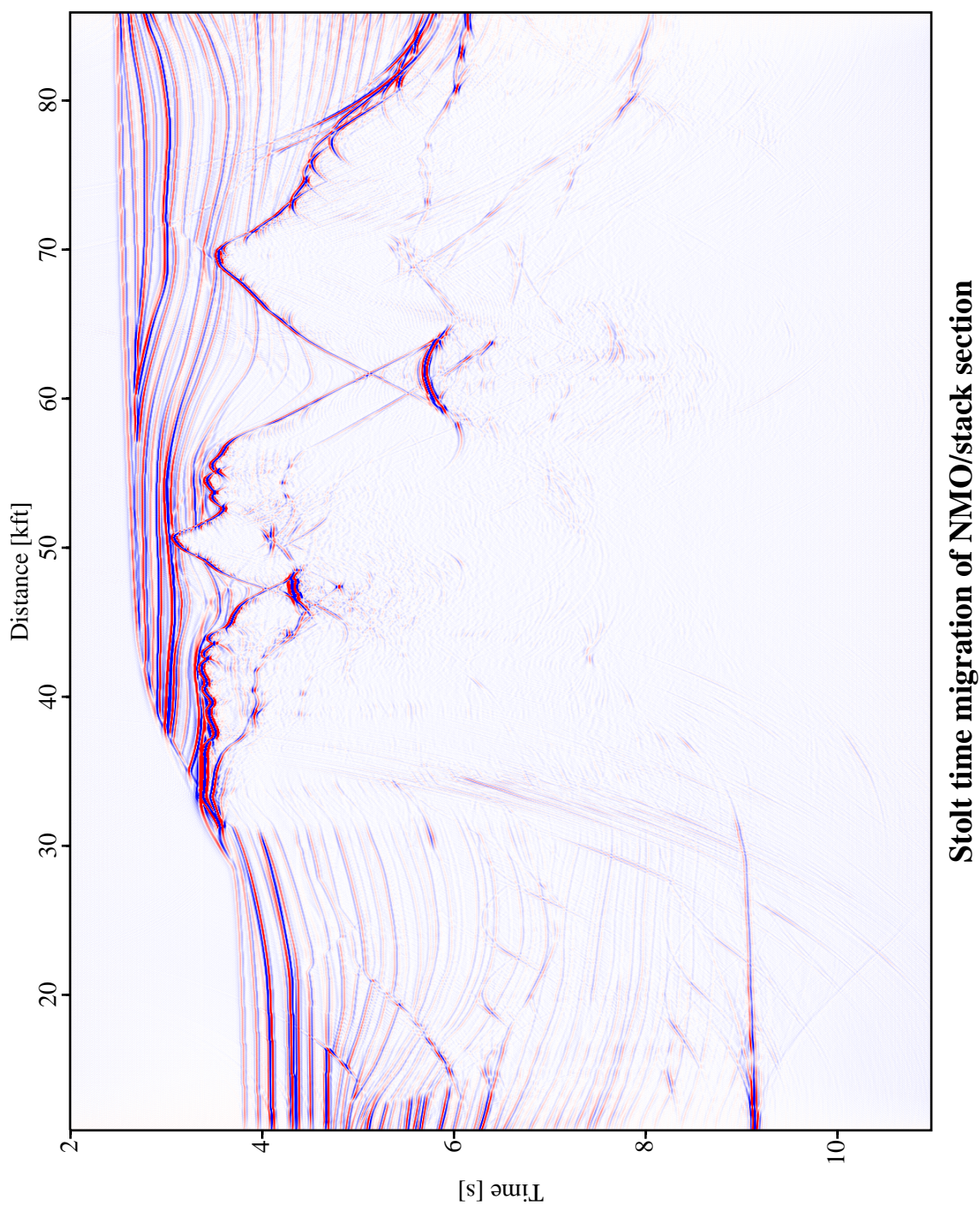


Figure 4.4: Sigsbee 2A data: constant velocity Stolt time migration of the NMO-corrected and stacked pre-stack data. Water velocity (4920 ft/s) was used for the NMO correction and the migration.

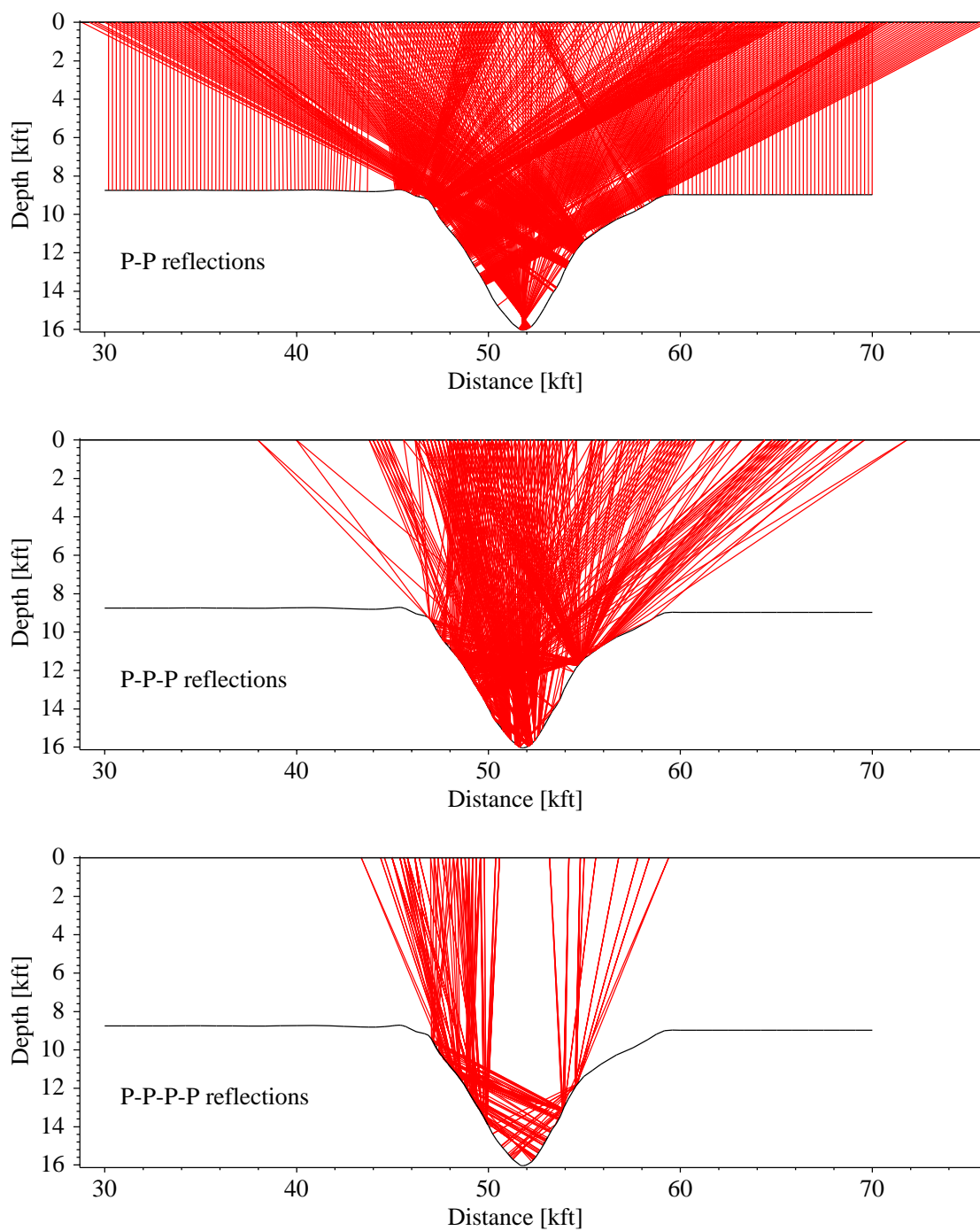


Figure 4.5: Sigsbee 2A data: a simple model consisting of two homogeneous layers. The syncline structure mimics a feature of the salt top. The red lines represent unconverted ZO rays reflected at the interface once (top), twice (middle), and three times (bottom), respectively.

Context	Processing parameter	Setting
General parameters	Dominant frequency	20 Hz
	Coherence measure	Semblance
	Data used for coherence analysis	Original traces
	Temporal width of coherence band	56 ms
Velocity and constraints	Near surface velocity	4920 ft/s
	Tested stacking velocities	4500...20000 ft/s
Target zone	Simulated ZO traveltimes	2...11 s
	Simulated temporal sampling interval	8 ms
	Number of simulated ZO traces	2053
	Spacing of simulated ZO traces	37.5 ft
Aperture and taper	Minimum ZO aperture	1700 ft @ 2 s
	Maximum ZO aperture	5830 ft @ 11 s
	Minimum CMP aperture	6000 ft @ 2.3 s
	Maximum CMP aperture	25000 ft @ 11 s
	Relative taper size	30 %
Automatic CMP stack	Initial moveout increment for largest offset	16 ms
	Number of refinement iterations	3
Linear ZO stack	Tested emergence angles	-60...60°
	Initial emergence angle increment	1°
	Number of refinement iterations	3
Hyperbolic ZO stack	Initial moveout increment for largest ZO distance	8 ms
	Number of refinement iterations	3
Hyperbolic CS/CR stack	Initial moveout increment for largest offset	8 ms
	Number of refinement iterations	3
Conflicting dip handling	Maximum number of dips	3
	Absolute coherence threshold for global maximum	0.5
	Relative coherence threshold for local maxima	0.25
Local optimization	Coherence threshold for smallest traveltime	0.05
	Coherence threshold for largest traveltime	0.02
	Maximum number of iterations	100
	Maximum relative deviation to stop	10 ⁻⁴
	Initial variation of emergence angles	6°
	Initial variation of R_{NIP}	5 %
	Initial variation of transformed R_N	6°
	Transformation radius for R_N	350 ft

Table 4.2: Sigsbee 2A data: processing parameters used for the ZO simulation by means of the CRS stack.

Processing step	absolute CPU time [h]	relative CPU time [%]
Automatic CMP stack	2.5	0.6
Zero-offset stacks	65.5	15.2
Initial stack	26.7	6.2
Local optimization	335.8	78.0
Total	430.5	100.0

Table 4.3: Sigsbee 2A data: absolute and relative CPU times required for the successive processing steps. All times refer to a 400 MHz Pentium II processor and the processing parameters compiled in Table 4.2.

- Compared to the pre-stack data, the signal-to-noise ratio should be higher.
- Events associated with low stacking velocities compared to their neighborhood might indicate multiple events.
- Coincident discontinuities of the stacking velocity and the coherence along an event indicate an inappropriate range of tested stacking velocities.
- High coherence values for most events roughly indicate that the aperture was chosen too small, and vice versa.

The first two criteria are not applicable for this particular data set, as the pre-stack data contains a) virtually no noise and b) no water column multiples with significant moveout anomalies. However, these criteria turned out to be very useful for the real data examples discussed in the following chapters.

The CMP stacked section is depicted in Figure 4.6, the associated stacking velocities and coherence values in Figures 4.7 and 4.8, respectively. I did not observe any consistent indications for events with negative moveouts in this data set, thus only real stacking velocities were tested.

For the events stemming from reflectors above and to the left of the salt, the CMP stacked section (Figure 4.6) is very similar to the reference section (Figure 4.2). The bow-tie structures and diffraction patterns stemming from the top of salt are also well simulated to a large extent.

However, the base segments of the bow-tie structures are now reduced to single dominant events instead of a multitude of neighboring events. The complexity of the ZO section has been strongly reduced around these base segments, but I have to investigate which kind of event has been actually imaged at these locations. The velocity range displayed in Figure 4.7 is too large to show sufficiently subtle details for this analysis. Instead, I picked the stacking velocities at several locations along the bow-tie base segment with its apex at $\approx(5.7 \text{ s}, 61.88 \text{ kft})$ and—as a reference—at the deepest visible reflector above this location. The latter one is about 5210 ft/s, the base segment is, however, associated with stacking velocities as low as 4500 ft/s, the smallest tested velocity. A discontinuity in the stacking velocity along this event indicates that there are events associated with even lower velocities at this location. From this observation I have to conclude that the

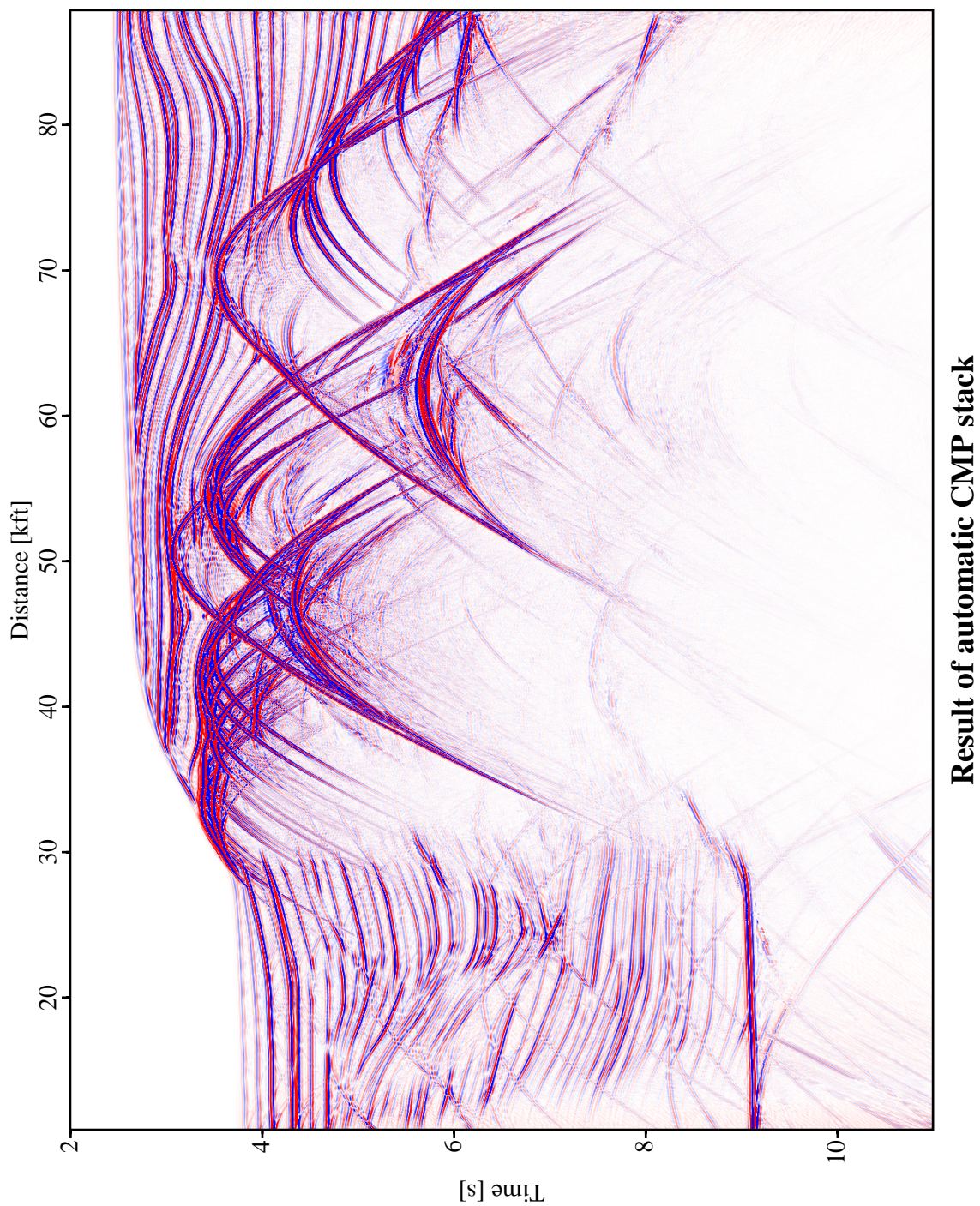


Figure 4.6: Sigsbee 2A data: result of the automatic CMP stack.

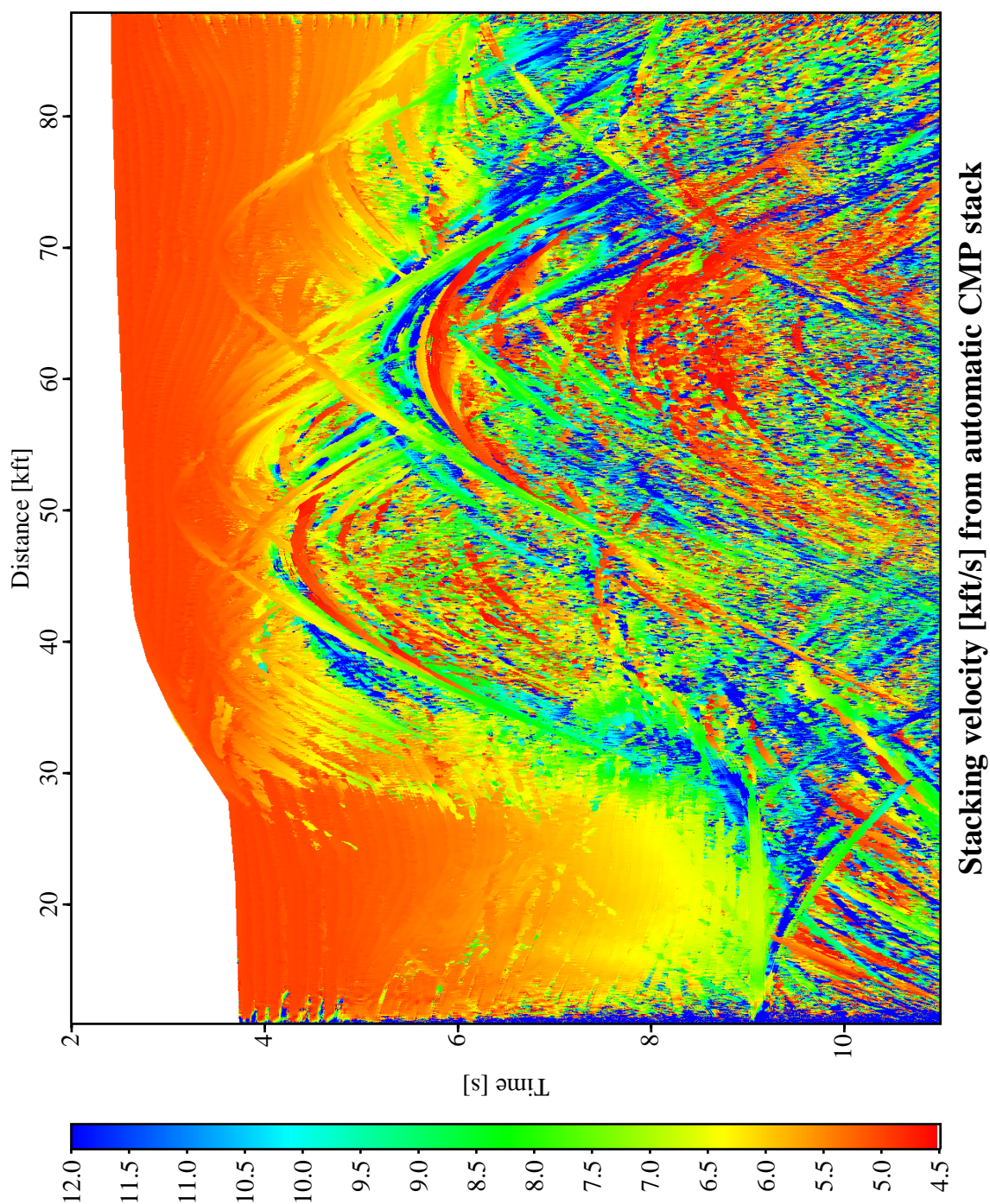


Figure 4.7: Sigsbee 2A data: stacking velocity section associated with the CMP stacked section shown in Figure 4.6. The artifacts at the sides are due to the low coverage at these areas.

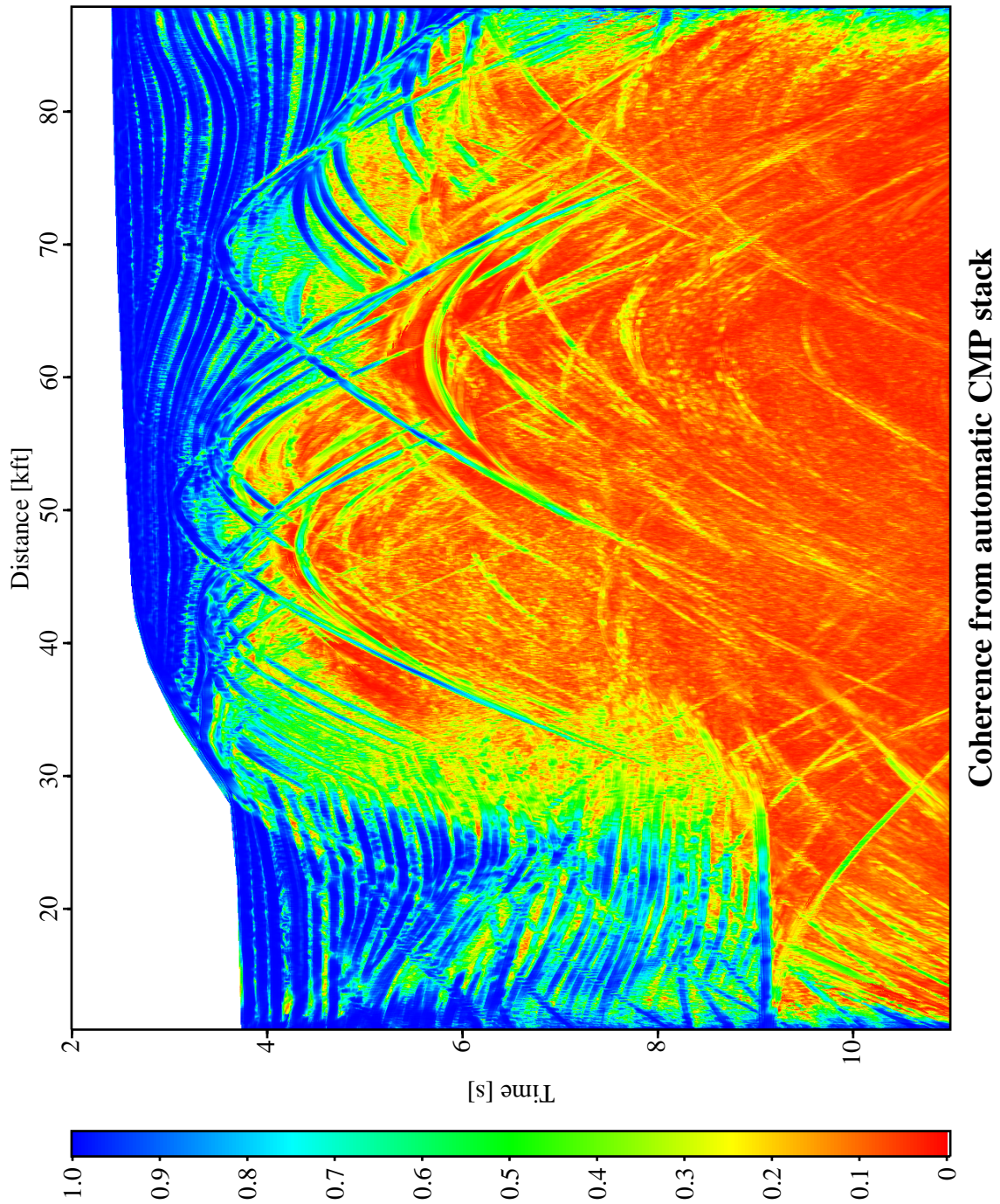


Figure 4.8: Sigsbee 2A data: coherence section associated with the CMP stacked section shown in Figure 4.6.

imaged event is *not* the searched-for primary event, but most likely a composite of at least two different multiple events. Consequently, I cannot rely on either the imaged bow-tie base segments or their associated attributes.

Below the salt, the simulated amplitudes are in general lower than in the reference section. By applying an automatic gain control, the amplitude differences can be removed. The corresponding sections (not displayed) reveal that most events below the salt have been simulated. Due to the complex overburden, the hyperbolic approximation used by the automatic CMP stack only partially fits the actual non-hyperbolic events, yielding low coherence and amplitude values. Furthermore, I observe that some events are shifted in time (approximately up to the dominant period of the source pulse), in some cases one and the same event is split into two separate branches. The explanation for this phenomenon is that separate hyperbolic CMP stacking operators are fitted to the near- and far-offset ranges of the non-hyperbolic events, respectively.

The coherence section (Figure 4.8) helps to identify the detected events and to estimate where the given aperture is appropriate to fit a hyperbolic operator: the events above and left to the salt are associated with high coherence values, as well as the complicated events stemming from the top of salt. With increasing complexity of the overburden, the coherence reduces, indicating the non-hyperbolic moveout of the events.

Finally, conflicting dips situations are not yet resolved in the CMP stacked section. In these situations, the event associated with the higher coherence is selected, whereas the other event is suppressed.

4.2.2 Linear and hyperbolic ZO stack

The CMP stacked section obtained from the preceding processing step serves as input for the determination of the wavefield attributes α , the emergence angle, and R_N , the radius of the emerging normal wavefront. Using the near-surface velocity v_0 , these attributes are directly related to the slopes and the curvatures of the events in the ZO section.

Firstly, the slopes of the events are determined by means of a linear stacking operator within a relatively small aperture. At this stage, conflicting dips are considered, i. e., several slopes are determined for one and the same location, provided that the associated coherence values reach the given absolute and relative thresholds. Secondly, the curvatures of the events are determined with a hyperbolic operator separately for each detected slope. The coherence thresholds are applied again to reject events with too small lateral extension that are most likely artifacts.

This processing step yields a set of (in this case) three sections with the emergence angles and a set of three R_N sections. These attributes are used as initial values in the final local optimization process. The sections with the initial values are not displayed, but their optimized counterparts are discussed in Section 4.2.3. In addition, one R_{NIP} section is calculated from the emergence angle section of the dominant events and the stacking velocity section obtained from the preceding automatic CMP stack. This section also provides the initial values for the final local optimization. However, due to the inherent ambiguity in conflicting dip situations, the values from this section can only be used for ZO locations where only one event has been detected.

To allow for a correct handling of conflicting dip situations in the subsequent processing steps, a map with the number of detected contributing events is generated. The conflicting dip problem (together with the second and third attribute sections) is discussed later in Section 4.2.4. Here, I only want to indicate that this map can be used to check the appropriate choice of the coherence thresholds for the detection of conflicting dip situations.

In addition, separate ZO stacked sections and coherence sections are generated with the linear and the hyperbolic operators, respectively. Although not displayed in this thesis, they serve for quality control during the process.

4.2.3 Final results

The initial wavefield attributes determined in the preceding processing steps can now be used to perform stack and coherence analysis along the entire spatial CRS stacking operators. In conflicting dip situations, however, R_{NIP} is not yet separately determined for each contributing event. An additional internal search with a hyperbolic operator in the CS/CR gather provides the missing attributes.

For the Sigsbee 2A data, the CRS stacked section obtained with the initial attributes (not displayed) already has a sufficiently high quality. However, the accuracy of the wavefield attributes can be further increased by performing a local optimization of the spatial CRS stacking operator with all three wavefield attributes. The local optimization is very time consuming, thus I applied it only to ZO samples that appear to be located on a event. The coherence sections (not displayed) obtained with the initial attributes allow to select time dependent coherence thresholds for this decision. For this data set, I have chosen rather low thresholds to obtain the best possible result. However, I expect no significant differences in the results with higher thresholds. In other words, the computation time could be strongly reduced without much loss of accuracy. A systematic test of the effect of the optimization thresholds on the accuracy was not yet performed as it would require far too much computational effort.

The CRS stacked section obtained with the final, optimized attributes is displayed in Figure 4.9. The stack was restricted to the projected first Fresnel zone (with the given ZO aperture as upper limit) estimated from the wavefield attributes. Compared to the CRS stack within the given ZO aperture (not displayed), this restriction increases the lateral resolution in areas with significant variations of the events' curvatures. To the left and above of the salt body, the optimized CRS stacked section is almost identical to the reference section (Figure 4.2). Below the salt, the events can be revealed by means of an automatic gain control (not displayed). The major events have been imaged with slight shifts in time and location.

The coherence section for the dominant events (Figure 4.10), i. e., the events associated with the highest coherence at each particular ZO location, allows to identify the detected events and to estimate the reliability of the image as well of its associated wavefield attributes. Please note that the coherence was calculated inside the given time-dependent aperture rather than inside the projected first Fresnel zone. The top salt event and the events above and left to the salt are associated with high coherence values. Obviously, these events can be approximated by the hyperboloid given by

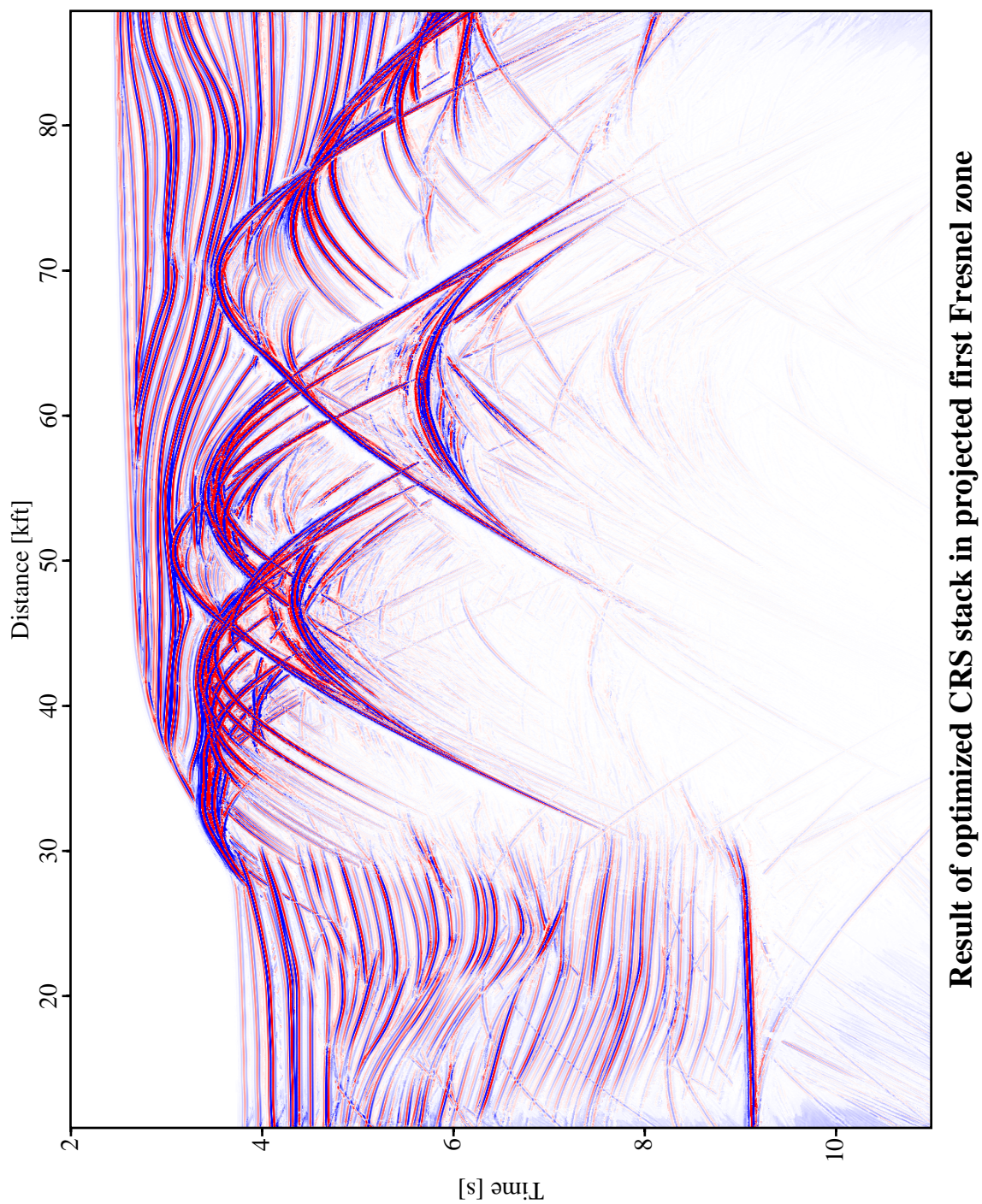


Figure 4.9: Sigsbee 2A data: result of the optimized CRS stack restricted to the projected first Fresnel zone.

the CRS stacking operator to a sufficient extent. According to the low coherence values below the salt, only few of the events can there be described in this way. Thus, I cannot trust in their images and attributes.

Please note that the coherence section as well as the attribute sections are separately available for each contributing event in case of conflicting dip situations. Here, I only refer to the sections associated with the dominant events. See Section 4.2.4 for details on the conflicting dip handling.

In Figure 4.11, I depicted the optimized emergence angle section for the dominant events. Due to the simple relation between the emergence angles and the slopes of the ZO events, the consistency of this section can readily be observed. The same applies to the section with the optimized curvatures of the normal wavefront in Figure 4.12 that is related to the curvature of the ZO events. Again, the attributes associated with the dominant events are shown. To allow for an easier interpretation, I prefer to display the curvature $1/R_N$ rather than the radius R_N itself.

As final attribute section, the values of the radius of curvature of the NIP wavefront are shown in Figure 4.13 for the dominant events. For the stratified areas above and left to the salt, R_{NIP} continuously increases with increasing travelttime. Below the salt, the section is dominated by the tails of bow-tie structures and diffraction patterns stemming from the top and possibly also the bottom of the salt body. There are only few indications of events related to reflectors actually located below the salt.

4.2.4 Conflicting dip handling

The processing parameters used for the Sigsbee 2A data allow up to three contributing events at each simulated ZO location. Due to the multitude of steep bow-tie structures and diffraction patterns in the data, I have to consider conflicting dip situations to account for the intersections of these steep events with other events. The differences in the CRS stacked section with and without conflicting dip handling are hard to detect if the entire sections are displayed. Therefore, a subset of these results is shown in Figure 4.14: in the result obtained with the pragmatic CRS strategy that considers only the dominant events, the strongly curved events are suppressed at most locations, whereas the result of the extended strategy allows to follow these events. In the latter case, the interference of the intersecting events has been simulated at most locations. Thus, the ZO simulation is more realistic in this case. The steep events in Figure 4.14 will later on turn out to be diffraction patterns.

For all ZO locations where more than one contributing event is detected that exceeds the given absolute and relative coherence thresholds, separate sets of wavefield attributes are determined. The attributes can be used to verify the consistency of the results and to reveal the nature of the steep intersecting events: in Figure 4.15, I depicted the emergence angles detected for the dominant events and the events associated with the largest local coherence maximum, respectively. To avoid a sparse representation of the latter and to preserve the spatial context in that section, both figures coincide at locations where only one contributing event has been detected. The different contributing events can easily be distinguished by means of their different emergence angles. The diffraction patterns appear distributed in both sections, depending on which of the intersecting

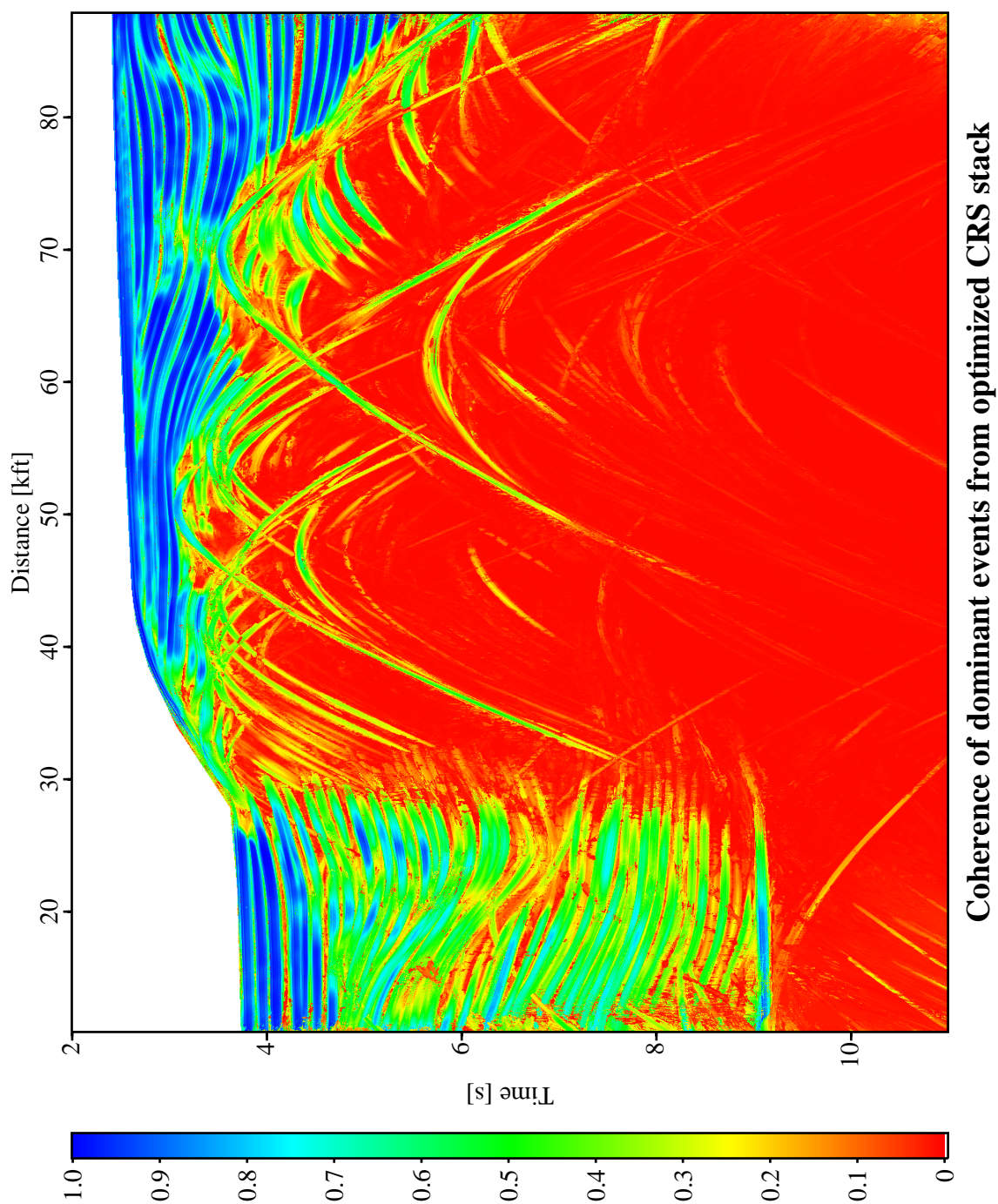


Figure 4.10: Sigsbee 2A data: coherence section for the dominant events associated with the CRS stacked section shown in Figure 4.9. The coherence was calculated in the given ZO aperture.

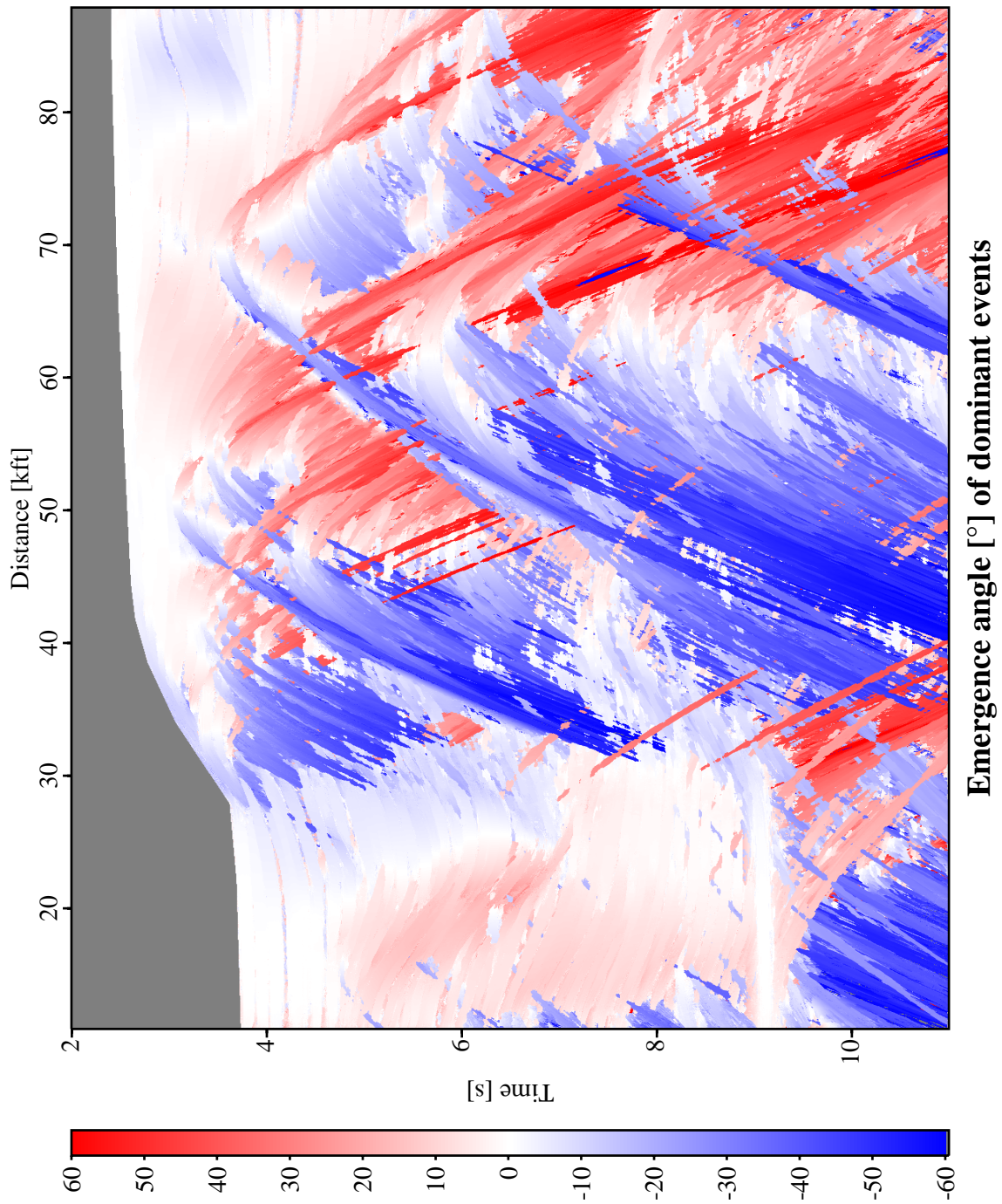


Figure 4.11: Sigsbee 2A data: emergence angle section for the dominant events associated with the CRS stacked section shown in Figure 4.9. The emergence angle is directly related to the slopes of the events.

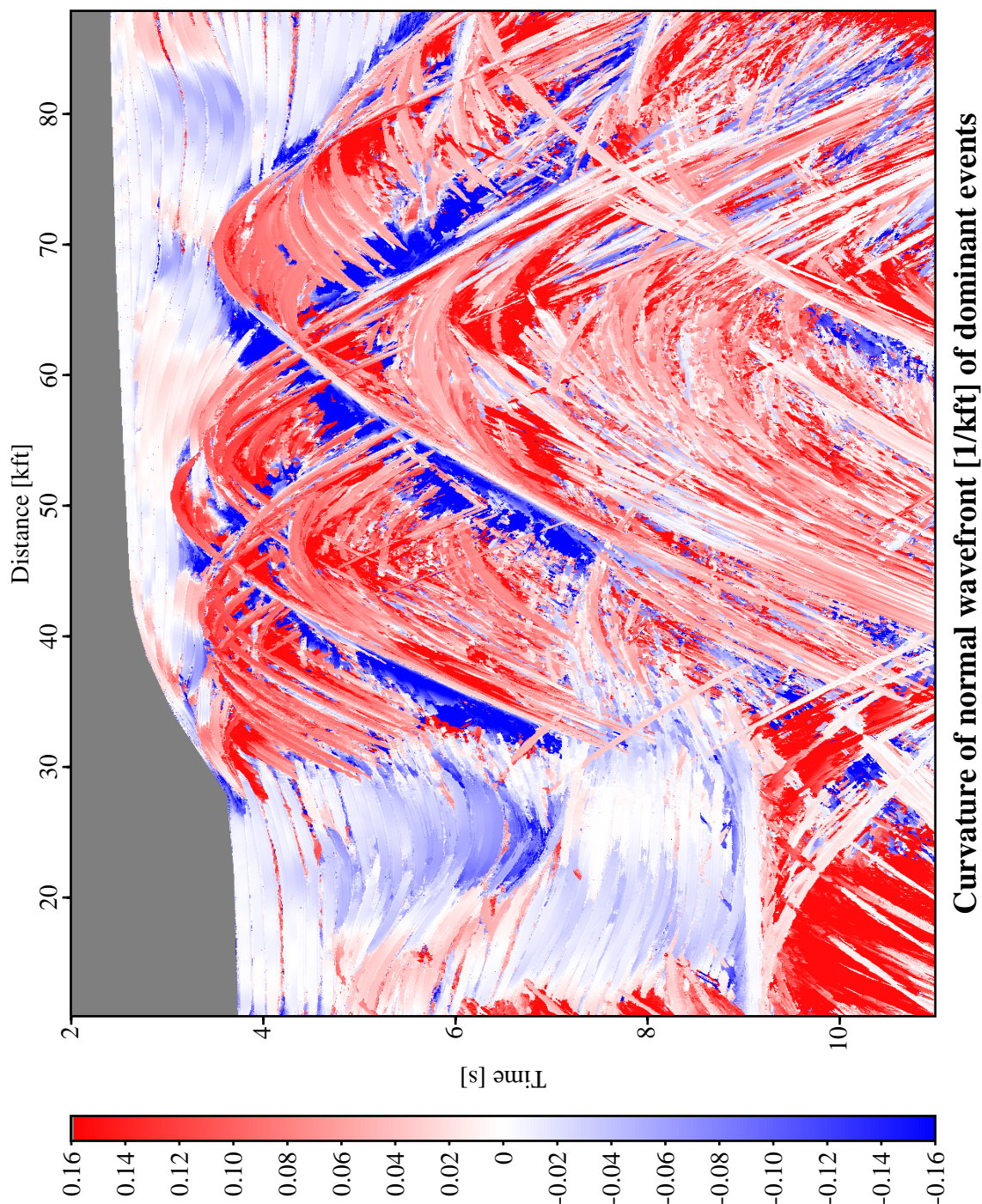


Figure 4.12: Sigsbee 2A data: section with the curvature of the normal wavefront for the dominant events associated with the CRS stacked section shown in Figure 4.9. This curvature is directly related to the curvature of the events.

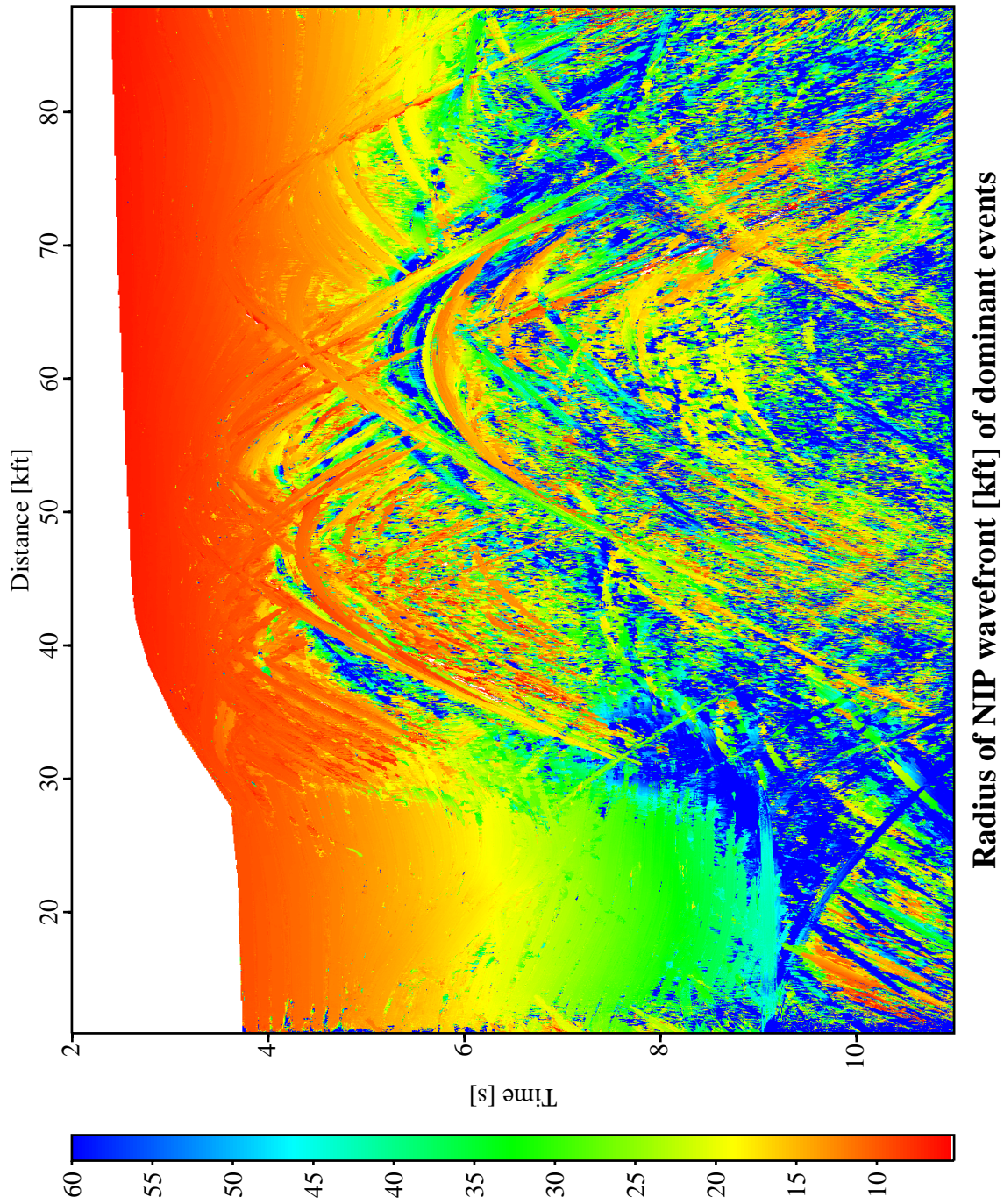


Figure 4.13: Sigsbee 2A data: section with the radius of curvature of the NIP wavefront for the dominant events associated with the CRS stacked section shown in Figure 4.9.

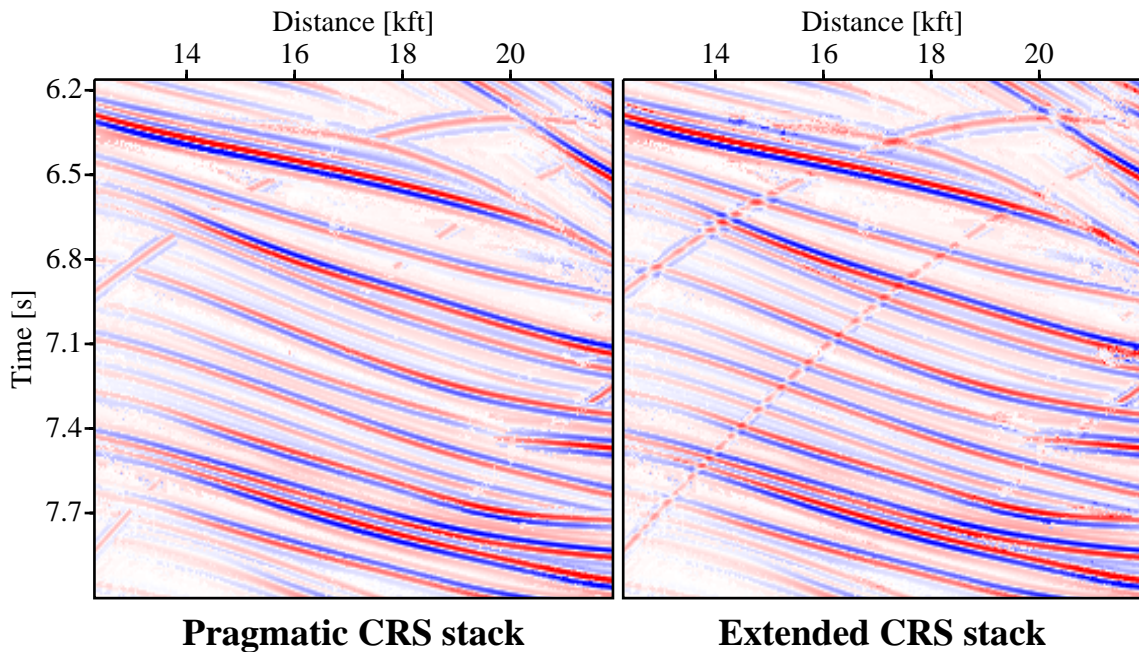


Figure 4.14: Sigsbee 2A data: subsets of the optimized CRS stack result obtained with the pragmatic (left) and the extended (right) CRS stack strategy. At intersections with the flat events, the steep diffraction patterns are suppressed in the former case, whereas their interference with the flat events is simulated in the latter case.

events yields the higher coherence at each particular ZO location. At locations with significant differences of the amplitude of the intersecting events, the weaker event is sometimes lost, i. e., the conflicting dip situation was not detected.

I already indicated that the steep events appear to be diffraction patterns. This can be easily verified if we consider the eigenwave experiments described in Section 2.1.2: for a diffractor, both eigenwave experiments coincide. Consequently, the radii of curvature R_{NIP} and R_{N} should also coincide for diffraction patterns. The ratio of both radii is displayed in Figure 4.16, again for the dominant events and those associated with the largest local coherence maximum, respectively. This representation clearly reveals that the steep events are actually diffraction patterns—the ratio is very close to 1 along these events. Furthermore, the consistency of the wavefield attributes is demonstrated for situations with intersecting events.

4.3 Applications of the wavefield attributes

The kinematic wavefield attributes determined by the CRS stack can be used for various subsequent applications or during the stacking process itself. For the Sigsbee 2A data, I focus on two applications that have to be considered *internally* in the stacking process.

The first one is the estimation of the projected first Fresnel zone that allows to adapt the stack

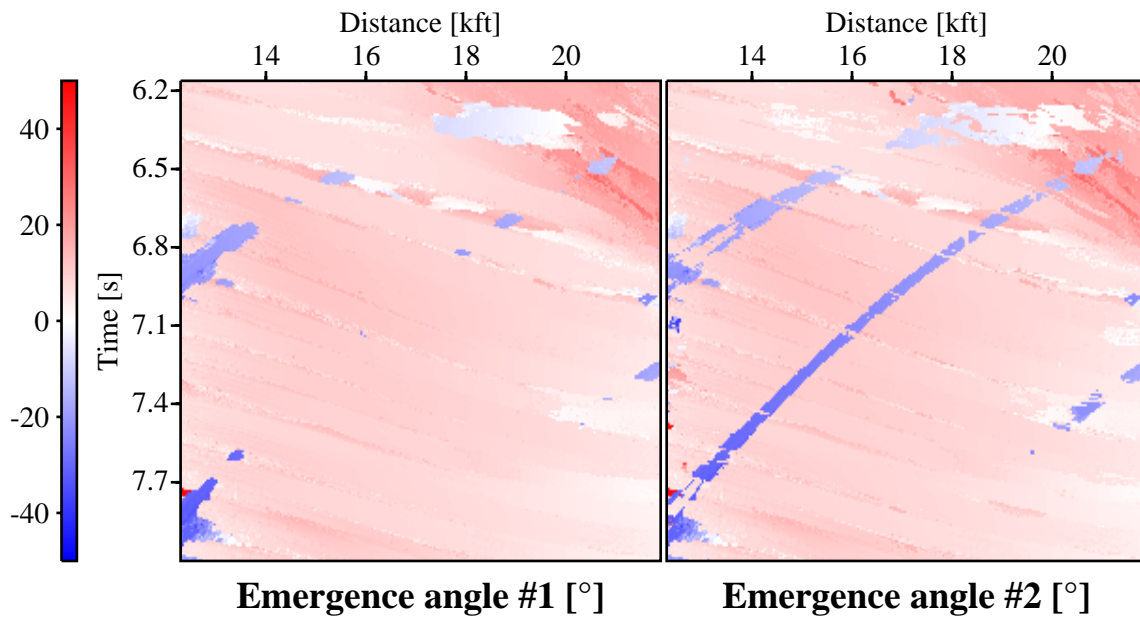


Figure 4.15: Sigsbee 2A data: emergence angles detected for the CRS stacked section obtained with the extended CRS stack strategy (Figure 4.14 right). The emergence angles refer to the dominant events (left) and the events associated with the largest local coherence maximum, respectively. Both sections coincide at locations with only one detected contributing event.

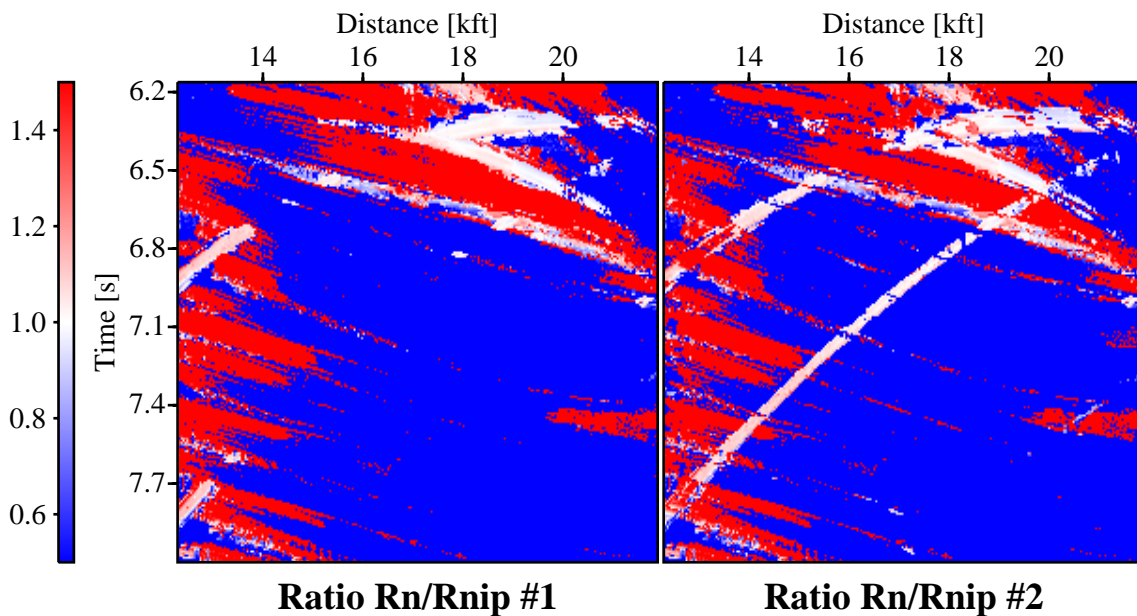


Figure 4.16: Sigsbee 2A data: ratio of curvatures of the normal and NIP wavefronts for the same events as shown in Figure 4.15. A ratio close to 1 indicates diffraction patterns.

aperture to the local complexity of the recorded wavefield. This application affects the amplitudes and the lateral resolution of the stack result. Thus, it has to be integrated into the implementation of the CRS stack as no post-stack operation is available to achieve the same results.

The second application is the attribute-based time migration that places the stacking results of each detected contributing event for each ZO location into the approximated image location of the corresponding time migration operator. In conflicting dip situations, each event detected at a particular ZO location is migrated separately. This requires the availability of the separate stack results for the contributing events *before* they are superimposed to simulate the complete ZO section. Consequently, this application of the attributes has to be performed during the CRS stack, too.

4.3.1 Projected first Fresnel zone

The CRS wavefield attributes allow to estimate the size of the projected first Fresnel zone by means of the traveltimes difference between the approximated *reflection* response and the approximated *diffraction* response associated with one and the same (unknown) point in depth (see Section 2.7). The projected first Fresnel zone is not only suited for subsequent post-stack processes like limited aperture migration (see, e. g. Vieth, 2001), but also a) to check if the user-given ZO aperture was chosen appropriately and b) as stacking aperture for the CRS stack itself.

The appropriate choice of the ZO aperture is crucial for the successful application of the CRS stack, as all coherence analyses to determine the optimum stacking operators are performed within this aperture. To ensure that the entire projected first Fresnel zone that, of course, also extends along the offset axis is covered by the symmetric aperture ellipse of the current CRS stack implementation, the latter should always be larger than the projected first Fresnel zone. Depending on the dips of the events, a factor of 2-4 turned out to be appropriate.

To check if this condition is actually met, I displayed the size of the projected first Fresnel zone relative to the user-given ZO aperture in Figure 4.17 for the dominant events. Above and to the left of the salt body, the given aperture is about twice as large as the projected Fresnel zone, indicating an adequate choice of the ZO aperture. For synclinal events, the projected Fresnel zone shrinks as expected from its definition. Along the bow-tie structures and the diffraction patterns, the projected first Fresnel zone is far larger than the user-given aperture (the displayed values are clamped to a maximum of 1). In this case, the user-given aperture is used as the upper limit.

4.3.2 Attribute-based time migration

As discussed in Section 2.6, the CRS stacking operator not only approximates the kinematic reflection response of a curved reflector segment in depth, but also the kinematic response of a diffractor located at the same (unknown) location in depth if I simply set $R_N := R_{NIP}$. The apex of the resulting operator approximates the image location of a Kirchhoff time migration.

The stacking result along each detected contributing event for each simulated ZO location is not only assigned to the respective ZO sample, but also to the approximated image location of a time

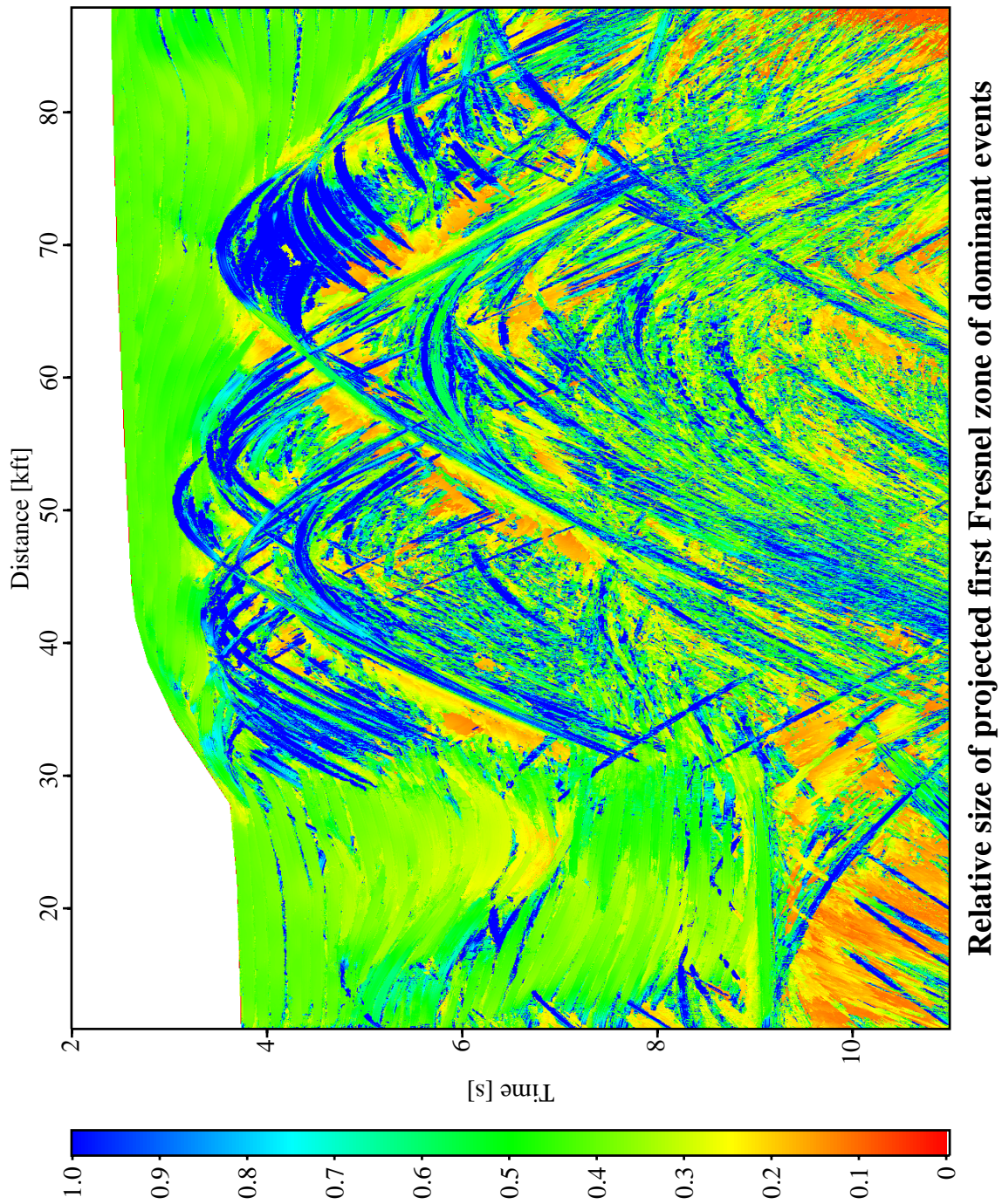


Figure 4.17: Sigsbee 2A data: size of the attribute-derived projected first Fresnel zone of the dominant events relative to the user-given ZO aperture. The display is clamped to an upper limit of 1.

migration. Multiple contributions to the same image location are superimposed. This by-product of the CRS stack is shown in Figure 4.18. As for the CRS stacked section in Figure 4.9, the stacking aperture was restricted to the projected first Fresnel zone.

The attribute-based time-migrated image reveals a set of diffractors obviously superimposed to the model on a regular grid. The faults in the model can also be observed, as well as the top of the salt body. Only the base segments of the bow-tie structures are wrongly imaged. This is due to the fact that these are apparently no primary but multiple events. However, the wavefield attributes for multiple events of unknown wave mode lead to a wrong approximation of the time migration image location.

4.4 Conclusions

The performance of the CRS stack on the Sigsbee 2A data strongly depends on the local complexity of the recorded wavefield. All primary events that can be sufficiently accurately approximated by a hyperboloid given by the CRS stacking operator are well imaged in the CRS stacked section. This applies to all events stemming from features above and left to the salt body. Also, the parameterization of these events by means of the wavefield attributes is consistent and, thus, well suited for various internal and subsequent applications. Successful examples of the former are the estimation and application of the projected first Fresnel zone and the attribute-based time migration. With the extended CRS stack strategy, I was able to resolve most of the conflicting dip situations in the data. In this way, not only a more realistic ZO section with interfering events was simulated, but also a more complete set of wavefield attributes is available.

Most of the event stemming from the top of the salt body is imaged correctly. The steep synclinal features of the top of salt cause multiple events in the vicinity of the associated bow-tie structures. Wherever such multiples were imaged, they are associated with wavefield attributes that are no longer related to the expected geometrical meaning. This leads to wrong images of these multiples in the attribute-based time migration.

Due to the complicated geometry of the salt body, all events associated with reflectors beneath the salt cannot be approximated by a hyperbolic operator. Consequently, the CRS stacked section provides a rather poor image of these events. To obtain a useful image of the subsalt events, the complexity of the recorded wavefield has to be reduced by an iterative redatuming approach. Glogovsky et al. (2001) applied an integrated depth imaging approach to the Sigsbee 2A data including wavefield redatuming. For the same data, a redatuming approach based on the Common Focuspoint (CFP) technology was presented by Hindriks et al. (2001). The incorporation of such redatuming approaches usually requires the construction of a velocity model in depth, a topic that is beyond the scope of this thesis. Nevertheless, the CRS wavefield attributes provide the information required to build a depth model. Such an inversion of the attributes was discussed by Majer (2000). Its application for iterative redatuming approaches remains for future research.

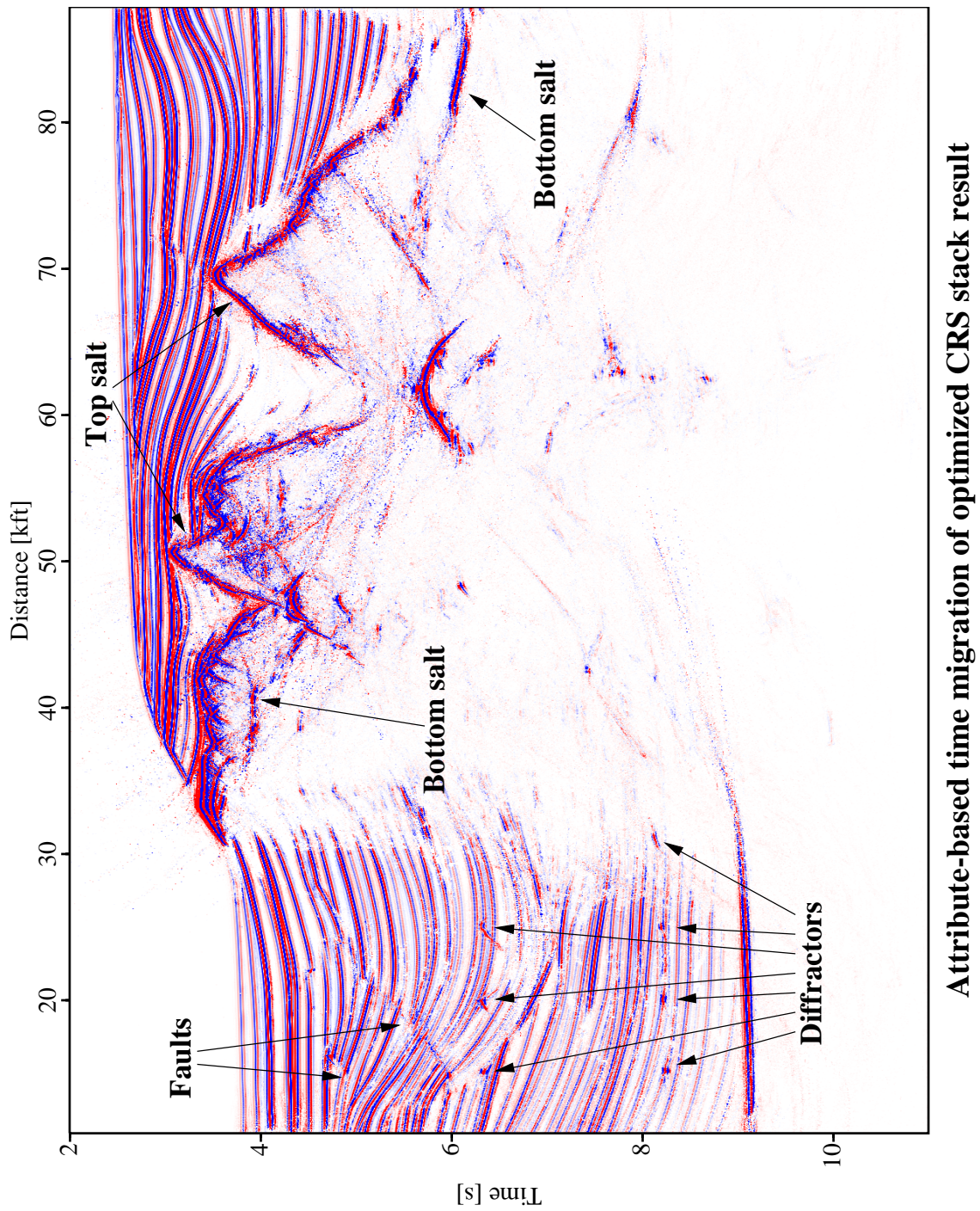


Figure 4.18: Sigsbee 2A data: attribute-based time migration corresponding to the optimized CRS stacked section shown in Figure 4.9. The stack was restricted to the projected first Fresnel zone.

Chapter 5

Real data example: CINCA SO104-13

5.1 Data acquisition and pre-processing

The seismic line SO104-13 was acquired off-shore Chile in 1995 by the survey vessel *Sonne*. The cruise SO104 is part of the *Crustal Investigations off- and onshore Nazca Plate/Central Andes* (CINCA) program performed by the Federal Institute for Geoscience and Natural Resources (BGR), Germany, in cooperation with other partners. The acquisition covers the Nazca Plate, the Peru-Chile trench, and the Chile margin for latitudes ranging from 18°S to 26°S. The intention is to investigate the evolution and structure of the continental margin of North Chile. The total length of the seismic lines is 4500 km recorded with a digital 120 channel streamer. The location of the entire seismic line SO104-13 is depicted in Figure 5.1, the acquisition parameters of the processed subset of this line are compiled in Table 5.1.

The locations of all shot and receiver pairs are depicted in Figure 5.2 together with the CMP fold distribution. Obviously, 6 of the 120 receivers are dead, the acquisition geometry is slightly irregular. The largest acquired offset of about 3 km is rather small compared to the target depth: the interpreted time section of the seismic line SO104-13 shown in Figure 5.3 indicates a water depth of up to ≈ 7.5 km. The area covered by the subset of the data presented in this thesis is roughly marked in this figure. It basically covers the Peru-Chile trench with its complicated structures. The interpreted time section was provided by the BGR and is based on a joint inversion of wide angle refraction data and the pre-stack data described below.

The BGR kindly provided the pre-processed pre-stack data and the conventional processing results obtained by means of NMO/DMO/stack. The latter serves as reference result for the CRS stack processing. The pre-processing of the data includes a bulk shift of -10 ms, spike removal, bandpass filtering, spherical divergence correction, and predictive deconvolution. All results discussed in the following refer to the pre-processed data *after* deconvolution. The ZO section obtained by NMO/DMO/stack is displayed in Figure 5.4. Please note that the lateral range of this section slightly differs from the target zone processed with the CRS stack.

Obviously, these data are strongly dominated by a multitude of steep diffraction events stemming from the rugged seafloor. Therefore, an interpretation of the unmigrated results is almost impossi-

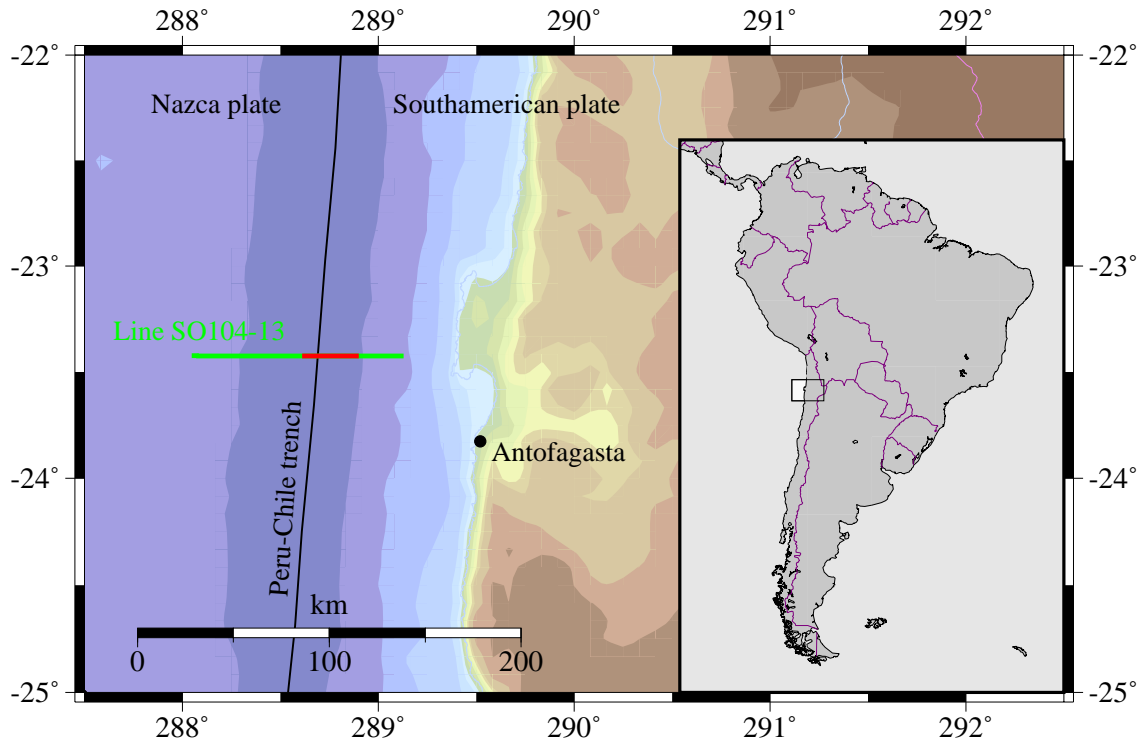


Figure 5.1: CINCA SO104-13 data: location of the acquisition line. The shot locations of the entire line are shown in green, the subset processed for this thesis is depicted in red. The actual coastline is depicted as light blue line. The colored topography deviates from the coastlines due to its low resolution. The streamer was towed from west to east.

Shot and receiver geometry		Midpoint and offset geometry	
Number of shots	590	Number of CMP bins	2367
Shot interval	50 m	Maximum CMP fold	36
Number of receivers	114 (6 dead)	CMP bin interval	12.5 m
Receiver interval	25 m	Offset range	277...2952 m
Recording parameters		Frequency content	
Recording time	14.3 s	Dominant frequency	≈ 30 Hz
Sampling interval	4 ms	Maximum frequency	50 Hz

Table 5.1: CINCA SO140-13 data: acquisition parameters of the pre-stack data set. The provided data represents a subset of the complete acquisition line. The dominant frequency refers to the data before deconvolution.

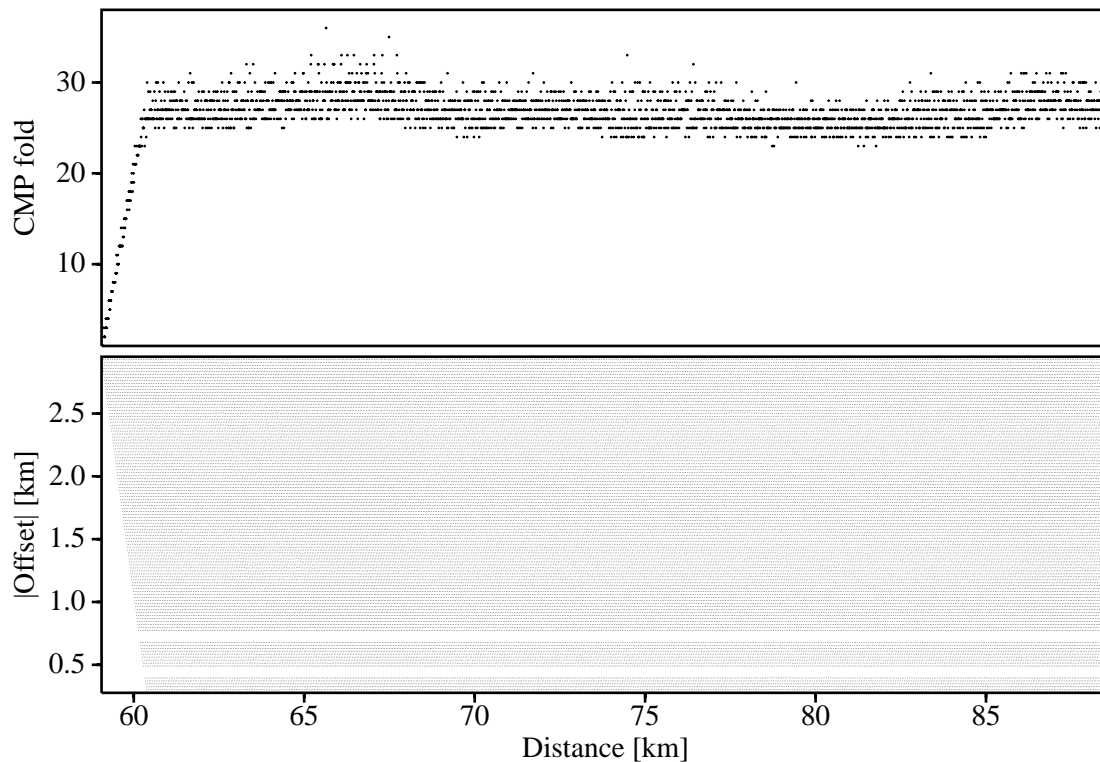


Figure 5.2: CINCA SO104-13 data: CMP fold and locations of the pre-stack data traces. Six of the 120 receivers are dead, the acquisition geometry is slightly irregular. The original offsets are negative. The midpoint coordinate increases in the towing direction of the streamer, i. e., from west to east.

ble. To collapse these diffraction events, I applied a constant velocity Stolt time migration (Stolt, 1978) with water velocity (1500 m/s) to the result of the NMO/DMO/stack processing chain. The time-migrated section is displayed in Figure 5.5. Apart from some migration artifacts, this figure reveals a clear picture of the seafloor and several events stemming from the subsurface. However, they are most likely wrongly positioned due to the applied constant velocity assumption.

For the SO104-13 data, an interval velocity model in depth is available. This model was built by César R. Ranero and co-workers at GEOMAR in Kiel, Germany. Unfortunately, these results are not yet published. I was told that a respective paper by C. R. Ranero and R. v. Huene (and possibly other co-authors) was recently submitted to the Journal of Geophysical Research. According to Ranero (personal communication), the model has been created using focusing panels and CRP gathers by means of the Sirius package from GX technology. Eight iterations of Kirchhoff pre-stack depth migration were performed to obtain the final model. Considering the streamer length of ≈ 3 km, the velocities are said to be relatively well constrained down to $\approx 4 - 5$ km below seafloor. For deeper regions, a combination of focusing panels, CRP gathers, and information from a coincident wide-angle profile were used. No velocity analysis was performed for the oceanic

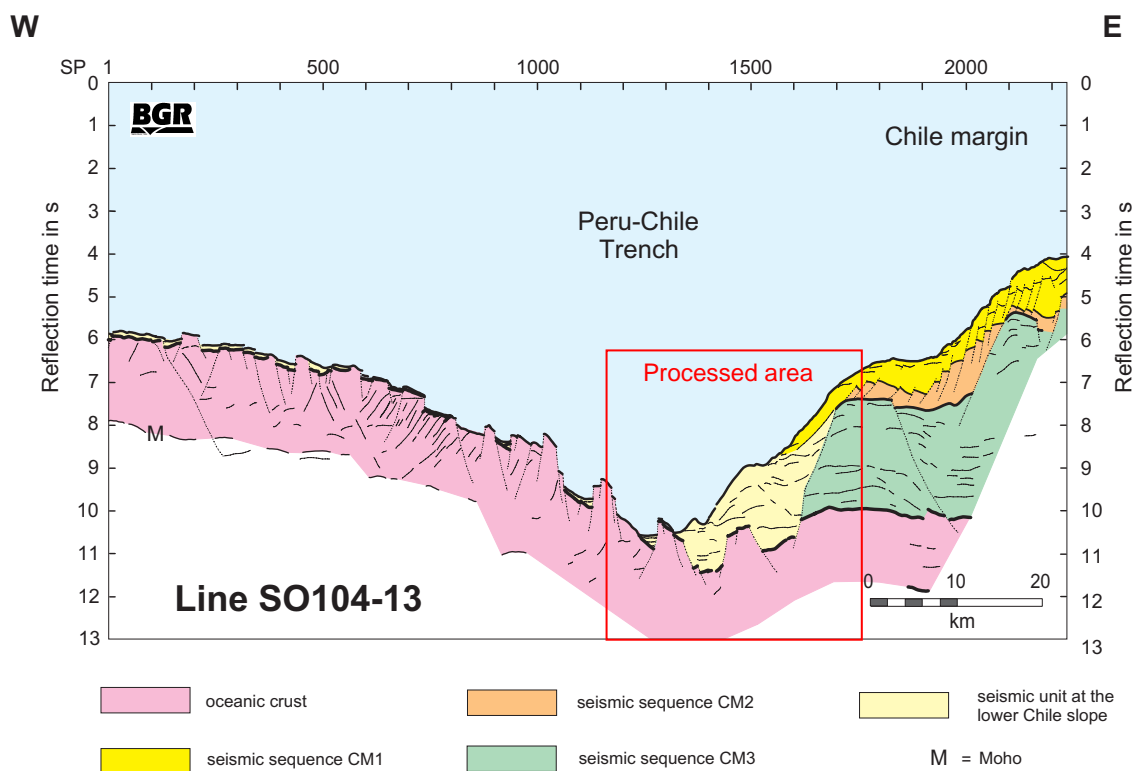


Figure 5.3: CINCA SO104-13 data: interpreted time section provided by the BGR. The red rectangle depicts the area processed for this thesis. The pull-up of the subducted oceanic crust on the right hand side is due to the representation in the time domain.

crust.

This model includes structural details of the subsurface. Such details tend to introduce according structures in the migrated image. To avoid that these details have an overemphasized influence on the migration results, I smoothed this model by means of a convolution with the auto-convolution of a rectangle with a height of 500 m and a width of 312.5 m. The smoothing filter was applied to the squared slowness values. The smoothed interval velocity model is displayed in Figure 5.6.

Based on this interval velocity model, a Green's function table (GFT) was calculated by means of the NORSAR software package based on a wavefront construction algorithm. The theory of this method was discussed by Vinje et al. (1993, 1996a,b), applications can be found in Vinje et al. (1994, 1999). The GFT served as input for a Kirchhoff post-stack depth migration. Contributions along the migration operator were fully considered up to an operator dip of $\pm 35^\circ$, followed by a cosine-taper up to $\pm 45^\circ$. The post-stack depth migration of the ZO simulation obtained by NMO/DMO/stack is shown in Figure 5.4. It serves as reference result for the post-stack depth-migrated result obtained for the CRS stacked section.

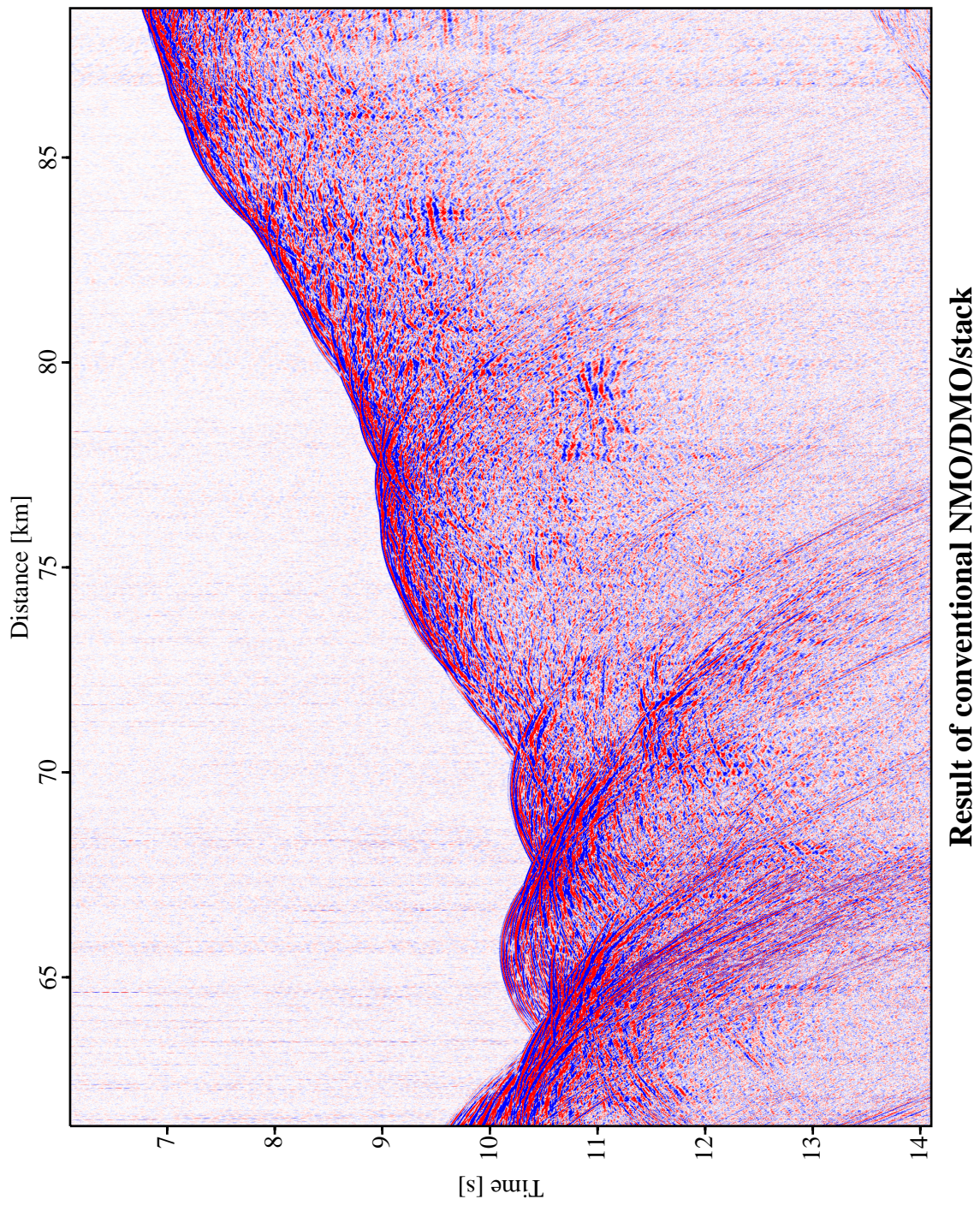


Figure 5.4: CINCA SO104-13 data: ZO simulation obtained from the conventional NMO/DMO/stack processing chain.

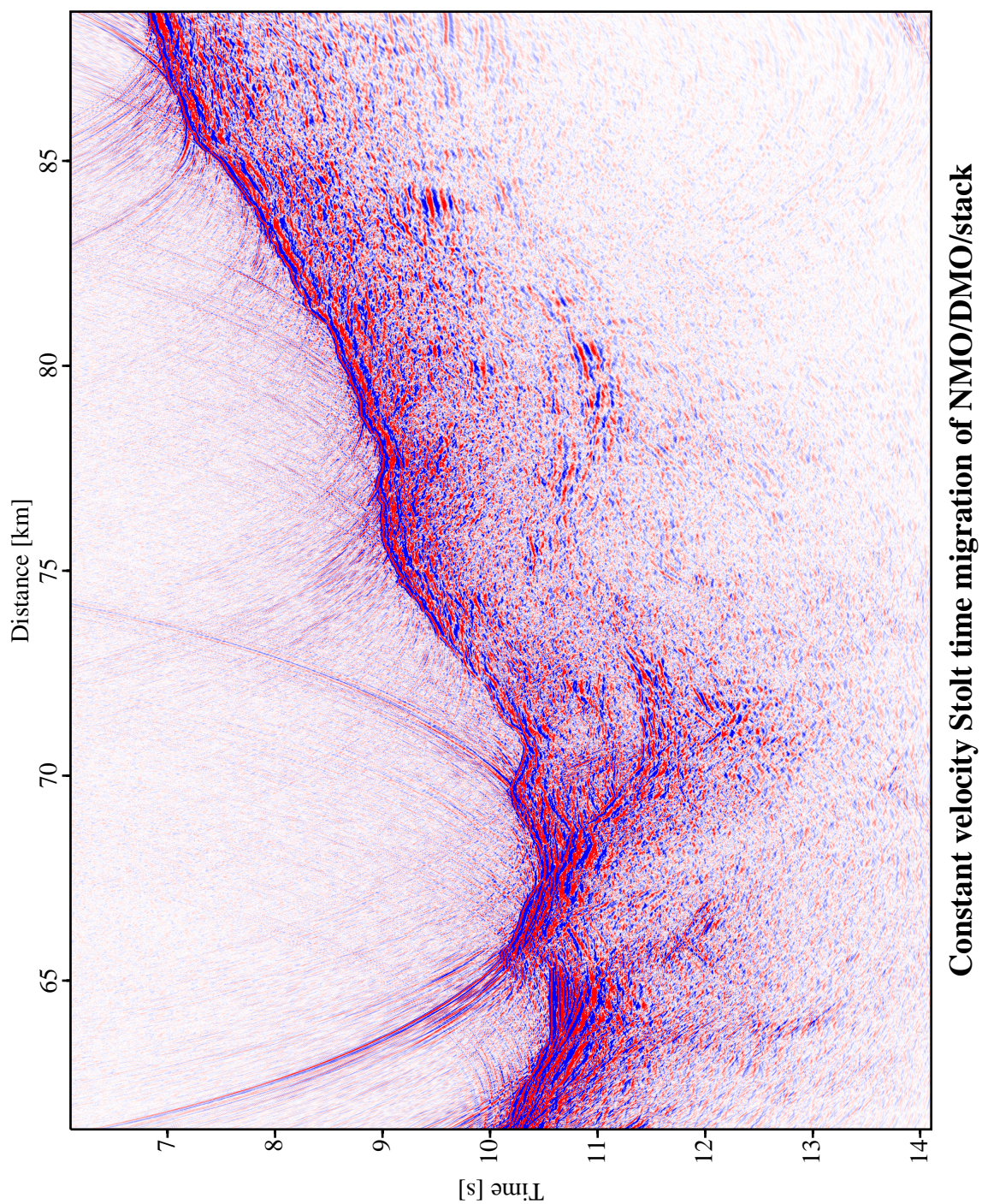


Figure 5.5: CINCA SO104-13 data: constant velocity Stolt time migration of the ZO section shown in Figure 5.4. Water velocity (1500 km/s) was used for the migration.

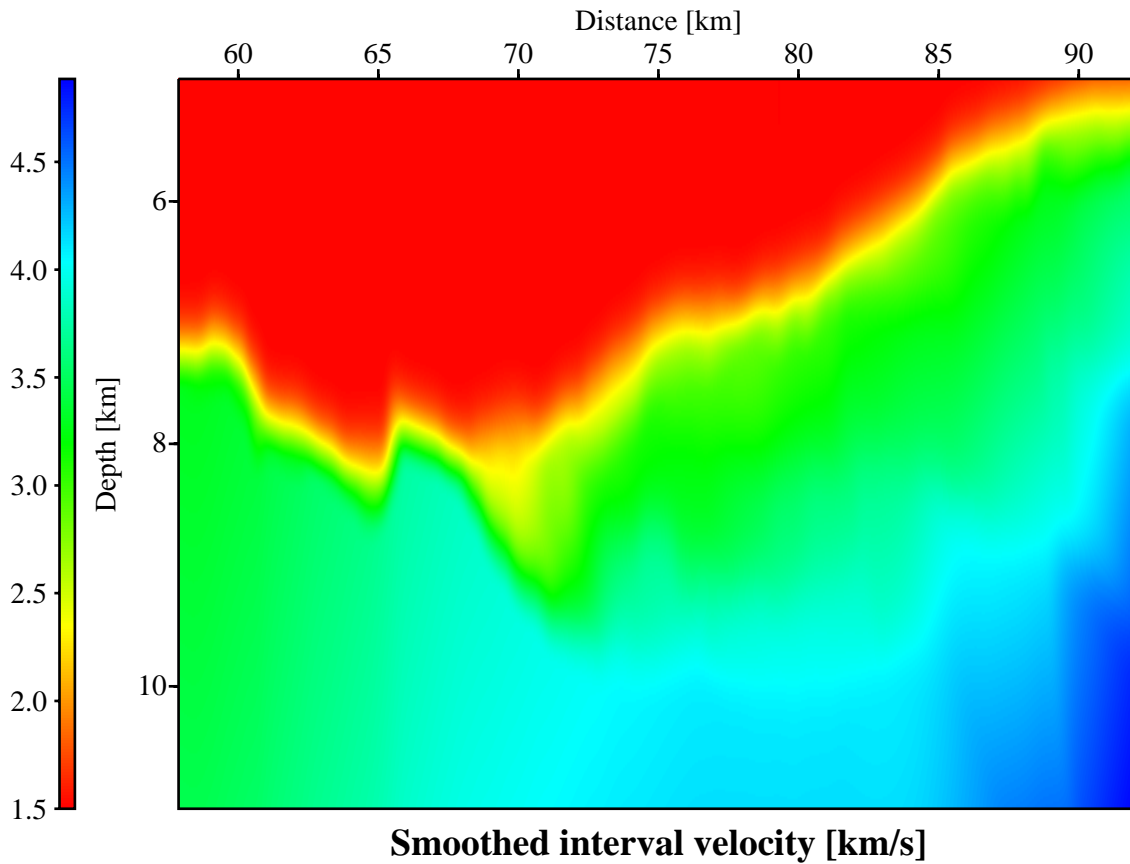


Figure 5.6: CINCA SO104-13 data: smoothed interval velocity model used for post-stack Kirchhoff depth migration. The original, unsmoothed model was provided by C. R. Ranero and co-workers at GEOMAR, Kiel, Germany.

5.2 Application of the CRS stack

The SO104-13 data set was processed by different groups with different approaches. Thus, independent reference results are available that allow to evaluate the performance of the CRS stack for these data. In the scope of this thesis, I compare the CRS-based results with the conventional results presented in the preceding section. For the processed subset of the data, I did not observe any consistent indications for multiple events interfering with detectable primary events. This fact reduces the risk to detect and wrongly characterize multiple events that might—even worse—obscure searched-for primary events. For these data, the CRS stack approach also benefits from the very deep seafloor at the Peru Chile trench: the large, almost homogeneous water layer reduces the complexity of the wavefield due to wavefront healing. I can expect that the hyperbolic approximation is sufficiently accurate under these conditions.

The application of the CRS stack to the SO104-13 data provided a large number of stacked sec-

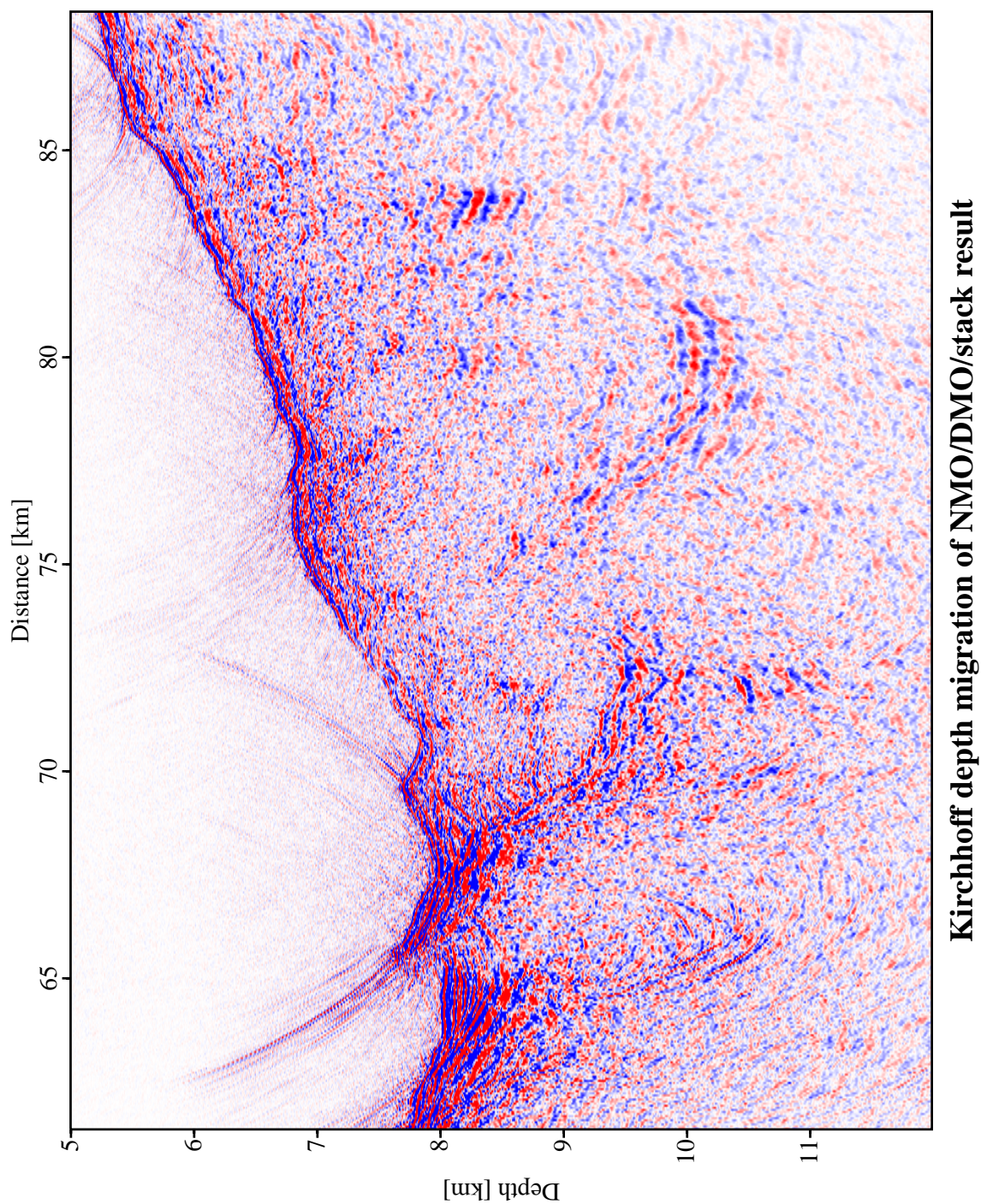


Figure 5.7: CINCA SO104-13 data: Kirchhoff post-stack depth migration of the ZO section shown in Figure 5.4. The smoothed velocity model in Figure 5.6 was used to compute this result.

tions, wavefield attribute sections, and auxiliary results that cannot be completely discussed in this thesis. All unmigrated time-domain results are strongly dominated by the diffraction patterns stemming from the rugged seafloor. As a consequence, the interpretation of the results and their comparison with the conventional results are difficult. For this data set, I focus on the final results of the CRS stack, i. e., the simulated ZO section and the wavefield attribute sections. Results better suited for a comparison with the conventional results will be discussed later on in the Sections 5.3.3 and 5.4.

The basic processing parameters used for the SO104-13 data are compiled in Table 5.2. For this real data set, I used normalized traces, i. e., the original traces divided by the envelope of the associated analytic signal, for the coherence analysis. This removes amplitude variations from trace to trace and relates the coherence analysis closer to the phase information rather than the amplitudes. However, the stack itself is performed with the original traces because the normalization strongly boosts the noise level. As the acquired offset range is quite small compared to the target depth, the chosen CMP aperture is almost constant and limited by the streamer length. The ZO aperture was also chosen relatively small to preserve a high lateral resolution.

The computation times required for the successive processing steps are listed in Table 5.3. As already mentioned in Section 4.2, these times depend on the hardware and software properties (see Appendix F). Comparing the relative CPU times in Tables 4.3 and 5.3, I observe that the computation times also strongly depend on the given acquisition geometry and the chosen ZO and offset apertures. The computation time for the final local optimization step not only depends on the user-given thresholds for optimization, but also on the distribution of the values in the coherence section, i. e., the relative number of ZO samples with reliably detected events in the simulated target zone. Thus, the numerical effort required for this step is hard to estimate in advance.

The final, optimized ZO simulation obtained from the CRS stack is displayed in Figure 5.8. Whenever the attribute-derived projected first Fresnel zone is smaller than the given ZO aperture, the stack was restricted to the projected Fresnel zone, only. Compared to the reference result shown in Figure 5.4, the CRS result provides a higher signal-to-noise ratio and an increased continuity of the imaged events. Only fragments of the top of the subducted oceanic crust can be observed. The steeper flanks of its rugged structure are not illuminated due to the limited streamer length. Possible near-offset reflections from these flanks might only emerge at shot/receiver locations outside the processed subset of the data. Obviously, the various diffraction events stemming from the rugged seafloor intersect the events associated with deeper structures. Most of the related conflicting dip situations were detected, but the improvement of the result due to the separate handling of the contributing events at such locations can hardly be seen from the simulated ZO section itself. They can be seen better in the time-migrated domain as presented in Section 5.3.3. The event in the lower right corner of the target zone is a water-column related multiple of the seafloor. This is obvious from the stacking velocity section (not displayed) where this event is associated with a velocity—due to the dip of the event—slightly above water velocity. There is no need for any attempt to attenuate this multiple as it does apparently not interfere with any detectable primary events.

The coherence section associated with the simulated ZO section is depicted in Figure 5.9. Due to the large dynamic range of the coherence values, only few events stemming from the subsurface

Context	Processing parameter	Setting
General parameters	Dominant frequency	30 Hz
	Coherence measure	Semblance
	Data used for coherence analysis	Normalized traces
	Temporal width of coherence band	20 ms
Velocity and constraints	Near surface velocity	1500 m/s
	Tested stacking velocities	1400 ... 6000 m/s
Target zone	Simulated ZO traveltimes	6.1 ... 14.1 s
	Simulated temporal sampling interval	4 ms
	Number of simulated ZO traces	2167
	Spacing of simulated ZO traces	12.5 m
Aperture and taper	Minimum ZO aperture	900 m @ 6.1 s
	Maximum ZO aperture	900 m @ 14.1 s
	Minimum CMP aperture	2800 m @ 6 s
	Maximum CMP aperture	2952 m @ 14 s
	Relative taper size	30 %
Automatic CMP stack	Initial moveout increment for largest offset	8 ms
	Number of refinement iterations	3
Linear ZO stack	Tested emergence angles	-60 ... 60°
	Initial emergence angle increment	1°
	Number of refinement iterations	3
Hyperbolic ZO stack	Initial moveout increment for largest ZO distance	4 ms
	Number of refinement iterations	3
Hyperbolic CS/CR stack	Initial moveout increment for largest offset	4 ms
	Number of refinement iterations	3
Conflicting dip handling	Maximum number of dips	3
	Absolute coherence threshold for global maximum	0.4
	Relative coherence threshold for local maxima	0.5
Local optimization	Coherence threshold for smallest traveltimes	0.05
	Coherence threshold for largest traveltimes	0.05
	Maximum number of iterations	100
	Maximum relative deviation to stop	10 ⁻⁴
	Initial variation of emergence angles	6°
	Initial variation of R_{NIP}	5 %
	Initial variation of transformed R_N	6°
	Transformation radius for R_N	100 m

Table 5.2: CINCA SO104-13 data: processing parameters used for the ZO simulation by means of the CRS stack.

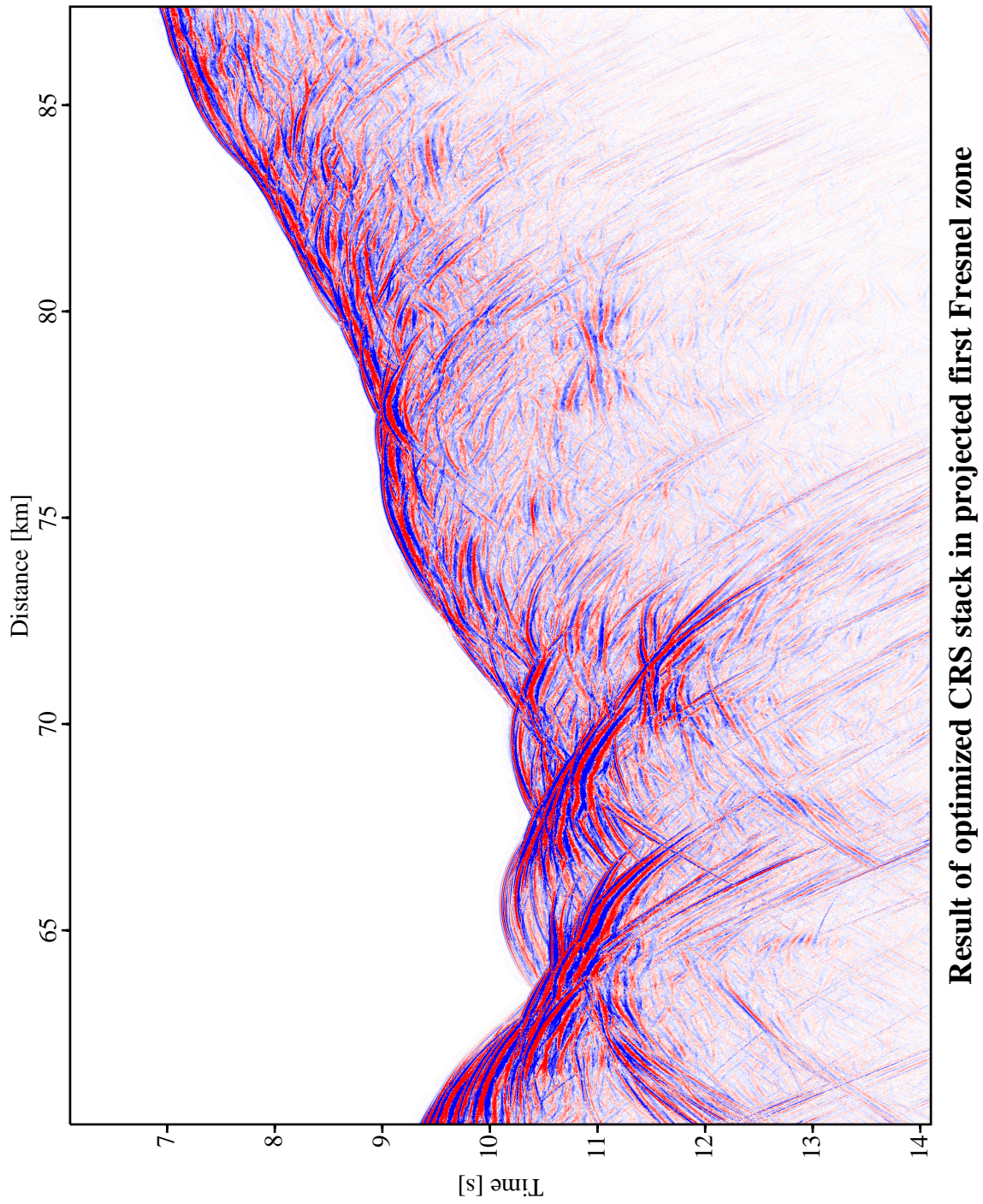


Figure 5.8: CINCA SO104-13 data: result of the optimized CRS stack restricted to the projected first Fresnel zone.

Processing step	absolute CPU time [h]	relative CPU time [%]
Automatic CMP stack	1.1	0.6
Zero-offset stacks	66.9	38.0
Initial stack	10.8	6.1
Local optimization	97.6	55.3
Total	176.4	100.0

Table 5.3: CINCA SO104-13 data: absolute and relative CPU times required for the successive processing steps. All times refer to a 400 MHz Pentium II processor and the processing parameters compiled in Table 5.2.

can be identified in this representation. A similar figure clamped to a smaller range of coherence values (not displayed) reveals further events. The overall quite small coherence values are due to the noise in the data and, possibly, the more or less non-hyperbolic nature of the actual reflection events that was not entirely removed due to wavefront healing.

For the dominant events, i. e., the events associated with the highest coherence at each particular ZO location, the wavefield attributes are depicted in Figures 5.10-5.12. Wherever conflicting dip situations were detected, up to 2 additional sets of wavefield attributes are available. Although these attributes are not displayed here, the stacking operators defined by these attributes also contribute to the simulated ZO section. The consistency of the emergence angle section and the section with the curvature of the normal wavefront (Figures 5.10 and 5.12, respectively) is obvious due to their simple relation to the slopes and curvatures of the events in the simulated ZO section. The section with the radius of curvature of the NIP wavefront (Figure 5.11) is more difficult to interpret: basically, the radius smoothly increases with increasing traveltime. This behavior is over-lain by the diffraction patterns stemming from the seafloor for which the radius increases with increasing distance from the events' apices. The speckled appearance of the attribute sections is caused by the areas without detectable primary events. There, the wavefield attributes have no defined meaning. Their reliability can be estimated by means of the associated coherence values.

5.3 Applications of the wavefield attributes

Two applications of the wavefield attributes were already presented for the synthetic Sigsbee 2A data in Section 4.3: the estimation of the projected first Fresnel zone and the attribute-based time migration. Both applications have to be performed during the stacking process as they cannot be substituted by any post-stack operations.

The estimation of the projected first Fresnel zone is useful for any data set and will therefore be also shown for the SO104-13 data: it adapts the ZO aperture to the local complexity of the wavefield and, thus, increases the lateral resolution of the simulated ZO section. The attribute-based time migration is even more attractive for this particular data, as it provides a migrated image without the need for additional model information. The various diffraction patterns and bow-tie structures are collapsed and allow for an easier interpretation of the result.

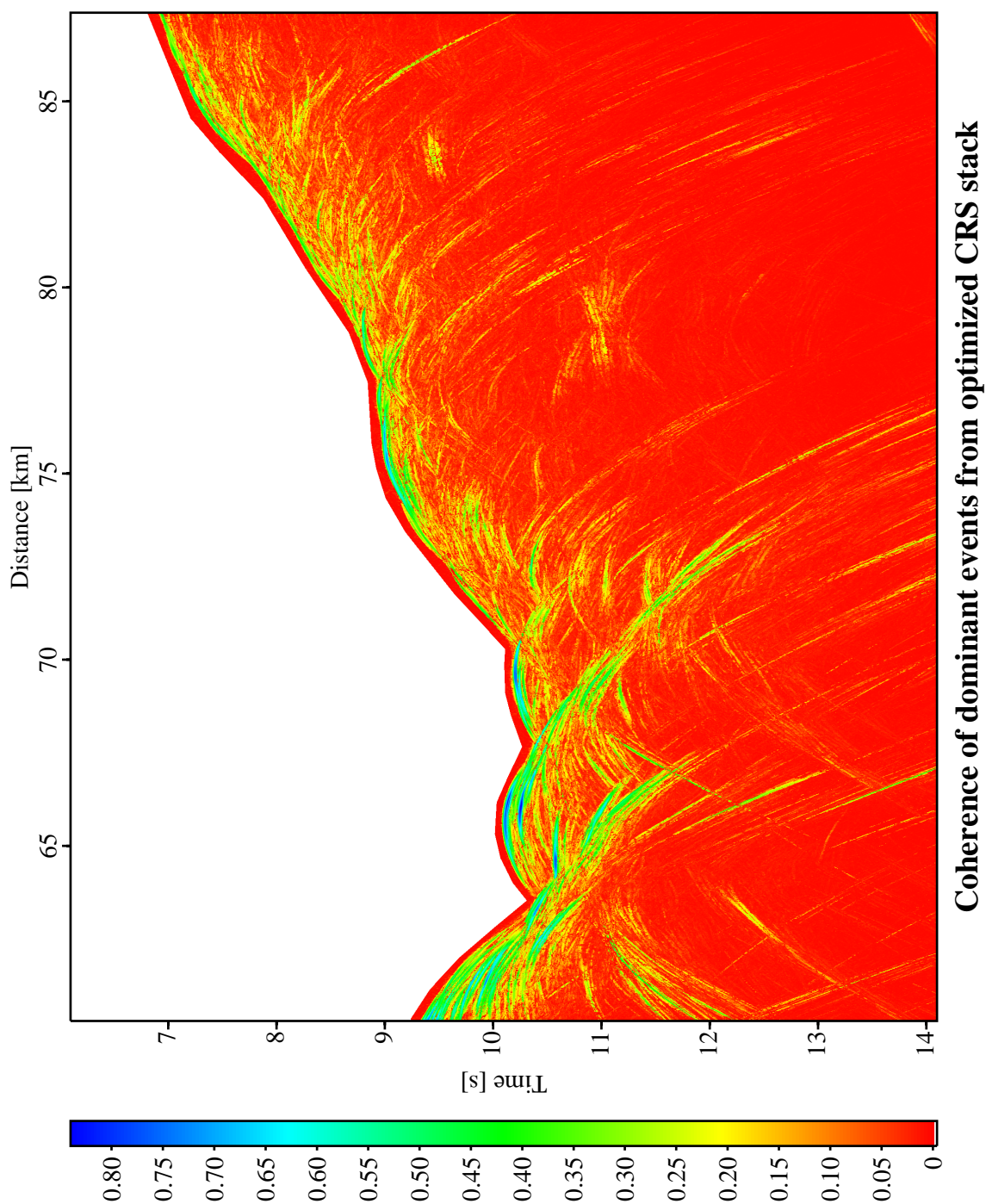


Figure 5.9: CINCA SO104-13 data: coherence section for the dominant events associated with the optimized CRS stack result shown in Figure 5.8. More events can be revealed by clamping the range of the coherence to smaller values.

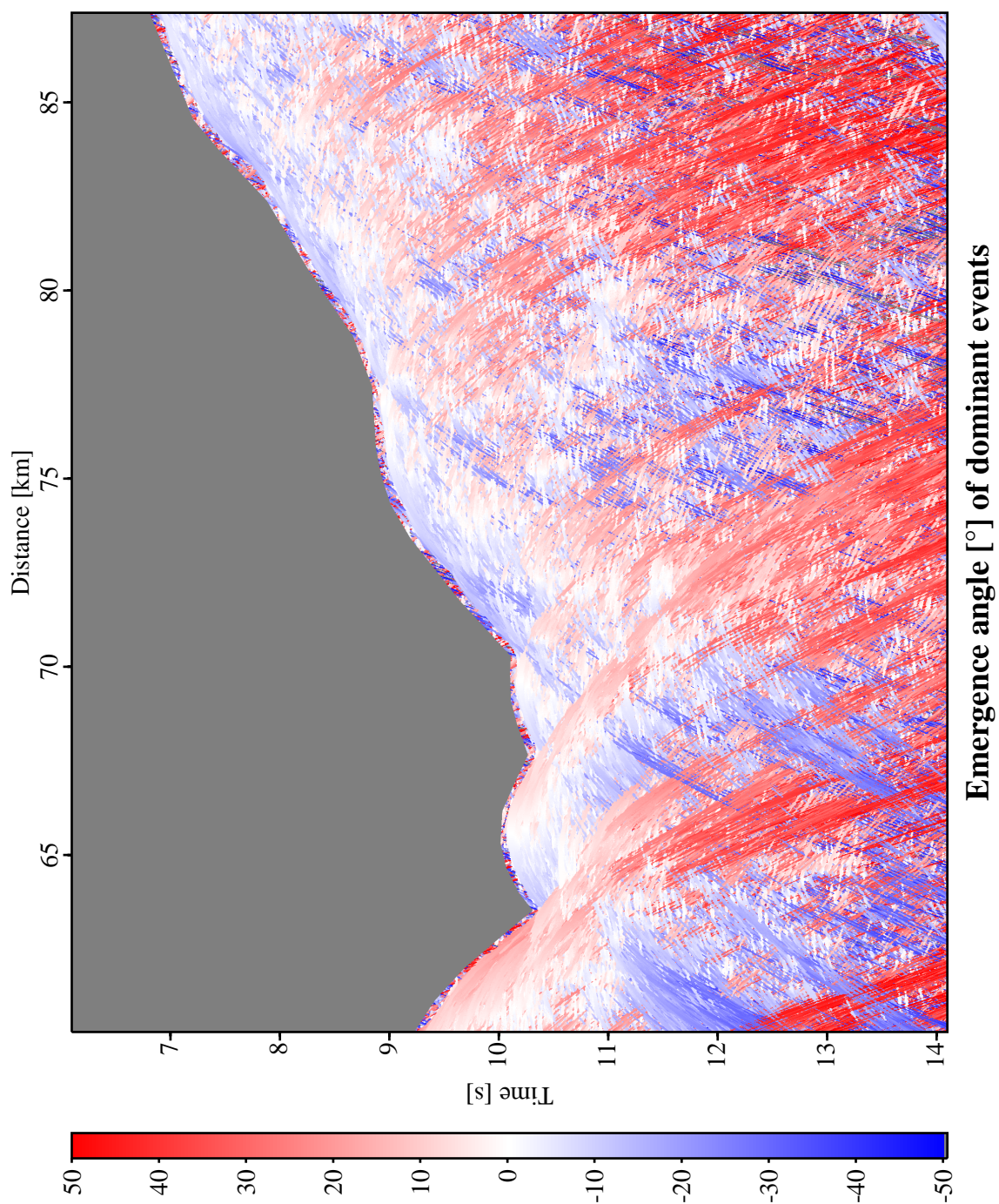


Figure 5.10: CINCA SO104-13 data: emergence angle section for the dominant events associated with the optimized CRS stack result shown in Figure 5.8.

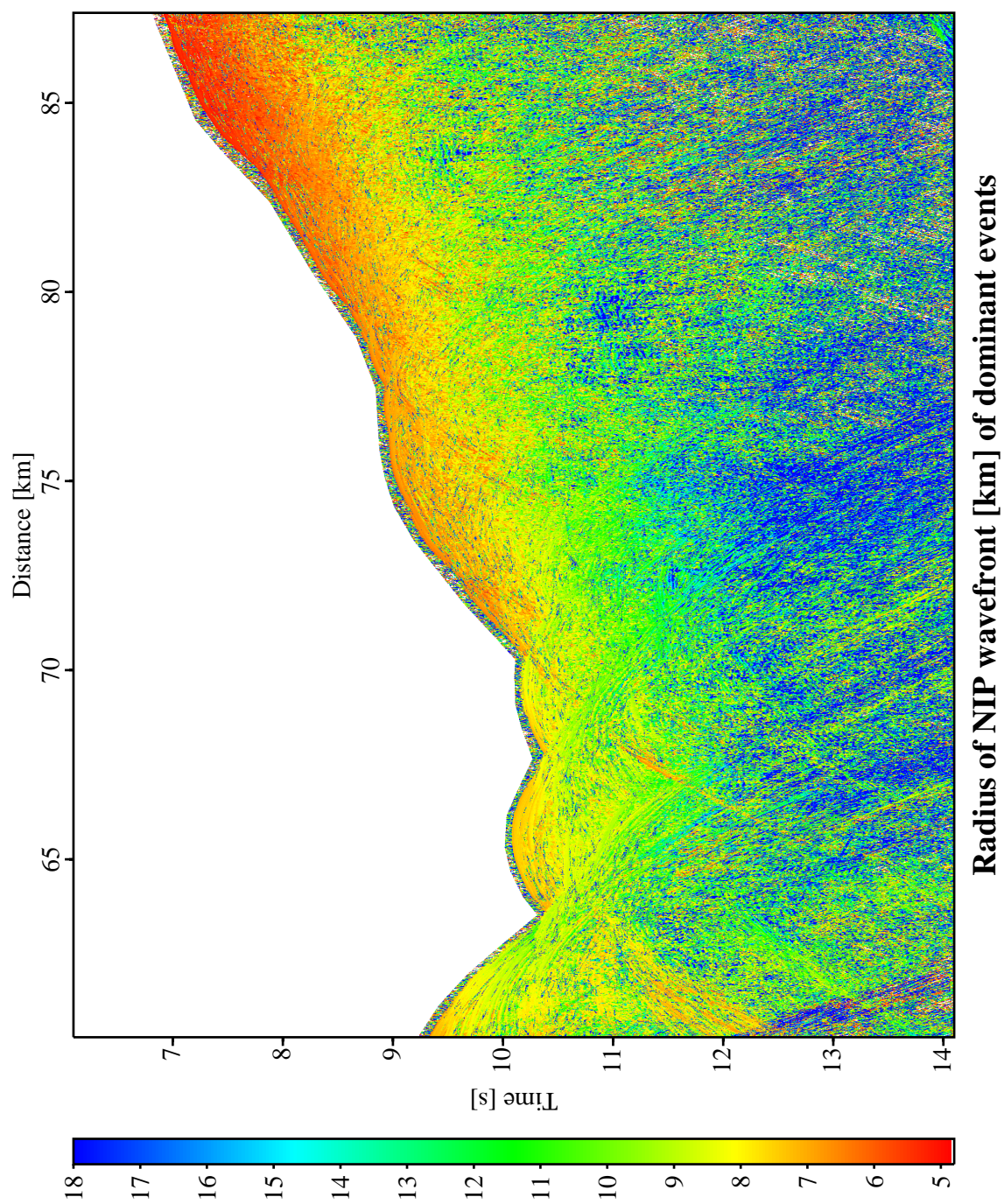


Figure 5.11: CINCA SO104-13 data: radius of curvature of the NIP wavefront for the dominant events associated with the optimized CRS stack result shown in Figure 5.8.

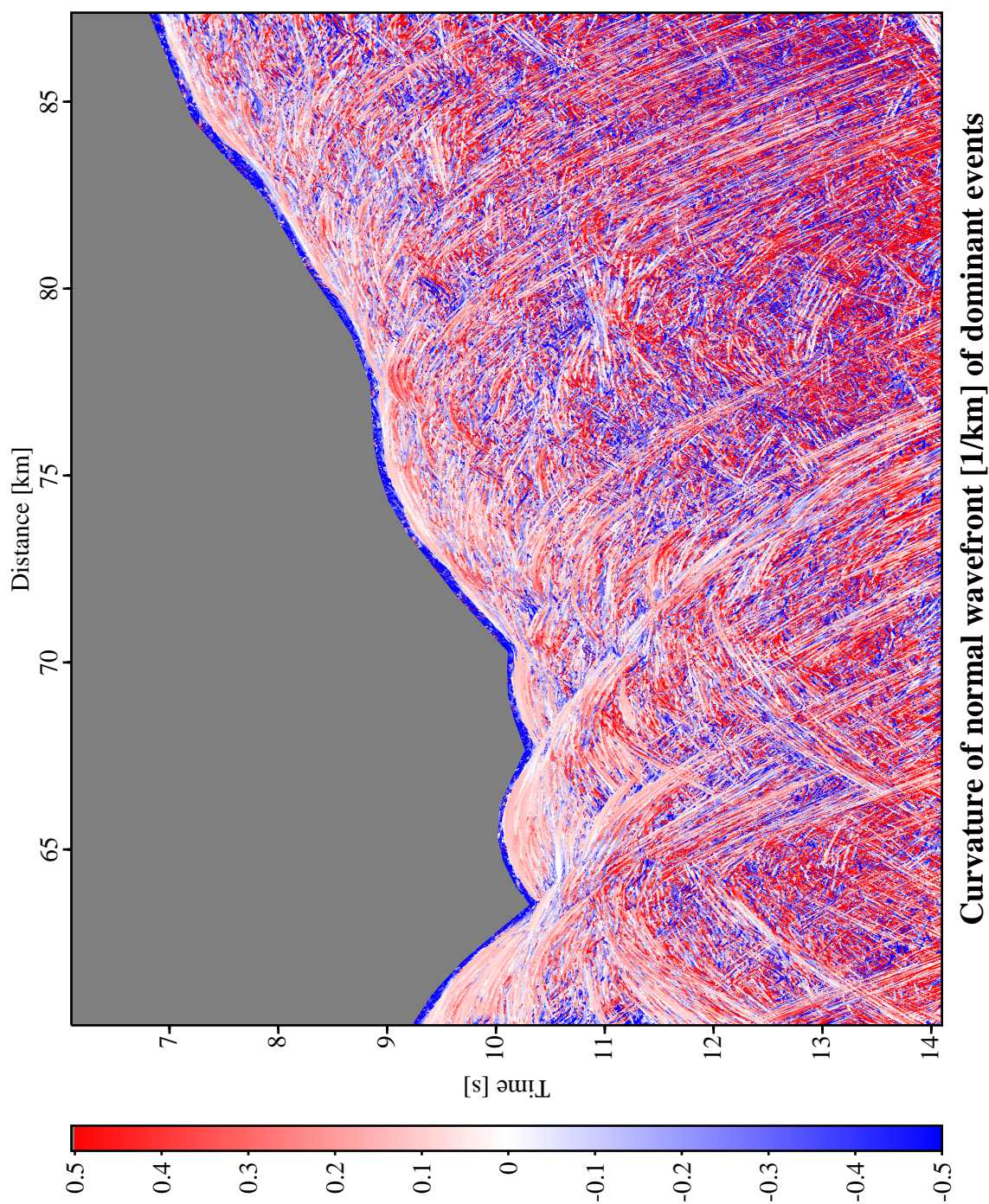


Figure 5.12: CINCA SO104-13 data: curvature of the normal wavefront for the dominant events associated with the optimized CRS stack result shown in Figure 5.8.

Another application of the wavefield attributes was already briefly indicated in the context of conflicting dip handling for the Sigsbee 2A data (Section 4.2.4): the classification of events with respect to the unknown curvature of the associated (and also unknown) reflector segment in depth. This allows to distinguish between reflection events and “diffraction” events. The latter ones are not related to diffractors in a strict sense, but to depth structures with large curvatures compared to the curvatures of the wavefronts that are reflected at them.

5.3.1 Projected first Fresnel zone

The size of the projected first Fresnel zone can be estimated by comparing the traveltimes of the approximated reflection response of a reflector segment in depth and the approximated diffraction response of a diffractor at the same (unknown) location in depth. Both can be expressed in terms of the CRS wavefield attributes (see Section 2.7). As already discussed for the synthetic Sigsbee 2A data in Section 4.3.1, the projected first Fresnel zone is not only suited as ZO aperture for the stack, but also to check the appropriate choice of the user-given ZO aperture.

The projected Fresnel zone is shown in Figure 5.13 relative to the user-given ZO aperture. The given aperture serves as upper limit for the actual stack to a) simplify the implementation and b) to account for the fact that the CRS operator is an approximation of the actual reflection response: according to its definition in Section 2.7, the size of the projected Fresnel zone is infinite for diffraction events in a strict sense and very large for strongly curved reflector segments. However, this does not imply that the CRS stacking operator approximates the respective events with sufficient accuracy inside an arbitrary large aperture.

For the majority of the simulated ZO samples depicted in Figure 5.13, the user-given ZO aperture is about 2-4 times larger than the estimated projected first Fresnel zone, a ratio that turned out to be appropriate for the determination of the attributes. Along strongly curved events, e. g., the seafloor event with its diffraction patterns, the ratio is—as expected—significantly higher.

5.3.2 Classification of events

According to the hypothetical experiments introduced in Section 2.1.2 that relate the CRS wavefield attributes to the properties of the associated (unknown) reflector segment in depth, the radii of curvature of the NIP and normal wavefront coincide for diffractors in depth. Thus, R_N and R_{NIP} allow to identify events stemming from strongly curved subsurface features usually considered as diffractors, of course not in the strict sense of a “point” diffractor.

A possible way to represent this feature is to calculate the ratio of R_N and R_{NIP} . A hypothetical ideal diffractor should yield a ratio of 1. However, a more comprehensive result can be obtained by considering the absolute value of R_N only, i. e., the ratio $|R_N|/R_{NIP}$ as shown in Figure 5.14: ideal diffraction events are still associated with a ratio of 1, but changes in the sign of R_N no longer lead to discontinuous images of the events. Figure 5.14 reveals that not all of the imaged steep events are related to diffractors in the depth, but also to steep “reflectors”, i. e., subsurface structures with comparatively small curvatures. Both kinds of events appear very similar and interfere with each

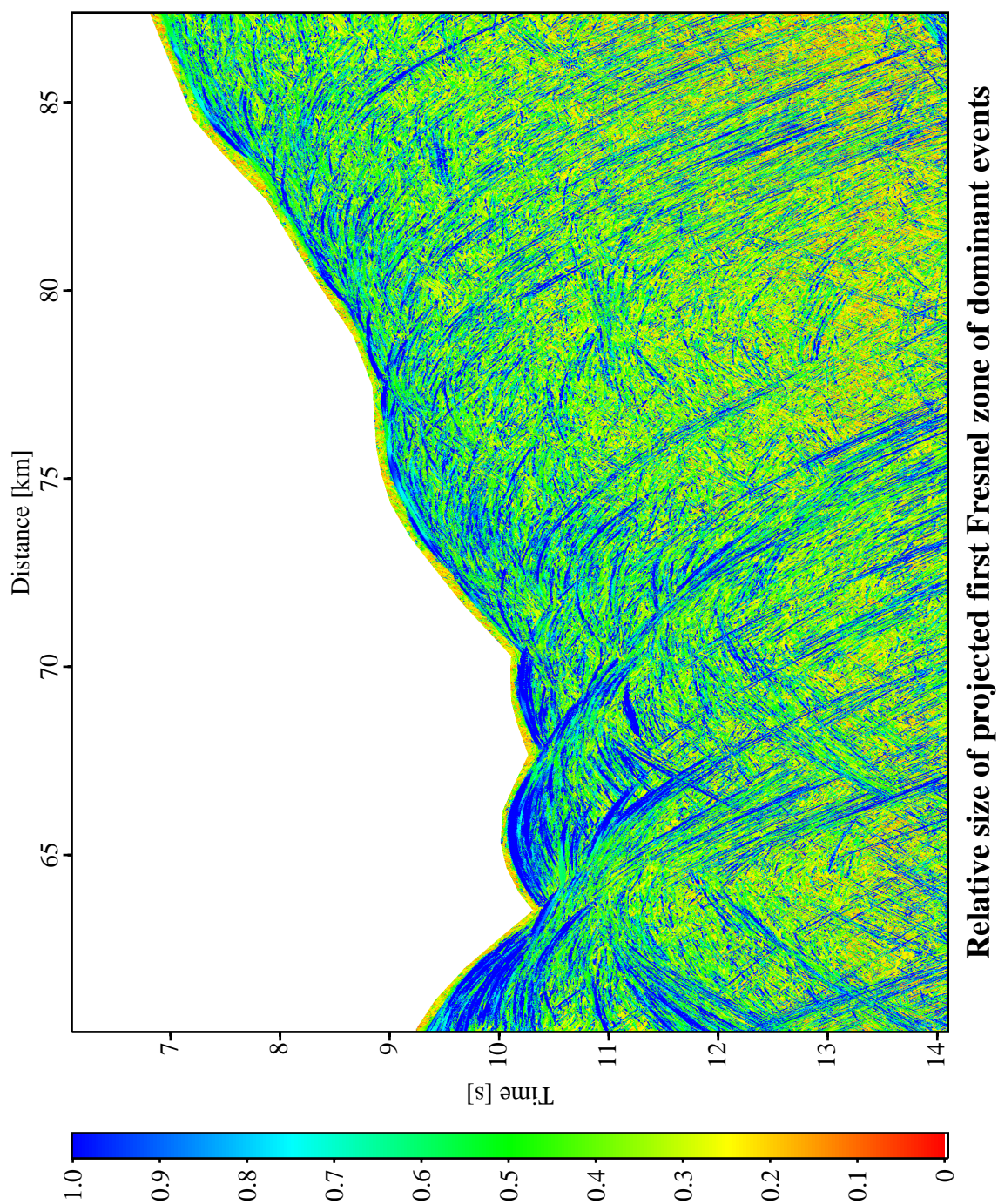


Figure 5.13: CINCA SO104-13 data: size of the projected first Fresnel zone of the dominant events relative to the given ZO aperture. The displayed range of this ratio is clamped to a maximum of 1.

other. Without the wavefield attributes, it is almost impossible to distinguish them in the simulated ZO section. The ratio of the radii of curvature might be used for a weight function during the stack to emphasize the diffraction patterns compared to the reflection events, or vice versa. Please note that Figure 5.14 does not represent the entire available information for such an approach, but separate curvature ratios are available at locations where conflicting dip situations have been detected.

Again, I would like to emphasize that there is no sharp separation between “reflection” and “diffraction” events, as the curvature along a subsurface structure might change continuously. This applies, e. g., for the events stemming from the rugged seafloor: the ratio $|R_N|/R_{NIP}$ continuously changes from reflection type values far from 1 to diffraction type values close to 1. Most of the reflections events are associated with a ratio larger than 1. Ratios below 1 occur at locations where either a) no events have been detected (and the attributes are meaningless) or b) the normal wavefront passes a caustic on its way up to the acquisition line. In the latter case, the normal wavefront might start with a negative curvature at the reflector (concave reflector segment) and/or might be focused on its way to the surface due to the structure of the overburden.

5.3.3 Attribute-based time migration

The CRS wavefield attributes are suited to approximate the image location for a time migration associated with a particular simulated ZO location. This approach was discussed in Section 2.6 and demonstrated for the synthetic Sigsbee 2A data in Section 4.3.2. Considering the various steep and extended diffraction patterns in the SO104-13 data, the attribute-based time migration is very useful to collapse such features and to obtain a result that is more similar to the actual structures in depth. The time-migrated section is generated as a by-product of the CRS stack by simply re-mapping the stacking results from the simulated ZO location to the approximated image location of a time migration, i. e., the apex of the Kirchhoff migration operator.

The result of the attribute-based time migration for the SO104-13 data is depicted in Figure 5.15. The ZO aperture was restricted to the projected first Fresnel zone estimated from the attributes, with the user-given aperture as upper limit. I observe that all diffraction patterns are completely collapsed. The image of the seafloor is now continuous and fragments of the event stemming from the top of the oceanic plate can be identified. This event is better defined than in the constant velocity Stolt migration result of the conventional ZO simulation shown in Figure 5.5. However, the attribute-based result appears very speckled. This is due to the fact that every ZO sample is mapped to its new image location completely independently of the neighboring samples. The wavefield attributes slightly fluctuate along the events, and so do the approximated image locations. As a consequence, the migrated image points are scattered on a small scale. Nevertheless, they form continuous events on a larger scale. In contrast, a migration based on a smooth (or even constant) velocity model always maps a continuous event in the unmigrated domain into a continuous one in the migrated domain. By smoothing the attributes before the migration step, the speckled appearance could be removed—with a loss of resolution in the attributes.

Please note that the result shown in Figure 5.5 is only intended to provide a first idea of the subsurface structures. Without a smoothing of the wavefield attributes and/or a low-pass filtering

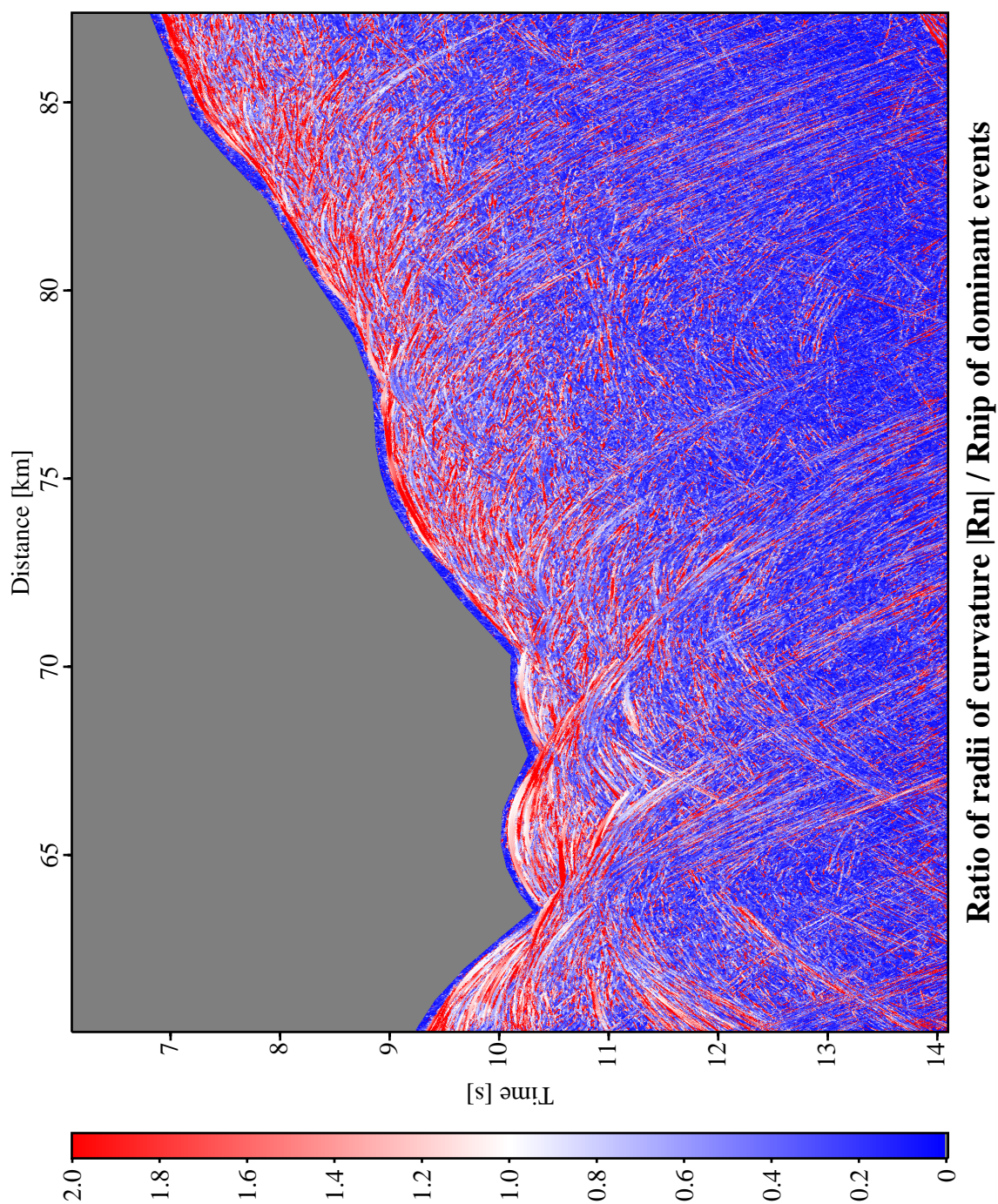


Figure 5.14: CINCA SO104-13 data: ratio of the radii of curvatures $|R_N|/R_{NIP}$ of the dominant events. An ideal diffraction event yields a ratio of 1.

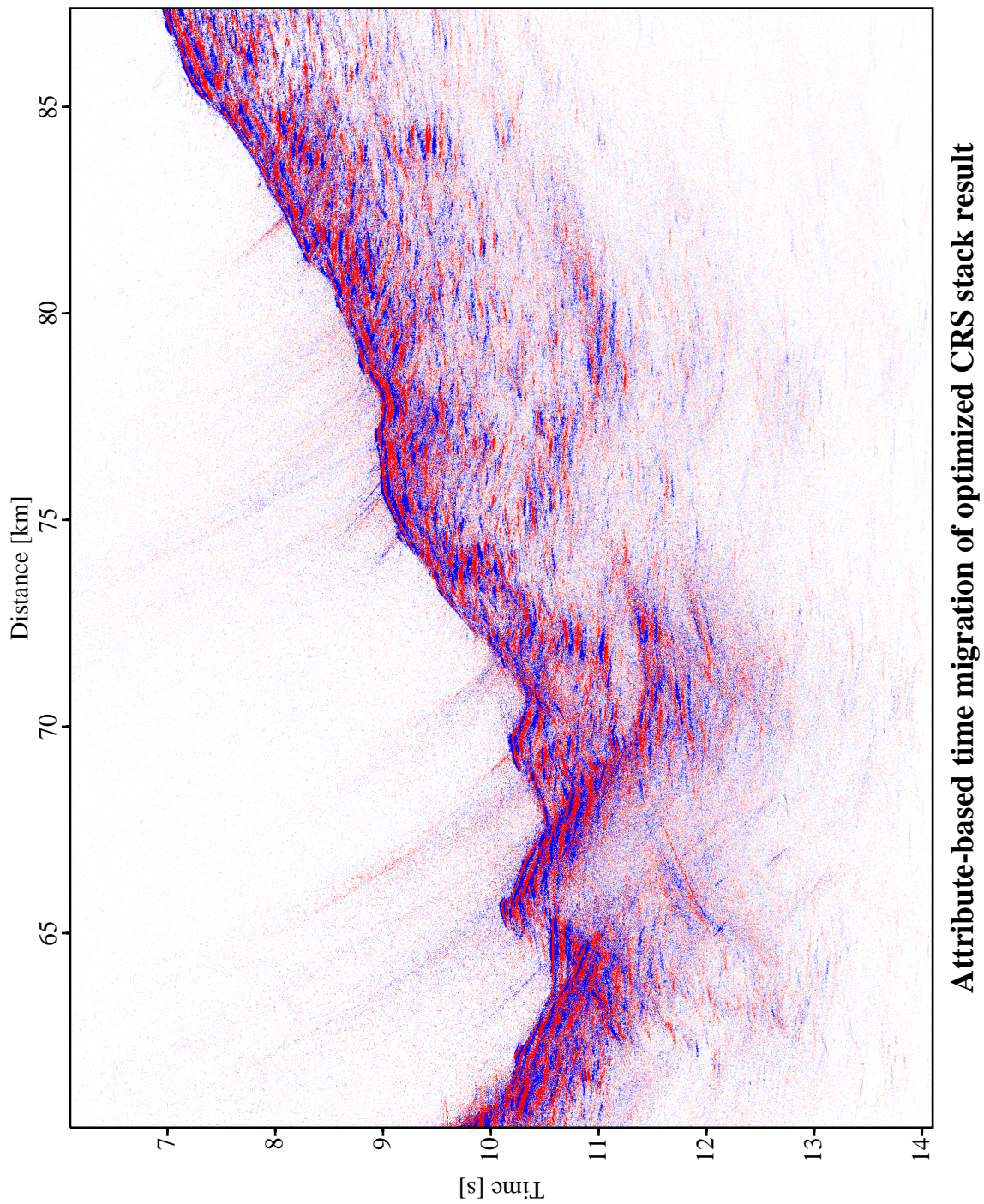


Figure 5.15: CINCA SO104-13 data: attribute-based time migration of the optimized CRS stack result shown in Figure 5.8. The ZO aperture was restricted to the projected first Fresnel zone.

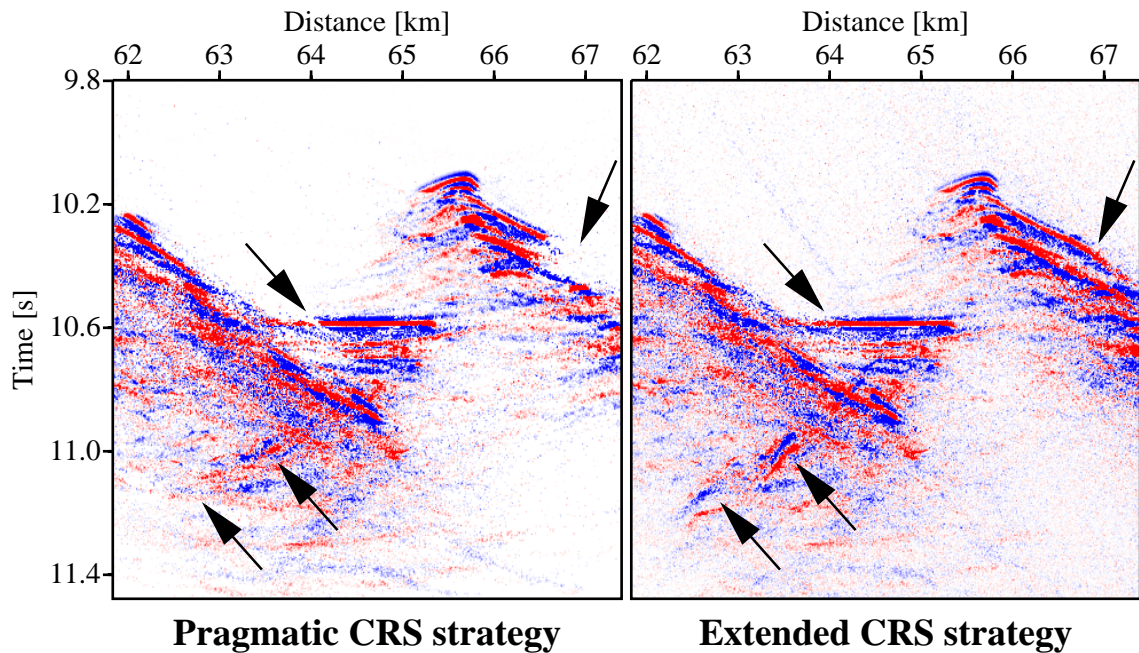


Figure 5.16: CINCA SO104-13 data: a detail of the attribute-based time migration of the optimized CRS stack result computed with the pragmatic CRS strategy (left) and the extended CRS strategy (right). The arrows indicate the major differences.

to remove the artificial high frequency speckles, the result is hardly suited for further processing like a subsequent time to depth transformation.

In the unmigrated time-domain results of the CRS stack, it is almost impossible to observe the influence of the conflicting dip handling according to the extended CRS stack strategy. However, in the time-migrated result this influence is clearly visible: in Figure 5.16 I depicted a subset of the time-migrated section shown in Figure 5.15 computed with the pragmatic CRS strategy and the extended CRS strategy, respectively. Several events can only be observed in the latter case, i. e., if I explicitly account for conflicting dip situations. This again demonstrates the advantages of the extended CRS strategy.

5.4 Post-stack depth migration

For the final comparison of the results obtained by means of the conventional NMO/DMO/stack chain and the CRS results, I applied a Kirchhoff post-stack depth migration to the optimized CRS stack result shown in Figure 5.8. The migration is based on the same GFT and parameters used for the depth migration of the NMO/DMO/stack result presented in Section 5.1. The migration result depicted in Figure 5.17 substantially differs from the reference result, especially the top of the oceanic crust is better defined in the CRS-based result. The areas showing the most significant difference between both results are marked by boxes.

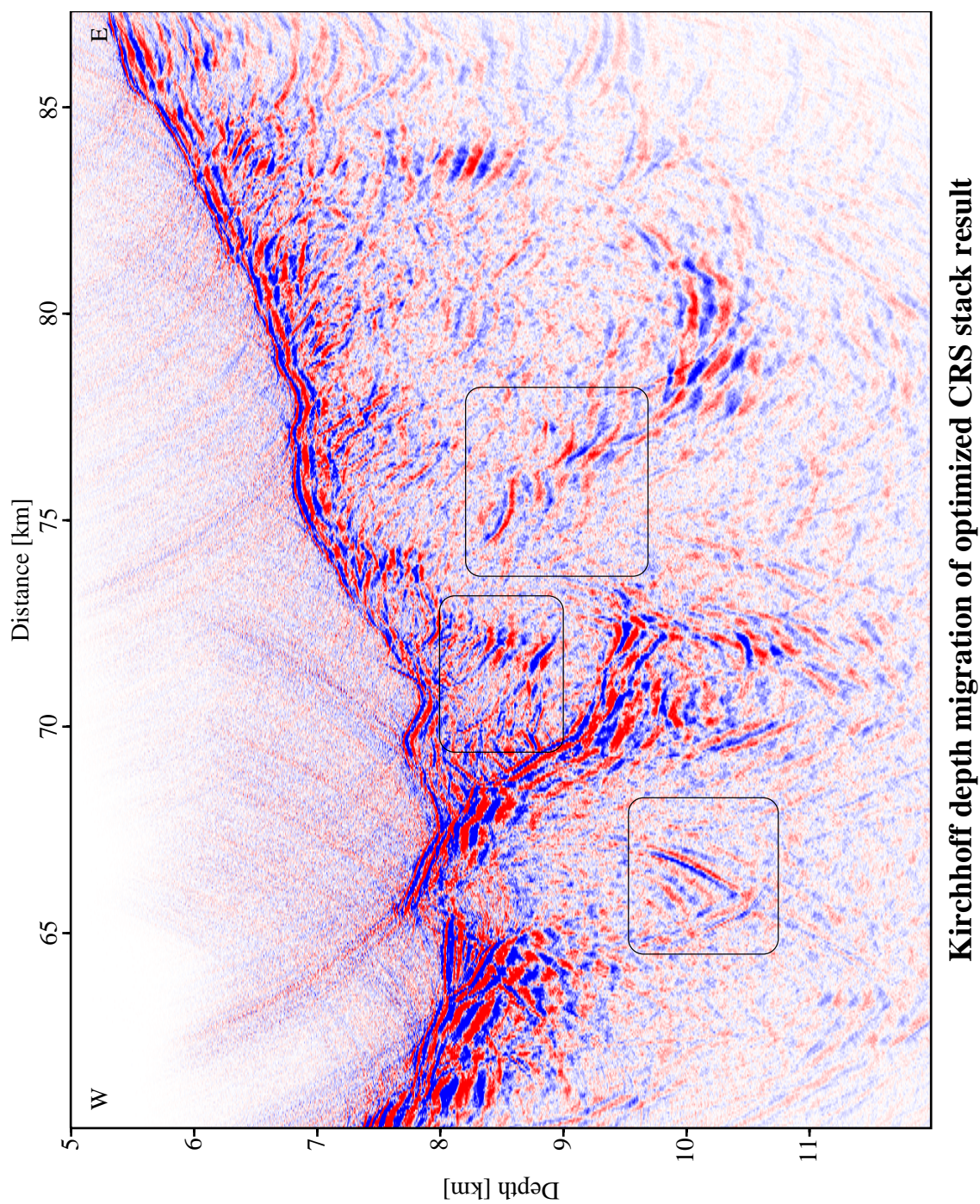


Figure 5.17: CINCA SO104-13 data: post-stack depth migration of the optimized CRS stack result shown in Figure 5.8. Some areas with the most significant differences compared to the reference result (Figure 5.7) are marked with boxes.

I would like to emphasize again that the model used for the calculation of the GFT was built by means of iterative pre-stack depth migration. Neither the stacking velocities obtained from the NMO/DMO/stack chain nor the CRS wavefield attributes were considered for this model. In other words, the model was obtained independent of the two processing methods compared here and, thus, was not tuned to improve the results obtained from one of these two methods.

A further aim of the CRS stack approach is to derive the macro-velocity model from the wavefield attributes instead of using a model obtained by means of other methods. However, such an inversion is beyond the scope of this thesis. Examples of the inversion of CRS wavefield attributes assuming a model set up by homogeneous layers separated by arbitrarily curved interfaces can be found in Majer (2000).

5.5 Conclusions

The application of the CRS stack to the marine CINCA SO104-13 data yields results that substantially differ from the conventional results obtained by means of the NMO/DMO/stack processing chain. However, the comparison and interpretation of the results is very difficult in the unmigrated time domain: the data is dominated by a multitude of steep events, most of them stemming from the rugged seafloor. As a consequence, the wavefield attribute sections are also quite complicated. Nevertheless, they provide useful information to classify the events and to perform an attribute-based time migration that yields a result much more similar to the actual depth structure than the simulated ZO section. As I did not smooth or filter the fluctuating wavefield attributes for this migration approach, the result appears speckled on a small scale, but continuous events can still be identified.

In the time-migrated result obtained with the pragmatic and the extended CRS strategy, respectively, I observe a significant improvement of the result in the latter case. This again demonstrates that the explicit handling of conflicting dips situations is advantageous for the post-stack processing of the simulated ZO section as well as for applications of the wavefield attributes. This applies for this data set although the differences due to the two CRS strategies can hardly be observed in the unmigrated time-domain results.

For a final comparison of the two different ZO simulations, I applied a model-based Kirchhoff post-stack depth migration to both results. The depth-migrated images show substantial differences that can hardly be observed in the unmigrated time domain. To allow for a fair comparison, I used a model for the migration that was derived neither from the NMO velocities of the NMO/DMO/stack chain nor from the CRS wavefield attributes. The CRS-based result contains several events that are difficult to identify in conventional result: especially the top of the oceanic crust is better defined in the CRS results.

Chapter 6

Real data example: BGR99-07

6.1 Data acquisition and pre-processing

The seismic line BGR99-07 was acquired off-shore Costa Rica in 1999 by the seismic vessel *Prof. Polshkov*. During the entire cruise BGR99 a total seismic line length of 3004 km was acquired for the Federal Institute for Geoscience and Natural Resources (BGR), Germany. One of the research aims was to provide a seismic survey in the vicinity of a proposed ocean drilling project (ODP) site. The location of the entire line BGR99-07 is displayed in Figure 6.1. The line covers the Middle America trench that separates the Cocos plate and the Caribbean plate. I compiled the acquisition parameters of the data subset presented in this thesis in Table 6.1. The data were recorded with a digital 360 channel streamer with a length of 4.5 km.

The CMP fold distribution of the processed subset of the BGR99-07 data is depicted in Figure 6.2. The acquisition geometry is almost regular, therefore the locations of the shot and receiver pairs are not displayed for these data.

The pre-processed pre-stack data, the conventional result obtained from the NMO/DMO/stack processing chain, and an f-k domain time migration (see, e. g., Yilmaz, 1987) of the latter result were provided by the BGR. The conventional processing result serves as reference for the CRS-based results. The pre-stack data was pre-processed with bandpass filtering, spherical divergence correction, and predictive deconvolution. The ZO simulation obtained from the conventional NMO/DMO/stack chain is displayed in Figure 6.3. To account for the strong variations of the amplitudes, I applied an automatic gain control (AGC) within a time window of 0.5 s. A Gaussian taper was applied inside this time window. This kind of representation also reveals the weaker events. However, the original amplitude information is lost.

The f-k domain time migration of the conventional result is displayed in the same way in Figure 6.4. In contrast to the two other data sets presented in this thesis, the BGR99-07 data contain strong water-column related multiples interfering with primary events stemming from the subsurface. Especially at the proposed ODP site with a target depth of about 1100 m below the seafloor, the multiple stemming from the seafloor intersects the event stemming from the top of the Cocos

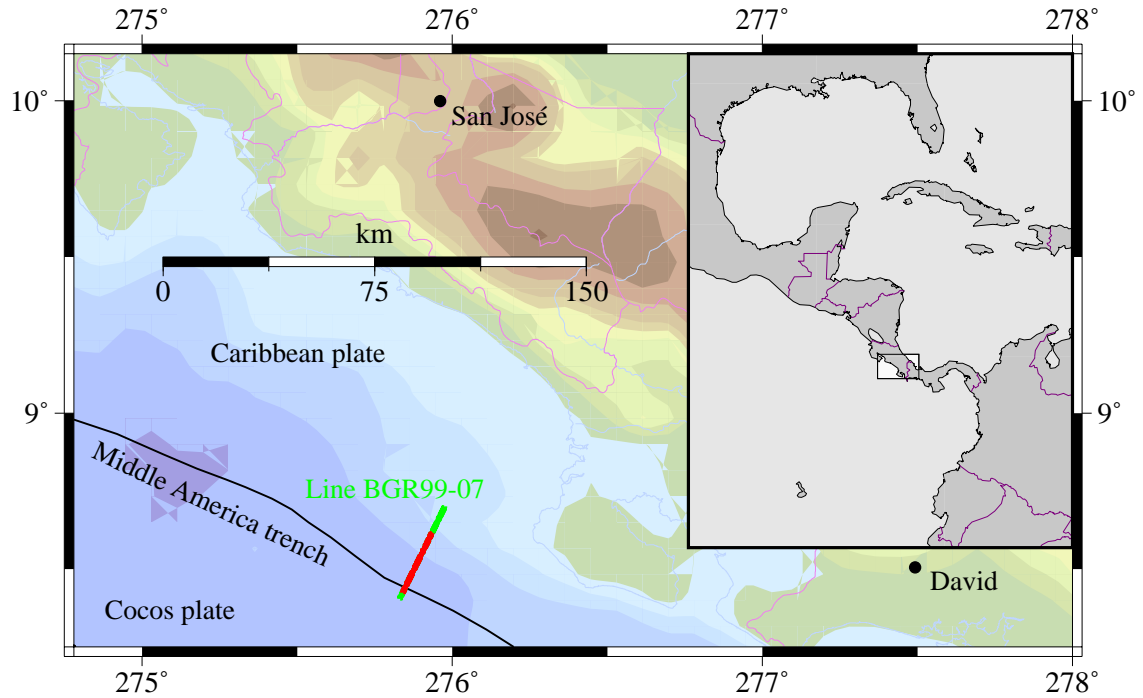


Figure 6.1: BGR99-07 data: location of the acquisition line. The shot locations of the entire line are shown in green, the subset processed for this thesis is depicted in red. The actual coastline is depicted as light blue line. The colored topography deviates from the coastlines due to its low resolution. The streamer was towed from north-east to south-west.

Shot and receiver geometry		Midpoint and offset geometry	
Number of shots	480	Number of CMP bins	3500
Shot interval	50 m	Maximum CMP fold	49
Number of receivers	360	CMP bin interval	6.25 m
Receiver interval	12.5 m	Offset range	141 ... 4607 m
Recording parameters		Frequency content	
Recording time	6 s	Dominant frequency	n/a
Sampling interval	4 ms	Maximum frequency	50 Hz

Table 6.1: BGR99-07 data: acquisition parameters of the pre-stack data set. The provided data represent a subset of the complete acquisition line. Due to the applied deconvolution no dominant frequency can be determined.

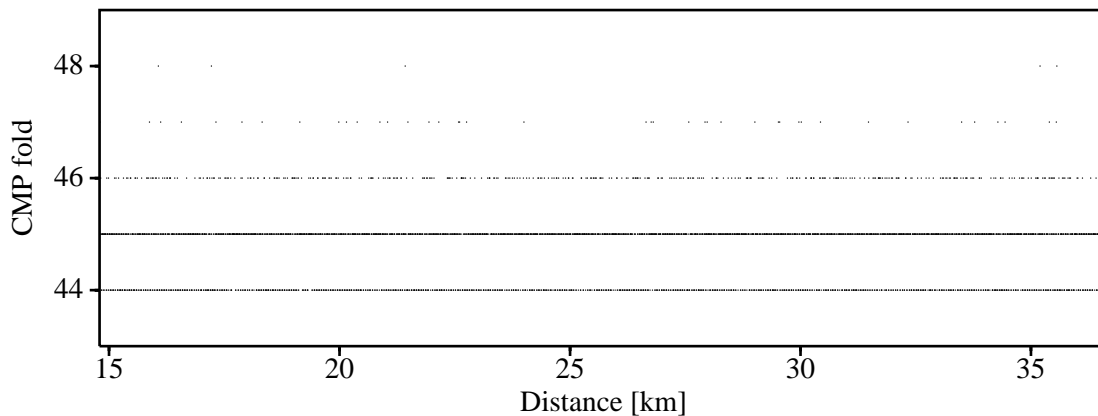


Figure 6.2: BGR99-07 data: CMP fold of pre-stack data traces. The locations of the pre-stack traces are not displayed due to the limited printable resolution. The acquisition geometry is almost regular. The midpoint coordinate increases in the towing direction of the streamer, i. e., from north-east to south-west.

plate. Below the seafloor event, an event associated with a so-called *bottom simulating reflector* (BSR) can be observed. This event is caused by gas hydrates in the subsurface: gas hydrates exhibit relatively high elastic velocities (see, e. g., Stoll, 1974; Tucholke et al., 1977) and are only stable within a small temperature and pressure range. The lower boundary of this region of stability acts as a trap for free gas that reduces the elastic velocities. Consequently, the lower boundary of the gas hydrates represents a negative impedance contrast in the subsurface. The associated event can be easily identified by the inverse polarity of the seismic wavelet and its almost constant time offset with respect to the seafloor event.

In Figures 6.3 and 6.4, I observe significant variations of the dominant frequency of the events: the central lobe of the primary event stemming from the seafloor has a width of ≈ 16 ms, whereas for the event stemming from the top of the Cocos plate I observe a width of ≈ 64 ms. This affects any processing algorithms that assume a more or less constant frequency content in the data. Such strong variations were not observed in the two other data sets presented in this thesis.

6.2 Application of the CRS stack

For the BGR99-07 data, I have to face two phenomena that are not or only partly present in either the synthetic Sigsbee 2A data or the marine CINCA SO104-13 data presented in the preceding chapters: strong multiple events interfering with much weaker primary events and a strong variation of the frequency content. The former phenomenon can be addressed in the CRS stack to some extent by introducing appropriate constraints for the tested stacking velocities. Therefore, the result of the automatic CMP stack with and without constraints will be discussed in detail, followed by the final CRS results.

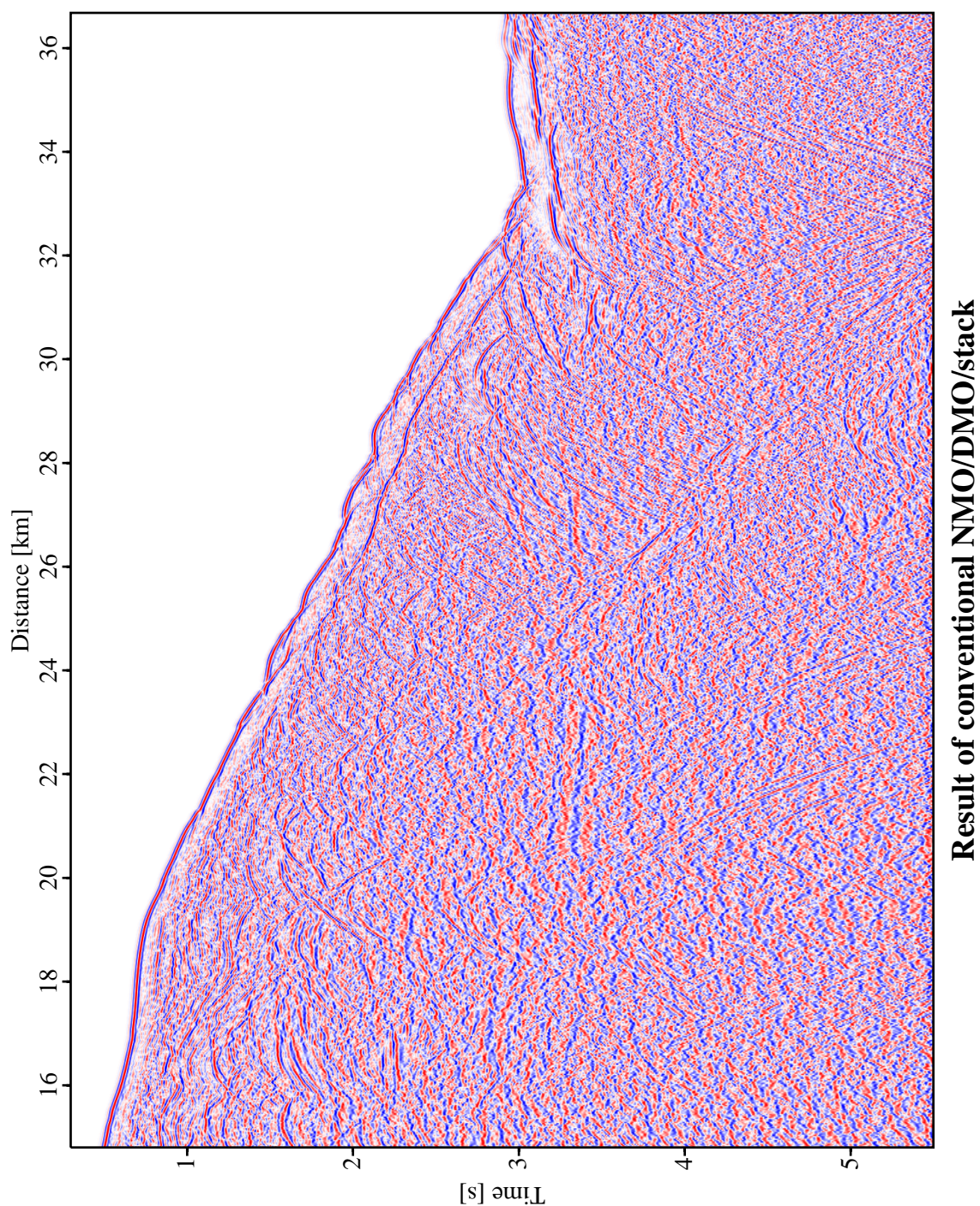


Figure 6.3: BGR99-07 data: ZO simulation obtained from the conventional NMO/DMO/stack processing chain. An automatic gain control with 0.5 s window width and a Gaussian taper was applied to reveal weak events.

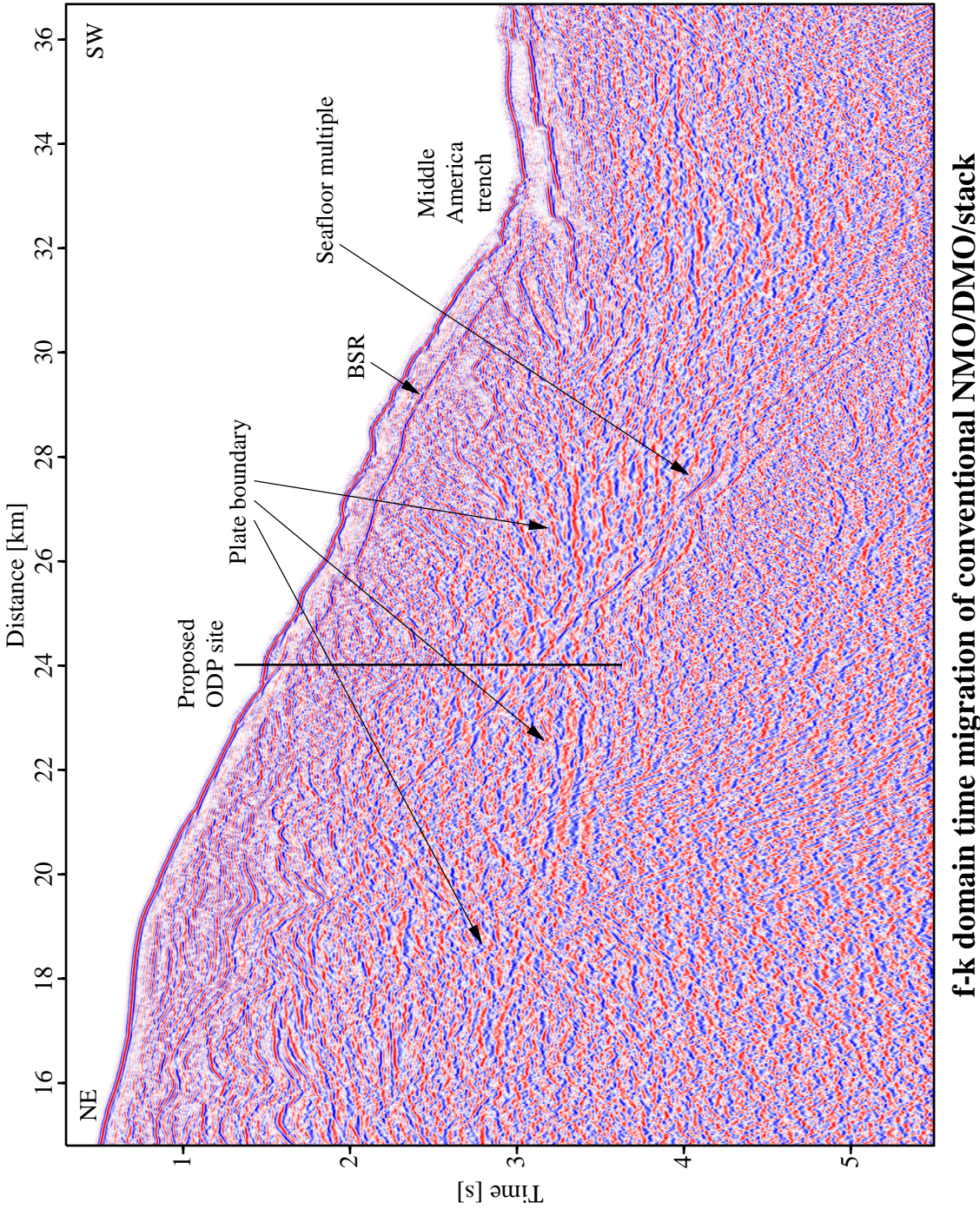


Figure 6.4: BGR99-07 data: f-k domain time migration result of the ZO section shown in Figure 6.3. An automatic gain control with 0.5 s window width and a Gaussian taper was applied to reveal weak events.

The processing parameters used for these data are compiled in Table 6.2. Due to the varying frequency content of the data, there is no obvious way to select appropriate values for the dominant frequency (which affects the size of the ZO aperture) and the temporal width of the coherence band. A too low selected frequency generates large ZO apertures, a loss of lateral resolution, and increased computational costs. A large coherence band also increases the required computational effort and reduces the temporal resolution. On the other hand, if the coherence band is chosen too small, low frequency events will be split into separate coherent events associated with the different lobes of the wavelet. The latter case appears to be less critical, therefore I decided to choose parameters appropriate for the high frequency events.

The processing times required for the successive processing steps are compiled in Table 6.3. Again, they strongly depend on the chosen processing parameters and the implementation. The specification of the used hard- and software can be found in Appendix F.

6.2.1 Automatic CMP stack and multiple attenuation

In a first processing iteration¹, I applied the automatic CMP stack within a stacking velocity range of 1400...5000 m/s that should be sufficient to detect any reasonable hyperbolic event in the CMP gathers. This velocity range was applied to all ZO locations, irrespective of their coordinates. In other words, I made no attempt to attenuate any multiples at this stage by means of velocity constraints. Thus, I refer to this processing step as the *unconstrained* automatic CMP stack.

The simulated ZO section from the unconstrained automatic CMP stack is displayed in Figure 6.5. No AGC was applied for this representation to preserve the original amplitudes. For larger traveltimes, the multiples of the seafloor event and the BSR event are by far stronger than any primary event. Both can be easily identified in the associated stacking velocity section shown in Figure 6.6: the stacking velocity along the multiple events is significantly lower than for neighboring events. This significant moveout differences between multiple and primary events not only allow to identify the multiples but also bear the potential to attenuate the multiple events by introducing constraints on the stacking velocities to be tested.

The attenuation of the multiples strongly increases the probability that the extended CRS stack strategy detects and characterizes primary events interfering with the multiples. Therefore, I picked the traveltimes associated with the seafloor multiple event by means of a joint interpretation of the CMP stacked section and the stacking velocity section. Afterwards, these traveltimes were reduced by about twice the dominant period of the wavelet to ensure that all multiple events are located beyond them. I used these traveltimes to set up a simple model (not displayed) for the smallest stacking velocity to be tested: for traveltimes below the picked traveltimes, I assigned a minimum stacking velocity of 1400 m/s. For the remaining ZO locations, a minimum stacking velocity of 1775 m/s was chosen.

I again generated the CMP stacked section but now considering the built minimum stacking velocity model instead of a constant minimum stacking velocity for all ZO locations. I refer to this

¹This first processing iteration is not included in the CPU times listed in Table 6.3. As the tested stacking velocity range for the unconstrained automatic CMP stack is larger than for its constrained counterpart referred to in Table 6.3, it requires slightly more CPU time.

Context	Processing parameter	Setting
General parameters	Dominant frequency	30 Hz
	Coherence measure	Semblance
	Data used for coherence analysis	Normalized traces
	Temporal width of coherence band	28 ms
Velocity and constraints	Near surface velocity	1500 m/s
	Tested stacking velocities	Model ... 5000 m/s
Target zone	Simulated ZO traveltimes	0.3 ... 5.5 s
	Simulated temporal sampling interval	4 ms
	Number of simulated ZO traces	3500
	Spacing of simulated ZO traces	6.25 m
Aperture and taper	Minimum ZO aperture	135 m @ 0.3 s
	Maximum ZO aperture	806 m @ 5.5 s
	Minimum CMP aperture	500 m @ 0.3 s
	Maximum CMP aperture	4000 m @ 5.5 s
	Relative taper size	30 %
Automatic CMP stack	Initial moveout increment for largest offset	8 ms
	Number of refinement iterations	3
Linear ZO stack	Tested emergence angles	-60 ... 60°
	Initial emergence angle increment	1°
	Number of refinement iterations	3
Hyperbolic ZO stack	Initial moveout increment for largest ZO distance	4 ms
	Number of refinement iterations	3
Hyperbolic CS/CR stack	Initial moveout increment for largest offset	4 ms
	Number of refinement iterations	3
Conflicting dip handling	Maximum number of dips	3
	Absolute coherence threshold for global maximum	0.4
	Relative coherence threshold for local maxima	0.3
Local optimization	Coherence threshold for smallest traveltime	0.01
	Coherence threshold for largest traveltime	0.003
	Maximum number of iterations	100
	Maximum relative deviation to stop	10 ⁻⁴
	Initial variation of emergence angles	6°
	Initial variation of R_{NIP}	5 %
	Initial variation of transformed R_N	6°
	Transformation radius for R_N	100 m

Table 6.2: BGR99-07 data: processing parameters used for the ZO simulation by means of the CRS stack.

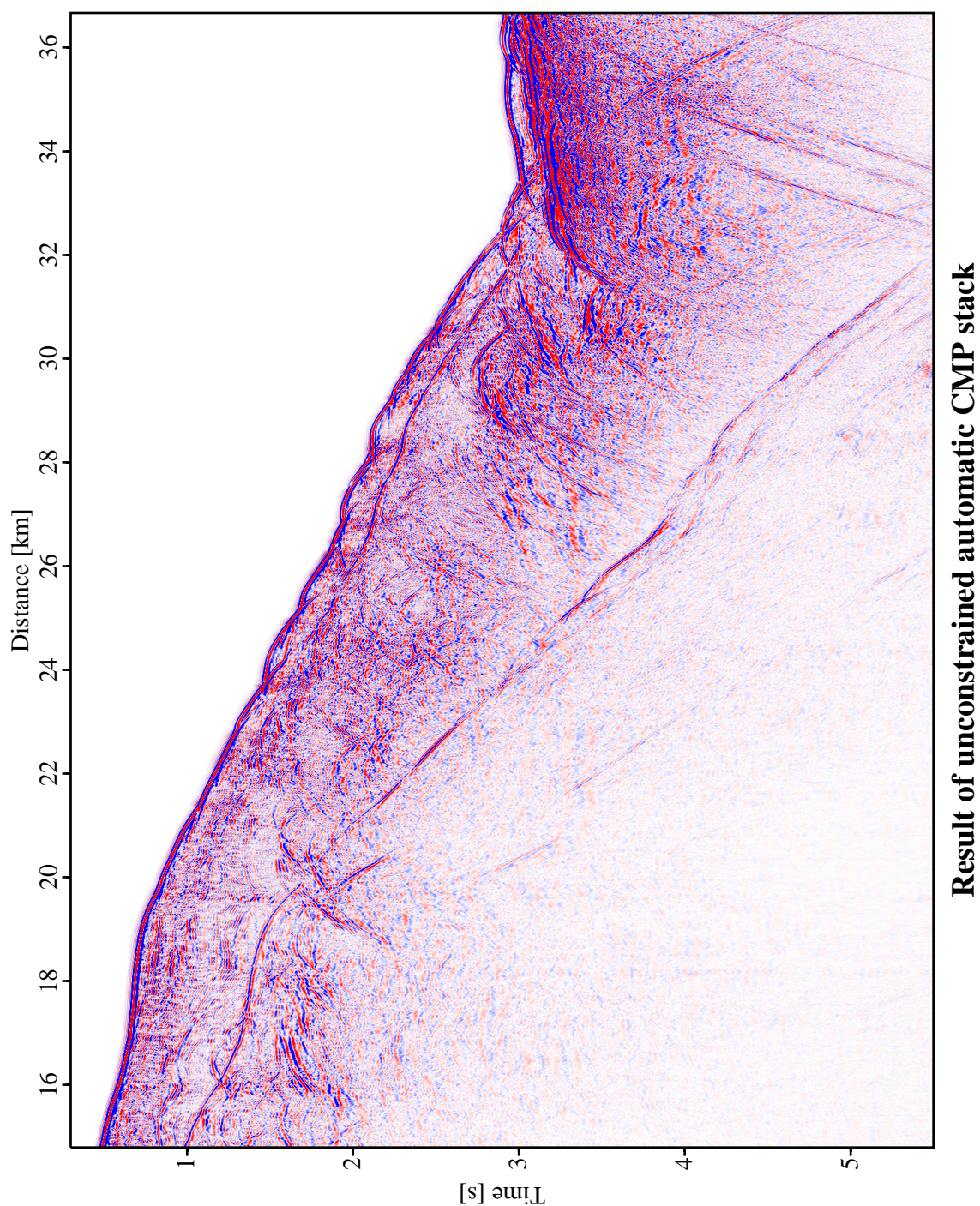


Figure 6.5: BGR99-07 data: result of the unconstrained automatic CMP stack. The smallest tested stacking velocity was 1400 m/s for all ZO locations. Multiples stemming from the seafloor and the BSR are clearly visible.

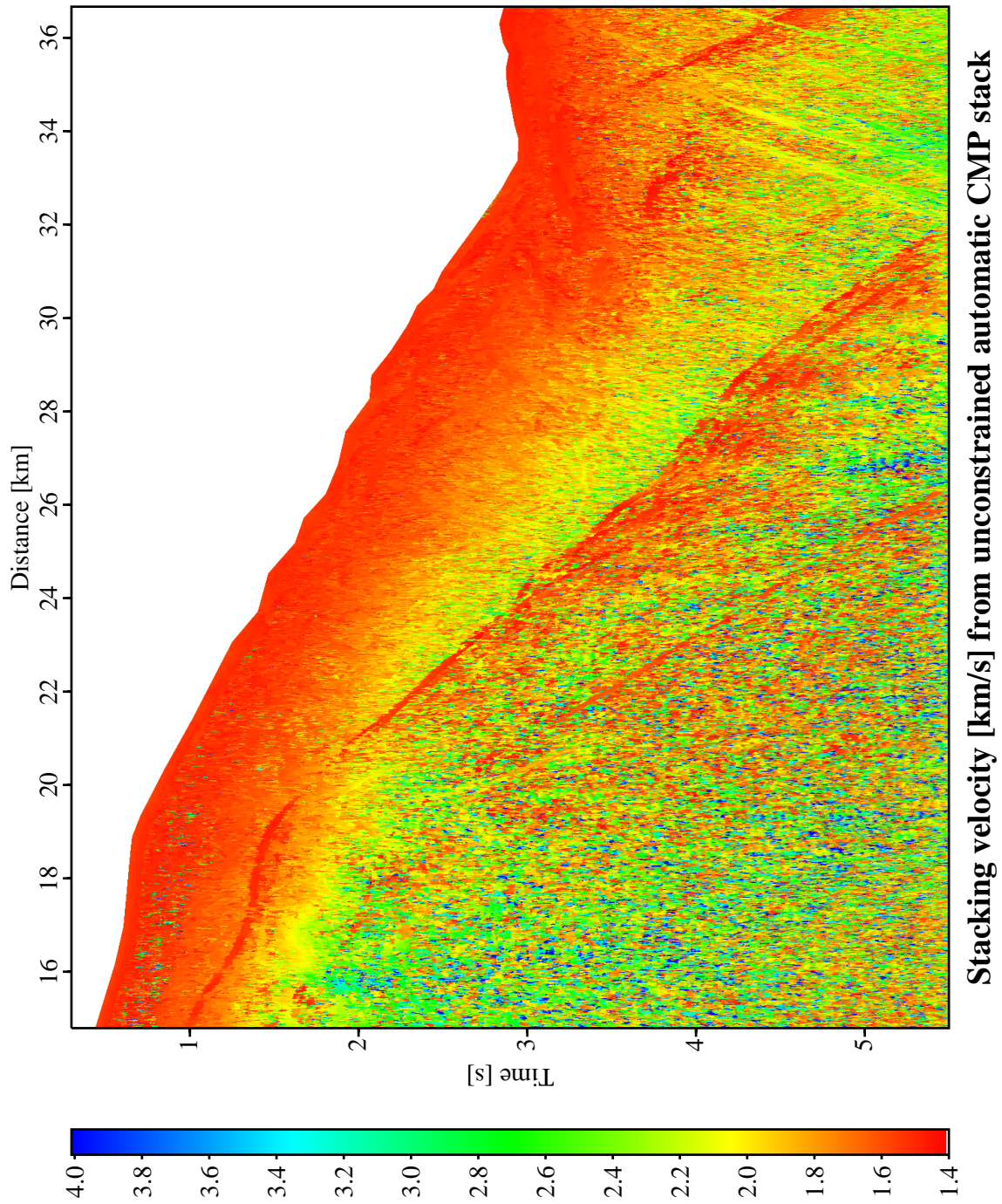


Figure 6.6: BGR99-07 data: stacking velocity section associated with the ZO section shown in Figure 6.5. Low stacking velocities compared to the neighborhood indicate the multiples.

Processing step	absolute CPU time [h]	relative CPU time [%]
Automatic CMP stack	2.0	0.7
Zero-offset stacks	84.5	28.8
Initial stack	23.8	8.1
Local optimization	183.0	62.4
Total	293.3	100.0

Table 6.3: BGR99-07 data: absolute and relative CPU times required for the successive processing steps. All times refer to a 400 MHz Pentium II processor and the processing parameters compiled in Table 6.2. The first line refers to the constrained automatic CMP stack.

processing step as the *constrained* automatic CMP stack. The resulting ZO section is displayed in Figure 6.7. I observe that the multiple events are actually attenuated at many ZO locations. However, some fragments of the multiple events are still quite dominant. Nevertheless, this simulated ZO section is better suited for the subsequent processing steps than the result obtained from the first processing iteration. In the vicinity of the upper left part of the seafloor multiple event, the neighboring events were apparently also attenuated. There, the stacking velocity constraints seem to affect the primary events, too. As this region is far away from the area of interest (the vicinity of the proposed ODP site), I decided to retain this usually undesired situation to see how the entire CRS processing sequence behaves in the case of (locally) inappropriate stacking velocity constraints.

A closer look at the stacking velocity sections reveals why fragments of the multiple events were not attenuated: whereas the primary seafloor event is associated with a smoothly varying stacking velocity, the corresponding multiple event is associated with strong variations of the stacking velocity. Wherever the stacking velocity exceeds the smallest tested value, the velocity constraints have no effect. Considering the quite uncomplicated shape of the primary seafloor event, it is not obvious if this strong variations are realistic.

To verify this, I performed a constant velocity (1500 m/s) Kirchhoff depth migration of the optimized CRS stacked result (that will be presented later on). The migrated image (not displayed) allows to pick the true location of the seafloor. Furthermore, it indicates that not all of the bow-tie kind structures along the seafloor event in the time domain are actually bow-ties: some of them were not resolved by the migration, although the used constant interval velocity is correct down to the seafloor. I assume that at these locations, the seafloor has a dip component in cross line direction and that the image of the seafloor is split as it was generated from two independent out-of-plane events. However, this violation of the 2.5-D assumption only affects the depth migration—the ZO simulation is still consistent.

With the picked true location of the seafloor, I forward-calculated the ZO traveltimes and the wavefield attributes of the P-P primary and the P-P-P multiple by means of ray tracing. The forward-calculated traveltimes (not displayed) are in good agreement with the seafloor multiple event in Figure 6.6. The stacking velocities, however, have a very complicated behavior. They are displayed in Figure 6.8 together with the stacking velocity associated with the primary P-P reflection and the smallest tested velocity. Note that the wavefield attributes were calculated along

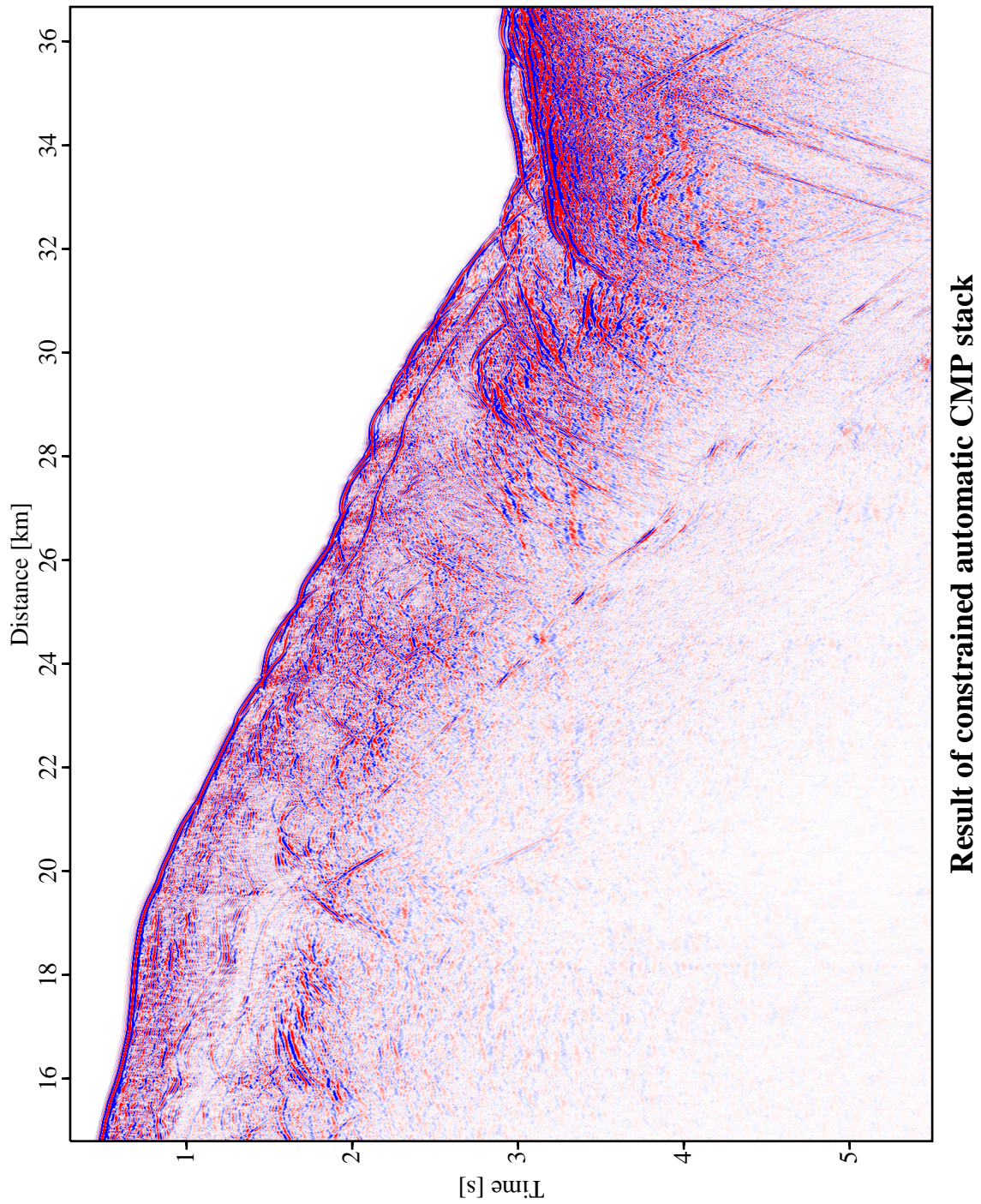


Figure 6.7: BGR99-07 data: result of the constrained automatic CMP stack. The smallest tested stacking velocity is a function of the ZO location. The multiples stemming from the seafloor and the BSR are partly attenuated.

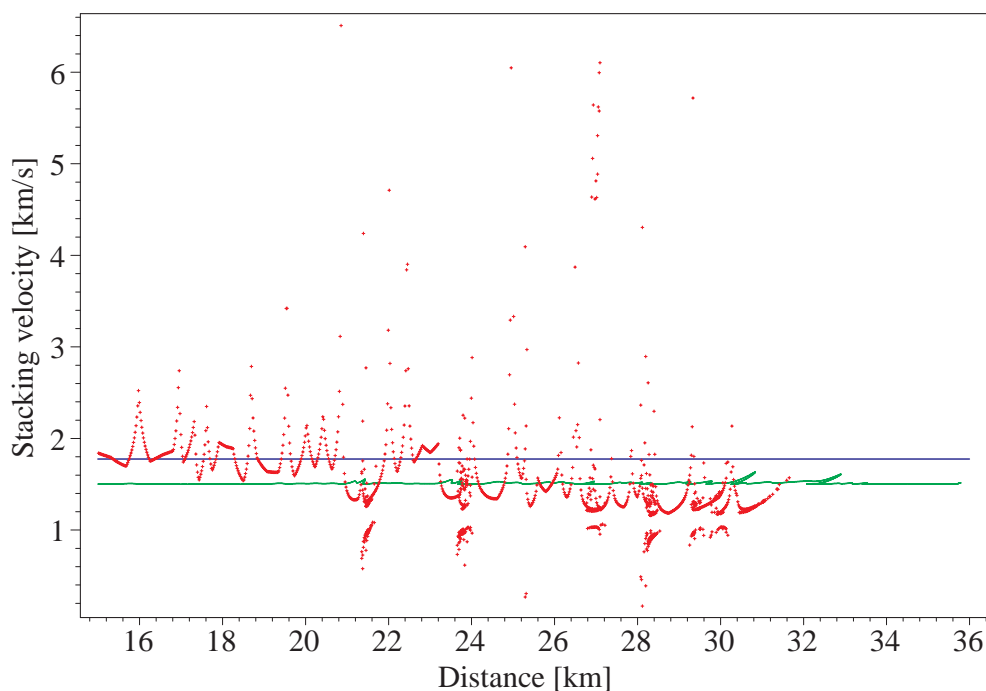


Figure 6.8: BGR99-07 data: forward-calculated stacking velocities associated with the P-P primary event (green) and the P-P-P-P multiple event (red) stemming from the seafloor. The blue line indicates the velocity threshold applied in the constrained automatic CMP stack.

the ZO rays. Whereas the fluctuations along the primary event are negligible (apart from the obvious bow-tie structures), they are extremely strong for the multiple event. For many surface locations, the ray tracing yielded an entire set of ZO P-P-P-P rays, thus providing conflicting stacking velocities, especially along bow-tie structures.

This forward calculation clearly demonstrates that the attributes along multiple events might behave quite unpredictable, even for events stemming from such an apparently uncomplicated seafloor geometry. Accordingly, the generation of an appropriate model of minimum stacking velocities is a non-trivial task.

6.2.2 Final results

Based on the result of the constrained automatic CMP stack (Figure 6.7), the subsequent processing steps, linear and hyperbolic ZO stack, were applied to obtain initial values of the wavefield attributes. Up to three conflicting events were allowed for each ZO location. During the initial CRS stack phase, i. e., the stack along the spatial CRS stacking operator with the initial wavefield attributes, the ambiguities at detected conflicting dip situations were resolved by means of an additional one-parameter search for R_{CS} that is related to the curvature of the stacking hyperbola in the CS/CR gathers. As R_{CS} can be expressed in terms of the stacking velocity v_{stack} , the emergence

angle α , and the radius of curvature R_N of the normal wavefront, the tested range of its values can be readily computed according to the constrained stacking velocity range. In other words, the stacking velocity model introduced to attenuate the water-column multiples was consistently considered in this processing step, too. The various intermediate and auxiliary results obtained from these processing steps are not displayed for the sake of brevity.

A local three-parameter optimization of the wavefield attributes provided the final, optimized CRS wavefield attributes. The result of the optimized CRS stack along the stacking operators defined by these attributes is displayed in Figure 6.9, followed by the coherence section for the dominant events, i. e., the events associated with the highest coherence values at each particular ZO location (Figure 6.10). To increase the lateral resolution, the ZO aperture for the stack was restricted to the attribute-based projected first Fresnel zone with the user-given ZO aperture as upper limit. Again, I applied an AGC with a window length of 0.5 s and a Gaussian taper. The AGC destroys the original amplitude information, but without it hardly any events are visible at larger traveltimes.

The optimized CRS stacked section appears quite different compared to the result of the NMO/DMO/stack processing chain (Figure 6.3). To some extent, these differences are due to the AGC that was applied independently to both results: the amplitudes in both results are no longer comparable. The events of the seafloor and the BSR as well as some other events at low traveltimes are very similar in both results. The CRS result has a larger signal-to-noise ratio in these areas. For larger traveltimes, the frequency content of the CRS result is significantly lower than in the NMO/DMO/stack result (apart from very steep flanks of diffraction patterns that are better imaged by the CRS stack). This is quite surprising, as the CRS processing parameters were chosen to account for the high frequency events, thus not preferring low frequency events.

One might conclude that there are no coherent high frequency events in the pre-stack data and that the high frequency content in the conventional results simply represents noise, but there is another possible explanation: assume random and/or systematic deviations between the actual event and the best-fitting hyperbolic operator. In this case, high frequency events will appear less coherent, as a given traveltime error will shift them out of phase faster than events with lower frequency content. Overall, the CRS stacked section reveals more coherent events than the conventional result.

The multiple events associated with the seafloor and the BSR are still visible in the CRS stacked result. They were attenuated during the stack but again emphasized by the applied AGC. Due to the attenuation, many events interfering with these multiples have been detected and characterized. At such locations the interference of primary and multiple events was simulated.

In the previous section, I mentioned that some of the primary events in the vicinity of the upper left part of the seafloor multiple appeared attenuated due to the applied velocity constraints. The coherence section (Figure 6.10) clearly indicates that the final, local optimization step was not able to correct for these inappropriate constraints: the coherence in the considered area is very low, in other words, no fitting stacking operators have been detected.

The sections with the detected emergence angle and the curvature of the normal wavefront are depicted in Figures 6.11 and Figure 6.12, again for the dominant events. These both attributes are directly related to the events' dips and curvatures. The emergence angle section demonstrates

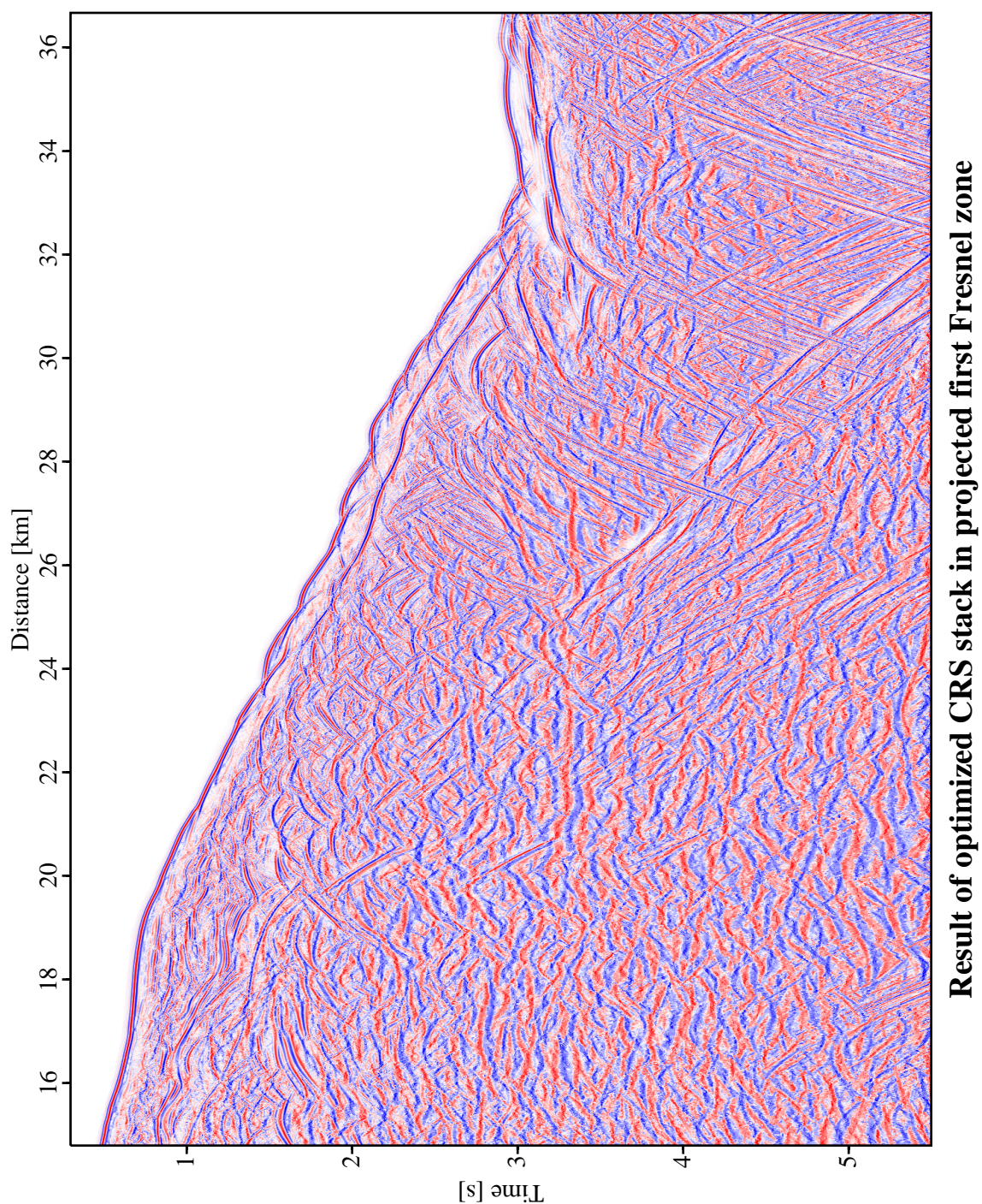


Figure 6.9: BGR99-07 data: result of the optimized CRS stack. An AGC with a window length of 0.5 s and a Gaussian taper was applied to reveal weak events. The ZO aperture was restricted to the attributed-based projected first Fresnel zone.

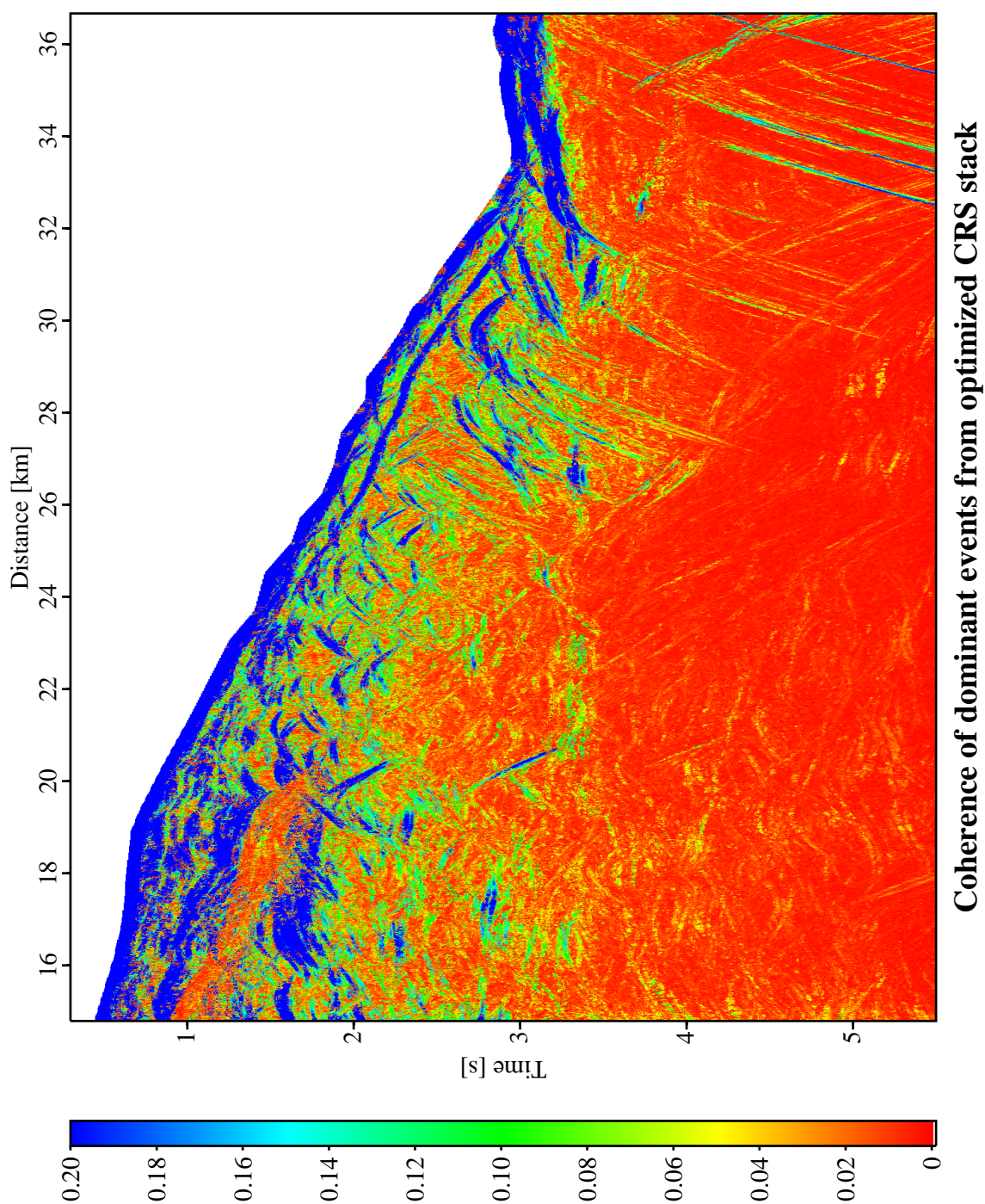


Figure 6.10: BGR99-07 data: coherence section associated with the optimized CRS stacked section shown in Figure 6.9 for the dominant events. The displayed range was restricted to a maximum of 0.2 to reveal events associated with low coherence values.

that steep diffractions patterns are the most dominant events at many locations. It also reveals that the low frequency event stemming from the plate boundary was decomposed in the separate strips associated with the different lobes of the wavelet. This is the expected behavior for the processing parameters that were chosen to account for the high frequency events: in the vicinity of the zero crossings of the wavelet, the used coherence band is too small to pick up sufficient coherent energy exceeding the noise level.

Finally, the radius of curvature of the NIP wavefront is depicted in Figure 6.13. As already observed for the other presented data examples, this radius continuously increases with increasing traveltimes (apart from the steep diffraction patterns). However, the section is quite noisy for larger traveltimes. Suspiciously low values compared to their neighborhood reveal some additional multiples: a steep event at (≈ 20 km, ≈ 2 s), most likely a segment of a bow-tie structure caused by a synclinal structure in the subsurface, appears again at traveltimes of ≈ 2.9 s and ≈ 3.8 s. The attributes associated with these events will be discussed Section 6.3.2.

6.3 Applications of the wavefield attributes

For the BGR99-07 data, I focus on two applications of the CRS wavefield attributes, namely the estimation of the projected first Fresnel zone and the identification of multiples. The former is used to verify the chosen ZO aperture and to increase the lateral resolution of the CRS stacked section. The identification of multiples is important to avoid misinterpretations of the results.

6.3.1 Projected first Fresnel zone

The projected first Fresnel zone represents the aperture in which the major contributions stemming from a reflector segment in the subsurface are expected in the pre-stack data. For ZO, the first projected Fresnel zone can be estimated by means of the CRS wavefield attributes by comparing the approximated kinematic reflection response of the subsurface reflector segment with the response of a hypothetical diffractor at the same (unknown) location in the depth domain (see Section 2.7).

As I already indicated for the two other data examples in Sections 4.3.1 and 5.3.1, the projected first Fresnel zone is suited for two purposes: on the one hand, it can be used to verify if the user-given ZO aperture was chosen appropriately. On the other hand, it serves as ZO aperture for the CRS stacking operator (with the user-given ZO aperture as upper limit) to increase the lateral resolution of the CRS stacked section, an application that was used for the CRS stacked section shown in Figure 6.9.

The projected first Fresnel zone for the dominant events is shown in Figure 6.14 relative to the user-given ZO aperture. Except for diffraction patterns (per definition associated with a projected first Fresnel zone of infinite extension), the user-given aperture is about 2-4 times larger than the projected first Fresnel zone. This ratio ensures that the region of tangency between the CRS stacking operator and the actual reflection events is considered during the coherence analysis for non-zero offset, too.

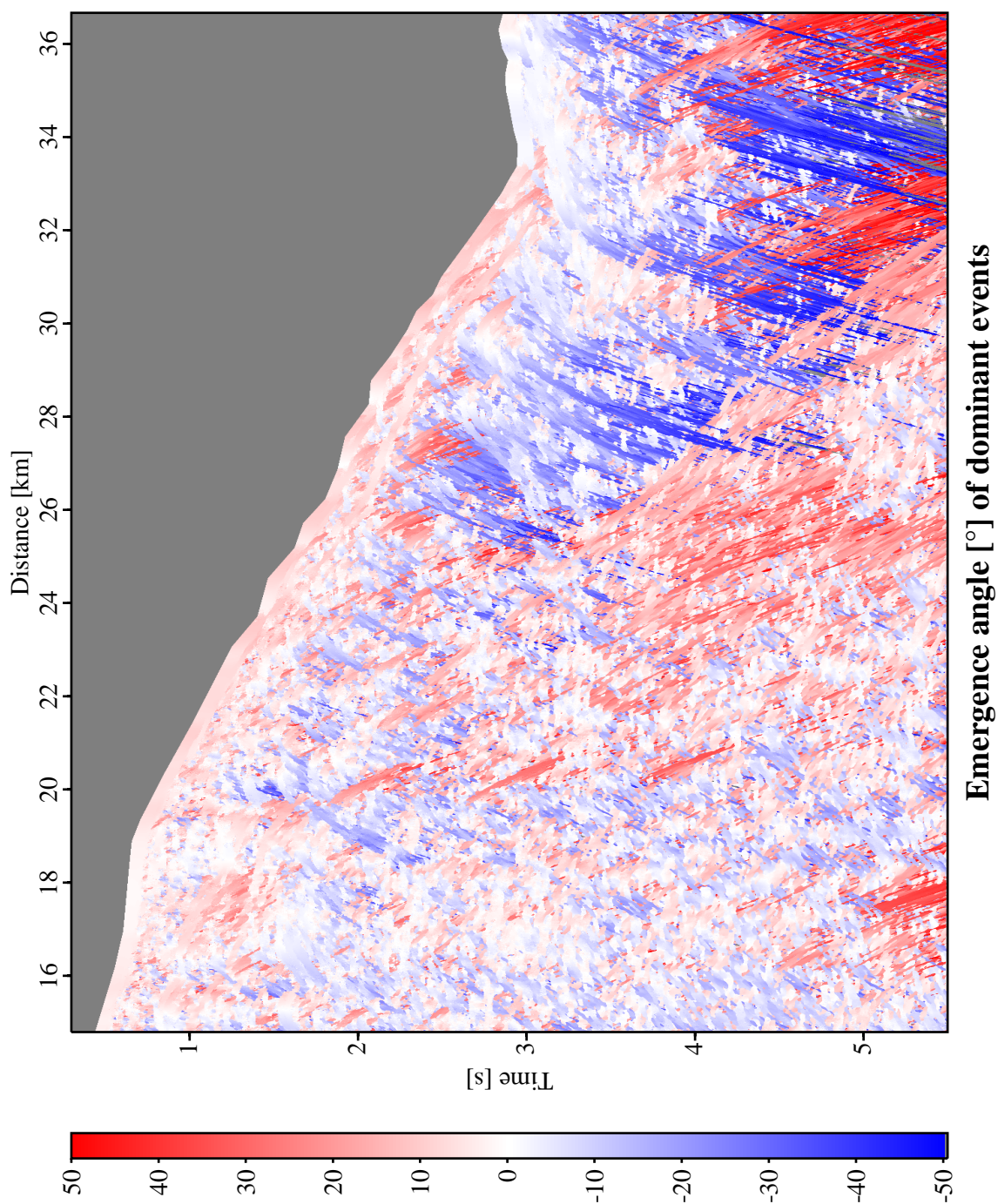


Figure 6.11: BGR99-07 data: emergence angle section associated with the optimized CRS stacked section shown in Figure 6.9 for the dominant events. The emergence angle is directly related to the dip of the events.

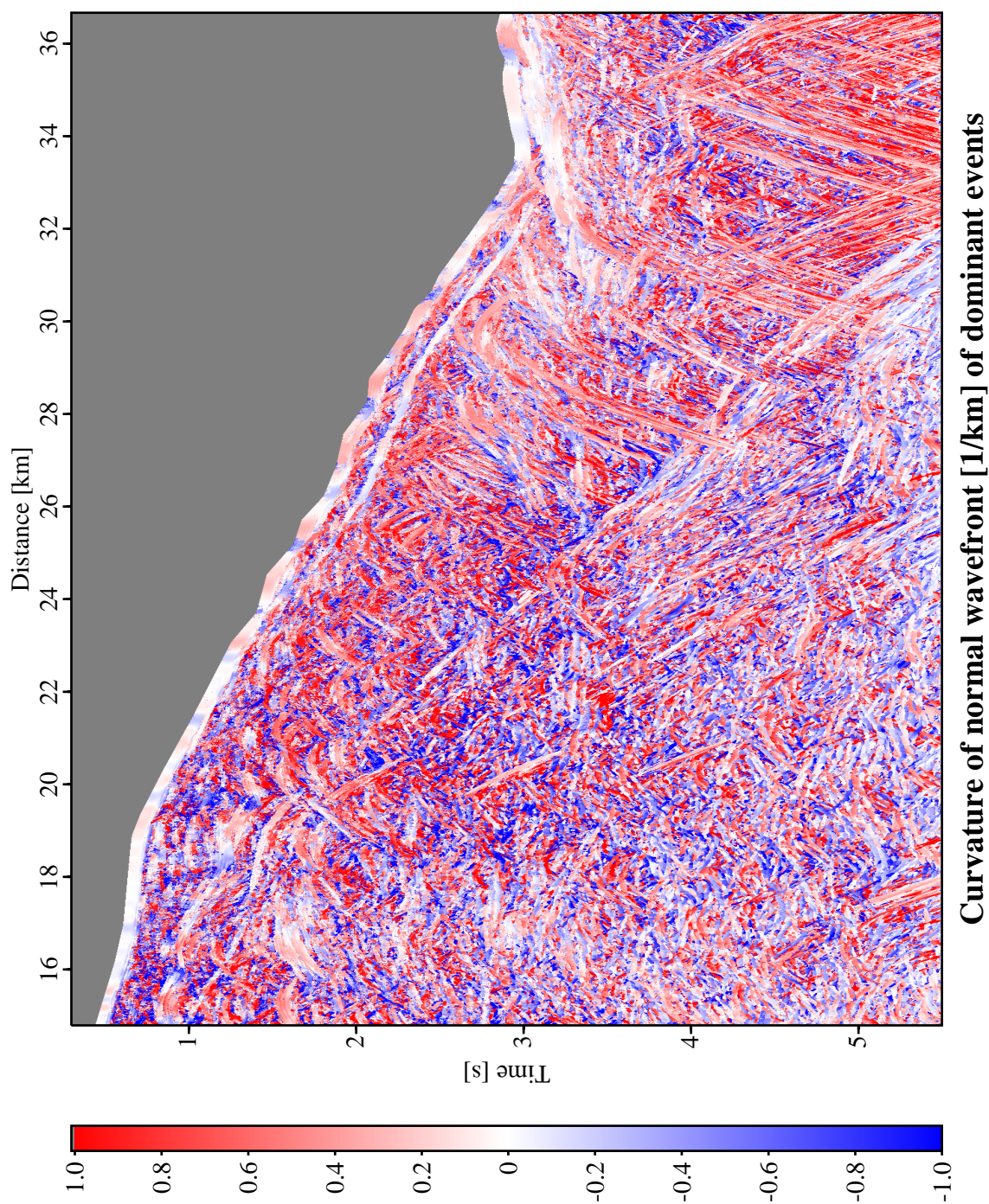


Figure 6.12: BGR99-07 data: section with the curvature of the normal wavefront associated with the optimized CRS stacked section shown in Figure 6.9 for the dominant events. This curvature is directly related to the curvature of the events.

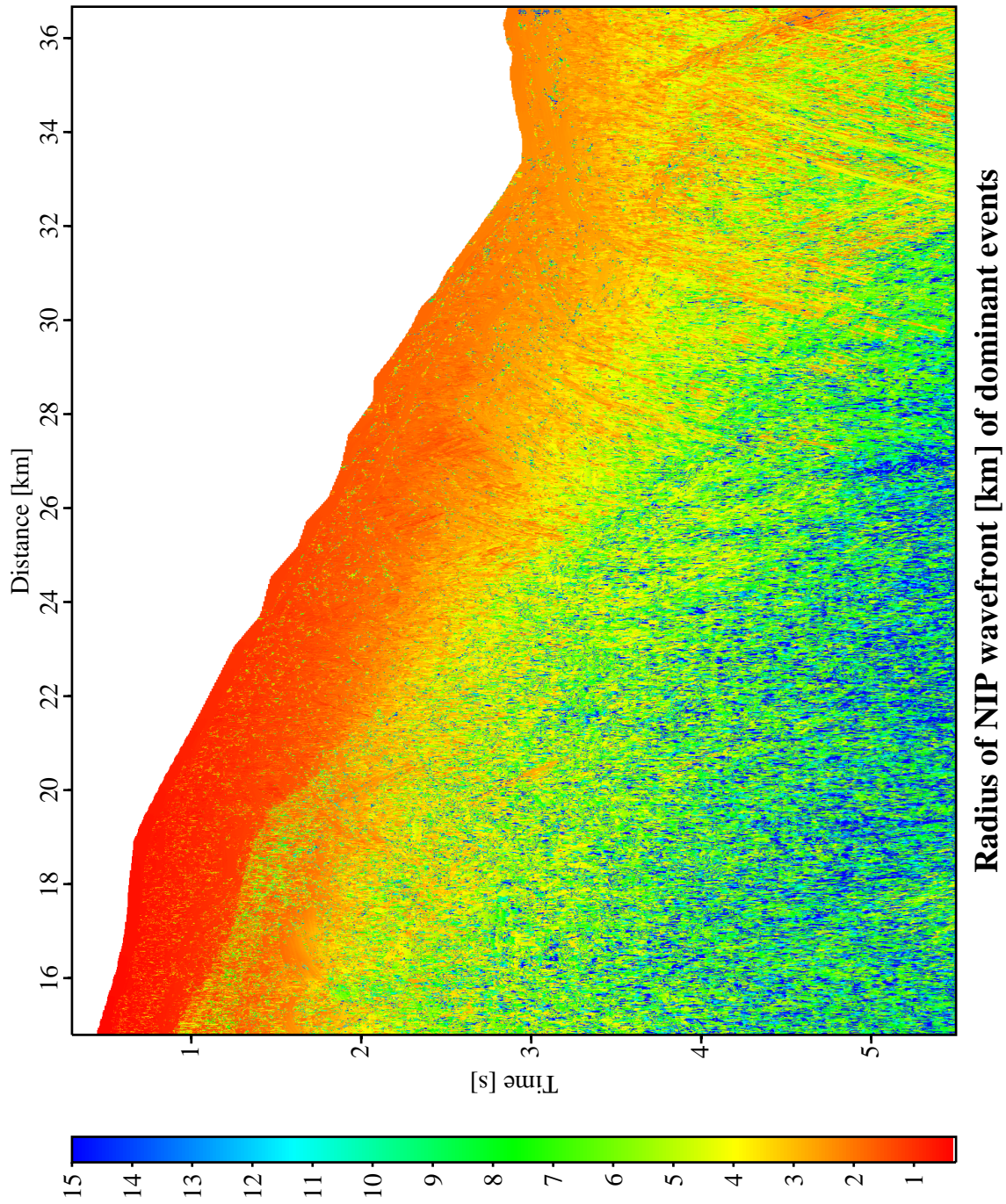


Figure 6.13: BGR99-07 data: section with the radius of curvature of the NIP wavefront associated with the optimized CRS stacked section shown in Figure 6.9 for the dominant events.

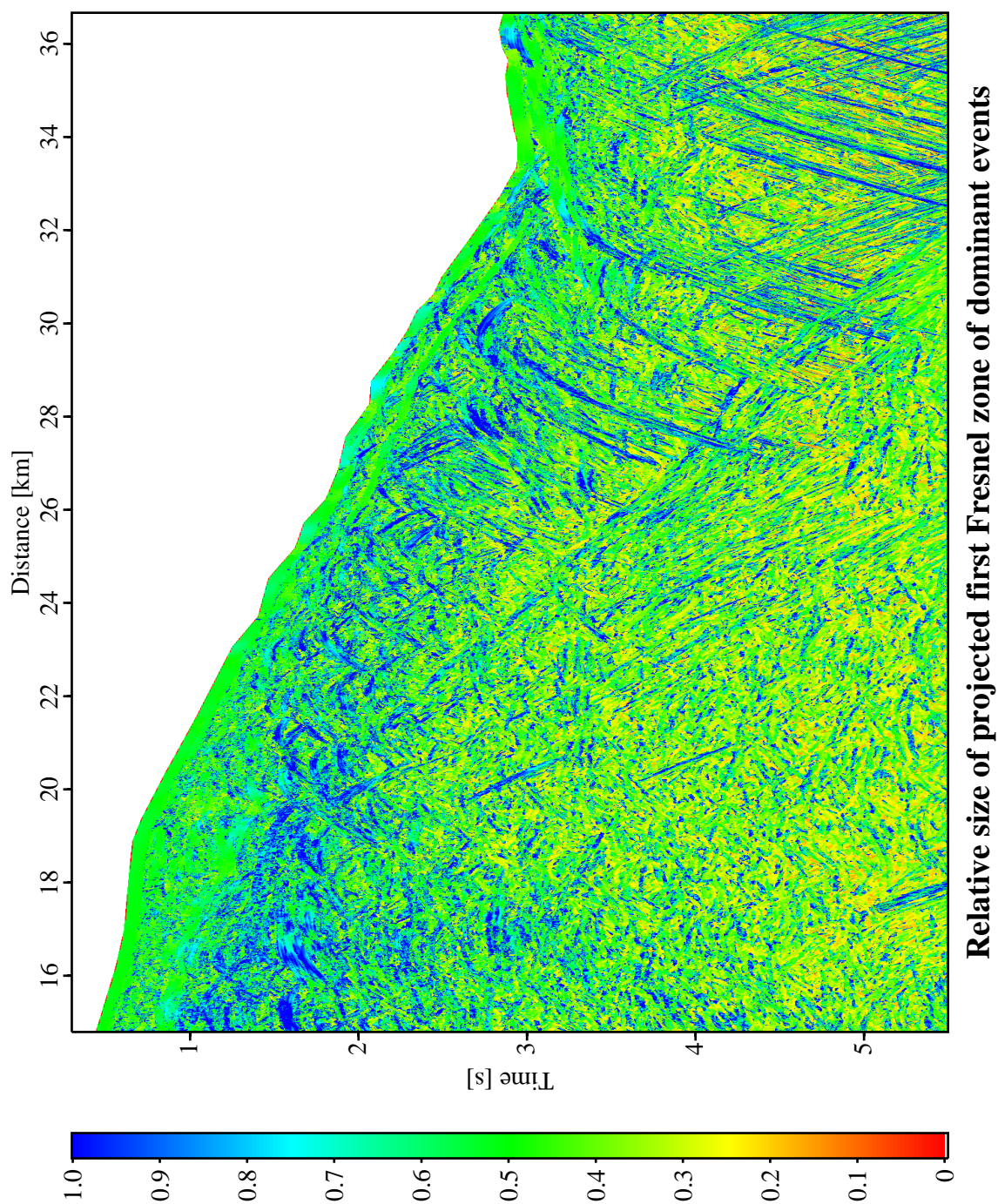


Figure 6.14: BGR99-07 data: size of the projected first Fresnel zone of the dominant events relative to the given ZO aperture. This displayed range is restricted to a maximum of 1.

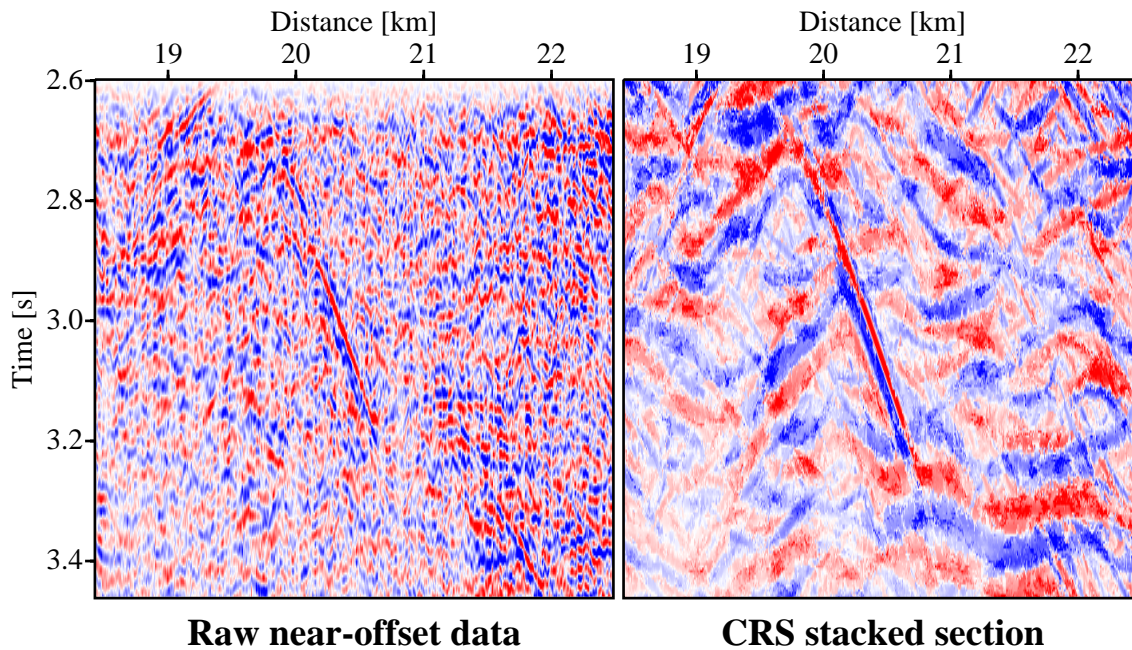


Figure 6.15: BGR99-07 data: subsets of the NMO corrected (1500 m/s) raw near-offset data (left) and the CRS stacked section (right).

6.3.2 Identification of multiples

The BGR99-07 data contain various water-column related multiples. Some of them can be very easily identified due to their associated stacking velocities and their shape which is similar to the corresponding primary events. Although the CRS stack is not specifically designed to remove or at least attenuate multiples, they can be attenuated to some extent by introducing constraints on the tested stacking velocities. However, multiples not affected by such constraints still appear in the simulated ZO section. Nevertheless, the CRS attributes allow to identify such multiple events.

To illustrate this, I extracted a subset of the raw near-offset data and the corresponding subset of the CRS stacked section (Figure 6.15). A constant velocity NMO correction with water velocity (1500 m/s) was applied to the raw data to reduce the offset-dependent moveout. The associated coherence section and the section with the radius of curvature of the NIP wavefront are depicted in Figure 6.16 for the dominant events.

In the raw data, the steep event in the center of the figure is the strongest coherent event that can be observed. The CRS stacked section shows a much higher signal-to-noise ratio and a set of coherent events, e. g., the event stemming from the plate boundary in the lower right part of the figure. The plate boundary event and the steep event intersect each other. Obviously, the extended CRS stack strategy detected the related conflicting dip situations and simulated the interference of both events at most ZO locations.

From the coherence section I observe that the steep event is associated with a coherence far larger than any other event in its vicinity. The associated radius of curvature of the NIP wavefront, R_{NIP} ,

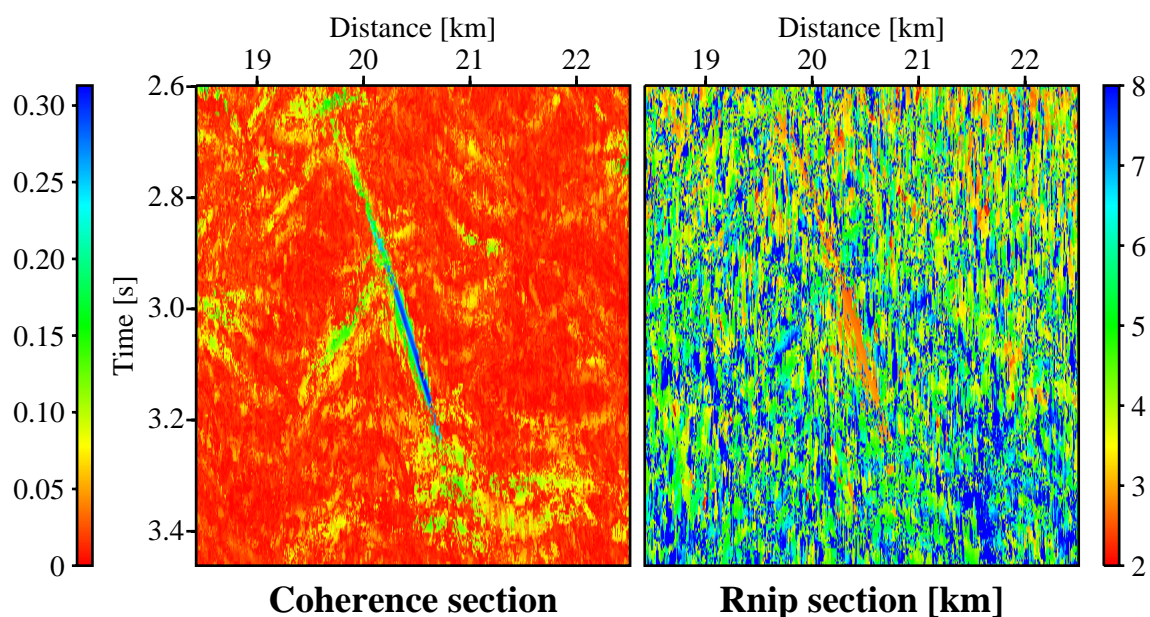


Figure 6.16: BGR99-07 data: Subsets of the coherence section (left) and the section with the radius of curvature of the NIP wavefront (right) of the dominant events.

is lower than for the surrounding events. This indicates that the steep event is a multiple. Considering the entire CRS stacked section (Figure 6.9) I am able to identify the associated primary event above at about 2 s. The primary event is most likely a fragment of a bow-tie structure due to a synclinal structure in depth. An additional reverberation in the water column causes the multiple event identified in Figure 6.15.

6.4 Conclusions

For the BGR99-07 data, I encountered complications not observed in the two other data sets presented in the preceding chapters: a significant variation of the frequency content for different events and strong multiple events due to reverberations in the water column.

The former problem turned out to be less critical concerning the stacked section itself if the used processing parameters are appropriate for the events with the highest frequency content. However, the low frequency events are no longer recognized as an entity along the pulse length, but are detected as separate events at the locations where the wavelet lobes exceed the background noise level. This leads to discontinuities in the wavefield attributes along the pulse length and, consequently, deteriorates subsequent applications of the wavefield attributes. As events with different frequency content interfere in the presented data, the current implementation is not able to detect and characterize all events with optimum temporal resolution *and* continuous attributes at the same time. In principle, the user has to select the frequency for which the events of interest can be characterized in an optimum way.

The CRS approach is based on the search for events in the pre-stack data that can be approximated by the hyperbolic CRS stacking operator. As this might also apply to multiple events in the data, the method is, in general, not able to distinguish between primary and multiple events. Nevertheless, some kind of multiples, like the water-column related multiples observed in the BGR99-07 data, can be identified by means of their associated attributes that indicate lower values for the radius of curvature of the NIP wavefront and the stacking velocity compared to neighboring primary events. I introduced a simple model for the lowest stacking velocity to be tested to attenuate the multiple events stemming from the seafloor and the BSR. This approach was successful to some extent but also revealed two problems: a) the stacking velocity along the multiple events fluctuates much stronger than for the associated primary event. If the actual stacking velocity exceeds the threshold given in the stacking velocity model, the multiple is not attenuated. b) the differences between the stacking velocities of neighboring primary and multiple events might be too small to allow a separation. In this case, the velocity constraints lead to an attenuation of the primary events, too.

The CRS stack detected various coherent events for larger traveltimes that can hardly be observed in the result of the NMO/DMO/stack chain. The steep flanks of diffraction patterns in the data were better imaged by the CRS stack. The conventional result contains less multiple energy compared to the CRS result. However, the multiple attenuation by means of the velocity constraints might be improved by using a more complex model for the lowest allowed stacking velocity. This would require a more intensive interpretation of the results of the automatic CMP stack.

Chapter 7

Conclusions and outlook

The task of 2-D seismic reflection imaging has been addressed with an entirely data-oriented approach: instead of parameterizing the (isotropic) subsurface model in terms of wave propagation velocities and density, the CRS stack approach directly parameterizes the reflection events in the pre-stack time domain. In this way, the inherent redundancy of the pre-stack data is used to collect information that pertains to common reflection surfaces in depth. These surfaces are described by means of their location, orientation, and curvature in depth. However, none of these properties has to be explicitly known: instead, the corresponding reflection response in the time domain is described by means of properties of (hypothetical) wavefronts. The CRS stack approach can be related to established imaging methods like Kirchhoff migration and NMO/DMO/stack that are based on particular reflector segment properties in the depth domain. The approach presented in this thesis provides three kinematic wavefield attributes and the simulated ZO response of the subsurface at every considered location in the post-stack time domain. Thus, the CRS stack does not directly generate a structural image of the subsurface in the depth domain, but firstly collects the redundant information in the pre-stack data in a model-independent way. The transformation from the post-stack time domain to the depth domain remains for a second imaging step that benefits from the high signal-to-noise ratio of the ZO simulation and the information provided by the wavefield attributes.

Following the geometrical approach of Höcht et al. (1999), I derived an approximate primary kinematic reflection response of an arbitrarily curved reflector segment in depth: approximate CRP trajectories are attached to the approximate ZO reflection response of the considered reflector segment. In terms of paraxial ray theory, this means that the paraxial rays are approximated on the basis of a central ray with offset zero and normal incidence on the reflector segment. Two hypothetical *eigenwaves*, the NIP and the normal wave, establish a relationship between the depth and the time domain. The second-order Taylor expansions of this response coincide with the expressions derived by Tygel et al. (1997) by means of paraxial ray theory. I discussed some useful applications of the wavefield attributes that should be directly integrated into the CRS stack implementation, e. g., the estimation of the projected Fresnel zone for ZO. Moreover, I introduced two new applications of the CRS attributes, namely the classification of events and the attribute-based time migration.

The application of the CRS stack poses a global optimization problem with three parameters, namely the radii of curvature of the two hypothetical wavefronts and their common angle of emergence. The objective function is a coherence measure calculated along the CRS operator in the pre-stack data. Müller (1999) proposed and implemented a decomposition of this optimization problem into three global optimizations with one parameter each, followed by an optional local optimization with all three parameters simultaneously. The one-parameter optimizations are performed in subsets of the entire pre-stack data. I extended this pragmatic search strategy to overcome some of its limitations: the extended CRS search strategy is able to also handle situations with intersecting reflection events, usually referred to as conflicting dip situations. Events contributing to the same ZO location can now be identified and parameterized separately, thus providing a more complete and more physical ZO simulation. I designed the extended search strategy such that the efficiency of the pragmatic search strategy is preserved as far as possible. The results of both strategies in case of only one contributing event are consistent and, thus, allow to use both strategies alternatively depending on the number of detected contributing events.

I presented an object-oriented implementation of the extended CRS search strategy that is meanwhile used for hydrocarbon exploration by several international companies. Compared to the preceding implementation of the pragmatic CRS strategy, it allows a generalized handling of real data and provides more powerful and flexible features to control the range of tested stacking velocities. As a consequence, a priori knowledge can be better integrated into the processing flow and some types of unwanted multiples can be easier attenuated. Based on considerations concerning the systematic processing artifacts usually met in Kirchhoff migration, the concept of operator tapering has been introduced into the CRS stack approach. The handling of conflicting dip situations, projected Fresnel zones for ZO, operator tapering, and the application of the attribute-based time migration are integrated into the implementation.

I applied the CRS stack implementation to three marine data sets: The first synthetic data set represents a situation with a complicated salt body embedded in a stratified medium without extreme lateral variations. This data set mimics subsurface features observed in the Gulf of Mexico. Due to the complicated shape of the salt body, the imaging of sub-salt structures is a very challenging task for any imaging method. The CRS stack is able to provide good images of the area above and beside the salt body. The image obtained for reflectors below the salt is of very poor quality and reflects the fact that a second-order approximation of the reflection traveltimes is not applicable in very complex situations. Moreover, some parts of the model might even be too complex for an application of zero-order ray theory at all, irrespective of further approximations related to paraxial ray theory. With its rather extreme variations of the complexity of the recorded wavefield, these synthetic data allow to observe all kinds of performance of the CRS stack approach and its implementation—ranging from superior images to almost entire failures.

The second data set was acquired deep-offshore Chile perpendicularly crossing the Peru-Chile trench. The strongly dominant diffraction events in this data set make it difficult to directly compare the CRS stack result to the conventional result. However, a subsequent post-stack migration of both simulated ZO section reveals the superior quality of the CRS results. For these data, the CRS wavefield attributes turned out to be useful to collapse diffraction patterns by means of an attribute-based time migration and to distinguish between reflection and diffraction events that are hard to separate by conventional means. The images of the steep structures in the subsurface suffer

from the poor illumination of their flanks. With the given acquisition geometry and the very deep seafloor, such structures hardly provide reflection responses. The CRS stack revealed its ability to better image such steep events compared to the established, conventional methods.

The third data set was acquired over the Middle America Trench off-shore Costa Rica. Compared to the two other data sets, this example posed additional problems like strong water-column multiples, significant variations of the local frequency content, and an overall poor data quality. I partly succeeded to tackle the multiple problem. However, the wavefield attributes associated with multiple events turned out to behave much more complicated than expected for the comparatively simple seafloor geometry. The crude stacking velocity model used for these data is not sufficient to attenuate the multiples at all locations. Both, the conventional and the CRS results, are difficult to interpret due to the poor data quality. Thus, it is almost impossible to decide which of the results is more reliable.

The CRS stack strategy and/or its implementation presented in this thesis rely on a set of restrictions and assumptions. Some of them, like the existence of coherent reflection events and, moreover, the applicability of a paraxial approximation, are inherent to the method such that they cannot be overcome at all. However, many generalizations of the method are possible to overcome other limitations. In the following, I will comment on such generalizations.

As shown by Höcht (2002), the CRS stack for 2-D is also applicable for 3-D models and provides a consistent subset of the 3-D ZO volume. However, in a strict sense, sources and receivers within the considered aperture have to be located along a straight line, in other words, 2-D refers to the acquisition geometry rather than to the subsurface model. The current implementation only supports a global straight acquisition line for the entire data, whereas a locally more or less straight acquisition line would be sufficient. This restriction is entirely a matter of the implementation and can be overcome by a more flexible parameterization of the acquisition line and local coordinate transformations instead of a global one.

The concepts of the CRS stack approach have been transferred to the 3-D case by Höcht (2002). The 3-D counterpart of the pragmatic search strategy has already been implemented by Cristini et al. (2001, 2002). The 3-D implementation of the extended CRS stack strategy and the integration of the wavefield attribute applications remain as future tasks. Furthermore, alternative strategies are required for many 3-D situations as the coverage in the subsets of the pre-stack data might be too low for an application of the pragmatic or extended search strategy. This especially applies to marine situations where the azimuthal coverage is usually very poor such that a complete determination of all CRS attributes is not possible without additional assumptions.

In this thesis, the central rays are ZO rays with normal incidence on the reflector. This allows to simulate ZO sections from the pre-stack data just as with conventional methods like NMO/DMO/stack. However, for large offsets the simulation of ZO sections is, in general, not useful: a ZO ray that actually illuminates the considered (unknown) depth point might not even exist. Even more important, the paraxial approximation may not hold over a large offset range. Therefore, it appears very attractive to approximate the reflection response of a subsurface reflector segment with respect to an arbitrary central ray rather than a ZO ray, only. For such central rays with *finite* source/receiver offset, Zhang et al. (2001) introduced two hypothetical experiments that establish a relationship between the depth and the time domain similar as the NIP and

normal wave experiments do for the ZO case. The implementation and application of the CRS stack for the finite-offset case and 2-D acquisition is subject of current research. The finite-offset CRS stack approach can also be extended to the 3-D case. Due to the large number of wavefield attributes in this case, namely thirteen, its efficient implementation is a very challenging task for future research. An overview of the generalizations can be found in Mann et al. (2002).

Finally, I would like to comment on the influence of the topography and variations of the near-surface velocity, a problem usually addressed by means of so-called *static corrections*. For the marine data examples presented in this thesis, none of these features matters. However, for data acquired on land these influences can, in general, not be neglected. In case of a (locally) constant near-surface velocity, the CRS stack strategy can be extended to directly consider the topography (Zhang et al., 2002): using the emergence angle and the near-surface velocity, the traveltimes measured on the actual acquisition surface can be transformed to a hypothetical datum such that the influence of the topography is removed. Obviously, these corrections depend on the CRS wavefield attributes that have to be determined at the same time. The implementation of the 2-D ZO case is currently in progress.

The variation of the near-surface velocity is a more difficult task: on the one hand, for simple situations like constant velocity gradients, it can be analytically considered in the traveltimes approximation (Chira-Oliva et al., 2001). On the other hand, in case of strong lateral variations, the entire CRS stack approach breaks down. Between these two extremes, the actual reflection responses might be slightly shifted with respect to the best-fitting stacking operator. The statistical handling of such time shifts is usually referred to as *residual static correction*. With its spatial operators close to the actual reflection events, the CRS stack bears the potential to provide superior input to algorithms addressing this correction. The first steps in this direction are subject of my current work.

Appendix A

Sign conventions and data visualization

A.1 Emergence and incidence angles

The angles between interfaces or the acquisition surface and propagating wavefronts are measured from the propagation direction of the wavefront (which is parallel to the corresponding ray in the considered isotropic case) to the interface or surface normal, respectively. This sign convention is depicted in Figure A.1 for an upgoing ray that is reflected and refracted at a planar interface.

With this definition, the sign of the emergence angle of the ZO rays emerging at the acquisition surface coincides with the sign of the ZO slope of the associated event in the time domain.

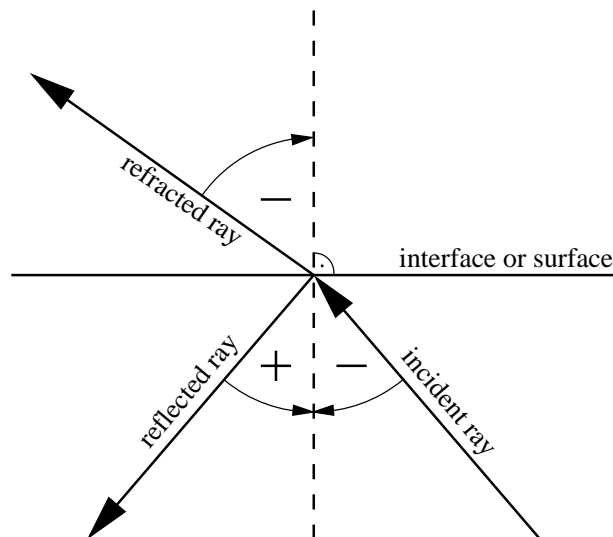


Figure A.1: Sign convention for emergence and incidence angles at interfaces and at the acquisition surface. At the acquisition surface, only the incident ray has to be considered for primary events.

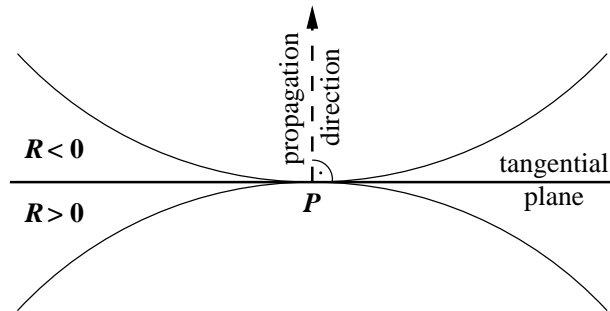


Figure A.2: Sign convention for the curvatures of propagating wavefronts. The arc segments represent the wavefront curvatures at P .

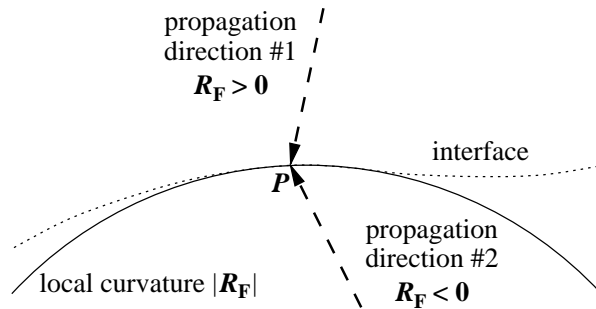


Figure A.3: Sign convention for the curvature of an interface (dotted line). The arc segment (solid line) represents its local curvature at P .

A.2 Wavefront and interface curvatures

The curvature of a wavefront is defined by means of its propagation direction and its tangent at the considered point P : if the wavefront lags behind its tangent, the radius of curvature R is considered as positive and vice versa. For an observer at the acquisition surface, an emerging wavefront with $R > 0$ appears convex, whereas a wavefront with $R < 0$ appears concave. This sign convention is depicted in Figure A.2.

For the application of the refraction law for wavefront curvatures (2.6b), the sign convention for the interface curvature is depicted in Figure A.3: if the interface appears convex for the incident wavefront, the interface curvature is considered as positive, and vice versa. Thus, the sign also depends on the propagation direction of the wavefront.

A.3 Seismic amplitudes

Due to the applied pre-processing steps, all data sets presented in this thesis reveal approximately zero-phase wavelets similar to a zero-phase Ricker wavelet, i. e., the second derivative of a Gaussian function. Consequently, the traveltimes are given by the central lobes of the wavelets. In “simple” situations without additional phase shifts due to caustics or super-critical reflections, the sign of the central lobe directly depends on the sign of the impedance contrast at the subsurface reflector.

Unfortunately, no common standard exists for the sign convention—as a matter of fact, the data sets in this thesis reveal different sign conventions. Even worse, there is also no common standard for the color assignment. To obtain a consistent representation of all data sets, I displayed all of them such that positive impedance contrasts correspond to negative amplitudes. This is the so-called *European polarity convention* (see, e. g., Brown, 2001). Positive amplitudes are displayed in blue, negative amplitudes in red, both with constant hue gradients. All seismograms shown in this thesis represent relative water pressure in arbitrary units. Thus, the figures include neither color legends nor units. Zero relative pressure always corresponds to the color white.

To preserve the amplitude information, most of the seismic sections are displayed without additional gain functions. I used the distribution of the amplitudes to define the displayed amplitude range by means of a percentile clip: a certain percentage of all amplitude values must be located inside the display range centered around zero, typically about 98 %. The amplitudes of the remaining samples are reduced to the limits of the display range.

If the amplitude variations are too large to reveal weak events with this percentile clip, I applied an automatic gain control (AGC): each amplitude is divided by the root mean square value of all amplitudes along the same trace within a given time window. The contributing amplitudes are weighted with a Gaussian taper with an half-width of $\approx 11\%$ of the window length. After an AGC, the amplitudes are no longer comparable on a global scale.

A.4 Wavefield attribute sections

All wavefield attribute sections are displayed within user given ranges. Thus, not all samples are displayed with their actual values. The display ranges were chosen to provide an appropriate resolution for the reliable attributes along identified reflectors. Each section is accompanied by an color legend. Areas where no attributes were calculated (above the seafloor events) are shown in a separate color that is not used for the visualization of the attributes. If no unit is given in the figure title, the unit is 1 (coherence sections, relative size of the projected first Fresnel zone etc.)

Appendix B

Coherence measure semblance

The CRS stacking operator fitting best an event in the pre-stack data is determined by means of coherence analysis along a multitude of test operators in the pre-stack data. In the current implementation of the CRS stack, I use the coherence measure semblance (Taner and Koehler, 1969; Neidell and Taner, 1971):

$$S = \frac{\sum_{j=k(i)-W/2}^{k(i)+W/2} \left(\sum_{i=1}^M f_{i,j(i)} \right)^2}{M \sum_{j=k(i)-W/2}^{k(i)+W/2} \sum_{i=1}^M f_{i,j(i)}^2} \quad \text{where } 0 \leq S \leq 1. \quad (\text{B.1})$$

The index i denotes the contributing traces, $k(i)$ the discrete traveltimes for each trace given by the stacking operator. The data samples are taken from a temporal window with a width of $W + 1$ samples centered around the stacking operator. The amplitude $f_{i,j(i)}$ is calculated by means of a linear interpolation along the trace i in the pre-stack data.

The semblance is usually described as the normalized ratio of output to input energy: the sums in the denominator represent the energy located in the evaluated subvolume of the pre-stack data, irrespective of its distribution. In the nominator, the coherent energy along the stacking operator and its time-shifted counterparts within the time window are calculated and summed. The maximum semblance value 1 is obtained if all amplitudes $f_{i,j(i)}$ are identical separately for each fixed value of j .

The result is insensitive to the scale of the amplitudes, but decreases if the amplitude varies along the (shifted) stacking operator. Even if the stacking operator perfectly matches the reflection event, the amplitudes along the stacking operator will in general vary: the reflection coefficient is a function of the (unknown) reflection and transmission angles. In addition, varying source signatures and source and receiver coupling might affect the amplitudes.

From a kinematical point of view, my aim is to fit the operator to a surface of constant instantaneous phase in the pre-stack data¹, irrespective of the actual amplitudes. To remove the (varying)

¹Phase shifts due to super-critical reflections are not considered in this context.

amplitude information, I propose to use *normalized* traces for the semblance analysis. These are defined as the input trace $f(t)$ divided by the envelope of the associated analytic signal $F(t)$. The latter reads

$$F(t) = f(t) - i\mathcal{H}[f(t)] , \quad (\text{B.2})$$

where i denotes the imaginary unit and \mathcal{H} the Hilbert transform (see, e. g., Buttkus, 1991). In the current implementation, the Hilbert transform is performed by means of a discrete convolution in the time domain. Although the normalization strongly amplifies the noise in the pre-stack data, the detected attributes are still reliable and the semblance values are usually higher, especially for real data.

Appendix C

Flexible polyhedron search

As discussed in Chapter 3, the determination of the CRS stacking operator represents a *global* optimization problem with three parameters. For specific subsets of the pre-stack data volume, the number of parameters reduces such that a sequence of one-parameter global optimization problems can be solved to obtain initial wavefield attributes. In most situations, these initial attributes are sufficiently close to the “true” wavefield attributes that yield the maximum coherence value (or, in conflicting dip situations, also a local maximum) to obtain a good stack result. For further applications of the wavefield attributes, however, their accuracy can be improved by a final optimization step with all three parameters. As initial values in the vicinity of the searched-for maximum are already available, a *local* optimization strategy with three parameters is sufficient for this task.

In the current implementation of the CRS stack, I use the *flexible polyhedron search* by Nelder and Mead (1965). For a scalar objective function $f(\mathbf{x})$, where \mathbf{x} is a vector with $n \geq 2$ components, this local optimization algorithm propagates a polyhedron with $n + 1$ vertices through the n -dimensional parameter space. Starting with a given polyhedron, the method only requires the values of the objective function f at the vertices \mathbf{x}_i and at internally calculated new potential vertex locations. Derivatives of the objective function are not required. The algorithm was originally introduced to minimize the objective function f which is, of course, equivalent to a maximization of $-f$.

For the CRS stack for 2-D ZO simulation discussed in this thesis, the parameter space has three dimensions, thus tetrahedra are used to determine the local maximum. In the next section, I will briefly describe the algorithm, followed by some adaptations for the CRS stack implementation.

C.1 The search algorithm

In the literature as well as in freely available implementations, several variations of the flexible polyhedron algorithm can be found. Here, I follow the description of Himmelblau (1972). The algorithm is based on four basic operations applied to the polyhedron: reflection, expansion, contraction, and reduction. In the following, $\mathbf{x}_i^{(k)}$ denotes the i th vertex of the polyhedron in the k th

iteration of the optimization, $i = 1, \dots, n+1$. The corresponding value of the objective function is $f(\mathbf{x}_i^{(k)})$. For a more comprehensive illustration of the algorithm, I introduce the following definitions:

- the vertex $\mathbf{x}_h^{(k)}$ associated with the highest value of the objective function such that $f(\mathbf{x}_h^{(k)}) = \max [f(\mathbf{x}_1^{(k)}), \dots, f(\mathbf{x}_{n+1}^{(k)})]$,
- the vertex $\mathbf{x}_s^{(k)}$ associated with the second highest value of the objective function such that $f(\mathbf{x}_s^{(k)}) = \max [f(\mathbf{x}_i^{(k)})] \forall i \neq h$, and
- the vertex $\mathbf{x}_l^{(k)}$ associated with the lowest value of the objective function such that $f(\mathbf{x}_l^{(k)}) = \min [f(\mathbf{x}_1^{(k)}), \dots, f(\mathbf{x}_{n+1}^{(k)})]$.

The process starts with an initial polyhedron which has to enclose a finite (hyper) volume. The definition of the initial values $\mathbf{x}_i^{(0)}$ will be discussed later on.

At the beginning of each iteration, the vertices $\mathbf{x}_h^{(k)}$, $\mathbf{x}_s^{(k)}$, and $\mathbf{x}_l^{(k)}$ have to be determined. For the basic operations reflection, expansion, and contraction, I have to calculate the centroid (center of gravity)

$$\mathbf{c}^{(k)} = \frac{1}{n} \left[\left(\sum_{i=1}^{n+1} \mathbf{x}_i^{(k)} \right) - \mathbf{x}_h^{(k)} \right]$$

of all vertices except $\mathbf{x}_h^{(k)}$. The first operation is to reflect the vertex $\mathbf{x}_h^{(k)}$ through the centroid $\mathbf{c}^{(k)}$ to obtain the new potential vertex

$$\mathbf{r}^{(k)} = \mathbf{c}^{(k)} + a(\mathbf{c}^{(k)} - \mathbf{x}_h^{(k)}) \quad \text{with } a > 0.$$

If $f(\mathbf{r}^{(k)}) \leq f(\mathbf{x}_s^{(k)})$, the searched-for minimum is expected to be found in the direction of the reflection. If even $f(\mathbf{r}^{(k)}) \leq f(\mathbf{x}_l^{(k)})$, the algorithm tries to “accelerate” the propagation in this direction by means of an expansion of the reflected polyhedron:

$$\mathbf{e}^{(k)} = \mathbf{c}^{(k)} + b(\mathbf{c}^{(k)} - \mathbf{x}_h^{(k)}) \quad \text{with } b > 1.$$

This expanded vertex is accepted if it provides a value below $\mathbf{x}_l^{(k)}$. Thus, two possible operations are performed in this case:

$$\begin{aligned} f(\mathbf{r}^{(k)}) \leq f(\mathbf{x}_l^{(k)}) \wedge f(\mathbf{e}^{(k)}) \leq f(\mathbf{x}_l^{(k)}) & \quad \text{Reflection and expansion: } \mathbf{x}_m^{(k)} := \mathbf{e}^{(k)}, \\ f(\mathbf{x}_l^{(k)}) < f(\mathbf{r}^{(k)}) \leq f(\mathbf{x}_s^{(k)}) \vee f(\mathbf{e}^{(k)}) > f(\mathbf{x}_l^{(k)}) & \quad \text{Reflection: } \mathbf{x}_m^{(k)} := \mathbf{r}^{(k)}. \end{aligned}$$

In the remaining cases, the algorithm assumes that the polyhedron is already close to the searched-for minimum. The reflection is accepted as intermediate vertex, i. e., $\mathbf{x}_h^{(k)} := \mathbf{r}^{(k)}$ if $f(\mathbf{r}^{(k)}) \geq f(\mathbf{x}_h^{(k)})$. The next operation is to contract the (reflected) polyhedron according to

$$\mathbf{k}^{(k)} = \mathbf{c}^{(k)} + c \left(\mathbf{x}_h^{(k)} - \mathbf{c}^{(k)} \right) \quad \text{with } 0 < c < 1.$$

This contraction with or without reflection is accepted if $f(\mathbf{k}^{(k)}) \leq f(\mathbf{x}_h^{(k)})$. If the contraction is not successful, the searched-for minimum is assumed in the vicinity of $\mathbf{x}_l^{(k)}$ and the polyhedron is expected to be too large to detect the minimum. Thus, the final operation is to reduce the (reflected) polyhedron around the vertex $\mathbf{x}_l^{(k)}$:

$$\mathbf{x}_i^{(k)} = \mathbf{x}_l^{(k)} + \frac{1}{2} \left(\mathbf{x}_i^{(k)} - \mathbf{x}_l^{(k)} \right) \quad i = 1, \dots, n+1.$$

Obviously, there are six different transformations that can be applied to the polyhedron in each iteration: reflection, reflection and expansion, contraction, reflection and contraction, reduction, reflection and reduction. These transformations enable the polyhedron to propagate through the parameter space (reflection) with the option to increase and decrease its propagation velocity (expansion and contraction, respectively). In the vicinity of the searched-for minimum or in narrow “valleys”, the polyhedron is also able to shrink (reduction).

The six transformations are depicted in Figure C.1 for a three-dimensional parameter space, i. e., $n = 3$ and the coefficients $a = 1$ for reflection, $b = 2$ for expansion, and $c = 1/2$ for contraction. These coefficients are also used for the CRS stack implementation.

Of course, after each iteration a stop criterion has to be evaluated. The criterion given in Himmelblau (1972) reads

$$\sqrt{\frac{1}{n+1} \sum_{i=1}^{n+1} \left[f(\mathbf{x}_i^{(k)}) - f(\mathbf{c}^{(k)}) \right]^2} \leq \varepsilon, \quad (\text{C.1})$$

the quadratic mean of the objective function at the vertices relative to the objective function’s value at the centroid.

C.2 Adaptation to the CRS stack method

Although the flexible polyhedron search is very robust, the optimization problem of the CRS stack method requires some considerations and adaptations for a successful and more efficient application. As already mentioned, the parameter space has three dimensions and the polyhedra are, thus, tetrahedra. Of particular importance are the following topics:

- a transformation of the parameter space to make it more linear and to avoid numerical problems
- the calculation of the initial tetrahedron from the initial wavefield attributes

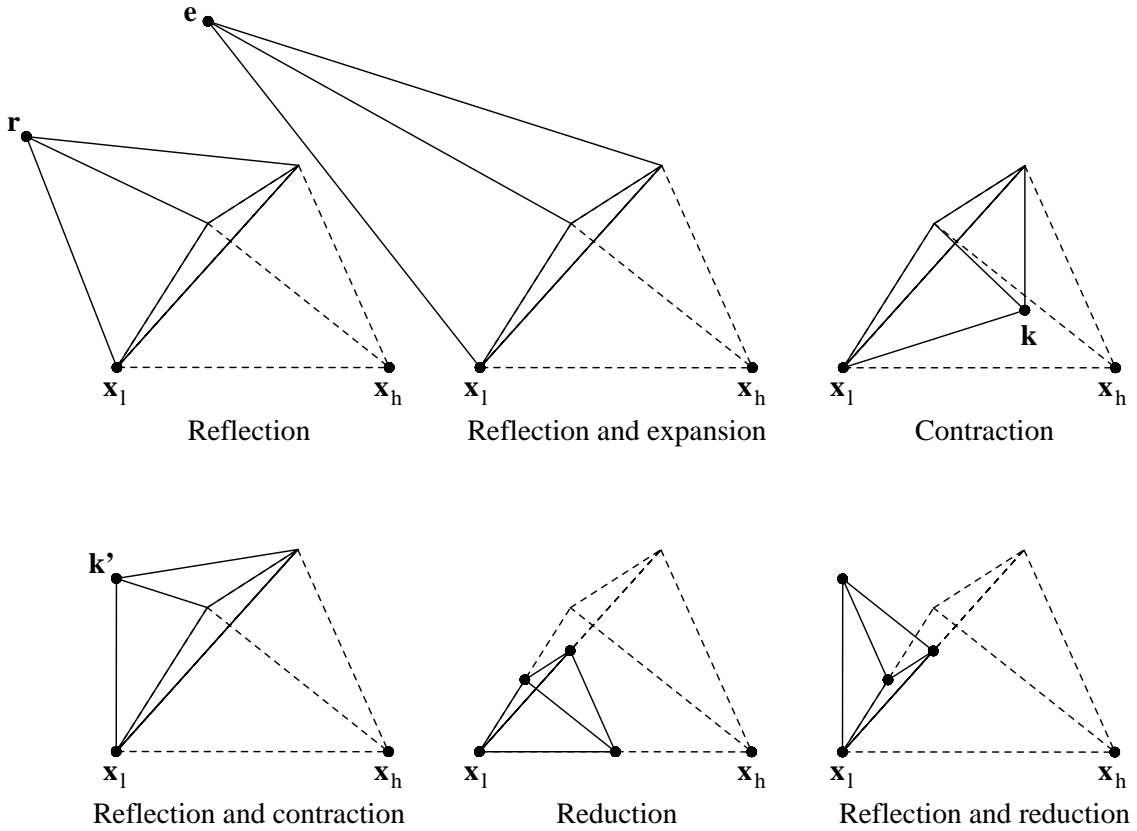


Figure C.1: Possible transformations of the tetrahedron in the flexible polyhedron search algorithm for three parameters. The dashed tetrahedron represents the result of the preceding iteration or the initial polyhedron (first iteration).

- the stop criterion

From the volume of coherence values shown in Figure 3.1 it is obvious that the coherence, i. e., the objective function of the local optimization, is a strongly non-linear function of the wavefield attributes, especially with respect to R_N (note the axes of the coherence volume). Furthermore, R_{NIP} and, more likely, R_N might be almost infinity, thus causing numerical problems. Due to the periodicity of trigonometric functions, α appears to be a less critical parameter—if it happens to leave the range of $-\pi/2 \leq \alpha \leq \pi/2$, a simple operation is sufficient to “unwrap” the emergence angle.

My initial idea to address these problems was to project the plane $(R_{NIP}, 1/R_N)$ onto a Riemann sphere with a given radius R_S . In this way, the radius R_{NIP} and the curvature $1/R_N$ are parameterized by angles that cause no numerical problems. Furthermore, it turned out that with an appropriate radius R_S , the parameter space appears more linear. This increases the performance of the search algorithm. Applications to various data sets demonstrated that the transformation

of R_{NIP} is less critical and can be avoided. In the current application, only R_{N} is transformed according to

$$\beta = \arctan \frac{R_{\text{S}}}{R_{\text{N}}},$$

where empirical values of R_{S} in the order of 100 m appear to be appropriate.

The flexible polyhedron search requires an initial tetrahedron with a finite volume to start the search. The initial wavefield attributes have to be varied to calculate the vertices of the initial tetrahedron. Due to the multitude of local maxima in the coherence volume, the size of the initial tetrahedron is crucial for a successful optimization: Jäger (1999) demonstrated that with a too large size, the optimization process immediately leaves the vicinity of the searched-for maximum, whereas a too small initial tetrahedron is usually trapped in a local maximum. In the current implementation, the initial tetrahedron is generated according to

$$\mathbf{x}_1^{(0)} = \begin{pmatrix} \alpha \\ \beta \\ R_{\text{NIP}} \end{pmatrix}, \quad \mathbf{x}_2^{(0)} = \begin{pmatrix} \alpha - \delta_1 \\ \beta - \delta_2 \\ R_{\text{NIP}} \delta_3 \end{pmatrix}, \quad \mathbf{x}_3^{(0)} = \begin{pmatrix} \alpha + \delta_1 \\ \beta - \delta_2 \\ R_{\text{NIP}} \end{pmatrix}, \quad \mathbf{x}_4^{(0)} = \begin{pmatrix} \alpha \\ \beta + \delta_2 \\ R_{\text{NIP}} / \delta_3 \end{pmatrix}.$$

Empirical values for the angle variations δ_1 and δ_2 are about 6° , the factor δ_3 for the variation of R_{NIP} is about 1.05, i. e., a variation of 5 %.

As a rule of thumb, the flexible polyhedron search in a n -dimensional parameter space converges after $\approx 20n$ iterations. For the CRS stack problem with $n = 3$ I actually observe typically 60-70 iterations in case of convergence. To avoid unnecessary computations in areas far off actual reflection events where the optimization does not converge at all, a maximum number of iterations k_{max} is introduced as an additional stop criterion, usually with values about 100.

Furthermore, the stop criterion (C.1) depends on the scale of the objective function that may strongly vary depending on the ZO location to be simulated and the used coherence criterion. To remove this dependency, I propose to normalize the quadratic mean with the objective function's value at the centroid.

Another specific problem of the CRS stack is that for small absolute values of R_{NIP} and/or R_{N} the operator becomes very steep and quickly leaves the available pre-stack data volume. In such situations, the number of contributing traces decreases. As already mentioned in Chapter 3, coherence values computed from different numbers of traces are not comparable, but tend to increase with decreasing number of traces. As a consequence, the optimization might converge by systematically reducing the number of contributing traces. To avoid this unwanted behavior, the optimization is stopped if the number of traces $n_T^{(k)}$ contributing to the last calculated vertex in iteration k is more than 10 % below the number of traces $n_T^{(0)}$ contributing to the vertex $\mathbf{x}_1^{(0)}$ given by the initial attributes.

With these extensions, the stop criterion now reads

$$\frac{1}{|f(\mathbf{c}^{(k)})|} \sqrt{\frac{1}{n+1} \sum_{i=1}^{n+1} [f(\mathbf{x}_i^{(k)}) - f(\mathbf{c}^{(k)})]^2} \leq \varepsilon \quad \vee \quad k > k_{\text{max}} \quad \vee \quad \frac{n_T^{(k)}}{n_T^{(0)}} < 0.9.$$

Appendix D

Pulse stretch and CRS stack

Conventional imaging methods often systematically distort the wavelet with respect to its length and its shape. The former leads to a reduced frequency content in the resulting image and the latter bears the risk of a misinterpretation of the results. These inherent effects occur even if the stacking operators are kinematically correct: they are due to the usually smooth parameterization of the model, irrespective if this model is explicitly given (model-based imaging methods like Kirchhoff migration) or implicitly derived from the pre-stack data (data-oriented methods like NMO/DMO/stack).

This kind of unwanted changes of the wavelet do not occur during the CRS stack and similar data-oriented imaging methods like Multifocusing (Berkovitch et al., 1994; Landa et al., 1999) or the delayed hyperbola approaches by de Bazelaire (1988); Thore et al. (1994). To explain this fact, I will briefly review the reasons for the pulse stretch in conventional imaging methods for a simple example where the respective operators are kinematically correct: I consider a horizontal planar reflector at depth z with a homogeneous overburden with the velocity v_0 . In terms of midpoint and half-offset coordinates, the kinematic reflection response of this reflector is, of course, simply given by

$$t(h) = \frac{2}{v_0} \sqrt{h^2 + z^2} = \sqrt{t_0^2 + \frac{4h^2}{v_0^2}}, \quad (\text{D.1})$$

where $t_0 = 2z/v_0$ denotes the ZO traveltimes. For a medium without attenuation, the pre-stack data can be represented as a temporal convolution of the source wavelet with the temporal length T with the kinematic reflection response.¹ In other words, the pulse length is identical for all shot and receiver locations. An undistorted imaging result can be obtained by stacking along the kinematic reflection response (D.1) vertically shifted to all locations in the time domain within the temporal length of the wavelet:

$$t(h, \Delta t) = \sqrt{t_0^2 + \frac{4h^2}{v_0^2}} + \Delta t \quad \text{with} \quad -\frac{T}{2} \leq \Delta t \leq \frac{T}{2}, \quad (\text{D.2})$$

¹For critical and super-critical reflection angles, an additional phase shift occurs. However, I will not consider this case here.

where I assume that the wavelet is zero-phase and centered around the traveltime t . In the following, I will discuss how different imaging methods handle this simple situation.

A NMO correction with the constant velocity v_0 yields the correct traveltime (D.1) and, thus, the correct operator for the center of the wavelet. However, the NMO operators attached to all other ZO traveltimes differ from the iso-phase curves (D.2) in the data: the moveout difference between the two operators attached to the ZO traveltimes $t_0^{(\pm)} = t_0 \pm T/2$

$$\Delta t_{\text{NMO}} = \sqrt{t_0^{(+)^2 + \frac{4h^2}{v_0^2}} - \sqrt{t_0^{(-)^2 + \frac{4h^2}{v_0^2}}} \leq T \quad (\text{D.3})$$

is not constant, but decreases with increasing offset. This leads to the well known NMO pulse stretch.

A pre-stack Kirchhoff migration collects the constructively interfering contributions along the CRP trajectory and its vicinity. For this simple example, the CRP trajectory coincides with the NMO operator and the CMP stack operator. Thus, the same considerations concerning the pulse stretch also apply to Kirchhoff migration: the vertical distance between neighboring Kirchhoff operators in the CRP gather is again not constant.

The pulse stretch is due to the fact that the shape of the operators not only depends on the velocity v_0 , but also on the ZO traveltime (NMO and Kirchhoff time migration) or the considered depth point (Kirchhoff depth migration). This is an inherent property of the hyperbolic traveltime expressions used for NMO, CMP stack, and Kirchhoff migration. Parabolic representations like Equation (2.16) avoid the pulse stretch as their shape remains unchanged for neighboring points. However, such representations are less accurate, especially in the considered case where the hyperbolic representations are exact.

The CRS operator (2.17) is also an hyperbolic representation and its shape also explicitly depends in the ZO traveltime t_0 . Thus, one might conclude that the CRS stack approach also suffers from the pulse stretch problem. For the considered example where $\alpha = 0$ and $R_N = \infty$, the CRS operator reduces to

$$t(x_m, h) = \sqrt{t_0^2 + \frac{2t_0 h^2}{v_0 R_{\text{NIP}}}} \quad (\text{D.4})$$

for any midpoint location x_m . For the center of the wavelet this represents the exact kinematic reflection response of the reflector with $R_{\text{NIP}} = z = v_0 t_0 / 2$. If I use this expression for R_{NIP} for neighboring ZO locations, I obtain the same pulse stretch as for an NMO correction. However, the CRS stack fits the stacking operator separately to the actual reflection response for each ZO location to be simulated. In the ideal case, the coherence analyses yield operators corresponding to the actual iso-phase surfaces (D.2) in the pre-stack data. Thus, the simple relation between R_{NIP} and z only applies for the center of the wavelet. For all other locations, R_{NIP} varies such that the pulse stretch is avoided. Similar considerations apply not only in the CMP gather, but in the entire CRS super gathers.

Appendix E

Acquisition geometry of pre-stack data

The CRS stack method as presented in this thesis is designed to handle pre-stack data acquired along a straight line. For the marine data examples discussed in Chapters 4-6 the acquisition surface can be considered as a perfect plane. However, the shots and receivers are not necessarily distributed along a straight line.

The current implementation of the CRS stack allows to automatically determine a straight line that provides the best possible fit to all shot/receiver midpoints given by the input data. This is performed by means of a least square fit, namely a linear regression. However, this approach does not minimize the distance between the midpoints and the regression line, but only one component of the distance vector. Nevertheless, an iterative application of the linear regression is suited to fit the problem to the least square method rather than vice versa. With the midpoint vectors $\mathbf{m}^{(i)} = (m_{x,i}, m_{y,i})^T$, the strategy can be summarized as follows:

- apply linear regression to determine the coefficients a_1, b_1 of $m_{y,i} = a_1 + b_1 m_{x,i}$
- apply linear regression to determine the coefficients a_2, b_2 of $m_{x,i} = a_2 + b_2 m_{y,i}$
- the line with the smaller slope is closer to the searched-for solution, thus if $b_2 < b_1$, substitute $b_1 := 1/b_2$ and $a_1 := a_2/b_2$
- rotate coordinate system by $-\arctan b_1$ and re-perform linear regression according to step 1
- repeat preceding step until $|b_1|$ is negligible: the minimization of $\sum_i (m_{y,i} - a_1)^2$ then coincides with the minimization of the euclidian distances between the midpoints and the regression line.

In the transformed coordinate system of the last iteration, the shot and receiver coordinates are given in inline and crossline components. The former serve to compute the 1-D midpoint coordinate $x_{m,i}$ along the 2-D line, in other words, the midpoints of all traces are projected onto the

acquisition line. The half-offset h , however, is half the actual euclidian distance between shot and receiver, i. e., $h_i = |\mathbf{h}^{(i)}| = |\mathbf{x}_s^{(i)} - \mathbf{x}_g^{(i)}|/2$.

The current implementation also allows to reject traces with

- a midpoint located too far from the regression line, $y_{m,i} > y_{m,\max}$,
- a too large offset azimuth compared to the regression line, $\phi = \arccos \left[\mathbf{h}^{(i)} \cdot (1, 0)^T \right] > \phi_{\max}$,
- or traces for which the product of ϕ_i and $y_{m,i}$ exceeds a given threshold.

The third option allows to accept input traces with large offset azimuths but small offsets. All criteria refer to the rotated coordinate system, i. e., crossline ($y_{m,i}$) and inline ($x_{m,i}$) coordinates.

The approximation of a straight acquisition line is appropriate for the data sets presented in this thesis. For the 2-D CRS stack I only assume that the actual acquisition line is sufficiently straight within the considered midpoint and offset aperture. Thus, one might also fit any arbitrary smooth curve to the midpoints given in the data instead of a straight line.

Appendix F

Used hardware and software

The CRS stack implementation was installed and applied on various platforms with different operating systems (for details, see Mann, 2001c). However, all results shown in this thesis and the thesis itself were entirely processed on a PC with two 400 MHz Intel Pentium II processors, 512 MB RAM, and the operating system SuSE Linux 6.1.

The CRS stack implementation is entirely written in C++ (Stroustrup, 1997) and requires the standard libraries as well as the Standard Template Library (STL). Processing parameters can be passed to the implementation via the command line and optional parameter files. I designed the input and output routines such as to achieve a wide compatibility with the Seismic Un*x format (see below). The code was compiled with the GNU project C++ compiler version 2.91.66 and optimization level 3. The CPU times listed in Tables 4.3, 5.3, and 6.3 represent user plus system time consumed by the respective processing steps.

Additional data processing and most of the data visualization, on screen as well as in PostScript format, was performed with various utilities of the Seismic Un*x package release 3.4 (Cohen and Stockwell, 2000). This freely available package uses a data format that is very similar to the industry standard SEG-Y and allows to handle irregular acquisition geometries. Further information about Seismic Un*x can be found in Stockwell (1997) and Stockwell (1999).

The Green's function table for the CINCA104-13 data was computed by means of the NORSAR-3D ray modeling package (see <http://www.norsar.no>). The post-stack depth migrations based on this GFT were performed with Uni3D, a true-amplitude migration and demigration software developed at the Geophysical Institute, University of Karlsruhe.

For the analyses of the multiples in the Sigsbee 2A and BGR99-07 data and the examples in the theory chapter, I performed the ray tracing and the forward calculation of the CRS wavefield attributes with rayx. This extended 2-D ray tracer for iso-velocity layers with arbitrarily curved interfaces was also developed at the Geophysical Institute, University of Karlsruhe.

The thesis itself was entirely processed with the document preparation system L^AT_EX (Lamport, 1986) which, in turn, is a macro package for the typesetting system T_EX (Knuth, 1991). The maps (Figures 5.1 and 6.1) were generated with the Generic Mapping Tools (GMT) package (Wessel and Smith, 1991).

List of Figures

Chapter 2 – Theory	7
2.1 Simple model consisting of three homogeneous layers. The hypothetical NIP and normal wavefronts are depicted for a chosen reflection point.	11
2.2 Circular normal wavefronts stemming from the image point \mathfrak{X}_N^* for two different ZO rays.	14
2.3 Model with three iso-velocity layers and two chosen central ZO rays reflected at the second interface.	20
2.4 True ZO reflection response of second interface, true diffraction response of point P_1 and their attribute-based approximations.	21
2.5 True ZO reflection response of second interface, true diffraction response of point P_2 and their attribute-based approximations.	22
2.6 The first Fresnel zones at the reflector for the two ZO rays shown in Figure 2.3 and their projected counterparts for the different approximations.	24
2.7 Definition of the observation plane in the 3-D case. The plane is given by the acquisition line and the emerging central ray.	28
 Chapter 3 – Implementation	 31
3.1 Coherence values as a function of the wavefield attributes for a ZO sample located on a reflection event.	32
3.2 Simplified flowchart of the pragmatic search strategy.	37
3.3 Coherence as a function of emergence angle α calculated along a linear operator in the CMP stacked section for a ZO location with three intersecting events.	39
3.4 Simplified flowchart of the extended CRS search strategy.	41
3.5 Tested stacking operators for the automatic CMP stack.	42

3.6	Coherence as a function of the stacking velocity for a ZO sample located on a reflection event intersecting a multiple event.	44
3.7	Hyperbolic stacking operators in the ZO section.	45
3.8	ZO, CMP, and spatial CRS apertures.	50
Chapter 4 – Synthetic data example: Sigsbee 2A		53
4.1	CMP fold and area covered with pre-stack data.	54
4.2	Near-offset section extracted from the pre-stack data.	56
4.3	Constant velocity Stolt time migration of the NMO-corrected near-offset section.	57
4.4	Constant velocity Stolt time migration of the NMO-corrected and stacked pre-stack data	59
4.5	A simple model consisting of two homogeneous layers. The syncline structure mimics a feature of the salt top.	60
4.6	Result of the automatic CMP stack.	63
4.7	Stacking velocity section associated with the CMP stacked section shown in Figure 4.6.	64
4.8	Coherence section associated with the CMP stacked section shown in Figure 4.6.	65
4.9	Result of the optimized CRS stack restricted to the projected first Fresnel zone.	68
4.10	Coherence section for the dominant events associated with the CRS stacked section shown in Figure 4.9.	70
4.11	Emergence angle section for the dominant events associated with the CRS stacked section shown in Figure 4.9.	71
4.12	Section with the curvature of the normal wavefront for the dominant events associated with the CRS stacked section shown in Figure 4.9.	72
4.13	Section with the radius of curvature of the NIP wavefront for the dominant events associated with the CRS stacked section shown in Figure 4.9.	73
4.14	Subsets of the optimized CRS stack result obtained with the pragmatic and the extended CRS stack strategy, respectively.	74
4.15	Emergence angles detected for the CRS stacked section obtained with the extended CRS stack strategy.	75
4.16	Ratio of curvatures of the normal and NIP wavefronts for the same events as shown in Figure 4.15.	75
4.17	Size of the attribute-derived projected first Fresnel zone of the dominant events relative to the user-given ZO aperture.	77
4.18	Attribute-based time migration corresponding to the optimized CRS stacked section shown in Figure 4.9.	79

Chapter 5 – Real data example: CINCA SO104-13	81
5.1 Location of the acquisition line.	82
5.2 CMP fold and locations of the pre-stack data traces.	83
5.3 Interpreted time section provided by the BGR.	84
5.4 ZO simulation obtained from the conventional NMO/DMO/stack processing chain.	85
5.5 Constant velocity Stolt time migration of the ZO section shown in Figure 5.4.	86
5.6 Smoothed interval velocity model used for post-stack Kirchhoff depth migration.	87
5.7 Kirchhoff post-stack depth migration of the ZO section shown in Figure 5.4.	88
5.8 Result of the optimized CRS stack restricted to the projected first Fresnel zone.	91
5.9 Coherence section for the dominant events associated with the optimized CRS stack result shown in Figure 5.8.	93
5.10 Emergence angle section for the dominant events associated with the optimized CRS stack result shown in Figure 5.8.	94
5.11 Radius of curvature of the NIP wavefront for the dominant events associated with the optimized CRS stack result shown in Figure 5.8.	95
5.12 Curvature of the normal wavefront for the dominant events associated with the optimized CRS stack result shown in Figure 5.8.	96
5.13 Size of the projected first Fresnel zone of the dominant events relative to the given ZO aperture.	98
5.14 Ratio of the radii of curvatures $ R_N /R_{NIP}$ of the dominant events.	100
5.15 Attribute-based time migration of the optimized CRS stack result shown in Figure 5.8.	101
5.16 A detail of the attribute-based time migration of the optimized CRS stack result computed with the pragmatic CRS strategy and the extended CRS strategy, respectively.	102
5.17 Post-stack depth migration of the optimized CRS stack result shown in Figure 5.8.	103
Chapter 6 – Real data example: BGR99-07	105
6.1 Location of the acquisition line.	106
6.2 CMP fold of pre-stack data traces.	107
6.3 ZO simulation obtained from the conventional NMO/DMO/stack processing chain.	108
6.4 f-k domain time migration result of the ZO section shown in Figure 6.3.	109

List of Figures

6.5	Result of the unconstrained automatic CMP stack.	112
6.6	Stacking velocity section associated with the ZO section shown in Figure 6.5. . .	113
6.7	Result of the constrained automatic CMP stack.	115
6.8	Forward-calculated stacking velocities associated with the P-P primary event and the P-P-P-P multiple event, respectively, stemming from the seafloor.	116
6.9	Result of the optimized CRS stack.	118
6.10	Coherence section associated with the optimized CRS stacked section shown in Figure 6.9 for the dominant events.	119
6.11	Emergence angle section associated with the optimized CRS stacked section shown in Figure 6.9 for the dominant events.	121
6.12	Section with the curvature of the normal wavefront associated with the optimized CRS stacked section shown in Figure 6.9 for the dominant events.	122
6.13	Section with the radius of curvature of the NIP wavefront associated with the optimized CRS stacked section shown in Figure 6.9 for the dominant events.	123
6.14	Size of the projected first Fresnel zone of the dominant events relative to the given ZO aperture.	124
6.15	Subsets of the NMO corrected (1500 m/s) raw near-offset data and the CRS stacked section, respectively.	125
6.16	Subsets of the coherence section and the section with the radius of curvature of the NIP wavefront of the dominant events, respectively.	126
Appendices		133
A.1	Sign convention for emergence and incidence angles at interfaces and at the acquisition surface.	133
A.2	Sign convention for the curvatures of propagating wavefronts.	134
A.3	Sign convention for the curvature of an interface.	134
C.1	Possible transformations of the tetrahedron in the flexible polyhedron search algorithm for three parameters.	142

List of Tables

Chapter 4 – Synthetic data example: Sigsbee 2A	53
4.1 Acquisition parameters of the pre-stack data set.	54
4.2 Processing parameters used for the ZO simulation by means of the CRS stack. . .	61
4.3 Absolute and relative CPU times required for the successive processing steps. . .	62
Chapter 5 – Real data example: CINCA SO104-13	81
5.1 Acquisition parameters of the pre-stack data set.	82
5.2 Processing parameters used for the ZO simulation by means of the CRS stack. . .	90
5.3 Absolute and relative CPU times required for the successive processing steps. . .	92
Chapter 6 – Real data example: BGR99-07	105
6.1 Acquisition parameters of the pre-stack data set.	106
6.2 Processing parameters used for the ZO simulation by means of the CRS stack. . .	111
6.3 Absolute and relative CPU times required for the successive processing steps. . .	114

References

- Bergler, S., Chira, P., Mann, J., Vieth, K.-U., and Hubral, P. (2002). Stacking velocity analysis with CRS Stack attributes. In *64th Mtg. Eur. Assn. Geosci. Eng., Extended Abstracts*, Session B003.
- Bergler, S., Höcht, G., Chira-Oliva, P., Zhang, Y., and Hubral, P. (2001). Hyperbolic reflection moveout revisited. In McBarnet, A., editor, *EAGE 1951-2001 — Reflections on the first 50 years*, pages 64–66. Blackwell Science.
- Berkovitch, A., Gelchinsky, B., and Keydar, S. (1994). Basic formulae for multifocusing stack. In *Extended Abstracts*. 56th Mtg. Eur. Assoc. Expl. Geophys. Session: P140.
- Bleistein, N. (1984). *Mathematical methods for wave phenomena*. Academic Press Inc., Orlando.
- Born, M. and Wolf, E. (1959). *Principle of optics*. Pergamon Press Inc.
- Bortfeld, R. (1989). Geometrical ray theory: Rays and traveltimes in seismic systems (second-order approximations of the traveltimes). *Geophysics*, 54(3):342–349.
- Brown, A. R. (2001). Calibrate yourself to your data! A vital first step in seismic. *Geophys. Prosp.*, 49(6):729–733.
- Buttkus, B. (1991). *Spektralanalyse und Filtertheorie in der angewandten Geophysik*. Springer-Verlag.
- Chira-Oliva, P., Tygel, M., Zhang, Y., and Hubral, P. (2001). Analytic CRS stack formula for 2D curved measurement surface and finite-offset reflections. *J. Seis. Expl.*, 10:245–262.
- Cohen, J. K. and Stockwell, J. J. W. (2000). *CWP/SU: Seismic Unix Release 34: a free package for seismic research and processing*. Center for Wave Phenomena, Colorado School of Mines.
- Cristini, A., Cardone, G., Chira, P., Hubral, P., and Marchetti, P. (2001). 3D zero-offset Common Reflection Surface Stack for land data. In *Workshop on velocity model independent imaging for complex media, Extended Abstracts*, Session W5-13, <http://www.seg.org/research/2001/W5>. Soc. of Expl. Geophys.
- Cristini, A., Cardone, G., and Marchetti, P. (2002). 3D zero-offset Common Reflection Surface Stack for land data – real data example. In *64th Mtg. Eur. Assn. Geosci. Eng., Extended Abstracts*, Session B015.

References

- de Bazelaire, E. (1988). Normal moveout revisited – inhomogeneous media and curved interfaces. *Geophysics*, 53(2):143–157.
- de Bazelaire, E. and Thore, P. (1987). Pattern recognition applied to time and velocity contours. In *Expanded Abstracts*, volume 87. 57th Annual Internat. Mtg., Soc. Expl. Geophys. Session: POS2.14.
- de Bazelaire, E. and Viallix, J. R. (1994). Normal moveout in focus. *Geophys. Prosp.*, 42(5):477–499.
- Deregowski, S. M. (1986). What is DMO? *First Break*, 4(7):7–24.
- Deregowski, S. M. and Rocca, F. (1981). Geometrical optics and wave theory of constant offset sections in layered media. *Geophysics*, 29(3):384–406.
- Dürbaum, H. (1954). Zur Bestimmung von Wellengeschwindigkeiten aus Reflexions-Seismischen Messungen. *Geophys. Prosp.*, 2(2):151–176.
- Gelchinsky, B., Berkovitch, A., and Keydar, S. (1997). Multifocusing homeomorphic imaging: Parts I and II. In *Course Notes*. Special Course on Homeomorphic Imaging, Seeheim, Germany.
- Gelchinsky, B., Berkovitch, A., and Keydar, S. (1999a). Multifocusing homeomorphic imaging - Part 1. Basic concepts and formulas. *J. Appl. Geoph.*, 42(3,4):229–242.
- Gelchinsky, B., Berkovitch, A., and Keydar, S. (1999b). Multifocusing homeomorphic imaging - Part 2. Multifold data set and multifocusing. *J. Appl. Geoph.*, 42(3,4):243–260.
- Gelchinsky, B. and Keydar, S. (1999). Homeomorphic imaging approach – theory and practice. *J. Appl. Geoph.*, 42(3,4):169–228.
- Glogovsky, V., Landa, E., and Pfaffenholz, J. (2001). Integrated approach for subsalt depth imaging: a synthetic case study. In *Workshop on velocity model independent imaging for complex media, Extended Abstracts*, Session W5-7, <http://www.seg.org/research/2001/W5>. Soc. of Expl. Geophys.
- Hale, D. (1984). Dip-moveout by Fourier transform. *Geophysics*, 49(6):741–757.
- Hertweck, T., Jäger, C., Goertz, A., and Schleicher, J. (2001a). Aperture effects in 2.5-D Kirchhoff migration. *Submitted to Geophysics*.
- Hertweck, T., Jäger, C., Goertz, A., and Schleicher, J. (2001b). Aperture effects in Kirchhoff migration. *Annual Report, Wave Inversion Technology Consortium*.
- Himmelblau, D. (1972). *Applied Nonlinear Programming*. McGraw-Hill, New York.
- Hindriks, C. O. H., Bolte, J. F. B., and Verschuur, D. J. (2001). CFP redatuming methodology for complex overburdens. In *Workshop on velocity model independent imaging for complex media, Extended Abstracts*, Session W5-6, <http://www.seg.org/research/2001/W5>. Soc. of Expl. Geophys.

-
- Höcht, G. (1998). The Common Reflection Surface Stack. Master's thesis, Universität Karlsruhe.
- Höcht, G. (2002). *Traveltime approximations for 2D and 3D media and kinematic wavefield attributes*. PhD thesis, Universität Karlsruhe.
- Höcht, G., de Bazelaire, E., Majer, P., and Hubral, P. (1999). Seismics and optics: hyperbolae and curvatures. *J. Appl. Geoph.*, 42(3,4):261–281.
- Hubral, P. (1983). Computing true amplitude reflections in a laterally inhomogeneous earth. *Geophysics*, 48(8):1051–1062.
- Hubral, P. and Krey, T. (1980). *Interval velocities from seismic reflection traveltime measurements*. Soc. Expl. Geophys.
- Hubral, P. and Mann, J. (2000). New aspects of zero-offset simulation from multi-coverage prestack data. In *Tagungsband*, pages 133–161. 20. Mintrop-Seminar, Deutsche Wissenschaftliche Gesellschaft für Erdöl, Erdgas und Kohle e. V.
- Hubral, P., Schleicher, J., Tygel, M., and Hanitzsch, C. (1993). Determination of Fresnel zones from traveltime measurements. *Geophysics*, 58(5):703–712.
- Jäger, R. (1999). The Common Reflection Surface Stack - Theory and Application. Master's thesis, Universität Karlsruhe.
- Jäger, R., Mann, J., Höcht, G., and Hubral, P. (2001). Common-reflection-surface stack: Image and attributes. *Geophysics*, 66(1):97–109.
- Judson, D. R., Lin, J., Schultz, P. S., and Sherwood, J. W. C. (1980). Depth migration after stack. *Geophysics*, 45(3):361–375.
- Knuth, D. E. (1991). *Computers & typesetting, Vol. A: The T_EXbook*. Addison-Wesley.
- Kravtsov, Y. A. and Orlov, Y. I. (1990). *Geometrical optics of inhomogeneous media*. Springer Verlag.
- Lamport, L. (1986). *L^AT_EX: A document preparation system*. Addison-Wesley.
- Landa, E., Gurevich, B., Keydar, S., and Trachtman, P. (1999). Application of multifocusing method for subsurface imaging. *J. Appl. Geoph.*, 42(3,4):283–300.
- Majer, P. (2000). Inversion of seismic parameters: Determination of the 2-D iso-velocity layer model. Master's thesis, Universität Karlsruhe.
- Mann, J. (1997). Herleitung und Implementierung der Seismic-Image-Wave-Theorie und Anwendung auf reflexionsseismische Meßdaten. Diplomarbeit, Geophysikalisches Institut der Universität Karlsruhe.
- Mann, J. (2001a). Common-Reflection-Surface Stack and conflicting dips. In *Extended Abstracts*, Session P 077. 63rd Mtg. Eur. Assn. Geosci. Eng.

References

- Mann, J. (2001b). Common-Reflection-Surface Stack and conflicting dips. In *Extended Abstracts*, Session SP 5.3. 71st Annual Internat. Mtg., Soc. Expl. Geophys.
- Mann, J. (2001c). *Common-Reflection-Surface Stack: User's manual to version 4.2*. Geophysical Institute, University of Karlsruhe.
- Mann, J. (2001d). Macro model independent seismic reflection imaging. In McBarnet, A., editor, *EAGE 1951-2001 — Reflections on the first 50 years*, pages 69–70. Blackwell Science.
- Mann, J., Bergler, S., and Hubral, P. (2001). Common-Reflection-Surface stack. In *Workshop on velocity model independent imaging for complex media*, *Extended Abstracts*, Session W5-4, <http://www.seg.org/research/2001/W5>. Soc. of Expl. Geophys.
- Mann, J., Bergler, S., Zhang, Y., Chira, P., and Hubral, P. (2002). Generalizations of the Common-Reflection-Surface Stack. In *64th Mtg. Eur. Assn. Geosci. Eng., Extended Abstracts*, Session E023.
- Mann, J., Höcht, G., Jäger, R., and Hubral, P. (1999a). Common Reflection Surface Stack – an attribute analysis. In *Extended Abstracts*. 61st Mtg. Eur. Assn. Geosci. Eng. Session P140.
- Mann, J. and Hubral, P. (2001). Common-Reflection-Surface Stack – Theorie und Praxis. *Mitteilungen der Deutschen Geophysikalischen Gesellschaft*, Sonderband II/2001:61–71.
- Mann, J., Hubral, P., Traub, B., Gerst, A., and Meyer, H. (2000). Macro-Model Independent Approximative Prestack Time Migration. In *Extended Abstracts*. 62nd Mtg. Eur. Assn. Geosci. Eng. Session B-52.
- Mann, J., Jäger, R., Höcht, G., and Hubral, P. (1999b). Common-reflection-surface stack and wavefield attributes. In *Extended abstracts*. 6th Internat. Congress, Sociedade Brasileira de Geofísica.
- Mann, J., Jäger, R., Müller, T., Höcht, G., and Hubral, P. (1999c). Common-reflection-surface stack – a real data example. *J. Appl. Geoph.*, 42(3,4):301–318.
- Mann, J., Müller, T., Jäger, R., Höcht, G., and Hubral, P. (1999d). Applications of the common-reflection-surface stack. In *Expanded Abstracts*. 69th Annual Internat. Mtg., Soc. Expl. Geophys.
- Mayne, W. H. (1962). Common reflection point horizontal data stacking techniques. *Geophysics*, 27(6):927–938.
- Müller, T. (1998). Common Reflection Surface Stack versus NMO/STACK and NMO/DMO/STACK. In *Extended Abstracts*. 60th Annual Internat. Mtg., Eur. Assn. Geosci. Eng. Session 1-20.
- Müller, T. (1999). *The common reflection surface stack – seismic imaging without explicit knowledge of the velocity model*. Der Andere Verlag, Bad Iburg.

-
- Müller, T., Jäger, R., and Höcht, G. (1998). Common reflection surface stacking method – imaging with an unknown velocity model. In *Expanded Abstracts*, pages 1764–1767. 68th Annual Internat. Mtg., Soc. Expl. Geophys.
- Neidell, N. S. and Taner, M. T. (1971). Semblance and other coherency measures for multichannel data. *Geophysics*, 36(3):482–497.
- Nelder, J. A. and Mead, R. (1965). A simplex method for function minimization. *Computer Journal*, 7:308–313.
- Perroud, H., Hubral, P., Höcht, G., and de Bazelaire, E. (1997). Migrating around in circles - part III. *The Leading Edge*, June:875–883.
- Pfaffenholz, J. (2001). Sigsbee2 synthetic subsalt data set: image quality as function of migration algorithm and velocity model error. In *Workshop on velocity model independent imaging for complex media, Extended Abstracts*, Session W5-5, <http://www.seg.org/research/2001/W5>. Soc. of Expl. Geophys.
- Schleicher, J. (1993). *Bestimmung von Reflexionskoeffizienten aus Reflexionsseismogrammen*. PhD thesis, Universität Karlsruhe.
- Schleicher, J., Hubral, P., Tygel, M., and Jaya, M. S. (1997). Minimum apertures and fresnel zones in migration and demigration. *Geophysics*, 62(01):183–194.
- Schleicher, J. and Santos, L. T. (2001). Resolution of Kirchhoff depth migration: offset and angle dependency. *Annual Report, Wave Inversion Technology Consortium*.
- Schleicher, J., Tygel, M., and Hubral, P. (1993). Parabolic and hyperbolic paraxial two-point traveltimes in 3D media. *Geophys. Prosp.*, 41(4):495–514.
- Stockwell, J. J. W. (1997). Free software in education: a case study of CWP/SU: Seismic Un*x. *The Leading Edge*, 16(7):1045–1049.
- Stockwell, J. J. W. (1999). The CWP/SU: Seismic Un*x Package. *Computers and Geosciences*, 25(4):415–419.
- Stoll, R. D. (1974). Effect of gas hydrates in sediments. In Kaplan, I. R., editor, *Nature of gases in marine sediments*, pages 235–248. Plenum press.
- Stolt, R. H. (1978). Migration by Fourier transform. *Geophysics*, 43(1):23–48.
- Stroustrup, B. (1997). *The C++ Programming Language*. Addison-Wesley, 3rd edition.
- Sun, J. (2000). Limited aperture migration. *Geophysics*, 65(2):584–595.
- Taner, M. T. and Koehler, F. (1969). Velocity spectra – digital computer derivation and applications of velocity functions. *Geophysics*, 34(6):859–881.
- Thore, P. D., de Bazelaire, E., and Ray, M. P. (1994). Three-parameter equation: An efficient tool to enhance the stack. *Geophysics*, 59(2):297–308.

References

- Tucholke, B. E., Bryan, G. M., and Ewing, J. J. (1977). Gas hydrate horizons detected in seismic-profile data from the western North Atlantic. *AAPG Bull.*, 61:698–707.
- Tygel, M., Müller, T., Hubral, P., and Schleicher, J. (1997). Eigenwave based multiparameter traveltimes expansions. In *Expanded Abstracts*, pages 1770–1773. 67th Annual Internat. Mtg., Soc. Expl. Geophys.
- Ursin, B. (1982). Quadratic wavefront and traveltimes approximations in inhomogeneous layered media with curved interfaces. *Geophysics*, 47(7):1012–1021.
- Vieth, K.-U. (2001). *Kinematic wavefield attributes in seismic imaging*. PhD thesis, Universität Karlsruhe.
- Vinje, V., Åstebøl, K., Iversen, E., and Gjøystdal, H. (1999). 3-D ray modeling by wavefront construction in open models. *Geophysics*, 64(6):1912–1919.
- Vinje, V., Iversen, E., Åstebøl, K., and Gjøystdal, H. (1996a). Estimation of multivalued arrivals in 3D models using wavefront construction – Part I. *Geophys. Prosp.*, 44(5):819–842.
- Vinje, V., Iversen, E., Åstebøl, K., and Gjøystdal, H. (1996b). Estimation of multivalued arrivals in 3D models using wavefront construction – Part II: Tracing and interpolation. *Geophys. Prosp.*, 44(5):843–858.
- Vinje, V., Iversen, E., and Gjøystdal, H. (1993). Traveltimes and amplitude estimation using wavefront construction. *Geophysics*, 58(8):1157–1166.
- Vinje, V., Lecomte, I., Åstebøl, K., Iversen, E., and Gjøystdal, H. (1994). Efficient Green's functions calculation for improved 3D seismic imaging in complex areas. In *56th Mtg. Eur. Assn. Geosci. Eng., Extended Abstracts*, Session B043.
- Wessel, P. and Smith, W. H. F. (1991). Free software helps map and display data. *EOS Trans. AGU*, 72(41):441–446.
- Yilmaz, O. (1987). *Seismic data processing*. Soc. Expl. Geophys., Tulsa.
- Yilmaz, O. and Claerbout, J. F. (1980). Prestack partial migration. *Geophysics*, 45(12):1753–1779.
- Zhang, Y., Bergler, S., and Hubral, P. (2001). Common-Reflection-Surface (CRS) stack for common-offset. *Geophys. Prosp.*, 49(6):709–718.
- Zhang, Y., Höcht, G., and Hubral, P. (2002). 2D and 3D ZO CRS stack for a complex top-surface topography. In *64th Mtg. Eur. Assn. Geosci. Eng., Extended Abstracts*, Session P166.

Danksagung

Zur Entstehung der vorliegenden Dissertation haben zahlreiche Personen in unterschiedlichster Weise beigetragen. Neben den Studenten, Doktoranden und Mitarbeitern des Geophysikalischen Instituts der Universität Karlsruhe sind hierbei die Mitglieder des *Wave Inversion Technology Consortium* sowie einige sehr kooperative Unternehmen im Bereich der Kohlenwasserstoff-Exploration zu nennen. Die *European Association of Geoscientists and Engineers* und die *Society of Exploration Geophysicists* haben mir mit ihren Tagungen und Publikationen die Möglichkeit zur Präsentation und Diskussion der Forschungsergebnisse vor einem internationalem Fachpublikum geboten.

Dem *Subsalt Multiples Attenuation and Reduction Technologies (SMAART) oil industry joint venture* und der Bundesanstalt für Geowissenschaften und Rohstoffe (BGR) in Hannover danke ich für die Bereitstellung der synthetischen und realen Datenbeispiele sowie die Erlaubnis zur Publikation meiner Ergebnisse. Die BGR hat meine Arbeit durch begleitende Forschungsprojekte maßgeblich unterstützt.

Die folgende Aufzählung ist keinesfalls vollständig. Ich möchte mich daher bei all denen entschuldigen, die im Folgenden zu Unrecht nicht explizit genannt werden. Im Einzelnen gilt mein besonderer Dank folgenden Personen:

Prof. Dr. Peter Hubral danke ich für die Betreuung meiner Arbeit. Er hat mich in den letzten Jahren in jeder Hinsicht unterstützt und eine leistungsfähige und innovative Arbeitsgruppe für datenorientierte reflexionsseismische Abbildungsverfahren aufgebaut, in der ich auch weiterhin gerne arbeiten werde.

Prof. Dr. Serge Shapiro danke ich für die Übernahme des Korreferats – und seine Geduld bei den reichlich komplizierten Terminvereinbarungen.

Dr. German Höcht hat mit mir jahrelang das Büro, aber in den seltensten Fällen die Ansichten über irgendwelche Problemstellungen geteilt – zumindest zu Beginn der Diskussionen. Seine vorbehaltlose und immer konstruktive Kritik hat mir so manchen Irrweg erspart. Ich kann nur hoffen, dass er in ähnlicher Weise von mir profitieren konnte. Seine Hilfe bei mathematischen Problemen und bei der Benutzung seiner Programme war für mich unverzichtbar.

Bärbel Traub und **Alexander Gerst** danke ich für Ihre Beiträge zur Implementierung und deren Entwicklung. Es war definitiv ein Verlust, dass sie die Arbeitsgruppe verlassen haben.

Paolo Marchetti von ENI AGIP, Milano, Italien, gilt mein besonderer Dank für die Einführung meines Programms in die professionelle Anwendung. Mit seiner Hilfe konnte ich zahllose Probleme

me lokalisieren und beseitigen. Sein Engagement hat erheblich zum bemerkenswerten Erfolg des *CRS stack* beigetragen.

Dr. Henning Trappe von TEEC, Isernhagen, und seine Mitarbeiter haben ebenfalls stark zur Popularität des *CRS stack* beigetragen. Ihre ursprünglich auf meinem Programm basierenden professionellen Dienstleistungen vermitteln diese Methode einem weiten Anwenderkreis.

Dr. Heinrich Meyer von der Bundesanstalt für Geowissenschaften und Rohstoffe in Hannover danke ich für die zuvorkommende Unterstützung im Zusammenhang mit den realen Datenbeispielen.

Dr. Thilo Müller hat den Grundstein für die Anwendung der CRS-Technologie gelegt. Sein Beitrag bildet die Grundlage meiner Arbeit. Ich danke ihm für seine Einführung in die Thematik und die gute Zusammenarbeit.

Rainer Jäger hat ebenfalls maßgeblich zur ersten Implementierung des *CRS stack* beigetragen. Mein besonderer Dank gilt ihm für seine bemerkenswerte Geduld, mich in die Grundlagen von C++ einzuweihen. Inzwischen kann ich guten Gewissens sagen: es war nicht umsonst. . .

Thomas Hertweck beeindruckt mich nach wie vor mit seinem souveränen Umgang mit Betriebssystemen. Kaum abzusehen, wie weit die Einrichtung und Wartung meines Rechners ohne ihn gediehen wäre. Desweiteren danke ich ihm für das sorgfältige und kritische Korrekturlesen meiner Arbeit sowie für seine Unterstützung bei der Anwendung der Kirchhoff-Migration.

Steffen Bergler danke ich neben dem Korrekturlesen der Arbeit für die Unterstützung bei meinem Kampf mit `Maple` und bei der Verarbeitung und Visualisierung der *ray tracing*-Ergebnisse.

Yonghai Zhang hat sich sehr intensiv mit meiner Implementierung des *CRS stack* befasst. Dank seiner Hilfe konnten einige sehr subtile Probleme identifiziert und beseitigt werden.

Lebenslauf

Persönliche Daten

Name: Jürgen Mann
Geburtsdatum: 24. März 1968
Nationalität: deutsch
Geburtsort: Leonberg



Schulbildung

1974 - 1978 Friedrich-Schiller-Grundschule Renningen
1978 - 1983 Johannes-Kepler-Gymnasium Weil der Stadt
1983 - 1987 Gymnasium Renningen
01.06.1987 Allgemeine Hochschulreife

Berufsausbildung

1987 - 1990 Ausbildung zum Groß- und Außenhandelskaufmann

Hochschulausbildung

1991 - 1998 Studium der Geophysik
an der Universität Karlsruhe (TH)
03.03.1998 Diplom
seit 1998 Doktorand an der Fakultät für Physik
der Universität Karlsruhe (TH)